COMBUSTION STUDY OF MIXTURES RESULTING FROM A GASIFICATION PROCESS OF FOREST BIOMASS

Eliseu Monteiro Magalhaes

THÈSE
Pour l'obtention du Grade de

DOCTEUR DE L'ENSMA
ÉCOLE NATIONALE SUPÉRIEURE DE MÉCANIQUE ET D'AÉROTECHNIQUE

(Diplôme National – Arrêté du 7 Août 2006)

École Doctorale: SIMMEA

Secteur de Recherche: Énergétique, Thermique, Combustion

Présentée par:

Eliseu MONTEIRO MAGALHAES

****

COMBUSTION STUDY OF MIXTURES RESULTING FROM A GASIFICATION PROCESS OF FOREST BIOMASS

****

Directeurs de Thèse: Marc BELLENOUE et Nuno MOREIRA

****

Soutenue le 13 Mai 2011

JURY

Rapporteurs

Mme Christine ROUSSELLE, Professeur des Universités, POLYTECH'Orléans
M. Edgar FERNANDES, Professeur des Universités, IST, Lisbonne

Examinateurs

Mr. Marc Bellenoue, Professeur des Universités, ENSMA, Institut P', Poitiers
Mr. Nuno Afonso Moreira, Professeur des Universités, UTAD, Vila Real
Mr. Jérôme Bellètre, Professeur des Universités, Polytech Nantes, Nantes
Mr. Julien Sotton, Maître de Conférences, ENSMA, Institut P', Poitiers
Mr. Abel Rouboa, Professeur des Universités, UTAD, Vila Real
Mr. Salvador Malheiro, Ingénieur, Docteur ès Sciences, ENGASP, Portugal

Acknowledgements

This dissertation has greatly benefited from the help, interest and support of many people from many parts of the world at who I would like to extend my deepest gratitude. Additional commendation goes to *Fundação para a Ciência e a Tecnologia* for the financial support through the research grant SFRH/BD/32699/2006.

First and foremost I am grateful to Professor Marc Bellenoue (ENSMA), Professor Nuno Afonso Moreira (UTAD) and Prof. Salvador Malheiro (UTAD) for their valuable help and research guidance. I am also indebted to Professor Julien Sotton (ENSMA) and Dr. Serguei Labouda (ENSMA) for guiding me to perform experimental work at the laboratory; to Dr. Bastien Boust (ENSMA), Dr. Camile Strozzi (ENSMA) and Mr. Djamel Karmed (ENSMA) for the assistance on numerical simulations.

Furthermore, I am grateful to Professor Zuohua Huang, from Xi'an JiaoTong University, China, and Dr. Xiaojun Gu, from Daresbury Laboratory, Warrington, United Kingdom, for the useful comments on laminar burning velocity calculations; to Professor Federico Perini, from University of Modena, Italy, for providing experimental data on methane engine; to Professor Sebastian Verhelst, from University of Gent, Belgium, for providing experimental data on hydrogen engine.

My sympathy goes also to the ENSMA staff especially to Mrs. Jocelyne Bardeau for her administrative support.

Finally, and most important, my thanks to my family and friends, who have continually demonstrated support in this long journey.

Résumé

Les gaz de synthèse (Syngas) sont reconnus comme sources d'énergie viables, en particulier pour la production d'électricité. Lors de cette étude, trois compositions de syngas ont été retenues. Elles sont représentatives de gaz issus de la gazéification de la biomasse forestière. Leur potentiel dans des systèmes de production d'énergie utilisant un Moteur à Combustion Interne (MCI) a été étudié. Leur vitesse de flamme en régime laminaire a été déterminée à partir de visualisation par strioscopie. Les effets du taux d'étirement ont été quantifiés au travers de la détermination du nombre de Karlovitz et de Markstein. En raison des lacunes de la littérature sur les caractéristiques de combustion de ces syngaz, la méthode de combustion sphérique a été utilisée pour déterminer la vitesse de flamme sur un domaine de pression de 1 à 20 bars. Ces résultats ont ensuite été utilisés dans un code de simulation multi-zones prenant en compte les transferts de chaleur aux parois afin d'estimer la distance de coincement.

Une analyse en régime turbulent a été menée en Machine à Compression Rapide (MCR), machine capable de reproduire un cycle compression-détente d'un moteur à combustion interne. En général, les applications stationnaires de production électrique utilisent le gaz naturel comme carburant, mélange majoritairement constitué de méthane. Pour servir de référence à la comparaison des capacités des trois syngaz retenus, un mélange méthane-air a été testé également. Afin d'identifier les différents paramètres liés au fonctionnement de la MRC, en particulier les transferts de chaleur aux parois, des essais sans combustion ont été réalisées.

Enfin un code de simulation du cycle d'un moteur à piston utilisant ces syngaz comme combustible a été développé. Sa validation a été réalisée en utilisant les données expérimentales disponibles dans la littérature concernant des mélanges hydrogène-air et méthane-air, et également à l'aide des données obtenues sur la MCR. Le modèle a finalement été utilisé pour déterminer les performances d'un moteur à piston fonctionnant avec ces sysngaz. Il a été observé que les compositions typiques de syngas, même avec des capacités calorifiques et la vitesse de flamme plus faibles, peuvent être utilisées pour les moteurs à allumage commandée et ceci à des vitesses de rotation élevées.

Mots-clés : Gazéification – Syngas -Combustion – Vitesse de flamme – Machine à compression rapide – Modélisation multizone.

Resumo

O syngas é mundialmente reconhecido como uma fonte de energia viável em particular para aplicações estacionárias. Neste trabalho, três composições típicas de syngas foram consideradas representativas do gás proveniente da gaseificação de biomassa florestal e estudada a possibilidade da sua utilização em motores de combustão interna. Primeiro, a velocidade de chama laminar fora determinada a partir de fotografia de schlieren a pressão constante. Em adição, o estudo dos efeitos da perturbação da chama é realizado através da obtenção dos números de Karlovitz e Markstein. Em segundo lugar, e dado existir lacunas na compreensão das características fundamentais da combustão de gás de síntese, em especial a pressões elevadas relevantes para aplicações práticas da combustão, é determinada a velocidade de chama laminar a volume constante para pressões até 20 bar. Esta informação é aplicada num código de simulação multi-zona da interacção chama-parede de modo a determinar a distância de extinção de chama. A combustão turbulenta em condições semelhantes ao motor de combustão interna (MCI) é reproduzida em máquina de compressão rápida (MCR) funcionando em modo de compressão seguido de expansão simulando o ciclo de potência de um MCI. As aplicações de produção de energia de pequena escala usam habitualmente gás natural como combustível, deste modo o metano é também incluído neste trabalho por questões de comparação de performance com as composições típicas de syngas em estudo. Testes de compressão são também realizados em MCR operando com e sem combustão de modo a identificar os diferentes parâmetros de funcionamento, nomeadamente a transferência de calor na parede. Um modelo termodinâmico de simulação do ciclo de potência de um MCI é desenvolvido. A sua validação é efectuada por comparação com dados de pressão obtidos na literatura para hidrogénio e metano. O modelo é ainda adaptado para a MCR por alteração de vários aspectos do mesmo, nomeadamente a função de volume do cilindro e o modelo de velocidade de chama. O código mostrou-se adequado para simular a evolução da pressão no interior do cilindro. O modelo validado é então aplicado a MCI a syngas de modo a determinar a sua performance. Conclui-se que as composições típicas de syngas, apesar do seu baixo poder calorífico e velocidade de chama, podem ser utilizadas em MCI a elevada velocidade de rotação.

Palavras-chave: Gaseificação – Syngas – Combustão – Velocidade de chama – Máquina de compressão rápida – Modelação multi-zona.

Nomenclature

Roman

A	Area of flame surface (m^2)
a	Cross section (m^2)
B	Bore (m)
c_p	Specific heat under constant pressure (J/kg.K)
c_v	Specific heat under constant volume (J/kg.K)
D	Diameter (m)
E_i	Ignition energy (J)
f	Focal length (m)
g_p	Pressure gain (bar)
h	Convective heat transfer coefficient ($W/m^2.K$)
h_g	Global heat transfer coefficient ($W/m^2.K$)
H(t)	Instantaneous height of chamber (m)
I	Current intensity (A)
k	Turbulence kinetic energy (m^2/s^2)
Ka	Karlovitz number
L(t)	Instantaneous combustion chamber height (m)
L_b	Markstein length of burned gases (m)
L_e	Lewis number
L_u	Markstein length of unburned gases (m)
m	Mass (kg)
M	Molar mass (mol)
Ma	Markstein number
N	Engine speed (rpm)
n	Normal
P	Pressure (bar)
Pe	Peclet number
$P_{mot\ (t)}$	Instantaneous motored cylinder pressure (bar)
Q_{WC}	Convective heat flux (W)
Q_{wr}	Radiative heat radiative flux (W)
r	Radius of burned gases sphere (m)
R	Radius of the spherical vessel (m)

R_u	Universal gas constant =8.314 J/Kmol.K
sp	Mean piston speed (m/s)
S_g	Unburned gas velocity (m/s)
S_n	Stretched Flame speed (m/s)
S_n^0	Unstretched Flame speed (m/s)
S_u	Stretched laminar burning velocity (m/s)
S_u^0	Unstretched laminar burning velocity (m/s)
T	Temperature (K)
t	Time (s)
U	Internal energy (J)
W	Lambert function
V	Volume (m^3); Voltage (V)
V_s	Swept volume (m^3)
x,y,z	Cartesian coordinates

Greek

α	Thermal diffusivity (W/m.K)
δ	Flame thickness (m)
δ_q	Quenching distance (m)
Δt	Time step (s)
ε	Compression ratio; emissivity
ϕ	Equivalence ratio
φ	Crank radius to piston rod length ratio
γ	Ratio of specific heat capacities (c_p/c_v)
η	Combustion efficiency (%)
κ	Stretch rate (s^{-1})
λ	Thermal conductivity (W/m.K)
μ	Kinematic viscosity (m^2/s)
θ	Angle
ρ	Density (kg/m^3)
σ	Stefan's constant ; Expansion factor
τ	Combustion time (s)

Subscripts

b	Burned
c	Curvature
d	Discharge
e	Final (end) condition
i	Initial conditions
g	Fresh gas
m	Mixture
n	Normal
max	Maximum
r, θ, ϕ	Spherical coordinates
s	Strain
u	Unburned
w	Wall
v	Adiabatic
0	Reference conditions

Superscripts

0	Unstretched
α	Temperature parameter
β	Pressure parameter

Abbreviations

ATDC	After top dead center
BDC	Bottom dead center
BTDC	Before top dead center
ºCA	Degrees of crank angle
CI	Compression ignition
EVC	Exhaust valve closing time
EVO	Exhaust valve opening time
HHV	Higher heating value
ICE	Internal combustion engine
IPCC	Intergovernmental Panel on Climate Change

IVC	Intake valve closing time
IVO	Intake valve opening time
LFL	Lower flammability limit
LHV	Lower heating value
RCM	Rapid compression machine
SI	Spark ignition
TDC	Top dead center
UFL	Upper flammability limit

Contents

CHAPTER 1

INTRODUCTION

One of the most debated environmental issues of the actuality is the global warming, which is caused by an enhanced greenhouse effect. Even though this issue is connected with large uncertainties, for instance the effects of climate change that might result in, the majority of scientists now agree that global warming is taking place and is caused by increased concentrations of greenhouse gases in the atmosphere.

Earth's temperature is determined by the greenhouse effect process, where the incoming short wave radiation from the sun is balanced by outgoing long wave radiation of the Earth's surface (Elvingson and Luften, 2001). This balance is, for example, affected by the absorption of outgoing radiation, which occurs in the atmosphere. Carbon dioxide (CO_2), water vapor (H_2O) and methane (CH_4) are examples of greenhouse gases absorbing long wave radiation in the atmosphere, hence contributing to a higher temperature at the Earth's surface. The share of the reflected radiation is known as the greenhouse effect and this is part of radiation that raises the mean temperature of the surface of the planet about 40°C above than they would be if there is no absorption. That is, the mean temperature on Earth would be about -15ºC (Hinrichs and Kleinbach, 2004). However, increased man-made concentrations of atmospheric greenhouse gases enhance the natural greenhouse effect and thus raise the mean temperature further. The Intergovernmental Panel on Climate Change, has estimated that the average temperature at the Earth's surface has increased by 0.6°C (with an uncertainty interval of ±0.2°C) during the last century.

The most significant greenhouse gas is CO_2, which contributes to the major part of the global warming. The main anthropogenic source of CO_2 is the burning of the fossil fuels such as coal, oil and natural gas. Energy supply is, to a large extent, comprised by fossil fuels, which have resulted in an increased atmospheric concentration of CO_2. The demand for energy has grown steadily last century and continues to grow nowadays. At the same time, the demand to decrease the use of fossil fuels is imperative in order to avoid severe consequences due to a changed climate. The main determinations of Kyoto Protocol, in order to tackle the climate change problem on a long-term basis, are the need of industrialized countries to reduce significantly their greenhouse gas emissions. To do this, different measures can be applied, for example a strong reduced energy use due to improved efficiencies and a shift from fossil fuels to renewable fuels.

The effort in recent years has enabled renewable energy to become more competitive compared with fossil fuels and nuclear energy. Biomass is an example of renewable energy that has been considered an interesting source of energy, particularly because:

- allows null net emission of CO_2 into the atmosphere, due to photosynthesis (Bhattacharya, 2001). The CO_2 assimilated by the biomass during growing phase corresponds to the amount of carbon in the biomass composition, about 48% in mass (Capintieri et al., 2005). Thus, for each kilogram of carbon in the biomass about 3,67 kg of CO_2 have been subtracted from the atmosphere;
- It is a by-product of low cost in agriculture or forest;
- It has enormous potential especially in the northern hemisphere.

Biomass has always been a major source of energy for mankind and is presently estimated to contribute of the order 10–14% of the world's energy supply. The IPCC advances that biomass will represent approximately 32% of global energy use in the year 2050. Their thermochemical conversion helps to improve the balance of carbon dioxide, nitrogen oxides and sulphur in the atmosphere, which is one of the main reasons that make the growing trend towards the use of biomass.

According with the European Directive 2001/77/EC biomass is the "biodegradable fraction of products and waste from agriculture (including plant and animal substances) of forest and related industries as well as the biodegradable fraction of industrial waste and urban." Thus, all belong to biomass plants and animals including all wastes and, more broadly, the organic waste processed as the wood processing industry and food industry.

Biomass can be converted into three main products: two related to energy – power/heat generation and transportation fuels – and one as a chemical feedstock (McKendry, 2002a). Conversion of biomass to energy is undertaken using two main process technologies: thermo-chemical and bio-chemical/biological. Bio-chemical conversion encompasses two process options: digestion (production of biogas, a mixture of mainly methane and carbon dioxide) and fermentation (production of ethanol). Within thermo-chemical conversion four process options are available: combustion, pyrolysis, gasification and liquefaction. A distinction can be made between the energy carriers produced from biomass by their ability to provide heat, electricity and engine fuels. Only pyrolysis and gasification can provide fuel as end product. Pyrolysis is adequate to produce liquid fuels and gasification to produce gaseous fuel. Table 1.1 shows the conversion efficiencies of both technologies, where gasification

proves to have higher efficiency. In fact, gasification is seen as one of the most promising ways to produce energy from biomass (Knoef, 2003).

Table 1.1 - Thermo-chemical processes efficiency (Bridgwater, 2003)

Process	Liquid	Coal	Gas
Pyrolysis	75%	12%	13%
Gasification	5%	10%	85%

The main attraction of this technology is the production of a fuel gas, elsewhere called produced gas or syngas, which can be used into an engine or turbine for power production. Besides, the low heating value of syngas its advantages over conventional combustion in terms of pollutants emissions, particularly of nitrous oxides (NO_x) and soot are determinant for its use.

1.1 Motivation and objective

Syngas obtained from gasification of biomass is considered to be an attractive new fuel, especially for stationary power generation. The research in this field has been focused upstream the syngas production, and therefore there is a lack of knowledge at the downstream level of the syngas production manly as far as combustion characteristics is concerned.

The considerable variation of syngas composition is a challenge in designing efficient end use applications such as burners and combustion chambers to suit changes in fuel composition. Designing such combustion appliances needs fundamental understanding of the implications of variation of different constituents of syngas fuel for its combustion characteristics, such as the burning velocity.

Burning velocity values for single component fuels such as methane and hydrogen are abundantly available in the literature for various operating conditions. Some studies on burning velocities are also available for binary fuel mixtures such as H_2–CH_4 (Halter et al., 2005; Coppens et al., 2007), and H_2–CO (Vagelopoulos and Egolfopoulos, 1994; McLean et al., 1994; Brown et al., 1996; Sun et al., 2007).

Natarajan et al., (2007) test an equally weighted, 50:50 H_2-CO, fuel mixture with 0 and 20% CO_2 dilution. Prathap et al. (2008) study the effect of N_2 dilution on laminar burning velocity and flame structure for H_2–CO (50% H_2–50% CO by volume) fuel mixtures. All these studies use unreal syngas compositions. Therefore, there is lack of knowledge in the fundamental combustion characteristics of actual syngas compositions where there is a combined effect of N_2 and CO_2 dilution in the H_2-CO-CH_4 fuel gases that composes the actual syngas fuel. This motivated the present work to

choose three typical compositions of syngas considered as mixture of five gases (H_2-CO-CH_4-CO_2-N_2) and make its combustion characterization under laminar and turbulent conditions with the objective to its application in stationary energy production systems based on internal combustion engines.

1.2 Thesis layout

This work was divided into seven chapters with the following contains:

Chapter 1– Introduction

In this introductory chapter a brief overview about the environmental problems caused by the extensively use of fossil fuels is given in order to provide reasons for the increasing use of renewable energy sources with focus on biomass. The technologies for converting biomass into fuels are summarized. The use of gasification as the right technology to apply when a gas fuel is the final product is justified, which was the spark that motivates this work. The objectives are defined.

Chapter 2 – Bibliographic revision

This chapter touches upon two topics of interest for the present work - gasification and combustion. A global perspective of the gasification process is given, namely: its definition, the main chemical reactions, the main types of reactors, the typical composition of the syngas, the end use for the syngas as well as the technical problems that still remains in this technology, pointing out the necessary research lines.

The influence of various process parameters in the final composition of the syngas is evaluated based on bibliographical data. It is evaluated the influence in the final composition of the syngas of biomass kind, reactor type, oxidizer and the reactor operational conditions.

The syngas coming from a gasification process is under study for energy proposes. This is accomplished by combustion. Therefore, premixed flames combustion theory is revised. Stretch rate and the corresponding Karlovitz and Markstein numbers are defined. Following, the experimental methods for burning velocity determination are described with emphasis for the constant volume and constant pressure methods.

Chapter 3 – Experimental set up and diagnostics

In this chapter the experimental devices used in this work are illustrated. The experimental procedures are described. The flammability limits of typical syngas syngas compositions are determined and several other combustion parameters like the combustion efficiency and pressure gain.

Chapter 4 – Experimental and numerical laminar syngas combustion

In this chapter, the experimental study of three typical syngas compositions is presented in terms of burning velocity, Markstein lengths and Karlovitz number. Constant volume spherically expanding flames are used to determine a burning velocity correlation valid for engine conditions.
This information about laminar burning velocity of syngas-air flames is then applied on a multi-zone numerical heat transfer simulation code of the wall-flame interaction. The adapted code allows simulating the combustion of homogeneous premixed gas mixtures within constant volume spherical chamber in order to predict the quenching distance of typical syngas-air flames.

Chapter 5 – Experimental study of engine-like turbulent syngas combustion

An experimental approach to syngas engine-like conditions on a rapid compression machine is made. Engine-like conditions can be reproduced in a RCM when working on two strokes mode simulating a single cycle of an internal combustion engine working with typical syngas compositions. Together with pressure measurements, direct visualizations are also carried out to follow the early stage of the ignition process.

The study of the compression process in a RCM operating without combustion is useful to identify different parameters related with its operation, namely the heat transfer to the walls. Once determined, these parameters can also be used during the usual firing cycle. In fact, a common practice in engine testing for combustion diagnostic is, prior to the usual firing tests. Stationary power applications usually use natural gas as fuel, thus a methane-air mixture, the main constituent of the natural gas, is also included in our work as a reference for comparison with syngas compositions.

Chapter 6 – Numerical simulation of a syngas engine

In this chapter a multi-zone thermodynamic combustion model is presented. The purpose is the prediction of the engine in-cylinder pressure. The validation of the code is made by comparison with experimental literature data and in addition with the rapid

compression machine results obtained in this work. For this propose some adaptations to the engine-like code are needed and are shown in advance.

Chapter 7 – Conclusions

In this last chapter a summary of the present work is made emphasizing the principal findings. As any research project is an open narrative some perspectives for future developments are also presented.

CHAPTER 2

BIBLIOGRAPHIC REVISION

This work touches upon mainly the topics of gasification and combustion. The syngas coming from a gasification process is under study for energy proposes. Therefore, a global perspective of the gasification process is given with emphasis in the gasification technologies and the dependence of the final syngas composition from the various parameters of the process.

Energy production based on syngas is accomplished by combustion. Therefore, premixed flames combustion theory is revised. Following, the experimental methods for burning velocity determination are described with emphasis for the constant volume and constant pressure methods.

2.1 Biomass gasification

2.1.1 Historical development

Wood, coal and charcoal gasifiers have been used for operation of internal combustion engines in various applications since the beginning of the 20th century. The utilization peaked during the Second World War when almost a million gasifiers were used all over the world, mainly vehicles operating on domestic solid fuels instead of gasoline.
Interest in the technology of gasification has shown a number of ups and downs since its first appearance. It appears that interest in gasification research correlates closely with the relative cost and availability of liquid and gaseous fossil fuels. These are the cases of the Second World War, the double fuel crises of 1973 and 1979, and nowadays the scarcity and rising oil prices. The relevant historical dates of gasification development are the following:

1788: Robert Gardner obtained the first patent with regard to gasification;

1792: First confirmed use of syngas reported, William Murdoch used the gas generated from coal to light a room in his house. Since then, for many years coal gas was used for cooking and heating;

1801: Lampodium proved the possibility of using waste gases escaping from charring of wood;

1812: Developed first gasifier which uses oil as fuel;

1840: First commercially used gasifier was built in France;

1850: most of the city of London was illuminated by ‘‘town gas’’ produced from the gasification of coal.

1861: Real breakthrough in technology with introduction of Siemens gasifier. This gasifier is considered to be first successful unit;

1878: Gasifiers were successfully used with engines for power generation;

1900: First 600 hp gasifier was exhibited in Paris. Thereafter, larger engines up to 5400 hp were put into service;

1901: J.W. Parker runs a passenger vehicle with syngas;

1901 to 1920: In the period 1901-1920, many gasifier-engine systems were sold and used for power and electricity generation;

1930: Nazi Germany accelerated effort to convert existing vehicles to syngas drive as part of plan for national security and independence from imported oil. Begin development of small automotive and portable gasifiers. British and French Governments felt that automotive charcoal syngas is more suitable for their colonies where supply of gasoline was scarce and wood that could charred to charcoal was readily available

1939: About 250,000 vehicles were registered in Sweden. Out of them, 90% were converted to syngas drive. Almost all of the 20,000 tractors were operated on syngas. 40% of the fuel used was wood and remainder charcoal.

Figure 2.1- Motor vehicle and tractor converted to run on syngas.

1940 to 1945: more than one million vehicles run in Europe during World War II with syngas due to shortages of gasoline (Reed and Das, 1988). However, the low value of fossil fuels soon after the war caused by the interruption and disaffection gasification

point today to be difficult to reproduce in the laboratory that was routine in the decade of 40.

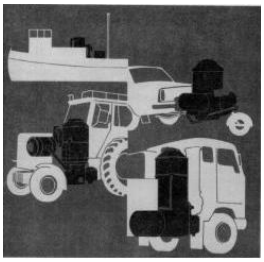

Figure 2.2 - Inland Sea and converted vehicles to run on syngas

1945: After end of Second World War, with plentiful gasoline and diesel available at low cost, gasification technology lost glory and importance.

1950 - 1970: During these decades, gasification was a “Forgotten Technology ". Many governments in Europe felt that consumption of wood at the prevailing rate will reduce the forest, creating several environmental problems.

The year 1970´s brought a renewed interest in the technology for power generation at small scale. Since then work is also concentrated to use fuels other than wood and charcoal.

Currently, due to the rising petroleum prices and the environmental problems associated with its use, it becomes imperative to search for alternatives and gasification is historically the chosen technology.

2.1.2 Gasification process

Gasification is the thermo-chemical conversion of a carbonaceous fuel at high temperatures, involving partial oxidation of the fuel elements (Higman and Burgt, 2003). The result of the gasification is a fuel gas - the so-called syngas - consisting mainly of carbon monoxide (CO), hydrogen (H_2), carbon dioxide (CO_2), water vapor (H_2O), methane (CH_4), nitrogen (N_2), some hydrocarbons in very low quantity and contaminants, such as carbon particles, tar and ash.

Gasification takes place in a reactor, called gasifier, in the presence of an oxidizing agent that may be the pure oxygen, steam, air or combinations of these. Inside the gasifier, regardless of their nature, occur simultaneously in several cases for which there is still no consensus within the scientific community. Three or four steps are usually referred to. In the context of thermal sciences, the reactions of gasification are

only those that occur between the gas and solid fuel devolatilized excluding the oxygen (Sousa-Santos, 2004). However, in general terms gasification is the partial or total transformation of a solid fuel into gas. Thus also the devolatilization and oxidation are an integral part of gasification.

In this work it is considered that gasification occurs in a set of four steps: drying, pyrolysis, oxidation and reduction (Demirbaş, 2002) with the following description:

- Drying – biomass fuels consist of moisture ranging from 5 to 35%. At temperatures above 373 K, the water is removed and converted into steam. In the drying, fuels do not experience any kind of decomposition.
- Pyrolysis – is the thermal decomposition of biomass in the absence of oxygen whereby the volatile components of a solid carbonaceous feedstock are vaporized in primary reactions by heating, leaving a residue consisting of char and ash. The ratio of products is influenced by the chemical composition of biomass fuels and the operating conditions.
- Oxidation – introduced air in the oxidation zone contains, besides oxygen and water vapors, inert gases such nitrogen and argon. These inert gases are considered nonreactive with fuel constituents. The oxidation takes place at temperatures of 975 to 1275 K. Heterogeneous reaction takes place between oxygen in the air and solid carbonized fuel, producing carbon monoxide. Plus and minus signs indicate the release and supply of heat energy during the process, respectively:

  $C + O_2 = CO_2 + 393.8$ MJ / kmol

Hydrogen in the fuel reacts with oxygen in the air blast, producing steam.

$H_2 + 1/2\ O_2 = H_2O + 242$ MJ / kmol.

- Reduction - in the reduction zone, a number of high temperature chemical reactions occur in the absence of oxygen. Assuming a gasification process using biomass as a feedstock, the first step of the process is the thermochemical decomposition of the lignocelluloses components with production of char and volatiles. The main gasification reactions that occur in the reduction are mentioned below (Maschio et al., 1994; Demirbaş, 2000; Neto et al., 2005):

- Boudouard reaction - balance between the reaction of carbon and its phases gaseous CO and CO_2. It is the reaction of Boudouard the limiting step of the reduction process.

$CO_2 + C = 2CO - 172.6$ MJ / kmol

- steam reaction

$C + H_2O = CO + H_2 – 131.4$ MJ / kmol

- water-shift reaction

$CO_2 + H_2 = CO + H_2O + 41.2$ MJ / kmol

- methanation

$C + 2H_2 = CH_4 + 75$ MJ / kmol

Main reactions show that heat is required during the reduction process. Thus, the temperature of the gas goes down during this stage. If complete gasification occurs, all the carbon is burned or reduced to carbon monoxide, and some other mineral matter that is vaporized. The remains are ash and some char (unburned carbon). Other reactions occur during the gasification process, such as: $C + CO_2 = 2CO$ and $CH_4 + H_2O = CO + 3H_2$.

Gasification process can be classified according to various criteria. The most important are:

Gasification process:

- Atmospheric;
- Pressurized.

Gasifier type:

- Fixed;
- Fluidized.

Oxidizing agent:

- Air;

- Oxygen;
- Steam;
- Other gases containing oxygen, such as CO_2 (Gañan et al., 2005).

Gasifier heating:

- Direct ;
- Indirect.

Heating value (McKendry, 2002b):

- Low: 4 -6 MJ/Nm^3 (using air or air / steam);
- Medium: 12 -18 MJ/Nm^3 (using oxygen and steam);
- High: 40 MJ/Nm^3, using hydrogen and hydrogenation.

2.1.3 Gasification plant

A gasification plant consists into three main units (McKendry, 2002a):

- Gasification unit – the reactor,
- Cleaning unit - filtration and cooling, and
- Energy conversion unit.

These are briefly described in the following sections.

2.1.3.1 Gasifier types

A variety of biomass gasifier types have been developed. They can be grouped into four major classifications: fixed-bed updraft, fixed-bed downdraft, bubbling fluidized-bed and circulating fluidized bed. Differentiation is based on the means of supporting the biomass in the reactor vessel, the direction of flow of both the biomass and oxidant, and the way heat is supplied to the reactor (Rampling and Gill, 1993). Table 2.1 lists the most commonly used configurations.

Table 2.1 – Gasifier classification (Reed and Siddhartha, 2001; Bridgwater and Evans, 1993)

Gasifier	Flow direction		Support	Heat source
	Fuel	Oxidant		
Fixed bed -Updraft	Descending	Ascending	Grate	Coal partial combustion
Fixed bed- Downdraft	Descending	Descending	Grate	Volatile partial combustion
Fluidized bed - Bubbling	Ascending	Ascending	None	Coal and volatile partial combustion
Fluidized bed- Circulating	Ascending	Ascending	None	Coal and volatile partial combustion

These types are reviewed separately below.

2.1.3.2 Fixed bed gasifiers

Typically the fixed bed gasifiers have a grate that serves to support the solid fuel and to maintain the area's reaction stationary. They are relatively easy to deploy and operate, and more suitable for applications from small or medium power (under 1 MW). However, there is some difficulty in maintaining uniform temperatures and ensure appropriate mixtures in the area of reaction. As a result, income is variable and the final composition of the gas fuel obtained. The two main types of fixed bed gasifiers are: counter-current (updraft) and co-current (downdraft).

Updraft

The oldest and simplest type of gasifier is the counter current or updraft gasifier shown schematically in Fig.2.3.

In the updraft gasifier the downward-moving biomass is first dried by the upflowing hot product gas. After drying, the solid fuel is pyrolysed, giving char which continues to move down to be gasified, and pyrolysis vapours which are carried upward by the upflowing hot product gas. The tars in the vapour either condense on the cool descending fuel or are carried out of the reactor with the product gas, contributing to its high tar content. The extent of this tar ‘bypassing’ is believed to be up to 20% of the pyrolysis products. The condensed tars are recycled back to the reaction zones, where they are further cracked to gas and char. In the bottom gasification zone the solid char from pyrolysis and tar cracking is partially oxidized by the incoming air or oxygen. Steam may also be added to provide a higher level of hydrogen in the gas.

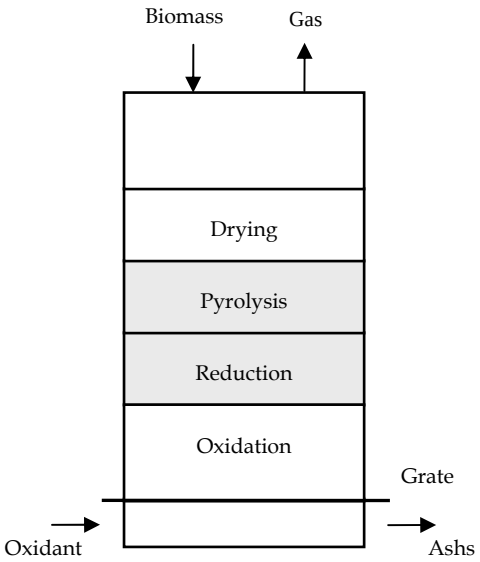

Figure 2.3 – Updraft gasifier

The advantages of updraft gasification are:

- simple, low cost process;
- able to handle biomass with a high moisture and high inorganic content;
- proven technology.

The primary disadvantage of updraft gasification is:

- syngas contains 10-20% tar by weight, requiring extensive syngas cleanup before engine, turbine or synthesis applications.

Downdraft

Downdraft gasification also known as co-current-flow gasification is simple, reliable and proven for certain fuels. The downdraft gasifier has the same mechanical configuration as the updraft gasifier except that the oxidant and product gases flow down the reactor, in the same direction as the biomass. A major difference is that this process can combust up to 99 % of the tars formed (Reed and Das, 1988). Low moisture biomass (<20%) and air or oxygen are ignited in the reaction zone at the top of the reactor. The flame generates pyrolysis gas/steam, which burns intensely leaving 5 to 15% char and hot combustion gas. These gases flow downward and react with the char at 800 to 1200ºC, generating more CO and H_2 while cooled to below 800ºC. Finally, unconverted char and ash (< 1 wt%) pass through the bottom of the grate and are sent to disposal.
Owing to the low content of tars in the gas, this configuration is generally favoured for small-scale electricity generation with an internal combustion engine. The physical limitations of the diameter and particle size relation mean that there is a practical upper limit to the capacity of this configuration of about 500 kg/h or 500 kW_e.

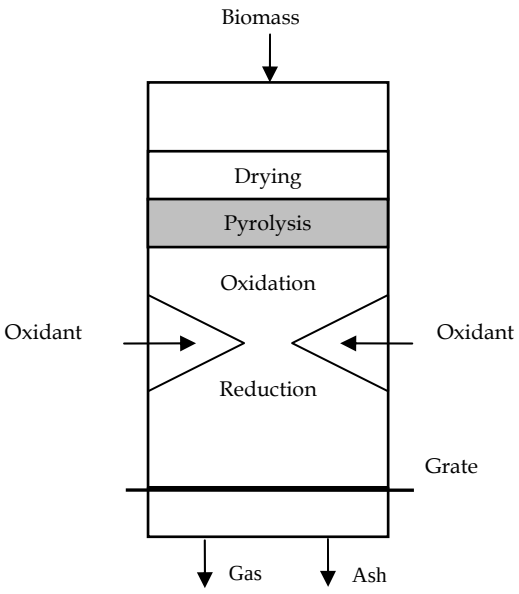

Figure 2.4 – Downdraft gasifier

The advantages of this gasifier are (Ciferno and Marano, 2002):

- About 99,9% of tar formed is consumed, requiring minimal or no tar cleanup;
- Minerals remain with the char /ash, reducing the need for a cyclone;
- Proven technology, simple and low cost process.

The disadvantages are:

- Requires feed drying to a low moisture content (<20%);
- The fuel gas produced leaves the gasifier the high temperatures, requiring cooling before use;
- 4 to 7% of carbon is not converted.

2.1.3.3 Fluidized bed gasifiers

Fluidized bed (FB) gasification has been used extensively for coal gasification for many years, its advantage over fixed bed gasifiers being the uniform temperature distribution achieved in the gasification zone. The uniformity of temperature is achieved using a bed of fine grained material into which air is introduced, fluidizing the bed material and ensuring intimate mixing of the hot bed material, the hot combustion gas and the biomass feed. Two main types of FB gasifier are in use:

- Circulating fluidized bed,
- Bubbling bed.

A third type of FB is currently being developed, termed a fast, internally circulating gasifier, which combines the design features of the other two types. The reactor is still at the pilot-stage of development (McKendry, 2002a).

Bubbling fluidized bed (BFB)

Bubbling FB gasifiers consist of a vessel with a grate at the bottom through which air is introduced. Above the grate is the moving bed of fine-grained material into which the prepared biomass feed is introduced. Regulation of the bed temperature to 700–900º C is maintained by controlling the air/biomass ratio. The biomass is pyrolysed in the hot bed to form a char with gaseous compounds, the high molecular weight compounds being cracked by contact with the hot bed material, giving a product gas with a low tar content, typically <1–3 g/Nm^3.

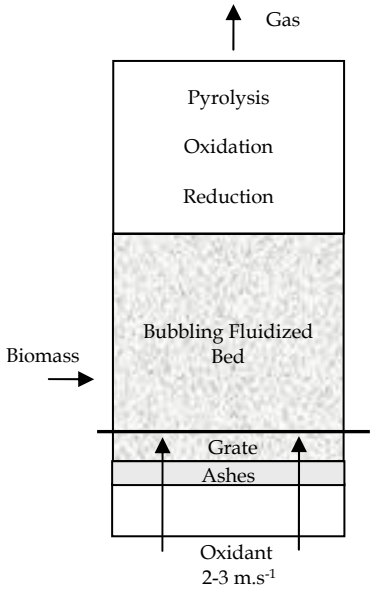

Figure 2.5 – Bubbling Fluidized Bed

The advantages of bubbling fluidized bed gasification are (Bridgwater and Evans, 1993):

- Yields a uniform syngas;
- Nearly uniform temperature distribution throughout the reactor;
- Able to accept a wide range of fuel particles sizes;
- Provides high rates of heat transfer between the inert material, fuel and gas;
- High conversion possible with low tar and unconverted carbon.

The disadvantages are the large bubble size may result in gas bypass through the bed.

Circulating Fluidized bed (CFB)

Circulating FB gasifiers are able to cope with high capacity throughputs and are used in the paper industry for the gasification of bark and other forestry residues.
The bed material is circulated between the reaction vessel and a cyclone separator, where the ash is removed and the bed material and char returned to the reaction vessel. Gasifiers can be operated at elevated pressures, the advantage being for those end-use applications where the gas is required to be compressed afterwards, as in a gas turbine.

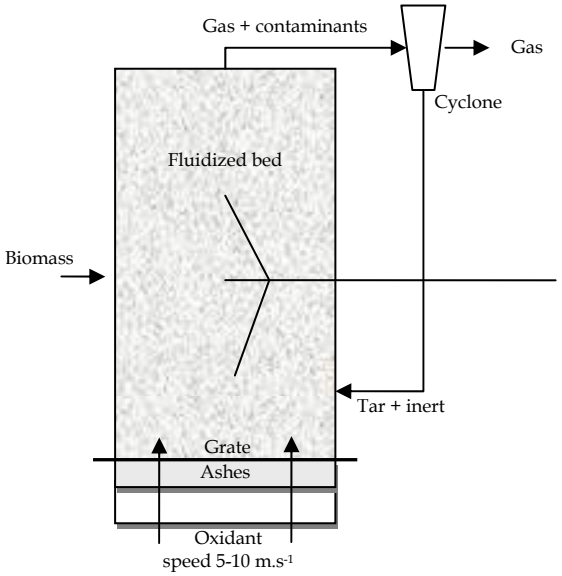

Figure 2.6 - Circulating fluidized bed gasifier

The advantages of such gasifier are (Bridgwater and Evans, 1993):

- Suitable for rapid reactions;
- High heat transport rates possible due to high heat capacity of bed material;
- High conversion rates possible with low tar and unconverted carbon.

. The disadvantages are (Bridgwater and Evans, 1993):

- Temperature gradients occur in direction of the solid flow;
- Size of fuel particles determine minimum transport velocity; high velocities may result in equipment erosion;
- Heat transfer less efficient than bubbling fluidized bed.

Apart from the described gasifiers, there are several other models that have been developed to improve the quality of the produced gas, such as: twin fluidized bed and entrained bed (Bridgwater, 1995). The first one aims to increase the heat value of the produced gas by promoting the production of H_2. The second operates at high temperatures 1200 to 1500°C in order to eliminate tar and condensable gases in the produced gas. In fact, it has conversion efficiencies close to 100%. However, some problems arise in the materials selection to withstand the high temperatures and liquefaction of ash. Readers interested in deepening this topic may consult the cited reference.

2.1.3.4 Syngas conditioning

Gases formed by gasification are contaminated by some or all of the constituents listed in Table 2.2. The level of contamination varies, depending on the gasification process and the feedstock. Gas cleaning must be applied to prevent erosion, corrosion and environmental problems in downstream equipment. Table 2.3 also summarizes the main problems resulting from these contaminants, and common cleanup methods.

Table 2.2 - Syngas contaminants (Bridgwater, 1995)

Contaminant	Examples	Problems	Cleanup method
Particulates	Ash, char, fluid bed material	Erosion	Filtration, scrubbing
Alkali metals	Sodium and potassium compounds	Hot corrosion	Cooling, condensation, filtration, adsorption
Nitrogen components	NH_3 e HCN	NO_x formation	Scrubbing, Selective catalytic reduction
Tars	Aromatics	Clog filters, difficult to burn, deposit internally	Tar cracking; Tar removal
Sulfur, Chloride	H_2S , HCl	Corrosion, emissions	Lime or dolomite scrubbing or absorption

Tars are mostly heavy hydrocarbons (such as pyrene and anthracene) that can clog engine valves, cause deposition on turbine blades or fouling of a turbine system leading to decreased performance and increased maintenance. In addition, these heavy hydrocarbons interfere with synthesis of fuels and chemicals. Conventional scrubbing systems are generally the technology of choice for tar removal from the product syngas. However, scrubbing cools the gas and produces an unwanted waste stream. Removal of the tars by catalytically cracking the larger hydrocarbons reduces

or eliminates this waste stream, eliminates the cooling inefficiency of scrubbing, and enhances the product gas quality and quantity.

2.2. Syngas applications

Applications for syngas can be divided into two main groups: fuels or chemical products and power or heat. Table 2.3 summarizes desirable syngas characteristics for various end-use options. In general, syngas characteristics and conditioning are more critical for fuels and chemical synthesis applications than for hydrogen and fuel gas applications.

Table 2.3 – Desirable syngas characteristics for different applications (Ciferno and Marano, 2002)

Product	Synthetic fuels	Methanol	Hydrogen	Fuel gas	
				Boiler	Turbine
H_2/CO	0.6 [(a)]	~2.0	High	Unimportant	Unimportant
CO_2	Low	Low [(c)]	Unimportant [(b)]	Not critical	Not critical
Hydrocarbons	Low [(d)]	Low [(d)]	Low [(d)]	High	High
N_2	Low	Low	Low	(e)	(e)
H_2O	Low	Low	High [(f)]	Low	(g)
Contaminants	<1ppm sulfur Low particulates	<1ppm sulfur Low particulates	<<1ppm sulfur Low particulates	(k)	Low particulates and metals
Heating value	Unimportant [(h)]	Unimportant (h)	Unimportant [(h)]	High [(i)]	High [(i)]
Pressure (bar)	~20-30	~50 (liquid phase) ~140 (vapor phase)	~28	Low	~400
Temperature (ºC)	200-300 [(j)] 300-400	100-200	100-200	250	500-600

(a) It depends on the catalyst type. For iron catalysts, value shown is satisfactory; for cobalt catalysts, near 2.0 should be used.
(b) Water gas shift will have to be used to convert CO to H_2; CO_2 in syngas can be removed at same as CO_2 is generated by the water gas shift reaction.
(c) Some CO_2 could be tolerated if the H_2/CO ratio remains above 2.0; if excess of H_2 is available, the CO_2 will be converted to methanol.
(d) Methane and heavier hydrocarbons need to be recycled for conversion to syngas and represent system inefficiency.
(e) N_2 lowers the heating value, but their percentage is not important as long as syngas can be burned with a stable flame.
(f) Water is required for the water gas shift reaction.
(g) Can tolerate relatively high water levels; steam sometimes added to moderate combustion temperature to control NOx.
(h) As long as H_2/CO ratio and impurities levels of impurities are met, heating value is not critical.
(i) Efficiency improves as heating value increases.
(j) Depends on the catalyst type, iron catalysts typically operate at temperatures higher than cobalt catalyst.
(k) Small amounts of contaminants can be tolerated.

A synthetic gas of high purity (i.e., low quantities of inerts such as N_2) is extremely beneficial for fuels and chemical synthesis since it substantially reduces the size and cost of downstream equipment. However, the guidelines provided in Table 2.3 should not be interpreted as stringent requirements. Supporting process equipment (e.g., scrubbers, compressors, coolers, etc.) can be used to adjust the condition of the

product syngas to match those optimal for the desired end-use, although, at added complexity and cost. Specific applications are discussed in more detail below.

2.2.1 Power production

Electricity generation is carried out by ICE, Stirling engines or turbines. Fuel cells have been proposed, but considerable development work is needed before these can be seriously considered. Data are available for gas turbines and engines operating on fossil fuels, but few robust data have been found on biomass-derived fuel gas machines, owing to the unknown costs of modification and maintenance and machine life.

Essentially all biomass power plants today operate on a steam-Rankine cycle. Biomass-steam turbine systems are less efficient than modern electricity coal-fired systems in large part due to more modest steam conditions. The modest steam conditions in biomass plants arise primarily because of the strong scale-dependence of the unit capital cost of steam turbine systems-the main reason coal and nuclear steam-electric plants are built at a large scale. Biomass plants are usually of modest scale (less than 100 MW), because of the dispersed nature of biomass supplies, which must be gathered from the countryside and transported to the power plant. If bio-electric plants were as large as coal or nuclear power stations (500-1000 MW), the cost of delivering the fuel to the plant would often be prohibitive. To help minimize the dependence of unit cost on scale, vendors use lower grade steels in the boiler tubes of small-scale steam-electric plants and make other modifications which reduce capital cost, but also require more modest steam temperatures and pressures, thereby leading to reduced efficiency. The best biomass steam-electric plants have efficiencies of 20-25% (Bridgwater, 1995). In order to make higher cost biomass resources economically interesting for power generation, it is necessary to have technologies which offer higher efficiency and lower unit capital cost at modest scale. One technological initiative aimed at improving the economics and efficiency of utility-scale steam cycle systems would use whole trees as fuel rather than more costly forms of biomass (e.g. woodchips).

Gasification with turbines

Gas turbines are noted for their efficiency; low emissions; low specific capital cost; short lead times by virtue of modular construction; high reliability and simple operation (Brander and Chase, 1992). Gas turbine integration with biomass gasification is not

established but there are many demonstration projects active with capacities 0.2-27 MW_e. There are several issues that must be resolved in the integration of gas turbines with biomass gasification, including:

- The reliable and environmentally sound operation of gas turbines with low heating value gases;
- The selection of gasification operating pressure and the consequent integration of the air flow to the gasifier and fuel gas flow to the gas turbine combustor with the rest of the system;
- Fuel gas cleaning and cooling;
- The selection of the gas turbine cycle, although generally combined cycles are preferred.

Gasification with engines

The operation of diesel and spark-ignition engines using a variety of low heating value gases is an established practice (Nolting and Leuchs, 1995; Vielhaber, 1996; Tschalamoff, 1997). Both dual fuel diesel and spark ignition engines for operation using low heating value gases may be regarded as fully developed, although integration of a biomass gasifier and engine is not fully established.

The main issue that must be resolved is the effective treatment of the fuel gas to cool and clean it to the specifications demanded by the engine. The fuel gas must be cool at injection to the engine and therefore wet scrubbing is the preferred gas treatment method (Bridgwater et al., 2002). In this approach the gases are cooled to under 150ºC and then passed though a wet gas scrubber. This removes particulates, alkali metals, tars and soluble nitrogen compounds such as ammonia.

Fuel cells

Fuel cells are static equipments that convert the chemical energy in the fuel directly into electrical energy. The operation principle of a fuel cell is similar to a battery. It is composed of a porous anode and a cathode, each coated on one side by a layer of platinum catalyst, and separated by an electrolyte. The anode is powered by the fuel, while the cathode is powered by the oxidant.

There are various different types of fuel cells:

- AFC - Alkaline Fuel Cell

- PEFC / PEM - Polymer Electrolyte Fuel Cell / Proton Exchange Membrane
- PAFC - Phosphoric Acid Fuel Cell
- MCFC - Molten Carbonate Fuel Cell
- SOFC - Solid Oxid Fuel Cell

SOFC fuel cell is the most suitable for integration with a gasifier (Klein, 2002). The kinetics of this cell is fast, and the CO in the syngas is a directly useable fuel. This type of fuel cell operates at a high temperature, and over 900°C the syngas can be reformed within the cell.

2.2.2 Fuels

Several synthetic fuels can be produced from syngas via the Fischer-Tropsch (FT) process. There are several commercial FT plants in South Africa producing gasoline and diesel from coal and natural gas.

The FT synthesis involves the catalytic reaction of H_2 and CO to form hydrocarbons chains of various lengths (CH_4, C_2H_6, C_3H_8, etc.). The FT synthesis reaction can be written in the general form (Ciferno and Marano, 2002):

$$(n/2+m)H_2 + mCO = C_mH_n + mH_2O \qquad (2.1)$$

where *m* is the average chain length of the hydrocarbons formed, and *n* equals *2m+2* when only paraffins are formed, and *2m* when only olefins are formed. Iron catalyst has water gas shift activity, which allows the use of syngas with low H_2/CO ratios. Syngas with H_2/CO ratios of 0.5 to 0.7 is recommended for iron catalysts. The water - gas shift reaction adjusts the ratio to match the requirements for hydrocarbon and produce CO_2 as the largest by-product.

On the other hand, cobalt catalysts do not have water-gas shift reaction activity, and H_2/CO ratio required is then (*2m + 2)/m*. Water is the primary by-product of FT synthesis over a cobalt catalyst.

As shown in Table 2.3, the composition of syngas required for fuel gas application is different from that required for the synthetic fuel or chemical synthesis. A high H_2, low CO_2 and low CH_4 content is essential for fuel or chemical production. In opposite, a high H_2 is not necessary for power production, as long as a high enough heating value is supplied by the CH_4.

Hydrogen

Hydrogen is currently produced in large quantities via steam reforming of hydrocarbons over a nickel catalyst at about 800ºC (Nieminen, 2004). This process produces a syngas that must be further processed to produce high-purity hydrogen. The syngas conditioning required for steam reforming is similar to that which would be required for a biomass gasification derived syngas. However, tars and particulates are not so worrying. To raise the hydrogen content, the syngas is fed to one or more water gas shift reactors, which converts CO in H_2 according with the reaction $CO + H_2O = H_2 + CO_2$.

Methanol

Methanol synthesis involves the reaction of CO, H_2 and steam in a copper-zinc oxide catalyst in the presence of small amounts of CO_2 at a temperature of about 260ºC and a pressure of about 70 bar (Paisley and Anson, 1997). The formation of methanol from syngas proceeds via the following reactions:

$CO + H_2O = H_2 + CO_2$ (water-gas shift reaction)
$3H_2 + CO_2 = CH_3OH + H_2O$ (hydrogenation of carbon dioxide)

$2H_2 + CO = CH_3OH$

Methanol production also occurs by means of direct hydrogenation of CO, but at a much slower rate (Engstrom, 1999):

$2H_2 + CO = CH_3OH$ (hydrogenation of carbon monoxide)

To best use the raw product syngas in methanol synthesis and limit the extent of additional treatment or steam reforming, it is essential to maintain the parameters indicated in Table 2.3.

2.3. Syngas characterization

The quality of the producer gas depends upon several factors including type of fuel, gasifier type and operational conditions (temperature, pressure and oxidizing agent). Following each one is described.

2.3.1 Influence of biomass type

In large samples there is a relatively constant atomic ratio of $C_{10}H_{14}O_6$ for all biomass kinds (Reed and Das, 1988). A direct link between the chemical composition of biomass and gas obtained by gasification exists. Table 2.4 shows experimental values of the chemical composition of syngas for different types of biomass in a downdraft gasifier.

Table 2.4 - Characteristics of syngas by biomass type

Residues	Gas produced (mol/kg)							HHV
	H_2	CO	CO_2	CH_4	C_2H_2	C_2H_4	C_2H_6	(MJ/m^3)
Rice husk [(a)]	0.00236	0.00651	0.00717	0.00209	6.2×10^{-5}	7.6×10^{-4}	1.1×10^{-4}	11.11
Nut shell [(a)]	0.00485	0.00788	0.00477	0.00293	4.9×10^{-5}	6.1×10^{-4}	2.1×10^{-4}	14.55
Pine [(a)]	0.00529	0.00722	0.00505	0.00272	1.2×10^{-4}	8.1×10^{-4}	1.7×10^{-5}	14.68
Eucalyptus [(a)]	0.00275	0.00712	0.00380	0.00316	2.6×10^{-5}	5.5×10^{-4}	1.5×10^{-4}	13.41
Vine Pruning [(b)]	0.0104	0.02378	-	0.00641	0.00199	8.8×10^{-4}	0.00121	11.41
Cherry Stone [©]	0.00639	0.00668	-	0.00371	0.00103	0.00217	0.00173	-

[a] (Gañan et. al., 2005) ; [b] (Cuellar, 2003), [c] (González et al., 2003).

As shown in Table 2.4 the influence of biomass type is not considerable. The highest heat value of the syngas obtained with pine and almond shell, being the lowest heat value obtained with husks.

The woods in the Table 2.4 (pine and eucalyptus) are largely the most available biomass resource in Portugal (Ferreira et al., 2009) and therefore some special attention should be given to them. The main combustible components of wood are cellulose, hemicelluloses, and lignin, which are compounds of carbon, hydrogen, and oxygen. Other minor combustible components in wood are fats, resins, and waxes. The major non-combustible component of wood is water, which makes up to 50% of freshly cut wood. Though the ash content is low (<1%), because of high oxygen content, the heat value is low (16-20 MJ/kg). Most wood species have ash contents below two percent and are therefore suitable fuels for fixed bed gasifiers. As wood contains high volatile matter, an updraft gasifier system produces gas containing tar, which needs to be cleaned out before use in engines. Cleaning of gas is a difficult and labour-intensive process. Hence wood is not suitable in updraft gasifier coupled with internal combustion engines. However, the gas containing tar from an updraft gasifier can be used for direct burning. Downdraft systems can be designed to deliver a virtually tar-free product gas in a certain capacity range when fuelled by wood blocks or wood chips

of low moisture content. After passing through a relatively simple cleanup train the gas can be used in internal combustion engines.

2.3.2. Influence of reactor type

Dry wood was experimental used by several workers in different types of gasifiers being the results shown in Table 2.5. Some values are just indicative due to unknown gasification conditions.

Table 2.5 – Characteristics of the produced gas for atmospheric gasifiers (Mehrling and Vierrath, 1989; Graham and Bain, 1993; Hasler et. al., 1994; Hasler and Nussbaumer, 1999)

Property	Downdraft	Updraft	BFB	CFB
Tar (mg/Nm^3)	10-6000	10000-150000	Not defined	2000 – 30000
Particules (mg/Nm^3)	100-8000	100-3000	Not defined	8000-100000
LHV (MJ/Nm^3)	4.0 – 5.6	3.7 – 5.1	3.7 – 8.4	3.6 – 5.9
H_2 (vol%)	15-21	10-14	5 – 16.3	15-22
CO (vol%)	10-22	15-20	9.9 – 22.4	13-15
CO_2 (vol%)	11-13	8-10	9 – 19.4	13-15
CH_4 (vol%)	1-5	2-3	2.2 – 6.2	2-4
C_nH_m (vol%)	0.5 -2	Not defined	0.2 – 3.3	0.1-1.2
N_2 (vol%)	Remaining	Remaining	41.6 – 61.6	Remaining

In the Table 2.6 typical syngas compositions are given relatively to the same type of reactors using air as oxidant.

Table 2.6 – Typical syngas compositions by reactor type (Bridgwater, 1995).

Gasifier	Gas composition (vol. %, dry)					HHV
	H_2	CO	CO_2	CH_4	N_2	(MJ/m^3)
Bubbling fluidized bed	9	14	20	7	50	5.4
Updraft	11	24	9	3	53	5.5
Downdraft	17	21	13	1	48	5.7

Comparing both Tables 2.5 and 2.6 is possible to see some discrepancies especially related to CO content. This situation emphasizes the influence of the gasification conditions in the final composition of the produced gas.

2.3.3 Influence of operational conditions

2.3.3.1 Temperature

Several authors have reported the increase of gas yield and the decrease in gas heat value with temperature, even when different feedstocks were employed and installation

with different characteristics were used, namely Herguido et al., (1992); Javier et al., (1997); Kim et al., (2001) and Rolando et al., (2002).

It is expected that the rise of temperature leads to an increase in the rate of the several reactions that took place during gasification process, which, globally, produce hydrogen and carbon monoxide and eliminates hydrocarbons. At higher gasification temperatures lower solids and tar emissions are observed, which means that the produced gas may require a lower cost on gas cleaning processes.

2.3.3.2. Pressure

Gasifiers can be operated at elevated pressures, the advantage being for those end use applications where the gas is required to be compressed afterwards, as in a gas turbine.

Pressurized gasifiers have the following significant features:

- Feeding is more complex and very costly, and has a high inert gas requirement for purging.
- Capital costs of pressure equipment are much higher than for atmospheric equipment, although equipment sizes are much smaller.
- Pressurized gasification systems can cost up to four times as much as atmospheric systems at power outputs up to 20 MW_e. This disadvantage is countered by the higher efficiency, and this effect becomes significant at 30-50 MW_e, above which pressure systems are believed likely to be more economic than atmospheric systems.
- Gas is supplied to the turbine at adequate pressure, removing the need for gas compression and also permitting relatively high tar contents in the gas; such tar needs to be completely burned in the turbine combustor.
- Hot gas cleanup with mechanical filters (such as sintered metal or ceramic candles) is usually used, which reduces thermal and pressure energy losses and in principle in simpler and of lower cost than are scrubbing systems.
- Overall system efficiency is higher owing to retention of sensible heat and chemical energy of tars in the product gas and the avoidance of a fuel gas compression stage ahead of the turbine. The only significant energy losses are to the environment and in provision of inert gas to the pressure feeders, and these can be as low as 5-8%, giving energy conversion efficiency for the gasifier itself of 92-95%. A corresponding atmospheric gasifier with water

scrubbing and product gas compression would have an analogous efficiency as low as 80-85%, depending on capacity and design.

Atmospheric gasifiers have the following significant features:

- For gas turbine applications the product gas is required to be sufficiently clean for compression before the turbine. Suggested specifications are given later. For engine applications the gas quality requirements are less onerous and pressure is not required.
- Atmospheric systems have a potentially much lower capital cost at smaller capacities of below 30 MW_e as discussed above.

Gas compositions and heating values are not significantly different for either system (Bridgwater, 1995).

2.3.4 Influence of the oxidizer

It is well-known that the heating value and the H_2 content of syngas are higher when gasification is made with steam than it is made with air (Javier et al., 1999).

Table 2.7 shows experimental results of wood gasification using different types of oxidizers.

Table 2.7 - Influence of the oxidizer in the final composition of syngas.

Oxidizing agent	Composition (% vol, dry base)					HHV	Reference
	H_2	CO	CO_2	CH_4	N_2	(MJ/m^3)	
Air (downdraft)	17	21	13	1	48	5.7	(Bridgwater, 1995)
Air (updraft)	11	24	9	3	53	5.5	(Bridgwater, 1995)
O_2 (downdraft)	32	48	15	2	3	10.4	(Bridgwater, 1995)
Air (BFB)	9	14	20	7	50	5.4	(Bridgwater, 1995)
Air (CFB)	14.1	18.7	14.7	3.5	47.7	n.d.	(Mehrling et al. , 1989)
Air (BFB)	9.5	18	13.5	4.5	45	n.d.	(Narvaez, 1996)
Steam (CFB)	34.2	27.2	22.7	11.1	4.8	n.d.	(Fercher et. al., 1998)
Steam (BFB)	52	23	18	7	n.d.	n.d.	(Herguido et. al., 1992)

It is verified that the use of steam or O_2 as oxidizer agent increases remarkably the production of H_2 and CO reflecting a significant increase of the syngas heat value. In the case of the fluidized bed reactors, an increase of the methane yields is also verified using steam as oxidizer.

Table 2.8 shows a comparison performed by Javier et al. (1999) based on results from Herguido et al. (1992), Javier et al. (1997) and Narváez et al. (1996) in order to determine the effect of gasifying agent on other results like tar content in the produced gas. Three basic ratios were used for comparison of results using different gasifying agents in a bubbling fluidized bed gasifier running with small chips of pine:

- Equivalence ratio (ϕ) for air;
- Gasifying ratio (GR) [(H_2O+O_2)/Biomass (kg/h)/(kg dry-ash free/h)], for steam-O_2 mixtures;
- Steam to biomass ratio (SB) [H_2O/Biomass (kg/h)/(kg dry-ash free/h).

Table 2.8 – Effect of gasifying agent on syngas composition

Parameter	Air (ϕ=0.3)	Steam/O_2 GR = 0.9	Steam SB=0.90
H_2 (vol.% dry basis)	8-10	25-30	53-54
CO (vol.% dry basis)	16-18	43-47	21-22
LHV (MJ/m^3, dry basis)	4.5-6.5	12.5-13.0	12.7-13.3
Ygas (m^3, dry basis/kg daf)	1.7-2.0	1.0-1.1	1.3-1.4
Y_{tar} (g/kg daf)	6-30	8-40	70
Tar (g/m^3)	2-20	4-30	30-80

Gasification with air produces a higher syngas yield. Tar yields are quite different between the gasifying agents being the lowest values obtained with air.

2.4. Concluding remarks about biomass gasification

Gasification is a versatile thermochemical conversion process which produces a gas mixture of H_2, CO and CH_4 the proportions being determined by the use of air, oxygen or steam as the gasification medium, with a concomitant range of heat values, low (4–6 MJ/Nm^3), medium (12–18 MJ/Nm^3) and high (40 MJ/Nm^3). Key parameters for successful gasification are the feedstock properties (moisture, ash, alkalis and volatiles) and feedstock pre-treatment (drying, particle size, fractionation and leaching).

Gasifiers are of two main types, fixed bed and fluidized bed, with variations within each type and specific characteristics which determine the need for and extent of feedstock preparation/pre-treatment.

For use in gas engines gas produced from a fixed bed, downdraft gasifier provides a low tar gas, with a high particulates loading: as tar is a major contaminant for engine operation and particulates can be relatively easily removed, this system is considered best for fuelling gas engines. Extensive development of wood gas-fuelled IC engines,

suggests that diesel-based engines, with large cylinder volumes/valve areas, operating at constant load and low rpm, provide optimum power output.

Regarding the influence of various parameters involved in the process of gasification in the final features of syngas, there is some discrepancy in the values given by various authors. This highlights the strong dependence on the final composition of the syngas on condition of biomass used, the type of gasifier and conditions of pressure and temperature. Thus, in order to make precise studies on the use of syngas it will be necessary to consider that its composition will be very difficult to maintain constant. The development of mathematical models for numerical simulation fully validated experimentally may be a very useful tool to determine the final composition of syngas by changes in initial conditions without laborious and expensive experimental tests.

2.5. Laminar premixed flames

A flame may be described as a reaction zone that moves with respect to the initial mixture. In practice the term is usually reserved for fast exothermic reactions of this type, and these are often also accompanied by emission of light. Flames may be either stationary flames on a burner and propagating into a flow of gas from a burner tube, or they may be freely propagating flames travelling in a gas mixture. There are two types of stationary flames:

- Premixed flames where the reactants are mixed before approaching the flame region. These flames can only be obtained if the initial fuel and oxidant mixture lies between certain composition limits called the composition limits of flammability.
- Diffusion flames where both fuel and air are separated and the combustion occur at the interface.

For defined thermodynamic starting conditions, the premixed system has a defined equilibrium adiabatic flame temperature and for the idealized situation of planar flame in a one-dimensional flow field, premixed flame has a defined adiabatic burning velocity or equivalent mass flux in a direction normal to its surface. An unstrained diffusion flame has no such simply defined parameters.

Many practical combustion problems are concerned with turbulent combustion, but laminar flame must firstly be well controlled. In premixed flames, the laminar burning velocity and flame structure data can be extremely useful in the analysis of

fundamental processes such as ignition, NO, and soot formation, and flame quenching. Moreover, some turbulent flame models prescribe the turbulent burning velocity as a function of laminar burning velocity. Thus, detailed information describing the dependence of the laminar burning velocity, flame thickness, ignition temperature, heat release rate and flame quenching on various system parameters can be a valuable diagnostic and design aid.

There is a significant discrepancy in measuring burning velocities, which gives an indication of the difficulties and uncertainties associated with experimental determination of flame properties. In the light of the earlier experimental studies of Markstein, (1964), the asymptotic analysis of Klimov, (1963), and the computations of laminar flame structure with detailed chemical kinetics by several researchers, all of which show the importance of the flame stretch rate (Dixon-Lewis, 1991). There can be little doubt that this is often neglected key variable (Law, 1989). It follows that any experimental or computed value of laminar burning velocity should be associated with a value of the flame stretch rate. Ideally, the stretch-free value of the burning velocity should be quoted and the influence of stretch rate upon this value should be indicated by the value of the appropriated Markstein length.

For these reasons this chapter begins with the definition of stretch rate and the corresponding Karlovitz and Markstein numbers. Following, the theory evolved with the burning velocity determination are described with emphasis for the constant volume and constant pressure methods due to be extensively used. This part of the chapter ends with the flammability limits description as is another important parameter of premixed laminar flames.

2.5.1 Flame stretch

A flame surface propagating in a uniform flow field is submitted to strain and curvature effects leading to changes in the frontal area. Karlovitz et al., (1953) and Markstein, (1964) initiated the study of stretched premixed flames and demonstrated the importance of the aerodynamic stretching and the preferential diffusion on the flame response in terms of flame front instability.

The flame stretch factor (κ) is defined as the relative rate of change of flame surface area (A) (Williams, 1985):

$$\kappa = \frac{1}{\delta A}\frac{d(\delta A)}{dt} = \frac{1}{A}\frac{dA}{dt} \tag{2.2}$$

The effect of stretch on the flame is to reduce the thickness of the flame front and hence the flame speed and influence the flame structure through its coupled effect with mass and heat diffusion. The concept of flame stretch can be applied to laminar flame speed; flame stabilization; flammability limits; and modeling of turbulent flames.

Let's first derive the basic relationship between the stretch rate and the strain rate, dilatation of the fluid element, and curvature of the flame surface. The three perpendicular coordinates on a curved flame surface are shown in Fig. 2.7, which has two unit vectors ($\vec{\nu}$ and $\vec{\eta}$) tangent to the flame surface and an outward normal unit vector $\vec{n}$, at the spatial point $\vec{r}(\nu,\eta,n)$ as a function of the three independent coordinates.

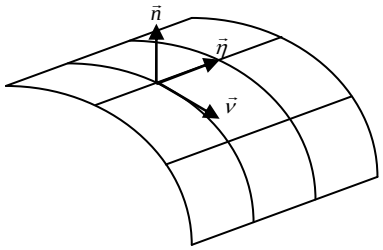

Figure 2.7 - Curved laminar flame front with three perpendicular curvilinear coordinates.

The elemental arc $(d\vec{s})_\nu$ in the direction $\vec{\nu}$ and the elemental arc $(d\vec{s})_\eta$ in the direction $\vec{\eta}$ are given by:

$$(d\vec{s})_\nu = \left(\frac{\delta\vec{r}}{\delta\nu}\right)d\nu \quad , \quad (d\vec{s})_\eta = \left(\frac{\delta\vec{r}}{\delta\eta}\right)d\eta \tag{2.3}$$

The elemental flame surface can be calculated by:

$$dA(t) = \left(\frac{\delta\vec{r}}{\delta\nu}\times\frac{\delta\vec{r}}{\delta\eta}\right)\cdot\vec{n}(d\nu)(d\eta) \tag{2.4}$$

In the orthogonal curvilinear coordinates system, the two unit vectors $\vec{e}_\nu$, $\vec{e}_\eta$ can be given by:

$$\vec{e}_\nu = \frac{\delta\vec{r}/\delta\nu}{|\delta\vec{r}/\delta\nu|},\ \vec{e}_\eta = \frac{\delta\vec{r}/\delta\eta}{|\delta\vec{r}/\delta\eta|} \quad \text{and} \quad \vec{e}_\nu\times\vec{e}_\eta = \vec{n} \tag{2.5}$$

Thus:

$$dA(t) = \left|\frac{\delta \vec{r}}{\delta \nu}\right| \left|\frac{\delta \vec{r}}{\delta \eta}\right| (d\nu)(d\eta) \tag{2.6}$$

Now let another surface that is close to the flame surface be represented by $\vec{r}^{\,*}\left(\nu,\eta,n^{*}\right)$, such that:

$$\vec{r}^{\,*} = \vec{r} + \vec{a}\,, \quad \frac{\partial \vec{r}^{\,*}}{\partial \nu} = \frac{\partial \vec{r}}{\partial \nu} + \frac{\partial \vec{a}}{\partial \nu}, \quad \frac{\partial \vec{r}^{\,*}}{\partial \eta} = \frac{\partial \vec{r}}{\partial \eta} + \frac{\partial \vec{a}}{\partial \eta} \tag{2.7}$$

Where $\vec{a}$ is a small magnitude displacement vector; then:

$$\begin{aligned} dA^{*}(t) &= \left(\frac{\delta \vec{r}^{\,*}}{\delta \nu} \times \frac{\delta \vec{r}^{\,*}}{\delta \eta}\right) \cdot \vec{n}^{\,*} (d\nu)(d\eta) \left|\frac{\delta \vec{r}^{\,*}}{\delta \nu}\right| \left|\frac{\delta \vec{r}^{\,*}}{\delta \eta}\right| (d\nu)(d\eta) \\ &\cong \left|\frac{\delta \vec{r}}{\delta \nu}\right| \left|\frac{\delta \vec{r}}{\delta \eta}\right| \left[1 + \nabla_t . \vec{a}\right](d\nu)(d\eta) = \left[1 + \nabla_t . \vec{a}\right] dA(t) \end{aligned} \tag{2.8}$$

Where $\nabla_t = \vec{e}_\nu \frac{\partial}{\partial \nu} + \vec{e}_\eta \frac{\partial}{\partial \eta}$, which represents the gradient operator along the tangential plane of the flame surface (Chung and Law, 1988).

It is useful to note that we can always decompose any arbitrary velocity into two components: a tangential to the flame surface and another normal to the flame surface as follows:

$$\vec{V} = \vec{V}_n + \vec{V}_t = \left(\vec{V} . \vec{n}\right)\vec{n} + \vec{V}_t \tag{2.9}$$

Now considering a curved flame surface *A(t)* moving in the space with local velocity $\vec{W}$ (note that each spatial point has its own velocity). Then, the rate of change of the flux of a vector $\vec{G}$ across the flame surface is given by the following expression based on the Reynolds' transport theorem.

$$\frac{d}{dt}\int_{A(t)} \vec{G} . \vec{n}\, dA = \int_{A(t)} \left[\frac{\partial \vec{G}}{\partial t} + \vec{W} . \nabla \vec{G} - \vec{G} . \nabla \vec{W} + \vec{G} \nabla . \vec{W}\right] . \vec{n}\, dA \tag{2.10}$$

By specifying $\vec{G} = \vec{n}$, Eq. (2.10) yields:

$$\frac{d}{dt}\int_{A(t)} dA = \int_{A(t)} \left[\frac{\partial \vec{n}}{\partial t} + \vec{W} . \nabla \vec{n} - \vec{n} . \nabla \vec{W} + \vec{n} \nabla . \vec{W}\right] . \vec{n}\, dA \tag{2.11}$$

Since $\vec{n}$ is a unit normal vector, we have:

$$\frac{\partial \vec{n}}{\partial t}.\vec{n} = \frac{1}{2}\frac{\partial \vec{n}^2}{\partial t} = 0 \tag{2.12}$$

$$\left(\vec{W}.\nabla \vec{n}\right).\vec{n} = \vec{W}.\nabla\left(\frac{n^2}{2}\right) = 0 \tag{2.13}$$

Therefore, the transport equation (2.11) can be written as follows:

$$\frac{d}{dt}\int_{A(t)} dA = \int_{A(t)}\left[-\vec{n}\,\vec{n} : \nabla\vec{W} + \nabla.\vec{W}\right]dA \tag{2.14}$$

Note that in tensor notation, the first term of the right side of the Eq. (2.14) can be written as:

$$-\vec{n}\,\vec{n} : \nabla\vec{W} = -n_i\, n_j \frac{\partial w_i}{\partial x_j} \tag{2.15}$$

If we consider a surface element, then *A(t)* can be substituted by δA. The flame stretch rate κ can be expressed as:

$$\kappa = \frac{1}{\delta A}\frac{d(\delta A)}{dt} = -\vec{n}\,\vec{n} : \nabla\vec{W} + \nabla.\vec{W} \tag{2.16}$$

The general velocity $\vec{W}$ can be considered to have two components: one in the normal direction at a speed S_u and the other is the local fluid velocity. Thus:

$$\vec{W} = \vec{S} + S_u\,\vec{n} \tag{2.17}$$

Several vector operations can be applied to Eq. (2.17) to give:

$$\nabla\vec{W} = \nabla\vec{S} + S_u\nabla\vec{n} + \vec{n}\nabla S_u \tag{2.18}$$

$$\vec{n}\vec{n} : \nabla\vec{W} = \vec{n}\vec{n} : \nabla\vec{S} + \vec{n}\nabla S_u \tag{2.19}$$

$$\nabla.\,\vec{W} = \nabla.\,\vec{S} + S_u\,\nabla.\,\vec{n} + \vec{n}.\nabla S_u \tag{2.20}$$

Substituting these expressions in the Eq. (2.16), we have:

$$\kappa = \frac{1}{\delta A}\frac{d(\delta A)}{dt} = -\vec{n}\,\vec{n} : \nabla\vec{S} + \nabla.\vec{S} + S_u\nabla.\vec{n} = -n_i\, n_j \frac{\partial S_i}{\partial x_j} + -\frac{1}{\rho}\frac{\partial \rho}{\partial t} + \frac{S_u}{r_c} \tag{2.21}$$

Where, r_c represents the local radius of the flame curvature. The first term of Eq. (2.21) represents the effect of the strain; the second term represents the effect of the fluid expansion of fluid (dilatation) and, the third term, the effect of the flame curvature. It is evident that the flame can be stretched by the combined effect of strain, volume expansion of the fluid and the curvature of the flame, which arises from the nonuniformities of the flow and the normal propagation of the flame front.

For the present purposes, an appropriate unified tensor expression, in terms of strain rate, κ_s, and the stretch rate due to flame curvature, κ_c, is that of Candel and Poinsot, (1990).

$$\kappa = \kappa_s + \kappa_c \tag{2.22}$$

With

$$\kappa_s = -\vec{n}\,\vec{n} : \nabla\vec{S} + \nabla.\vec{S} \tag{2.23}$$

$$\kappa_c = S_u \nabla.\vec{n} \tag{2.24}$$

In spherical expanding flames it is convenient to use spherical coordinates (r, θ, ϕ), the components of $\vec{n}$ and $\vec{S}$ are written as (n_r, n_θ, n_ϕ) and (s_r, s_θ, s_ϕ), respectively. Then:

$$\begin{aligned}\kappa_s = -\Bigg[& n_r^2\left(\frac{\partial s_r}{\partial r}\right) + n_\theta^2\left(\frac{1}{r}\frac{\partial s_\theta}{\partial \theta} + \frac{s_r}{r}\right) + n_\phi^2\left(\frac{1}{r\sin\phi}\frac{\partial s_\phi}{\partial \phi} + \frac{s_r}{r} + \frac{s_\theta \cot\theta}{r}\right) \\ & + n_r n_\theta\left(\frac{\partial s_\theta}{\partial r} + \frac{1}{r}\frac{\partial s_r}{\partial \theta} - \frac{s_\theta}{r}\right) + n_r n_\phi\left(\frac{\partial s_\phi}{\partial r} + \frac{1}{r\sin\theta}\frac{\partial s_r}{\partial \phi} - \frac{s_\phi}{r}\right) \\ & + n_\theta n_\phi\left(\frac{1}{r}\frac{\partial s_\phi}{\partial \theta} + \frac{1}{r\sin\theta}\frac{\partial s_\theta}{\partial \phi} - \frac{\cot\theta}{r}s_\phi\right)\Bigg] \\ & + \frac{1}{r^2}\frac{\partial\left(r^2 s_r\right)}{\partial r} + \frac{1}{r\sin\theta}\frac{\partial\left(s_\theta \sin\theta\right)}{\partial \theta} + \frac{1}{r\sin\theta}\frac{\partial s_\phi}{\partial \phi}\end{aligned} \tag{2.25}$$

$$\kappa_c = u_n + \left[\frac{1}{r^2}\frac{\partial\left(r^2 n_r\right)}{\partial r} + \frac{1}{r\sin\theta}\frac{\partial\left(n_\theta \sin\theta\right)}{\partial \theta} + \frac{1}{r\sin\theta}\frac{\partial n_\phi}{\partial \phi}\right] \tag{2.26}$$

For an outward spherically propagating flame, the flame surface is identified by the cold front of radius r_u, n_r =1, n_θ=n_ϕ=0, and s_r=s_g, s_θ=s_ϕ=0 (Bradley et al., 1996). The burning velocity, s_u, is associated with this surface and the gas velocity ahead of it is s_g. The flame speed, dr_u/dt, is equal to $s_g + n_r s_u$, and is indicated by S_n. Applying this conditions to Eqs. 2.25 and 2.26 gives

$$\kappa_s = n_r^2\left(\frac{\partial s_r}{\partial r}\right)+\frac{1}{r^2}\frac{\partial\left(r^2 s_r\right)}{\partial r}=2\frac{s_g}{r_u} \tag{2.27}$$

$$\kappa_c = u_n\frac{1}{r^2}\frac{\partial\left(r^2 n_r\right)}{\partial r}=2n_r\frac{s_u}{r_u} \tag{2.28}$$

and the total stretch rate is:

$$\kappa = 2\frac{s_n}{r_u} \tag{2.29}$$

The outwardly propagating flame, ignited from a central ignition point, is the most common spherical flame and because the stretch rates to which it is subjected are well defined, it is well suited to burning velocity measurements.

2.5.1.1 Karlovitz number

The Karlovitz number (Ka) is defined as the nondimensional stretch factor, using the thickness of the unstretched flame (δ_{u0}) and the normal unstretched laminar flame velocity (S_{u0}) to form a reference time (Kuo, 2005):

$$Ka = \frac{\delta_{u0}}{S_{u0}}\kappa = \frac{\text{Residence time for crossing an unstretched flame}}{\text{Characteristic time for flame stretching}} \tag{2.30}$$

For convenience, the Karlovitz number can be written as a sum of two parts due to the contribution from strain and curvature as follows:

$$Ka = Ka_s + Ka_c \tag{2.31}$$

Where

$$Ka_s = \frac{\delta_{u0}}{S_{u0}}\left(\vec{S}\vec{S}+\vec{\eta}\,\vec{\eta}\right):\nabla\vec{S}\quad;\quad Ka_c = \frac{\delta_{u0}}{S_{u0}}S_u\nabla\vec{n}=\frac{\delta_{u0}}{R}\frac{S_u}{S_{u0}} \tag{2.32}$$

2.5.1.2 Markstein number

Flame stretch can change the burning velocity of premixed flames significantly. It is important to know the relation between these two parameters, because the burning velocity is a crucial parameter in premixed combustion processes. Markstein, (1964) was the first to propose a phenomenological relation between the laminar burning velocity and the curvature of the flame front. Notice that the straining of the flow is not

taken into account here. In this relation the proportionality of the burning velocity to the flame stretch is represented by a parameter that was considered as a characteristic length scale of the flame. This parameter is now generally known as the Markstein length, which denotes the sensitivity of a flame to flame stretch. Asymptotic analyses of Clavin and Williams, (1982) and Matalon and Matkowsky, (1982) and detailed modeling of Warnatz and Peters, (1984) show a linear relationship between stretch rate and burning velocity in the low-stretch regime. Thus, it is assumed that,

$$S_n^0 - S_n = L_b \kappa \tag{2.33}$$

Where S_n^0 is the unstretched flame speed and L_b is the Markstein length of burned gases.

When the observation is limited to the initial part of the flame expansion where the pressure does not vary yet, then a simple relationship links the unstretched flame speed to the unstretched burning velocity.

$$\frac{S_n^0}{S_u^0} = \frac{\rho_u}{\rho_b} = \sigma \tag{2.34}$$

Where σ is the expansion factor and ρ_u and ρ_b are, respectively, the unburned and burned densities.

The same behavior of the unstretched burning velocity regarding the stretch can be observed (Lamoureux et al., 2003):

$$S_u^0 - S_u = L_u \kappa \tag{2.35}$$

where L_u represents the unburned Markstein length, which is obtained dividing the burned Markstein length by the expansion factor.

The normalization of the laminar burning velocity by the unstretched one introduces two numbers which characterize the stretch that is applied to the flame, the Karlovitz number (*Ka*), and its response to it, the Markstein Number (*Ma*):

$$\frac{S_u}{S_u^0} = 1 - MaKa \tag{2.36}$$

$$Ka = \kappa \frac{\delta}{S_u^0} \tag{2.37}$$

$$Ma = \frac{L_u}{\delta} \tag{2.38}$$

where δ is the flame thickness defined, in this work, using the thermal diffusivity, α:

$$\delta = \frac{\alpha}{S_u^0} \tag{2.39}$$

This evolution of the laminar flame velocity with the stretch rate was verified by Aung et al., (1997) for moderate stretch rate. As one can see, different definitions of a characteristic flame thickness lead to different Karlovitz and Markstein numbers. Bradley et al., (1996) use the kinematic viscosity of the unburned mixture to derive the flame thickness while Aung et al., (1997) use the mass diffusivity of the fuel in the unburned gas. However, this effect disappears in Eq. (2.36) since the flame thickness cancels out.

Clavin and Joulin, (1989) proposed a phenomenological law to take the effects of curvature and strain in flame stretch into account separately, thereby introducing a Markstein length for the curvature part of the flame and another one for the flow straining through the flame. This separation is used by several workers as Bradley et al., (1996) or Gu et al., (2000). However, Groot et al., (2002) investigated theoretically these separate contributions demonstrating that the Markstein number for curvature and the combined one for both curvature and strain are unique. However, it is not possible to introduce a separate and unique Markstein number for the flow straining that can be used to describe its influence in different combustion situations. Therefore, the modification of the burning velocity is characterized by the total stretch rate, and it is impossible to introduce the separate contributions into an arbitrary combustion situation.

A new methodology based on the resolution of Clavin's equation, linking the flame speed and the stretch linearly, was recently proposed by Tahtouh et al. (2009). This methodology is based on the following. Combining Eqs. 2.33-2.29 leads to:

$$\frac{dr}{dt} = S_n^0 - 2L_b \frac{dr}{rdt} \tag{2.40}$$

Which exact solution, allows avoiding noise generation due to the differentiation process. The function that solves Eq. (2.40) is:

$$r(t) = 2L_b W_0(Z) \tag{2.41}$$

With W the Lambert function and:

$$Z = \frac{e^{\frac{S_n^0 t + C_1}{2L_b}}}{2L_b} \tag{2.42}$$

Where C_1 is a constant to be determined. The Lambert function W is defined as the inverse function of $f(W) = We^W$. By definition, $\frac{dW}{dZ} = \frac{W(Z)}{Z(1+W(Z))}$ for $Z \neq \frac{-1}{e}$ and $W(Z) \neq -1$. If $L_b>0$, $Z>0$, and consequently $W_0(Z)$ is a positive real number. Thus L_b, S_n^0 and C_1 can be found by minimizing the following equation:

$$\sum_1^N (r_{original}(t) - r(t))^2 = \sum_1^N (r_{original}(t) - 2L_b W_0(Z))^2 \tag{2.43}$$

The flame speed and the stretch could also be linked based on a nonlinear methodology proposed by Buckmaster, (1977):

$$\left(\frac{S_n}{S_n^0}\right)^2 \ln\left(\left(\frac{S_n}{S_n^0}\right)^2\right) = \frac{2L_b\kappa}{S_n^0} \tag{2.44}$$

The derivation of this equation is based on the asymptotic hypothesis. The structure of the flames considered is characterized by a small flame thickness to which all the reaction is confined. Moreover, deformations occur on a long scale of the order of the dimensionless activation energy.

Based on Eq. (2.44), unstretched flame speed and burned gas Markstein length can be deduced by a minimization of the following expression:

$$\sum_1^n \left[\left(\frac{S_n}{S_n^0}\right)^2 \ln\left(\left(\frac{S_n}{S_n^0}\right)^2\right) + \frac{2L_b\kappa}{S_n^0}\right] \tag{2.45}$$

Where n is the number of flame images.

2.5.2 Burning velocity measurement methods

Burning velocity is a physicochemical constant for a given mixture. It is the velocity, relative of unburned gas, which a plane, one-dimensional flame front travels along the normal to its surface. Clearly, it is the volume of combustible mixture, at its own temperature and pressure, consumed in unit time by unit area of flame front. It is independent of flame geometry, burner size and flow rate. As indicated above, the burning velocity is essentially a measure of the overall reaction rate in the flame and is important, both in the stabilization of flames and in determining rates of heat release.

The burning velocity of a flame is affected by flame radiation, and hence by flame temperature, by local gas properties such as viscosity, thermal conductivity and diffusion coefficient, and by the imposed variables of pressure, temperature, air-fuel ratio and heat of reaction of mole of mixture. However, although its theoretical definition is straightforward, its practical measurement undoubtedly is not, and there is a considerable discrepancy between the results obtained by the various methods. One of the main problems in measuring the normal burning velocity is that a plane flame front can be observed only under very special condition. In nearly all-practical cases, the flame front is either curved or is not normal to the direction of velocity of the gas stream. Broadly speaking there are two types of measurements for burning velocity; one uses flames travelling through stagnant mixtures, whereas the other employs flames that are held stationary in space by a counter flow of fresh mixture.

The following will describe briefly some of the different techniques for measuring the laminar burning velocity for non-stationary flames. Emphasis will be given to propagating flames at constant volume and constant pressure since they are extensively used.

In these methods of measurements, the flame moves through the initially quiescent mixtures. The subsequent spread of such a flame is determined by the nature of the bounding surface between the mixture and its surroundings. These types of bounding surface have been used: rigid cylindrical tube, either closed at both ends or open at one end or both ends; soap bubble solution or thin elastic membranes; and rigid spherical vessels.

Burning velocity measurement can be made by direct measurement of flame propagation. This requires locating the position of the flame front at two (or more) known times. Rapid visualization is required, and it is necessary to know the flame front geometry and the flow constraints, and often the density change across the flame front.

The followings are the measurement techniques, which have been used for measuring the laminar burning velocity with non-stationary flames.

2.5.2.1 Tube method

This is one of the earliest methods and was first used by Mallard and LeChatelier, (1883) in which the mixture is ignited at the open end of a tube and the flame front is photographed as propagating toward the closed end. The expression for the burning

velocity is obtained from the equation of mass conservation for the unburned gas. It follows from the definition of burning velocity that:

$$\frac{\partial \rho_u V_u}{\partial t} = -\rho_u A S_u \tag{2.46}$$

This assumes that S_u is a constant value over the entire cross section of the tube. If ρ_u is also constant, then:

$$\frac{\partial V_u}{\partial t} = -A S_u \tag{2.47}$$

If the flame speed S_n is uniform over the tube cross section, then

$$\frac{\partial V_u}{\partial x} = -a \tag{2.48}$$

Where a is the cross-sectional area of the tube and x the abscissa along the tube axis. As $S_n = dx/dt$, it follows from equations (2.46) and (2.48) that

$$S_u = -\frac{a}{A} S_n \tag{2.49}$$

This is the expression founded experimentally by Coward and Hartwell, (1932). Unfortunately, the flame aerodynamics change as the flame propagates along the tube and invalidates the assumption of constant flame speed over the cross section. The flame area is also variable. For these reasons, there are significant errors (±20%) in the use of this method for burning velocity measurements.

2.5.2.2 Soap bubble method

Guénoche et al., (1948) have demonstrated theoretically and experimentally that an orifice placed at the ignition end of the tube reduces the pressure waves which disturb the flame. This give arise to the soap bubble method, where a homogeneous combustible mixture is used to blow a soap bubble around a pair of spark electrodes. At time zero, the gas mixture contained in the spherical soap bubble is ignited by the spark. Eq. (2.46) and (2.47) are still applicable, Eq. (2.49) is not. Consideration of the volume of unburned gas now gives:

$$\delta V_G = -a\,\delta x + S_g a\,\delta t \tag{2.50}$$

In which S_g, is the mean unburned gas velocity averaged over the tube cross-sectional area *a*. Equations (2.47) and (2.50) give

$$S_u = -\frac{a}{A}\left(S_n - S_g\right) \tag{2.51}$$

This equation was given by Coward and Payman, (1937) and applied by Gerstein et al., (1951), who measured the gas velocity from the growth of a soap bubble formed over the orifice. As the flame propagates along the tube, the viscous drag of the burned gas at the wall increasingly retards this gas flow and the pressure in both the burned gas near the flame front and the unburned gas increases.

2.5.2.3 Constant volume method

In this method, a containing envelope surrounds the explosive mixture. It is assumed that central ignition occurs and that laminar flame that is smooth and spherical propagates outwards without any significant movement due to natural convection. The pressure is equalized throughout the vessel and the unburned gas is isotropic.

Starting from the above assumptions, a differential equation for the pressure can be derived. Mass conservation gives:

$$m = m_u + m_b \tag{2.52}$$

$$\frac{dm_u}{dt} = -\frac{dm_b}{dt} = \rho_i V \frac{dx}{dt} \tag{2.53}$$

In which *m* is the mass of gas and subscripts *u*, *b* indicate de unburned and burned gas states at time *t*, and the initial reference state at time t equal to zero, *V* is the vessel volume. The burned mass fraction *x* is uniquely related to the pressure, so

$$\frac{dx}{dt} = \frac{dx}{dp}\frac{dp}{dt} \tag{2.54}$$

It follows from the definition of burning velocity, S_u, that:

$$\frac{dm_u}{dt} = -4\pi r_b^2 \rho_u S_u \tag{2.55}$$

Where r_b is the radius of the inner boundary of the unburned gas of density ρ_u. Combining the above relations results in

$$\frac{dp}{dt} = \frac{A_b}{V}\frac{\rho_u}{\rho_i}\left(\frac{dx}{dp}\right)^{-1} S_u \tag{2.56}$$

Isentropic compression of the unburned gases gives

$$\frac{\rho_u}{\rho_i} = \left(\frac{p}{p_i}\right)^{-1/\gamma_u} \tag{2.57}$$

Or, alternatively,

$$T_u = T_i\left(\frac{p}{p_i}\right)^{(\gamma_u - 1)/\gamma_u}. \tag{2.58}$$

Where $\gamma_u = c_{pu}/c_{vu}$, is the isentropic exponent of the unburned mixture. Surface area and volume of the flame are related to its radius as $A_b = 4\pi r^2$ and $V_b = \frac{4}{3}\pi r^3$, respectively. Realizing that $m_u = \rho_i V (1 - x)$, and $p_i = \rho_i R_u T_i$, the volume of the unburned mixture can be written as

$$V_u = \frac{m_u R_u T_u}{p} = \frac{p_i}{p}\frac{T_u}{T_i}(1 - X)V \tag{2.59}$$

Inserting $V_b = \frac{4}{3}\pi R^3$, R is the effective radius of the vessel and the above relations into $V=V_u+V_b$ yields:

$$r_b = R\left[1 - (1 - x)\frac{p_i}{p}\frac{T_u}{T_i}\right]^{1/3} \tag{2.60}$$

The area-to-volume ratio in Eq. (2.56) now becomes:

$$\frac{A_b}{V} = \frac{3}{R}\left[1 - (1 - x)\frac{p_i}{p}\frac{T_u}{T_i}\right]^{2/3} \tag{2.61}$$

Inserting Eqs. (2.57), (2.58) and (2.61) into Eq.(2.56) we finally obtain

$$\frac{dp}{dt} = \frac{3}{R}\left(\frac{dx}{dp}\right)^{-1}\left[1-\left(\frac{p_i}{p}\right)^{-\frac{1}{\gamma_u}}(1-x)\right]^{-\frac{2}{3}}\left(\frac{p}{p_i}\right)^{-\frac{1}{\gamma_u}} S_u \tag{2.62}$$

A result first derived by O´Donovan and Rallis, (1959). Rearranging Eq. (2.62) gives:

$$S_u = \frac{R}{3}\left(\frac{dx}{dp}\right)\left[1-\left(\frac{p_i}{p}\right)^{\frac{1}{\gamma_u}}(1-x)\right]^{-\frac{2}{3}}\left(\frac{p}{p_i}\right)^{-\frac{1}{\gamma_u}}\left(\frac{dp}{dt}\right) \tag{2.63}$$

In this equation, R is the effective radius of the vessel and $\gamma_u = c_{pu}/c_{vu}$, the isentropic exponent of the unburned mixture. Both *x* and its derivative d*x*/d*p* depend on pressure. The advantage of this expression of the burning velocity is the possibility of exploring a wide range of pressures and temperatures with one explosion. This is the main reason of its utilization for burning velocity determination in engine conditions. Several *x(p)* relations have been proposed in the literature. The most important of which are:

- O'Donovan and Rallis (1959)

Based on the same assumptions mentioned, O'Donovan and Rallis (1959) present an *x(p)* relation that in the present symbols reads,

$$x = \frac{p - p_i(T_u / T_i)}{p_e(\bar{T}_b / \bar{T}_e) - p_i(T_u / T_i)} = \frac{\bar{T}_e}{\bar{T}_b}\left(\frac{p - p_i\left(p / p_i\right)^{(\gamma_u - 1)/\gamma_u}}{p_e - (\bar{T}_b / \bar{T}_e)p_i\left(p / p_i\right)^{(\gamma_u - 1)/\gamma_u}}\right) \tag{2.64}$$

$\bar{T}_b$ is the mass averaged burnt temperature during combustion, with end value $\bar{T}_e$. T_b is determined for every burned shell from 3 consecutive increases. First its unburned temperature is determined from adiabatic compression. Its burned temperature is then obtained from energy conservation for the shell at constant pressure. Finally, the burned shell is further compressed (and heated) adiabatically.

As a further simplification to their model, O'Donovan and Rallis assume that $\bar{T}_b$ and $\bar{T}_e$ are equal during the whole combustion period. In this case one finds

$$x = \frac{p - p_i(p / p_i)^{(\gamma_u - 1)/\gamma_u}}{p_e - p_i(p / p_i)^{(\gamma_u - 1)/\gamma_u}} \tag{2.65}$$

This is compatible with the assumption that the (mass averaged) burned temperature does not vary over time in this model. O'Donovan and Rallis agree that this is a severe simplification, and suggest to measure the burned temperature at the centre of the bomb $T_{b,c}$ immediately after the start of combustion to evaluated T_e/T_b.

- Lewis and von Elbe (1987)

The most cited *x(p)* relation in literature equates the burnt mass fraction to the fractional pressure rise originally proposed by Lewis and von Elbe, (1987):

$$x = \frac{p - p_i}{p_e - p_i} \tag{2.66}$$

Because its appealing simplicity and reasonable accuracy, the linear relation has been used a lot for obtaining laminar burning velocities. Dahoe et al., (1996) give a derivation similar to the above, but immediately start from the linear relation (2.66). Eq. (2.62) then turns into

$$\frac{dp}{dt} = \frac{3(p_e - p_i)}{R}\left[1 - \left(\frac{p_i}{p}\right)^{\frac{1}{\gamma_u}} \frac{(p_e - p)}{(p_e - p_i)}\right]^{\frac{2}{3}} \left(\frac{p}{p_i}\right)^{\frac{1}{\gamma_u}} S_u \tag{2.67}$$

- Nagy et al., (1969)

Nagy et al., (1969) assume isentropic compression of the burned mixture and have used the following *x(p) e*xpression:

$$x(p) = \frac{p^{1/\gamma_u} - p_i^{1/\gamma_u}}{p_e^{1/\gamma_b} p^{(1/\gamma_u - 1/\gamma_b)} - p_i^{1/\gamma_u}} \tag{2.68}$$

- Luijten et al., (2009)

Luijten et al. proposed an extended linear analytical two-zone model, where both the burned and unburned zones have uniform temperatures and compositions. Conservation of specific volume *v* and internal energy *e* is expressed by

$$v_t = x v_b + (1 - x) v_u \tag{2.69}$$

$$e_t = x e_b + (1 - x) e_u \tag{2.70}$$

where the subscript *t* denotes 'total', hence $v_t = V/m_i$ and $e_t = U/m_i$ where U is the total internal energy. For ideal gases Eq. (2.69) can be written as

$$\frac{R_u T_i}{p_i} = x\frac{R_b T_b}{p} + (1-x)\frac{R_u T_u}{p} \tag{2.71}$$

The internal energy for a perfect gas can be written as $e = e_0 + c_v\,(T - T_0)$, where e_0 is the chemical energy stored in the mixture at a reference temperature T_0. Without loss of generality we can write,

$$e_u(T_u) = C_{vu}(T_u - T_0) + \Delta e \tag{2.72}$$

$$e_b(T_b) = C_{vb}(T_b - T_0) \tag{2.73}$$

where $\Delta e = e_{0,u} - e_{0,b}$. Inserting Eqs. (2.72) and (2.73) into Eq. (2.70) and rearranging gives

$$T_b = T_0 + \frac{1}{xC_{vb}}\left[x\Delta e + C_{vu}(T_i - T_0) - (1-x)C_{vu}(T_u - T_0)\right] \tag{2.74}$$

Now T_b can be eliminated from Eq. (2.71) resulting in

$$\frac{p}{p_i} = (1-x)\frac{T_u}{T_i} + \frac{R_b}{R_u}\left(x\frac{T_0}{T_i} + \frac{1}{C_{vb}T_i}\left[x\Delta e + C_{vu}(T_i - T_0) - (1-x)C_{vu}(T_u - T_0)\right]\right) \tag{2.75}$$

For the limiting case x =1 at $p = p_e$, we have

$$\frac{p_e}{p_i} = \frac{R_b}{R_u}\left(\frac{T_0}{T_i} + \frac{1}{C_{vb}T_i}\left[\Delta e + C_{vu}(T_i - T_0)\right]\right) \tag{2.76}$$

Inserting this expression for p_e back into Eq. (2.75) gives

$$\frac{p}{p_i} = (1-x)\frac{T_u}{T_i} + x\frac{p_e}{p_i} + (1-x)\left[\frac{R_b}{R_u} + \frac{C_{vu}}{C_{vb}}\frac{T_i - T_u}{T_i}\right] \tag{2.77}$$

The term in square brackets can be rewritten as

$$\frac{R_b}{R_u} + \frac{C_{vu}}{C_{vb}}\frac{T_i - T_u}{T_i} = \frac{\gamma_b - 1}{\gamma_u - 1}\left(1 - \frac{T_u}{T_i}\right) \tag{2.78}$$

Inserting into Eq. (2.77) and rearranging for x we obtain

$$x = \frac{p - p_i\left[\left(\frac{\gamma_b - 1}{\gamma_u - 1}\right) + \frac{T_u}{T_i}\left(\frac{\gamma_u - \gamma_b}{\gamma_u - 1}\right)\right]}{p_e - p_i\left[\left(\frac{\gamma_b - 1}{\gamma_u - 1}\right) + \frac{T_u}{T_i}\left(\frac{\gamma_u - \gamma_b}{\gamma_u - 1}\right)\right]} \tag{2.79}$$

As a final step, the above result is written fully in terms of pressure using Eq. (2.62). For later use, the result is given in a more concise form:

$$x = \frac{p - p_i f(p)}{p_e - p_i f(p)} \tag{2.80}$$

Where

$$f(p) = \left(\frac{\gamma_b - 1}{\gamma_u - 1}\right) + \left(\frac{\gamma_u - \gamma_b}{\gamma_u - 1}\right)\left(\frac{p}{p_i}\right)^{(\gamma_u - 1)/\gamma_u} \tag{2.81}$$

Differentiation is straightforward, yielding

$$\frac{dx}{dp} = \frac{1 - p_i f'(p)}{p_e - p_i f(p)} + \frac{p_i f'(p)\left[p - p_i f(p)\right]}{\left[p_e - p_i f(p)\right]^2} \tag{2.82}$$

Where

$$p_i f'(p) = \left(\frac{\gamma_u - \gamma_b}{\gamma_u}\right)\left(\frac{p}{p_i}\right)^{-1/\gamma_u} \tag{2.83}$$

The above methodology was extended to multiple zones by Luijten et al., (2009) without considerable improvement in the results.

The linear approximation, introduced by Lewis and Von Elbe, is still the most widespread analytical relation to interpret burning velocity data. Differences in laminar burning velocities between the varieties of *x(p)* were quantified by Luijten et al., (2009) for the example case of stoichiometric methane–air combustion, demonstrating that deviations between burning velocities from bomb data and other methods can at least partly be ascribed to the limited accuracy of the linear approximation. For the example case, differences up to 8% were found.

2.5.2.4 Constant pressure method

Laminar burning velocity and Markstein length can be deduced from schlieren photographs as described by Bradley et al., (1998). For a spherically expending flame,

the stretched flame velocity, S_n, reflecting the flame propagation speed, is derived from the flame radius versus time data as:

$$S_n = \frac{dr_u}{dt} \tag{2.84}$$

where r_u is the radius of the flame in schlieren photographs and t is the time. S_n can be directly obtained from the flame photo.

For expanding spherical flame with instantaneous surface area $A= 4\pi r_u^2$, the flame stretch rate is solely due to the change in curvature with time. From Eq. (2.2) and (2.29) the stretch rate can be simplified as

$$\alpha = \frac{1}{A}\frac{dA}{dt} = \frac{2}{r_u}\frac{dr_u}{dt} = \frac{2}{r_u}S_n \tag{2.85}$$

Where r_u is the instantaneous radius of the flame. Asymptotic analyses of Matalon and Matkowsky, (1982) and detailed modelling of Warnatz and Peters, (1984) show a linear relationship between stretch rate and burning velocity in the low-stretch regime. Thus, it is assumed that,

$$S_n^0 - S_n = L_b\kappa \tag{2.86}$$

where S_n^0 is the unstretched flame speed, and L_b is the Markstein length of burned gases. From Eqs. (2.84) and (2.85), the stretched flame speed, S_n, and flame stretch rate, κ, can be calculated.

The unstretched flame speed is obtained as the intercept value at κ = 0, in the plot of S_n against κ, and the burned gas Markstein length is the slope of S_n–κ curve. Markstein length can reflect the stability of flame (Liao et al., 2004). Positive values of L_b indicate that the flame speed decreases with the increase of flame stretch rate. In this case, if any kind of perturbation or small structure appears on the flame front (stretch increasing), this structure tends to be suppressed during flame propagation, and this makes the flame stability. In contrast to this, a negative value of L_b means that the flame speed increases with the increase of flame stretch rate. In this case, if any kinds of protuberances appear at the flame front, the flame speed in the flame protruding position will be increased, and this increases the instability of the flame.

2.5.3 Burning velocity empirical correlations

The simultaneous change in the pressure and temperature of the unburned mixture during a closed vessel explosion makes it necessary to rely on correlations which take these effects into account. While correlations for the laminar flame thickness are scarce, many have been proposed to describe the behavior of the laminar burning velocity. Because of their simplicity and the minimal computational burden they impose, this section is restricted to correlations which express the laminar burning velocity in terms of properties of the unburned mixture only (i.e. $S_u = f(T,P,\phi)$). These relationships may be classified as follows:

- Equations that separately describe the influence of pressure and temperature on the laminar burning velocity for a given equivalence ratio.
- Correlations describing the simultaneous influence of pressure and temperature on the burning velocity for a given equivalence ratio.
- Correlations describing the simultaneous influence of pressure, temperature and equivalence ratio.

The first group of correlations, when applied to closed vessel explosions, has the disadvantage that not all combinations of pressure and temperature, as these occur in the course of the combustion process, are covered. Clearly, correlations are needed which describe the simultaneous influence of pressure and temperature on the burning velocity. In the second group, this combined influence of pressure and temperature on burning velocity is covered for a given equivalence ratio. In the third group of correlations, in addition to describing the simultaneous effect of pressure and temperature on the burning velocity, also include the influence of equivalence ratio. Clearly, this latter group of correlations are more robust an practical and so it will be described and used in this work.

Sharma et al. (1981) proposed, for methane-air mixtures, a system of equations for predicting the laminar burning velocity (in $cm.s^{-1}$) for pressures from 1 to 8 atm, temperatures from 300 to 600 K, and equivalence ratios from 0.8 to 1.2:

$$S_u = \begin{cases} C\left(T/T_0\right)^{\frac{1.68}{\sqrt{\phi}}} \text{ if } \phi \le 1 \\ C\left(T/T_0\right)^{1.68\sqrt{\phi}} \text{ if } \phi > 1 \end{cases} \qquad (2.87)$$

$$C = -418 + \frac{1287}{\phi} - \frac{1196}{\phi^2} + \frac{360}{\phi^3} - 15\phi^{10}\log P$$

Iijima and Takeno (1986) proposed a correlation which expresses the laminar burning velocity, S_u (P, T), at an arbitrary pressure and temperature, in terms of the laminar

burning velocity at reference conditions, S_{u0} (P_0,T_0). The reference temperature, T_0, must be set equal to 291 K and the reference pressure, P_0, is 1 atm.

$$S_u = S_{u_0}\left(\frac{T}{T_0}\right)^{\alpha}\left[1+\beta \ln\left(\frac{P}{P_0}\right)\right] \tag{2.88}$$

Metghalchi and Keck (1980) found that

$$S_u = S_{u_0}\left(\frac{T}{T_0}\right)^{\alpha}\left(\frac{P}{P_0}\right)^{\beta} \tag{2.89}$$

Where, T_0 and P_0, are the reference temperature and pressure, respectively. The influence of the equivalence ratio is incorporated through the temperature and pressure exponents, α and β, as a linear function and through the reference burning velocity S_{u0} as a square function.

Only the last two correlations are general, and the latter has been used extensively, namely by: Bradley et al., (1998); Gu et al., (2000); Dahoe and Goey, (2003); Liao et al., (2004), due to its simplicity and will also be used in this in work to correlate the laminar burning velocity obtained the constant volume method.

The determination of the coefficients of Eq. (2.89) is made as follows. Applying Neper logarithmic, we have:

$$\mathrm{Ln}\, S_u = \mathrm{Ln}\, S_{u_0} + \alpha \mathrm{Ln}\left(\frac{T}{T_0}\right) + \beta \mathrm{Ln}\left(\frac{P}{P_0}\right) \tag{2.90}$$

Rewriting Eq. (2.90) into the form of linear equation system $AX=b$, the coefficients matrix A is defined to be rectangular with 3 columns and n lines as follows:

$$A = \begin{bmatrix} 1 & \ln(T_1/T_0) & \ln(P_1/P_0) \\ 1 & \ln(T_2/T_0) & \ln(P_1/P_0) \\ . & . & . \\ . & . & . \\ 1 & \ln(T_n/T_0) & \ln(P_n/P_0) \end{bmatrix} \tag{2.91}$$

The vector b is represented by:

$$b = \begin{bmatrix} \ln S_{u1} \\ \ln S_{u2} \\ . \\ . \\ \ln S_{un} \end{bmatrix} \tag{2.92}$$

And the vector of unknowns X as:

$$X = \begin{bmatrix} \ln S_{u0} \\ \alpha \\ \beta \end{bmatrix} \tag{2.93}$$

This linear equations system is solved applying expression (A-7) of the appendix A.

2.6 Concluding remarks about laminar premixed flames

The bibliographic revision made herein allows concluding that any experimental or computed value of laminar burning velocity should be associated with a value of the flame stretch rate. Ideally, the stretch-free value of the burning velocity should be quoted and the influence of stretch rate upon this value should be indicated by the value of the appropriated Markstein length. This is the main reason of the increasing use of the constant pressure method in which the stretch rate is clearly defined.

The main advantage of the constant volume method for the determination of the burning velocity is the possibility of exploring a wide range of pressures and temperatures with one explosion. This is the main reason of its utilization for burning velocity determination in engine conditions.

CHAPTER 3

EXPERIMENTAL SET UPS AND DIAGNOSTICS

In order to characterize the combustion of typical syngas-air mixtures, various experimental devices are required. Two static combustion chambers were used for burning velocity measurements by constant pressure and constant volume methods. A rapid compression machine (RCM) was also used for simulate the compression/expansion events of an engine. In the following subsections all this devices are described as well as the experimental procedures.

3.1. Experimental set ups

3.1.1. Syngas mixtures

The syngas-air mixtures were prepared using pressurized containers, vacuum pump and pressure transducer by the partial pressure method. The purity of all used gases is at least 99.9%.

The simplified chemical reaction that expresses the stoichiometric combustion of syngas for syngas typical compositions is:

$$aH_2 + bCO + cCH_4 + dCO_2 + eN_2 + \left(\frac{a}{2}+\frac{b}{2}+2c\right)(O_2+3.76N_2) \rightarrow (b+c+d)CO_2 + (a+2c)H_2O + \left[e+3.76\left(\frac{a}{2}+\frac{b}{2}+2c\right)\right]N_2 \quad (3.1)$$

The partial pressure of each gas of the syngas-air mixture is given by:

$$P_{H_2} = \frac{n_{H_2}}{n_m}P_m = \frac{a}{a+b+c+d+e+4.76(f/\phi)}P_m \quad (3.2)$$

$$P_{CO} = \frac{n_{CO}}{n_m}P_m = \frac{b}{a+b+c+d+e+4.76(f/\phi)}P_m \quad (3.3)$$

$$P_{CH_4} = \frac{n_{CH_4}}{n_m}P_m = \frac{c}{a+b+c+d+e+4.76(f/\phi)}P_m \quad (3.4)$$

$$P_{CO_2} = \frac{n_{CO_2}}{n_m}P_m = \frac{d}{a+b+c+d+e+4.76\,(f/\phi)}P_m \quad (3.5)$$

$$P_{N_2} = \frac{n_{N_2}}{n_m}P_m = \frac{e}{a+b+c+d+e+4.76(f/\phi)}P_m \quad (3.6)$$

$$P_{air} = \frac{n_{air}}{n_m} P_m = \frac{4.76(f/\phi)}{a+b+c+d+e+4.76\,(f/\phi)}\, P_m \qquad (3.7)$$

Where ϕ is the equivalence ratio. The syngas-air mixture was prepared within the combustion chamber. The initial conditions were strictly controlled in the experiments to realize the same initial pressure and temperature. For avoiding the influence of wall temperature on mixture temperature, an enough interval between two experiments is set, providing enough time for wall to cool down to the room temperature.

3.1.2 Rectangular chamber

The static rectangular combustion chamber shown in figure 3.1 has two transparent sides in ordinary glass (BK7) providing large enough optical access to schlieren photography. The inside size of the rectangular chamber is 70 mm width, 58 mm length and 120 mm height. The material of the chamber is duraluminum (AU4G).

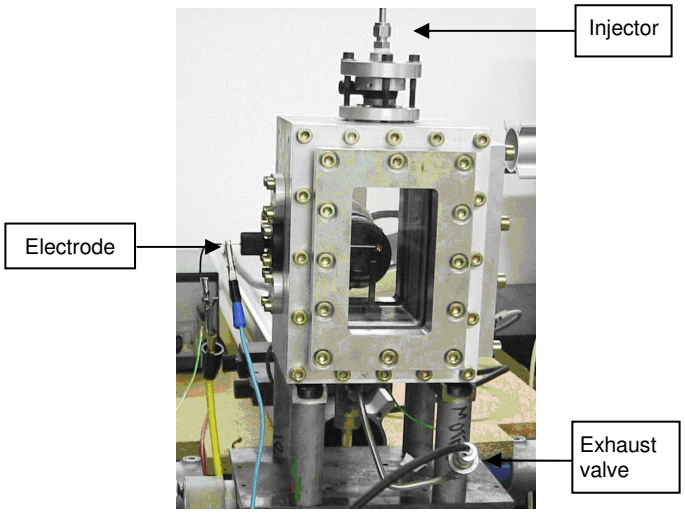

Figure 3.1 – Rectangular combustion chamber

The pressure is recorded by a dynamic sensor Kistler 601A installed in the bottom side of the chamber with resolution of 0.1 mbar. The chamber has an admission/exhaustion valve for mixture admission and combustion gases exhaustion.

The Synerjet-Orbital injector installed on the top surface of the chamber was conceived by Malheiro, (2002). This chamber is able to embrace the ignition electrode in three different positions. This type of electrodes conception allows the possibility to change the spark position in the combustion chamber and also allows the variation of the electrode gap. Such as Malheiro, (2002), the electrode gap employed in the experiments was 2.0 mm.

The ignition coil used is a traditional automobile spark coil (Siemens S10203000A), supplied by a 12 V battery, in which the load could be supplied by an electrical signal or optical command. In this work an electrical signal command was used with a load time of 5 ms.

The procedure to use this chamber for any combustion experiment is:

- Combustion chamber at vacuum. The vacuum was considered in this work to be 12 mbar or less;
- Mixture preparation within the chamber;
- Central ignition of the mixture by a spark;
- Burned gases exhaustion;
- Maximum initial pressure of 3.0 bar.

3.1.3 Spherical chamber

The spherical combustion chamber shown schematically in figure 3.2 is composed by three main parts. Two of which, are the spherical calottes and the third, supports the different devices such as the fast response pressure sensor, ignition electrodes and ionization probes. The inside sphere cavity is lodged in a stainless steel cylindrical block.

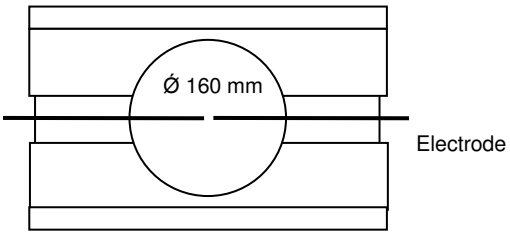

Figure 3.2– Spherical combustion chamber

Two typical automobile electrodes with 0.6 mm diameter are symmetrically introduced at the center of the sphere. The electrodes are feed by the coils at 12 Volts.

An electronic device developed by Fisson et al., (1994) is used to protect the ignition circuit from the measurement system. When current crosses the secondary circuit of the ignition coil, one diode in series generates an optic signal and a phototransistor creates a proportional voltage to the current. This signal is the command to the pressure signal to be recorded.

The pressure is measured during combustion through a piezo-electric pressure transducer KISTLER 601A. This sensor is connected to an amplifier Kistler 5011

regulated for pressures up to 40 bar. The dynamic response of the sensor is 2 µs. The signal acquisition is made by a digital oscilloscope with memory (Tektronix TDS 420A). The acquisition frequency may be varied from 10-200 kHz depending on the duration of the phenomena.

Pressure measurements are used to evaluate the quality of the combustion and the burning velocity in the constant volume method.

3.1.4 Rapid compression machine

A rapid compression machine (RCM) is an instrument to simulate a single cycle of an internal combustion engine, thus also allowing the study of spontaneous ignition under more comparable conditions than those existing in real engines (Strozzi et al., 2008).

The rapid compression machine of the Institute Pprime used in this work has the following configuration (Fig.3.3). All the characteristics of the RCM are summarized in Table 3.1.

Table 3.1 – Geometric and kinematic characteristics of the RCM.

Cylinder volume (cm^3)	Stroke (cm)	Square piston (cm)	Cylinder section (cm^2)	Compression time (ms)	Dead volume (cm^3)	Compression ratio (ε)
1043	41.9	5.63	24.89	44	58.5-128.5	9.1 – 18.8

This experimental set up is well-suited for optical visualization purposes. It features both large lateral and vertical optical accesses.

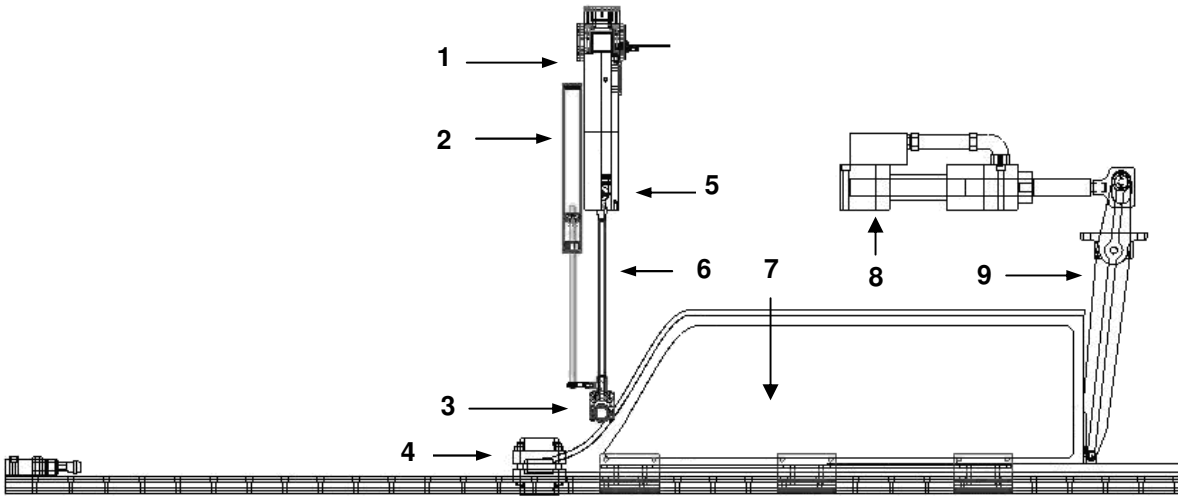

Figure 3.3 – RCM scheme. (1) cylinder/combustion chamber, (2) return cylinder, (3) guiding wheel, (4) Brake system, (5) Piston, (6) Connecting rod, (7) Cam, (8) hydraulic cylinder, (9) lever (Strozzi, 2008).

Running principle

Compression of reactive mixtures is obtained as follows. A hydraulic cylinder sets a cam into motion. The horizontal translation is transformed into a vertical motion via a guiding wheel. The RCM is equipped with a return cylinder to maintain the contact between the cam and the guiding wheel; this ensures that the volume of the chamber is well stabilized at top dead center (TDC).

RCM generally carry out the compression at constant piston velocity. In opposite, the cam of the Institute Pprime RCM has been designed in such a manner that the piston velocity evolves similarly as it does in a real engine. Acceleration and deceleration are moderate and the effect of the compression stroke becomes perceptible only several milliseconds after bottom dead center (BDC).

The RCM is fitted with a heating system in the chamber walls to vary the initial temperature at BDC between 293 and 373 ±1.5K. Moreover, by changing the clearance volume, volumetric compression ratio of the RCM can be varied from ε =9.1 to ε=18.8.

The RCM features a square cross/section with rounded corners piston (50×50, r=3.6 mm), allowing flat windows to be mounted on lateral sides of the chamber; this enables direct visualizations and planar laser sheet measurements within the whole dead volume. The windows are sealed with specifically designed square flat rings and circular rings are used for the cylinder head. The piston is equipped with a squared sealing ring but also with a square shaped guiding ring, to avoid asymmetric formation of corner vortex. Moreover the RCM features a long compression stroke (S=419 mm), providing a wider visualization window at TDC for a given compression ratio.

Mechanical part of RCM

The mechanical part of the RCM is based on the principle of the catapult. A cylinder, commanded by a high-speed servo valve (response time of approximately 5 ms) and supplied with a hydro-electric power station allowing a flow of 400 l/min, drives a steel rod of large dimensions (length 775 mm, thickness 50 mm, H section) which in turns drive a carriage of 40 kg at high speed installed horizontally on rails. This carriage is equipped with a cam whose profile actuates a roller that supports the piston vertical movement. The profile is calculated to reproduce the movement of an engine running at around 700 rpm. It was necessary to install hydraulic brakes (ordered in a

mechanical way, by safety) on the way of the carriage in order to stop it, which passes from 0 to 40 km/h and then from 40 km/h to 0. Everything will take 60 ms, which explains the 5 meters length of the machine.

Diagnostic systems of RCM

The RCM is equipped with various means of measurement: a laser sensor to measure displacement, inductive sensors positioned along the axis of the piston to start the optical instrumentation and to generate the spark, a sensor to measure the dynamic pressure in the combustion chamber, as well as a thermocouple used during special tests where the chamber is heated, and controlled in temperature. The chamber is equipped with valves intended for the draining and filling of gas mixtures, as well as a secondary cylinder to create controlled aerodynamic effects representative of those found in engines (swirl movement, tumble or homogeneous turbulence).

Acquisition and control

The RCM control is managed by a PC. The measuring signs (pressure, piston position, wall temperature, heat flux, etc.) are registered simultaneously by a data acquisition (National Instrument 6259) and integrated in the interface. Also some RCM controlling parameters (brakes pressure, hydraulic pressure, piston position, contact cam/lever, etc.) are taking into account for security reasons. The interface also controls the signals of the lasers and camera.

Pressure measurement

Pressure is measured by a piezoelectric sensor Kistler 601A coupled with an amplifier Kistler 5011B10. This system allows the dynamic measuring of pressure during compression, combustion and expansion. The theoretical precision is about ±1 bar before a significant heat release occurs and ±1.5 bar during and after the ignition. These values include sensor non-linearity error (±0.75 bar) and amplification error. Coupled with an amplifier this measuring system allows registering frequencies higher than 100 kHz in agreement with the used samples.

3.2. Combustion diagnostics

Combustion diagnostics used in this work are pressure measurements used for the determination of the flammability limits and burning velocity at constant volume,

schlieren visualizations used for the determination of the burning velocity at constant pressure. Each one is described in the next sub-sections.

3.2.1 Flammability limits

The flammability limit is a most widely used index for representing the flammability characteristics of gases. In accordance with generally accepted usage, the flammability limits are known as those regions of fuel–air ratio within which flame propagation can be possible and beyond which flame cannot propagate. And there are two distinct separate flammability limits for the fuel–air mixture, namely, the leanest fuel-limit up to which the flame can propagate is termed as lower flammability limit (LFL), and the richest limit is called as upper flammability limit (UFL).

There are several criteria to determine the flammability limits. A successful attempt can be determined by one or a combination of the following criteria: (1) inspection of the visualization of the flame kernel produced by the spark, namely visual criterion, and (2) measurements of pressure or temperature histories in the vessel and appropriate pressure or temperature rise criteria can be used to designate flammability rather than the purely visual observation of flame development. As we know, a successful ignition would induce a rapid pressure increase and temperature rise within a short time, as well as produce a propagating flame front that could be readily observed.

Previous gas flammability limit data were obtained mainly in flammability tubes, in those tests, a gas mixture in a vertical tube was ignited and flame propagation was inspected by a visual criterion. The wall quenching has a significant effect on the flammability measurement in flammability tube. The larger size of combustion chamber can minimize wall effects and can allow for the potential use of stronger igniters to ensure the absence of ignition limitations, so most of the flammability measurements are conducted in closed chambers recently (Liekhus et al., 2000).

For safety reasons, to prevent accidental explosions during chemical processes and to classify gas and gas mixtures for storage and transport, there are standards for the determination of the explosion limit in atmospheric conditions that can be found in Schroder and Molnarne, (2005). In general, the explosion limits are affected by the apparatus and material parameters. The most important are:

- Flammable mixture composition, type and amount of inert gas, fuel and oxidizer;
- Initial pressure and initial temperature;

- Flow state;
- Determination procedure (step size, criterion);
- Type and size of the ignition vessel (closed, open, dimensions, material);
- Ignition source (type, power, duration and location);
- Direction of flame propagation.

The purpose of this study is to determine the flammability limits of syngas-air mixtures as guidance for stationary energy production systems. As the conditions in an energy production scenario are different, namely in terms of pressure, some apparatus characteristics referred in the standards described above are not followed. The flammable region obtained will be narrower than the actual flammable region.

In this context, prior to our experimental work, we carry out measurements of the flammable region of syngas-air mixtures (at rest, initial conditions 293K, 1.0 bar and 3.0 bar) with our specific ignition system.

The syngas-air mixtures were prepared within the spherical chamber using two 10L bottles previously prepared with the syngas composition and another with compressed atmospheric air by the partial pressure method. The equivalence ratio was varied in 0.1 steps. The flammability limits using for different initial conditions of pressure is shown in figures 3.4 to 3.6. In the boundaries of the flammable region ten shots were made in order to get the ignition success.

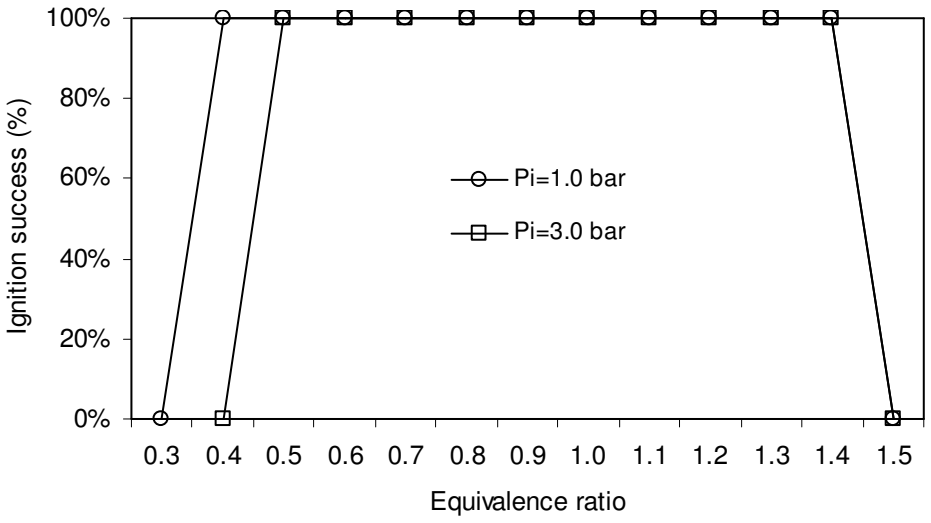

Figure 3.4– Flammability limits of the updraft syngas-air mixture.

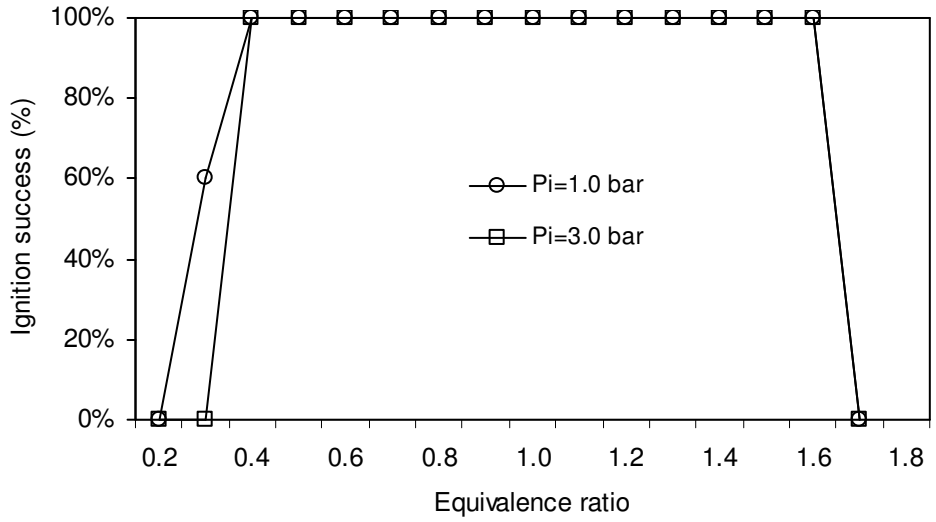

Figure 3.5– Flammability limits of the downdraft syngas-air mixture.

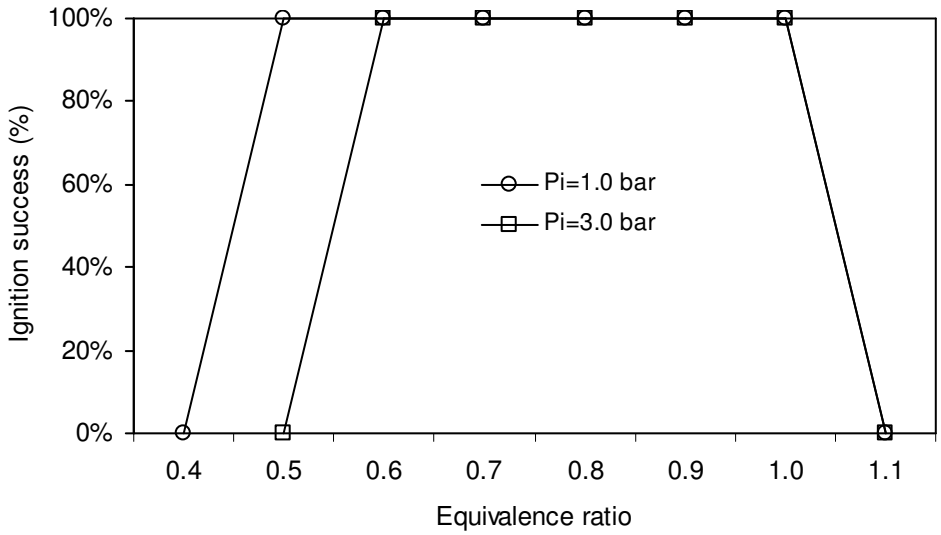

Figure 3.6 – Flammability limits of the fluidized bed syngas-air mixture.

Figure 3.4 shows that the flammable region for the updraft syngas-air mixture for 1.0 bar and 293K is between 0.4 and 1.4 equivalence ratios. Increasing the initial pressure to 3.0 bar, the lean flammability limit is reduced to ϕ=0.5.

Figure 3.5 shows that the flammable region for the downdraft syngas-air mixture for 1.0 bar and 293K is between 0.3 and 1.6 equivalence ratios. Pressure increase for ϕ=0.3 is only 20% of the initial pressure. Increasing the initial pressure to 3.0 bar, the lean flammability limit is reduced to ϕ=0.4.

Figure 3.6 shows that the flammable region for the fluidized bed syngas-air mixture for 1.0 bar and 293K is between 0.5 and 1.0 equivalence ratios. Increasing the initial pressure to 3.0 bar, the lean flammability limit is reduced to ϕ=0.6.

These results show that the pressure has a definite effect on flammability limits of the syngas-air mixtures reducing the flammable region in the lean side.

For hydrocarbon-air mixtures the rich limit become much wider with increasing pressure and the lean limit is not appreciably affected (Kuo, 2005). There is a dependence of the width of flammable region on the order of chemical reactions. The second order reactions that occur at low pressures give room to first order reactions at high pressures. To compare hydrocarbons flammability limits behavior with syngas higher pressure experiments are needed.

3.2.3 Pressure measurement on static chambers

A set of experiments were made in order to determine the repetition of the measured pressure versus time during the combustion of syngas-air mixtures. Figure 3.7 shows a set of three experiments with updraft syngas-air mixture in spherical chamber. Figure 3.8 shows a set of three experiments with updraft syngas-air mixture in rectangular chamber. In both cases the following initial conditions, P_i= 1.0 bar, T_i = 293 K and stoichiometric equivalence ratio where used. A very good repetition of the pressure signal was obtained in both cases. This behavior was verified for every syngas composition except for very lean mixtures. In those cases the number of experiments was increased to five, especially in the rectangular chamber due to higher leakages.

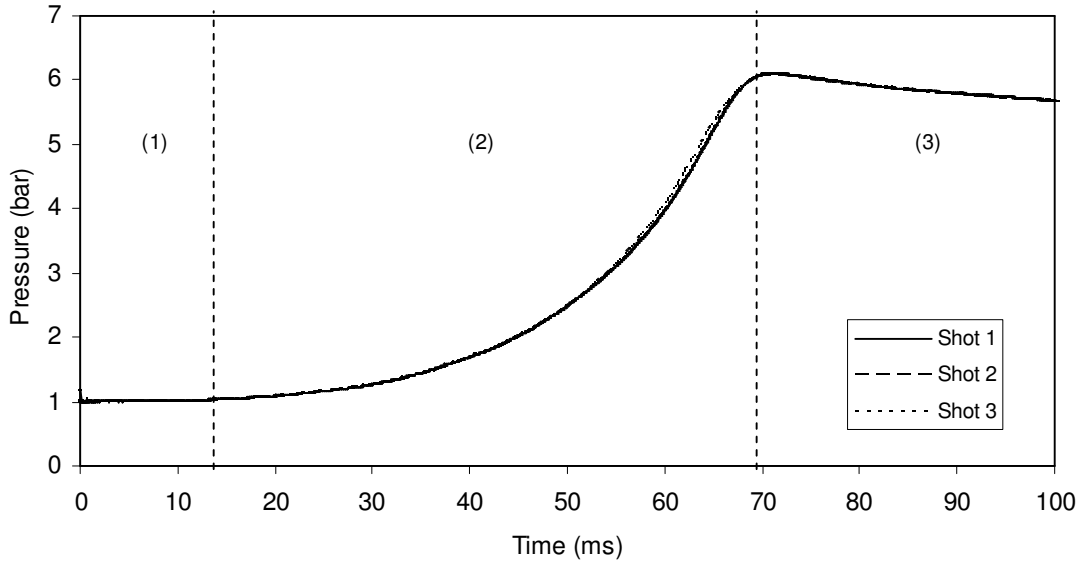

Figure 3.7 - Pressure versus time in spherical chamber

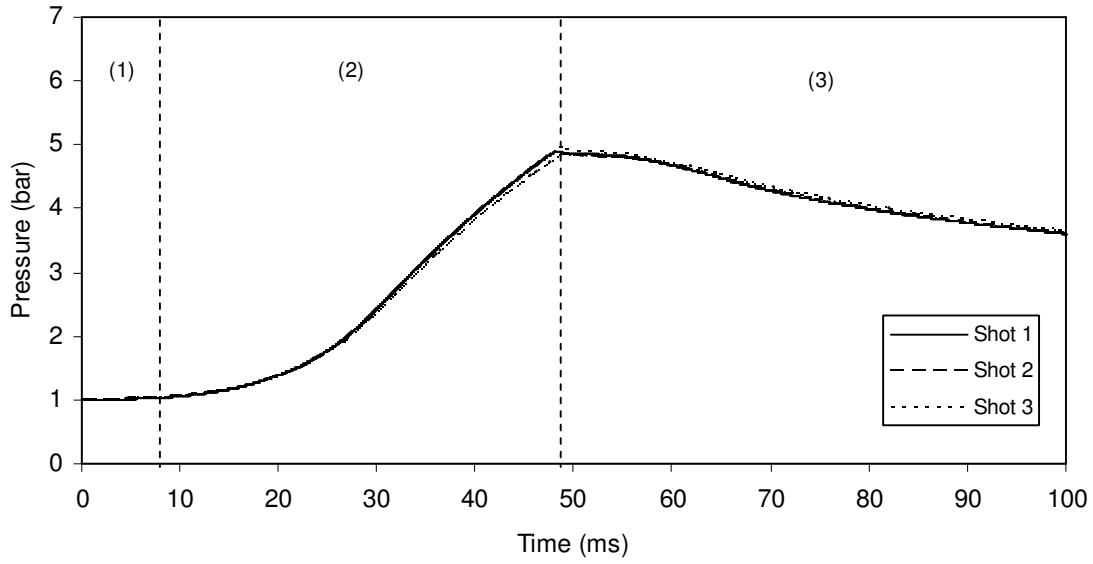

Figure 3.8 - Pressure versus time in rectangular chamber

Three combustion stages can be observed from the pressure versus time curves shown in the figures 3.7 and 3.8: (1) development of a flame kernel followed by flame propagation at constant pressure; (2) flame development followed by rapid pressure increase and (3) flame quenching followed by burned gases cooling.

The first stage, that has a changeable duration in accordance with the initial conditions of the mixture, corresponds to the formation of the initial flame kernel. The ignition is provoked by a spark of duration of approximately 5 ms and allows inflaming the mixture creating a flame kernel that develops at sensibly constant pressure. During this phase, flame development could be difficult. In one hand, the reduced flame radius makes the curvature effect more significant. On the other hand, the electrodes can provoke the quenching of the flame due to heat absorption. In the second stage, a stable flame is established. It begins when the pressure starts to increase and ends when the pressure reaches its maximum value. Fisson et al. (1994), shown that a well established flame is obtained when the pressure reaches 1.5 times the initial pressure. At the end of this stage, the flame approaches the wall magnifying the heat losses, which can violate the hypothesis of adiabatic compression. For this reason, the maximum pressure P_{max} is lower than the adiabatic pressure P_v which would be obtained if the process were adiabatic throughout all this phase. The third and last phase represents the end of combustion, where the flame reaches the wall non-uniformly. On the double effect of the thermal losses and the deactivation of the free radicals, the flame is quenched followed by the burned gases cooling.

Three global parameters that characterize the quality of the combustion can be obtained from pressure curves:

- Pressure gain:

$$g_p = \frac{P_{max}}{P_i} \tag{3.8}$$

- Combustion efficiency:

$$\eta = \frac{P_{max}}{P_v} \tag{3.9}$$

- Combustion time, τ, is defined as the time since the spark plug to the peak of pressure.

Table 3.2 shows the above combustion parameters for typical syngas-air mixtures under various initial conditions in spherical chamber.

Table 3.2 – Syngas-air combustion parameters in spherical chamber.

Parameter	Pi=0.5 bar				P_i = 1.0 bar				P_i = 5.0 bar			
	ϕ=0.6	ϕ=0.8	ϕ=1.0	ϕ=1.2	ϕ=0.6	ϕ=0.8	ϕ=1.0	ϕ=1.2	ϕ=0.6	ϕ=0.8	ϕ=1.0	ϕ=1.2
Updraft												
g_p	5.39	5.61	6.08	5.81	4.87	5.65	6.09	5.79	4.42	6.28	6.73	6.22
τ (ms)	161.2	129.0	61.7	58.84	172.2	93.7	71.0	65.0	650.3	167.2	119.1	143.2
η	90%	85%	87%	86%	70%	85%	87%	86%	74%	90%	95%	92%
Downdraft												
g_p	5.40	6.11	6.35	5.90	5.45	6.16	6.44	6.04	5.34	6.21	6.60	6.15
τ (ms)	114.3	64.8	54.5	49.9	126.6	71.7	57.7	58.0	226.1	107.2	84.3	98.8
η	93%	95%	94%	91%	94%	96%	95%	93%	92%	96%	96%	94%
Fluidized bed												
g_p	n.d.	n.d.	n.d.	n.d.	n.d.	5.58	5.70	n.d.	n.d.	4.44	4.54	n.d.
τ (ms)	n.d.	n.d.	n.d.	n.d.	n.d.	200.7	187.5	n.d.	n.d.	753	713.5	n.d.
η	n.d.	n.d.	n.d.	n.d.	n.d.	84%	88%	n.d.	n.d.	66%	71%	n.d.

These parameters show that the combustion of stoichiometric syngas-air mixtures is generally more efficient and faster than for other equivalence ratios.

Comparing the three typical syngas-air mixtures conclusion can be drawn that downdraft syngas-air mixture has higher pressure gains, higher efficiency and lower combustion times than remain syngas-air mixtures. These results could be endorsed to the higher heat of reaction and hydrogen content of the downdraft composition.

3.2.4 Pressure measurement on RCM

The RCM described on 3.1.4 can work on two distinctive modes: single compression and compression and expansion. Single compression is generally used for the study of

high pressure auto-ignition of combustible mixtures as it gives direct measure of ignition delay (Mittal, 2006). When the interest is the heat transfer to the walls then it is usually used an inert gas, with equal adiabatic coefficient as the reacting mixture, as a test gas. In this work instead of an inert gas a stoichiometric syngas-air mixture was used out of auto-ignition conditions. A set of three experiments were made for each syngas composition without combustion in order to verify its repetition. The pressure traces are shown in figure 3.9 for downdraft syngas composition.

Figure 3.9 shows rapid rise in pressure during the compression stroke followed by gradual decrease in pressure due to heat loss from a constant volume chamber, the clearance volume, at the end of compression. A very good repetition of signals was found during compression experiments being the maximum difference between pressure peaks around 0.3 bar (25 bar on average) from one experiment to another.

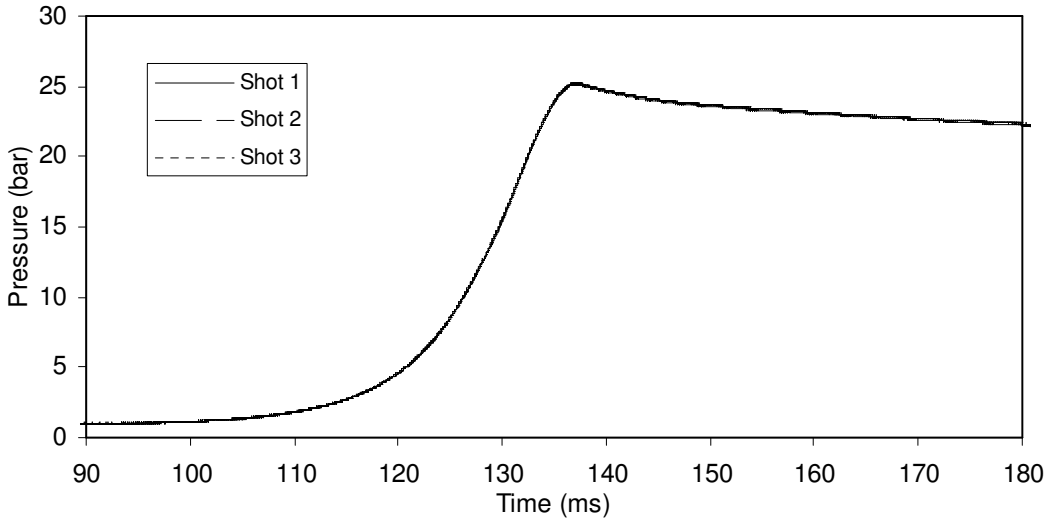

Figure 3.9 - Pressure versus time for compression of stoichiometric downdraft syngas-air in a RCM. Initial conditions: P_i = 1.0 bar; T_i = 293 K, ε=11.

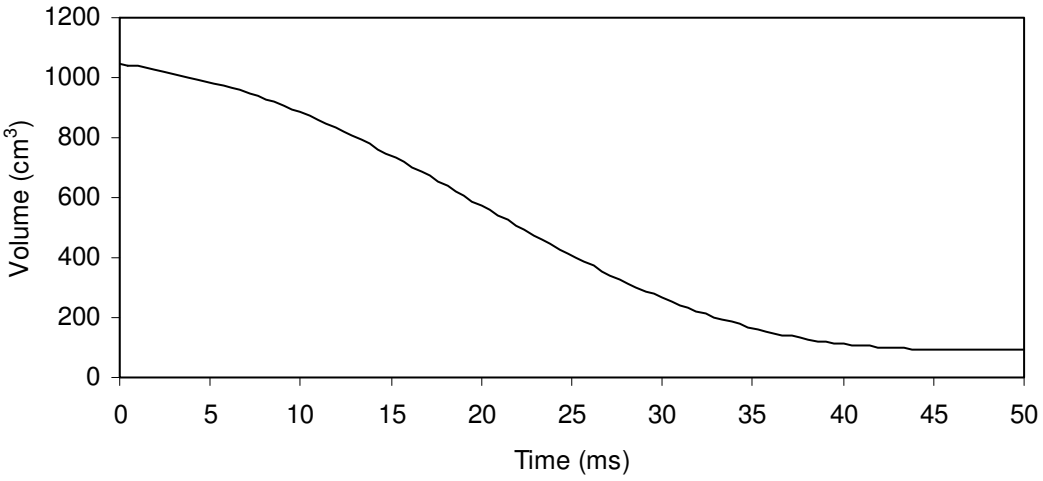

Figure 3.10 - Typical volume trace for compression of stoichiometric downdraft syngas -air in an RCM. Initial conditions: P_i = 1.0 bar; T_i = 293 K, ε=11.

In-cylinder volume during compression is reported in the figure 3.10. The volume is determined thanks to a laser piston positioning sensor being the compression time estimated on 44 ms. The piston velocity is comprised between 0 and 15 m/s, and it is around 9.5 m/s on average. In order to avoid measurements uncertainties, another laser piston position sensor was placed at TDC and the pressure and piston position signals synchronized.

The same procedure was followed when working with compression-expansion strokes without combustion (motored) being the pressure trace repetition verified in the figure 3.11.

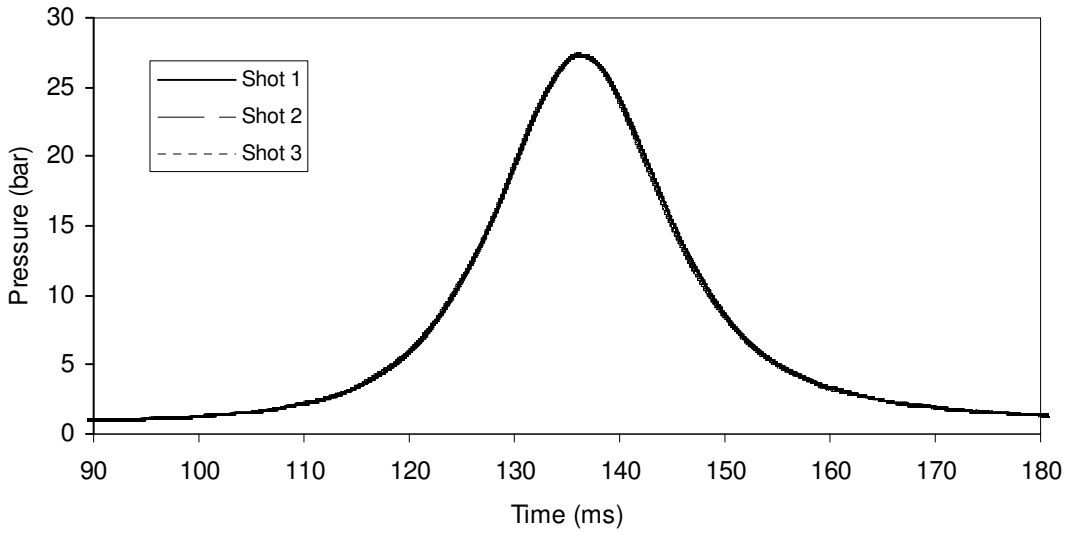

Figure 3.11 - Typical pressure trace for compression expansion of stoichiometric downdraft syngas-air mixture in a RCM. Initial Conditions: P_i = 1.0 bar; T_i = 293 K.

A very good repetition of signals was found during compression expansion experiments being the maximum difference between peak pressures around 0.4 bar (27 bar on average) from one experiment to another. Notice the higher pressure peak (>2.0 bar, 8%) of the compression expansion strokes compared with single compression stroke of the figure 3.9. To explain this difference the average piston displacement without combustion during the compression stroke for both working modes are shown in the figure 3.12.

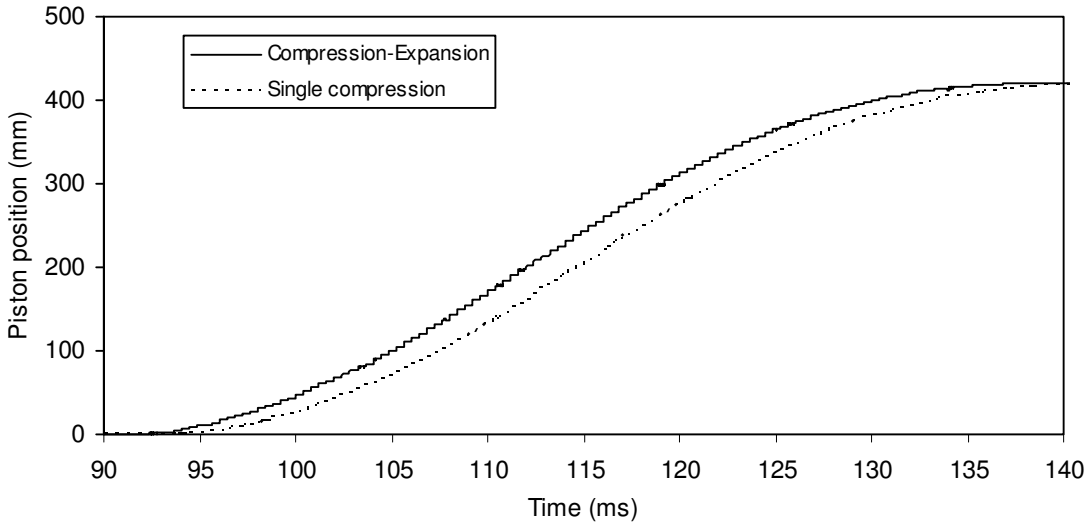

Figure 3.12 – Piston displacement during one and two strokes without combustion.

The difference on the figure 3.12 is around 2.0 ms in the initial, which indicates that the RCM cam of the compression-expansion strokes is shorter than the compression one. The corresponding in-cylinder volume versus time is lower for the compression-expansion case, which corresponds to higher in-cylinder pressures.

In an ideal spark-ignited internal combustion engine one can distingue three stages: compression, combustion and expansion. The entire pressure rise during combustion takes place at constant volume at TDC. However in an actual engine this does not happen as well as in the RCM. The pressure variation due to combustion in a compression and expansion rapid compression machine is shown in figure 3.13, where three stages of combustion can be distinguished.

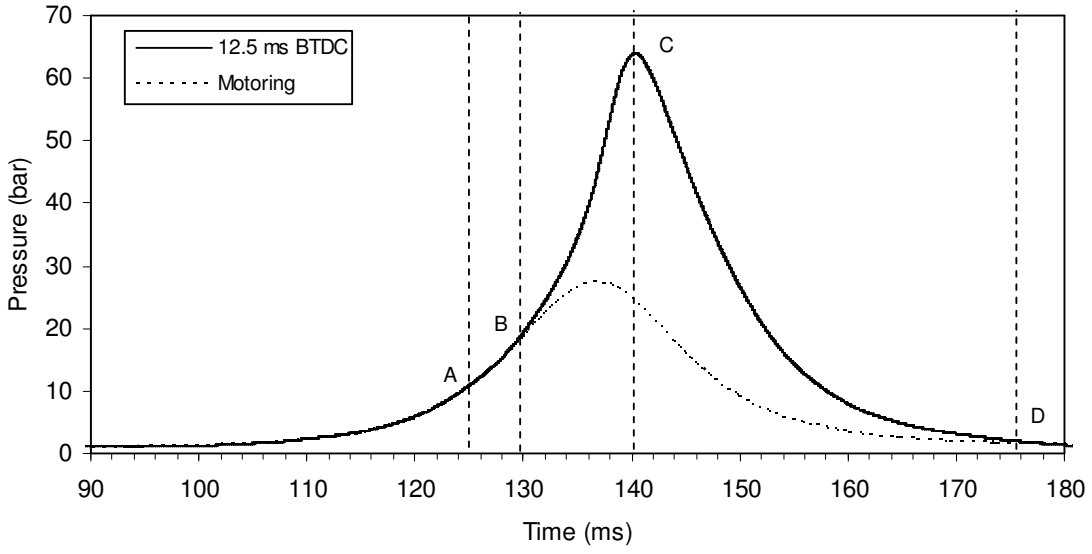

Figure 3.13 – Stages of combustion in a RCM.

In this figure, A is the point of passage of spark, B is point at which the beginning of pressure rise can be detected and C the attainment of peak pressure. Thus, AB represents the first stage, BC the second stage and CD the third stage (Ganesan, 1995).

The first stage is referred to as ignition lag or preparation phase in which growth and development of a self propagating nucleus of flame takes place. This is a chemical process depending upon both pressure and temperature and the nature of the fuel. Further, it is also dependent of the relationship between the temperature and the rate of reaction.

The second stage is a physical one and is concerned with the spread of the flame throughout the combustion chamber. The starting point of the second stage is where the first measurable rise of pressure is seen, i.e. the point where the line of combustion departs from the compression line (point B). This can be seen from the deviation from the compression (motoring) curve.

During the second stage the flame propagates practically at a constant velocity. Heat transfer to the cylinder wall is low, because only a small part of the burning mixture comes in contact with the cylinder wall during this period. The rate of heat release depends largely of the turbulence intensity and also of the reaction rate which is dependent on the mixture composition. The rate of pressure rise is proportional to the rate of heat release because during this stage, the combustion chamber volume remains practically constant (since the piston is near the TDC).

The starting point of the third stage is usually taken at the instant at which the maximum pressure is reached (point C). The flame velocity decreases during this stage. The rate of combustion becomes low due to lower flame velocity and reduced flame front surface. Since the expansion stroke starts before this stage of combustion, with the piston moving away from the TDC, there can be no pressure rise during this stage.

3.2.5 Aerodynamics inside a RCM

Although in principle RCM simulates a single compression event, complex aerodynamic features can affect the state of the reacting core in the reaction chamber. Previous studies of Griffiths et al., (1993) and Clarkson et al., (2001) have shown that the motion of the piston creates a roll-up vortex, which results in mixing of the cold gas

pockets from the boundary layer with the hot gases in the core region. However, substantial discrepancies have been observed between data taken from different rapid compression machines even under similar conditions of temperature and pressure (Minetti et al., 1996). These discrepancies are attributed partly to the different heat loss characteristics after the end of the compression stroke and partly to the difference in aerodynamics between various machines. The effect of aerodynamics is particularly more complicated because it does not show up in the pressure trace and it may lead to significant temperature gradients and ultimately to the failure of the adiabatic core hypothesis.

The aerodynamics inside a rapid compression machine is highly unsteady in nature; it plays a role in pre-ignition through turbulent mixing, but also because it drives the evolution of the temperature distribution. In order to characterize the temporal evolution of the flow, and quantify the distribution and turbulence intensity associated to the Institute Pprime RCM, the previous work of Strozzi, (2008) is referred.

Measurements on the total extent of the clearance volume and at the center of the chamber were made using an inert gas N_2 to simplify the diagnosis and avoiding the disruption of PIV images by possible oxidation of unwanted particles. The flow remains representative of the reactive case when the heat release is negligible. For more details on the experimental protocol see Strozzi, (2008).

3.2.5.1 Velocity fluctuations

The study of turbulent flows is generally based on the Reynolds decomposition, where the instantaneous velocity is decomposed into a mean part and a fluctuating part: $U = \langle U \rangle + u$.

In most cases, a global average is used to estimate mean velocity $\langle U \rangle$. Using this approach in an engine results in substantial overestimation of the turbulent intensity that can reach a factor of 2 (Liou and Santavicca, 1985). Indeed, the cyclical fluctuations of the overall movement (such as large eddy scale movement) are included in the fluctuating field as well as fluctuations in velocity caused by the turbulent nature of the flow.

Instantaneous velocity

Figure 3.14 shows the time evolution of the velocity field during an inert gas compression. It is observed 10 ms BTDC a laminar one-dimensional compression flow.

A zone of high velocities (5 to 8 m/s), where the flow is turbulent, that come in the center of the clearance volume 5 ms after. The laminar flow of this zone becomes two-dimensional and diverging to the walls. The turbulent zone reaches TDC and occupies a large part of the chamber at that moment. The flow in this zone is structured by two counter-rotating vortices, which is consistent with the literature where the movement of the piston brings the gas from the side wall toward the center of the chamber, forming vortices on the corners. These vortices then move to the side walls and after down the chamber. Simultaneously, the maximum velocity of the flow gradually decreases, and the size of the 'laminar' zone observed at the end of compression decreases. The disappearance of this zone occurs approximately 17 ms after TDC, although some low velocity zones remain. 40 ms after TDC, the corner vortices are replaced by a fragmented and highly three-dimensional flow.

The coexistence of laminar and turbulent regions is characteristic of MCR flat piston flow, where the gases are at rest before compression. One can observe a certain asymmetry in vortices velocity, with lower values at TDC and close to the walls (figure 3.14). This asymmetry reflects the exchange of kinetic energy that occurs in the strain layer between the vortex and the zone of lower flow. The velocity gradient direction at the zone interface may also be parallel to the mean flow, as is in the case of few milliseconds before TDC. In this case, if the inertia of the high speed zone regrowth clearly the core zone, the turbulent nature of the flow at the interface is also likely to accelerate the decrease in the extent of the core zone. This emphasis the existence of two ranges of scales associated with mixing phenomenon: those of the overall movement, and those of turbulence. Moreover, the overall velocity of the movement decreases rapidly if the flow stops. Thus, reflecting the kinetic energy transfer from large scales to the turbulent scales.

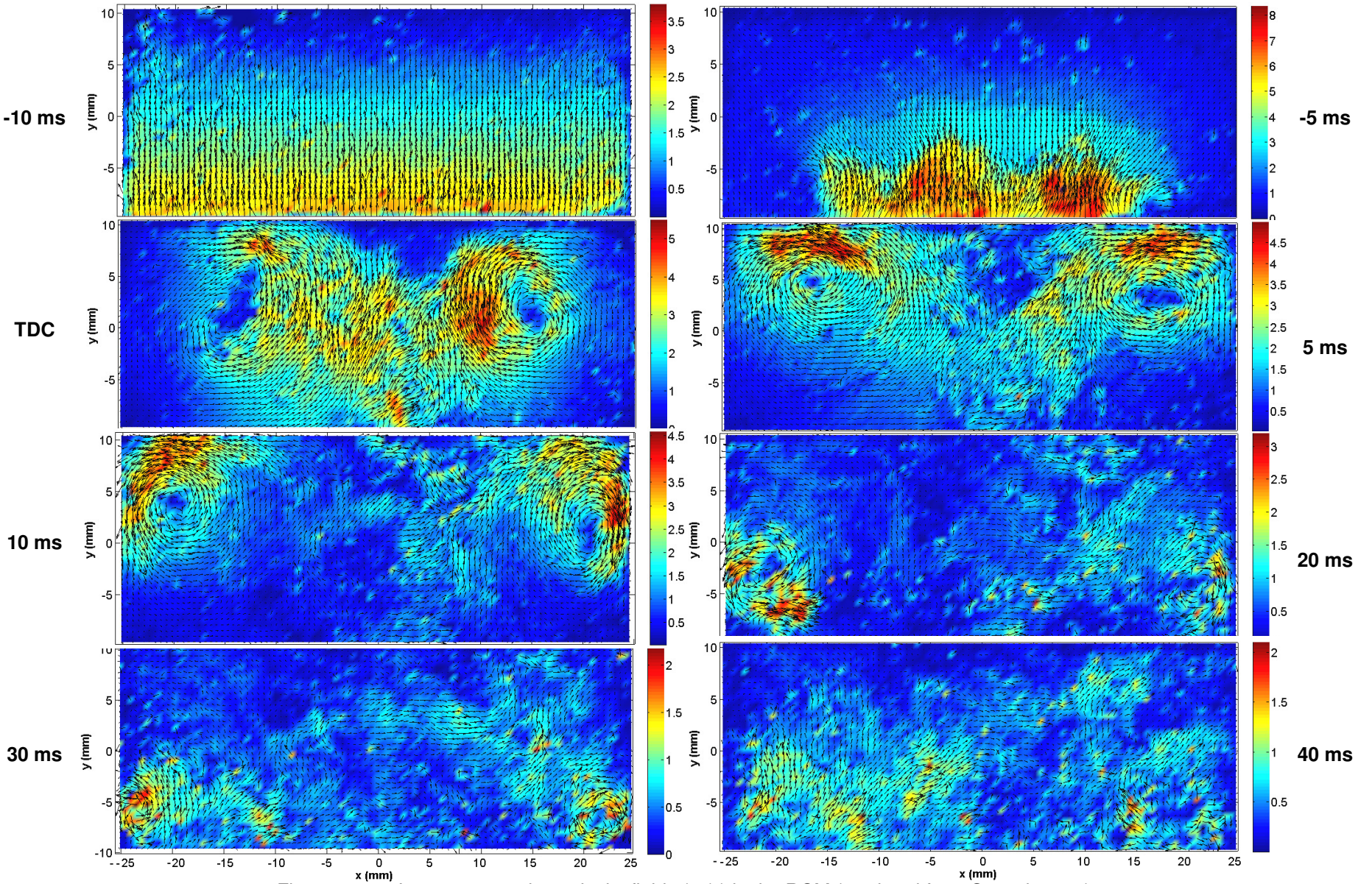

Figure 3.14 – Inert compression velocity fields (m/s) in the RCM (reprinted from Strozzi, 2008).

3.2.5.2 Analysis of the flow at the chamber core

The whole movement has been analyzed, and an initial assessment of turbulent fluctuations was provided from the whole filed measurements. Specific field measurements are now exposed to evaluate the properties of turbulence in detail. The turbulent characteristics are evaluated thanks to PIV measurements with time resolution of 5 kHz along one field of 13x13 mm and image resolution of 512x512 pixels. The investigated zone is close to the center of the chamber (1.5 mm to the left), where the mean and fluctuating velocities remain relatively elevated along a 10 ms period after TDC. Figure 3.15 shows the fluctuation velocity components in this zone.

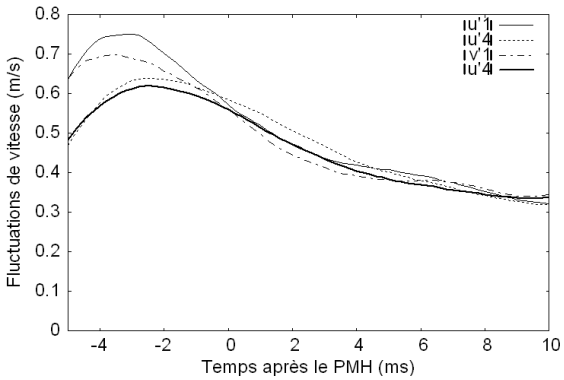

Figure 3.15 – Time evolution of the space speed fluctuations variation (reprinted from Strozzi, 2008). The zone 1 corresponds to the bottom left corner of PIV field, and the zone 4 corresponds to the entire field.

It is observed that both velocity components fluctuations decrease after TDC with similar amplitude. The kinetic energy is evaluated only from two velocity components as follows:

$$k = \sqrt{u'^2 + v'^2} \tag{3.10}$$

It is therefore, slightly underestimated (~20%) due to the lack of the third component.

Figure 3.16 represents the kinetic turbulent energy. The maximum of kinetic energy is obtained 2-3 ms before TDC. It is followed by a rapid decrease that reflects both the overall decrease of the turbulent kinetic energy but also the convection of the fastest zones outside the measured field.

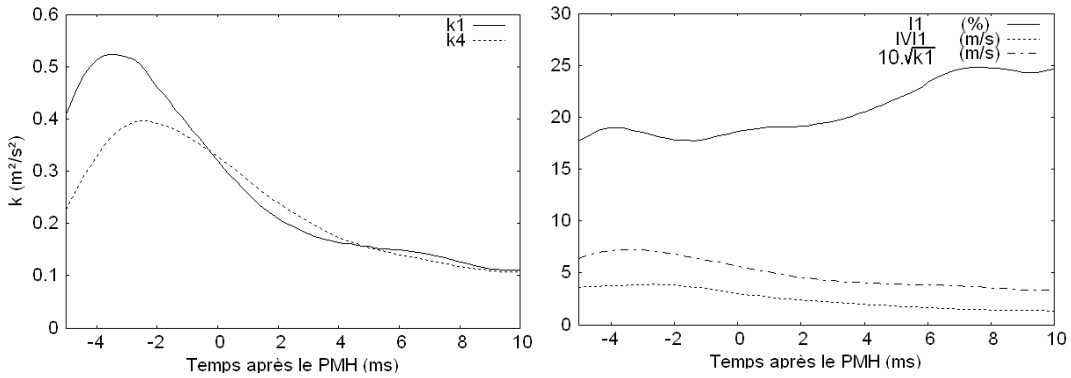

Figure 3.16– Kinetic energy (left) and turbulence intensity (right). Reprinted from Strozzi, (2008)

The turbulent intensity calculated in zone 1 is moderate, with a value of about 20% with minor variations over time. One should remind that this value corresponds to a high velocity turbulent zone. Furthermore, figure 3.16 suggests turbulence intensity much higher at the interface between the turbulent zones and low velocity zones.

3.2.6 Schlieren photography

Schliere (pl. Schlieren) is a German word denoting optical inhomogeneity in an otherwise transparent region. Such inhomogeneity causes refraction of light, which can be displayed on a screen and used as a source of information on the disturbance (Chomiak, 1990). The method is illustrated in Figure 3.17.

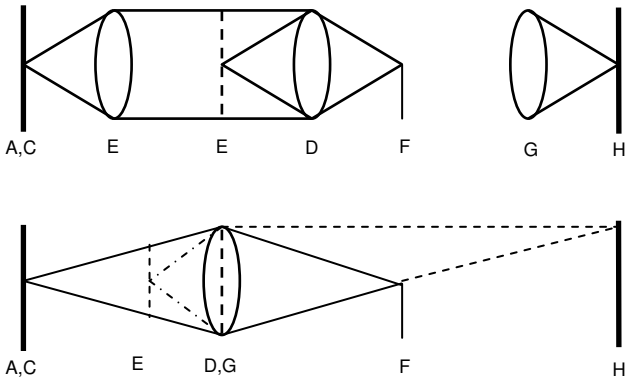

Figure 3.17– Typical (top) and single-lens (bottom) schlieren systems.

Light from a point source A is transformed into a parallel beam and let through the zone to be investigated, E. All the rays which are not deflected converge at the focus of lens D and are cut off by diaphragm F. refracted rays bypass the diaphragm and are collected by lens G, which projects them onto screen H. Lens G is placed in such a way as to produce a sharply defined image of plane E on the screen. Simple geometrical considerations are not sufficient to determine precisely the changes in screen illumination due to a given disturbance, since they are greatly influenced by the diffraction of light on the diaphragm and by the source dimensions. Approximately, however, the relative illumination at the image plane, $\Delta I/I$, is proportional to the beam deflection angle θ and the focal length f of lens D, as follows:

$$\frac{\Delta I}{I} \approx \theta f \tag{3.11}$$

The schlieren image is greatly influenced by the form and size of the light source and diaphragm. Placing a diaphragm at the lens focus amounts to removing a specific group of harmonics from the diffraction pattern, this, of course, introduces significant changes in the schlieren image. Hence all schlieren photography apparatus should consist of a large choice of diaphragms from which selection can be made experimentally to obtain the most contrasting picture of a given effect. By using a slit source of white light and a slit diaphragm color schlieren images can also be achieved.

The dependence of changes in illumination at the screen on the refraction angle implies that the schlieren image visualizes density gradients of the flame:

$$\frac{\Delta I}{I} \approx \frac{\partial Q}{\partial n} \tag{3.12}$$

Where n represents a normal to the surface of constant density. Superimposed on this relationship is a spatial function dependent on the structure of the system and its arrangement relative to the disturbance. The situation is therefore largely qualitative, although an appropriate setting of the apparatus (on removing the diaphragm, a sharm image of the flame should appear on the screen) should ensure fairly faithful representation of the disturbance pattern. To obtain quantitative estimates of the density gradients at a given setting of the apparatus, optical calibrations are used with known refraction angles.

Figure 3.18 shows a scheme of the used schlieren apparatus. The laser source (Laser Árgon Spectra Physics Series 2000) with a maximum power of 6 W generates a

continuous beam of light, composed for two respectively equal main rays with wave length of 488 and 514.5 nm. This laser beam is cut, by the acoustic-optical deflector (Errol) in a succession of luminous impulses of adjustable duration and frequency. At the exit of the acoustic-optical deflector, the rays cross a convergent lens making them to converge into a focal point in the image where is placed a diaphragm of 50µ diameter. The diaphragm is placed in the center of the object of a spherical mirror with focal length of 1m, in order to reflecting the luminous rays into a parallel beam that crosses the combustion chamber (Taillefet, 1999).

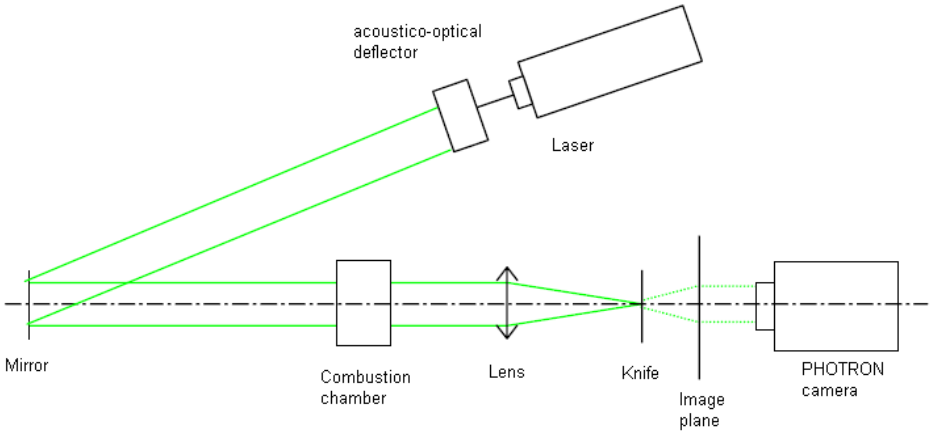

Figure 3.18– Schlieren scheme (Malheiro, 2002)

When a phenomenon in the chamber cause a change of the refractive index, the light is deviated and passes with the same dimensions to the screen that can be record by a camera. To this end, a fast camera APX RS PHOTRON (CMOS, 10 bits, run at 6000 fps, 1024×512 pixels) is used to record the schlieren flame images during combustion. Exposure time is imposed by the acoustic-optical deflector and is fixed to 5 ms.

CHAPTER 4

EXPERIMENTAL AND NUMERICAL LAMINAR SYNGAS COMBUSTION

Syngas obtained from gasification of biomass is considered to be an attractive new fuel, especially for stationary power generation.

As reported in chapter 2 there is considerable variation in the composition of syngas due to various sources and processing methods. Continuous variation in the composition of the generated syngas from a given gasification source is another challenge in designing efficient end use applications such as burners and combustion chambers to suit changes in fuel composition. Designing such combustion appliances needs fundamental understanding of the implications of syngas composition for its combustion characteristics, such as laminar burning velocity and flammability limits. Laminar burning velocity for single component fuels such as methane (Hassan et al., 1998; Gu et al., 2000); and hydrogen (Aung et al., 1997; Bradley et al., 2007) are abundantly available in the literature for various operating conditions. Burning velocity studies on H_2–O_2–inert (such as N_2, CO_2, Ar, and He) are also available (Aung et al., 1998; Lamoureux et al., 2003). Some studies on burning velocities are also available for binary fuel mixtures such as H_2–CH_4 (Halter et al., 2005; Coppens et al., 2007), and H_2–CO (Vagelopoulos and Egolfopoulos, 1994; Sun et al., 2007). Vagelopoulos and Egolfopoulos, (1994) measured burning velocities of H_2–CO mixtures using a counter flow flame technique and reported that addition of 6% or more hydrogen to H_2–CO made the response of the H_2–CO mixture more similar to the kinetics of hydrogen than to that of CO. McLean et al., (1994) measured unstretched laminar burning velocities for 5%H_2 – 95%CO and 50%H_2 – 50%CO mixtures using constant-pressure outwardly propagating spherical flames to evaluate the rate of the CO + OH reaction. Brown et al., (1996) reported flame stretch effects on burning velocities of H_2–air, 50%H_2–50%CO–air and 5%H_2–95%CO–air mixtures under atmospheric condition. Values of Markstein length for 50%H_2–50%CO–air mixtures were found to be very similar to those of pure H_2–air mixtures. It was concluded that H_2 was the dominant species and governed the Markstein length behavior for the 50% H_2– 50% CO–air mixture. Hassan et al., (1997) reported the effects of positive stretch rate on burning velocities of H_2–CO mixtures under different mixture conditions by varying the H_2 fraction in the fuel from 3 to 50% by volume using constant-pressure outwardly propagating spherical flames.

They stated that as the H_2 concentration in the H_2–CO mixture increased, the mixture started behaving similarly to the H_2–air mixture and the effect of flame stretch on burning velocity also became more pronounced. Sun et al., (2007) measured stretch-free burning velocities for CO–H_2–air mixtures at different mixing ratios (the values of the CO/H_2 ratio used were 50:50, 75:25, 95:5, and 99:1), equivalence ratios and pressures using expanding spherical flames at constant pressure. They used artificial air with helium instead of nitrogen to have stable flames at higher pressures. Burke et al., (2007) studied the effects of CO_2 on the burning velocity of a 25% H_2–75% CO mixture with 12.5%O_2–87.5%He oxidizer under stoichiometric conditions and they varied the CO_2 concentration in the fuel from 0 to 25% using spherically expanding flames. They stated that the largest flame radius for calculation of unstretched burning velocity should be less than 30% of the radius wall in a cylindrical chamber. Natarajan et al., (2007) investigated the effects of CO_2 on burning velocities of H_2–CO mixtures for different H_2/CO ratios, varying the CO_2 mole fraction in the fuel (0% and 20%), the equivalence ratio (0.5–1.0), the initial temperature (300–700K), and pressure (1–5 atm). Two measurement techniques were used: one using flame area images of a conical Bunsen flame and the other based on velocity profile measurements in a one-dimensional stagnation flame.

No extensive combustion study is available in the literature for typical syngas compositions like the ones expressed in chapter 2. This motivated the present work to choose three typical compositions of syngas and to study the laminar burning velocity and flame stability. These typical syngas compositions were selected from Bridgwater, (1995) and are shown in the Table 4.1.

Table 4.1 – Syngas compositions (% by volume)

Gasifier	Gas composition (% by volume)					HHV (MJ/m^3)
	H_2	CO	CO_2	CH_4	N_2	
Updraft	11	24	9	3	53	5.5
Downdraft	17	21	13	1	48	5.7
Fluidized bed	9	14	20	7	50	5.4

There are also gaps in the fundamental understanding of syngas combustion characteristics, especially at elevated pressures that are relevant to practical combustors. In this chapter, constant volume spherically expanding flames are used to determine a burning velocity correlation valid for engine conditions.

4.1 Laminar burning velocity

4.1.1 Constant pressure method

Laminar burning velocity and Markstein length can be deduced from schlieren photographs of the flame (Bradley et al., 1998). For an outwardly spherical propagating flame, the stretched flame speed, S_n, is derived from the flame radius versus time data as follows:

$$S_n = \frac{dr_f}{dt} \tag{4.1}$$

where r_f represents the flame radius in the schlieren photographs and t the time. The total stretch rate acting on a spherical expanding flame, κ, is defined as Bradley et al., (1996):

$$\kappa = \frac{1}{A}\frac{dA}{dt} = \frac{2}{r_f}\frac{dr_f}{dt} = \frac{2}{r_f}S_n \tag{4.2}$$

where A is the flame surface area. A linear relationship between the flame speed and the total stretch exists (Clavin, 1985), and this is quantified by a burned Markstein length, L_b, as follows:

$$S_n^0 - S_n = L_b\kappa \tag{4.3}$$

where S_n^0 is the unstretched flame speed, and L_b the Markstein length of burned gases.

The unstretched flame speed is obtained as the intercept value at $\kappa = 0$, in the plot of S_n against κ, and the burned gas Markstein length is the negative slope of S_n–κ curve. Markstein length can reflect the stability of flame (Liao et al., 2004). Positive values of L_b indicate that the flame speed decreases with the increase of flame stretch rate. In this case, if any kind of perturbation or small structure appears on the flame front (stretch increasing), this structure tends to be suppressed during flame propagation, and this makes the flame stability. In contrast to this, a negative value of L_b means that the flame speed increases with the increase of flame stretch rate. In this case, if any kinds of perturbation appear on the flame front, the flame speed in the flame front will be increased, and this increases the instability of the flame. When the observation is limited to the initial part of the flame expansion where the pressure does not vary yet,

then a simple relationship links the unstretched flame speed to the unstretched burning velocity.

$$\frac{S_n^0}{S_u^0} = \frac{\rho_u}{\rho_b} = \sigma \tag{4.4}$$

Where σ is the expansion factor and ρ_u and ρ_b are, respectively, the unburned and burned densities.

The same behavior of the unstretched burning velocity regarding the stretch can be observed (Lamoureux et al., 2003):

$$S_u^0 - S_u = L_u \kappa \tag{4.5}$$

where L_u represents the unburned Markstein length, which is obtained dividing the burned Markstein length by the expansion factor $L_u = L_b/\sigma$.

The normalization of the laminar burning velocity by the unstretched one introduces two numbers which characterize the stretch that is applied to the flame, the Karlovitz number (*Ka*), and its response to it, the Markstein Number (*Ma*):

$$\frac{S_u}{S_u^0} = 1 - MaKa \tag{4.6}$$

$$Ka = \kappa \frac{\delta}{S_u^0} \tag{4.7}$$

$$Ma = \frac{L_u}{\delta} \tag{4.8}$$

where δ is the flame thickness defined, in this work, using the thermal diffusivity, α:

$$\delta = \frac{\alpha}{S_u^0} \tag{4.9}$$

This evolution of the laminar flame velocity with the stretch rate was verified by Aung et al., (1997) for moderate stretch rate. As one can see, different definitions of a characteristic flame thickness lead to different Karlovitz and Markstein numbers. Bradley et al., (1998) use the kinematic viscosity of the unburned mixture to derive the flame thickness while Aung et al., (1997) use the mass diffusivity of the fuel in the unburned gas. However, this effect disappears in Eq. (4.6) since the flame thickness cancels out.

4.1.1.1 Flame morphology

Bradley et al., (1998) shown that flame speeds become independent of ignition energy when flame radius is greater than 6 mm. The existence of the critical flame radius was also observed by Lamoureux et al., (2003) and Liao et al., (2004). Their studies also gave approximately the same value. Thus, the flame radius is analyzed only beyond that radius, at which the spark effects could be discounted. In order to define the upper limit of the flame radius data exploration, the spherical pattern of the flame expansion and the corresponding pressure should be taking into account. The criterion used for sphericity considerations was a 0.5 mm radius difference between horizontal and vertical directions, which gives in our experimental conditions an upper limit for the radius of 20.0 mm. The maximum estimated experimental uncertainty is 8% for the radius 6.0 mm using this criterion. This also arises from the pixel resolution of the digital camera. Figure 4.1 shows schlieren images of updraft syngas-air flames at various equivalence ratios and initial pressure of 1.0 bar and 293 K.

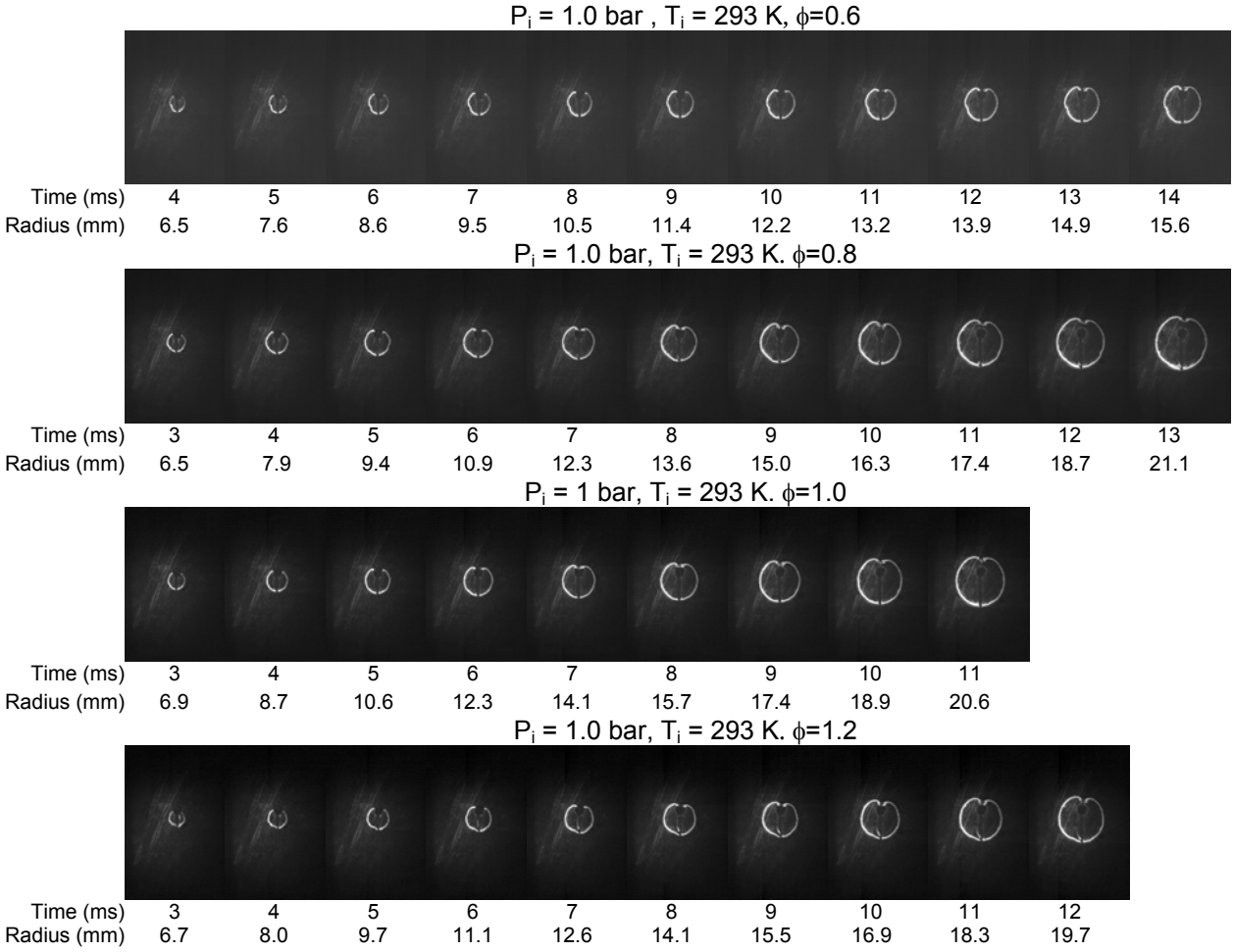

Figure 4.1 – Schlieren images of updraft syngas-air mixture flames at 1.0 bar.

These schlieren images show generally a spherical pattern. Stoichiometric mixture is the faster one, followed by the rich mixture (ϕ=1.2). Lean mixtures are slower and for ϕ=0.6 spherical flame start to be critical with a small crack formation. Figure 4.2 shows updraft flame speed and pressure rise versus flame radius under stoichiometric conditions.

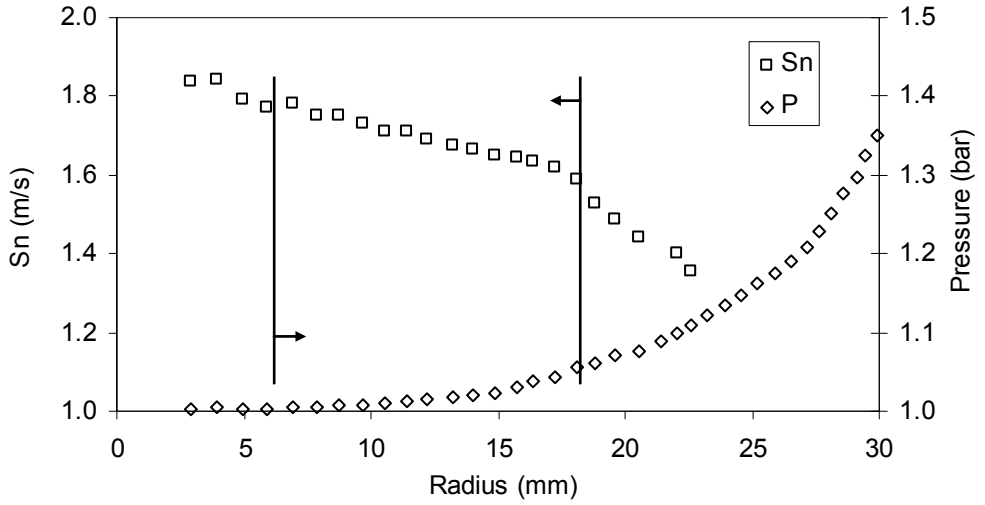

Figure 4.2 – Flame speed and pressure versus radius for updraft syngas-air mixture at 1.0 bar.

The radius range where the flame speed keeps a spherical pattern is defined between 6 -18 mm, where the pressure rise is only 0.05 bar and no influence of the chamber wall geometry is observed from flame images.

Figure 4.3 shows schlieren images of downdraft syngas-air mixtures for various equivalence ratios at 1.0 bar.

From figure 4.3 is possible to observe the spherical pattern of the flame expansion. Again, stoichiometric mixture is the faster one, followed closely by the rich mixture. Lean mixtures show to be slower. Another, finding is that downdraft syngas-air flames are a bit faster than updraft syngas-air flames for every equivalence ratios.

Figure 4.4 shows flame speed and pressure rise during stoichiometric combustion of downdraft syngas–air mixture. The radius range to explore is defined between 6 -18 mm, where the flame speed keeps a linear behavior. Pressure rise is only 0.03 bar and no influence of the chamber wall geometry is observed from flame images. This radius range is kept for the remaining equivalence ratios has similar behavior was found.

P_i = 1.0 bar, Ti = 293 K, ϕ=0.6

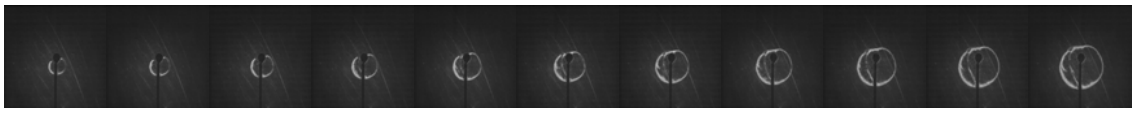

Time (ms)	5.0	6.0	7.0	8.0	9.0	10.0	11.0	12.0	13.0	14.0	15.0
Radius (mm)	6.4	7.4	8.5	9.4	10.5	11.5	12.4	13.3	14.2	15.1	15.9

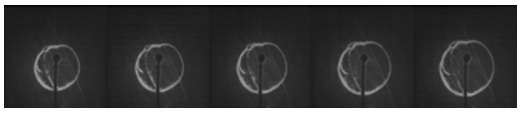

16.0	17.0	18.0	19.0	20.0
16.7	17.6	18.5	19.3	20.1

P_i = 1.0 bar, Ti = 293 K, ϕ=0.8

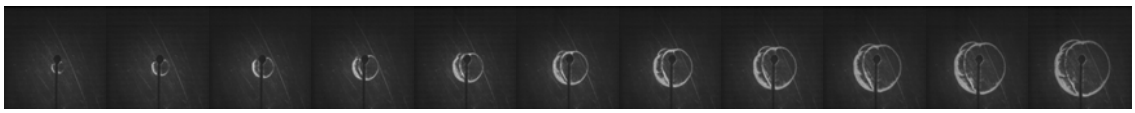

Time (ms)	3.5	4.5	5.5	6.5	7.5	8.5	9.5	10.5	11.5	12.5	13.5
Radius (mm)	6.0	7.6	9.2	10.8	12.4	13.9	15.5	17.0	18.4	19.7	21.0

P_i = 1.0 bar, T_i = 293 K, ϕ=1.0

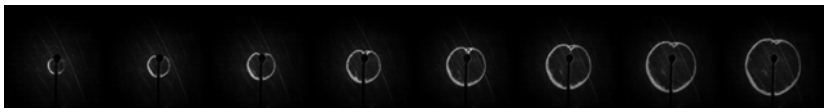

Time (ms)	4.0	5.0	6.0	7.0	8.0	9.0	10.0	11.0
Radius (mm)	6.6	8.7	10.9	13.0	15.0	17.1	19.1	21.0

P_i = 1.0 bar, Ti = 293 K, ϕ=1.2

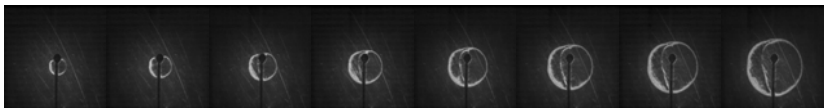

Time (ms)	4.0	5.0	6.0	7.0	8.0	9.0	10.0	11.0
Radius (mm)	6.4	8.5	10.4	12.5	14.5	16.6	18.6	20.5

Figure 4.3 - Schlieren images of downdraft syngas-air mixture flames at 1.0 bar.

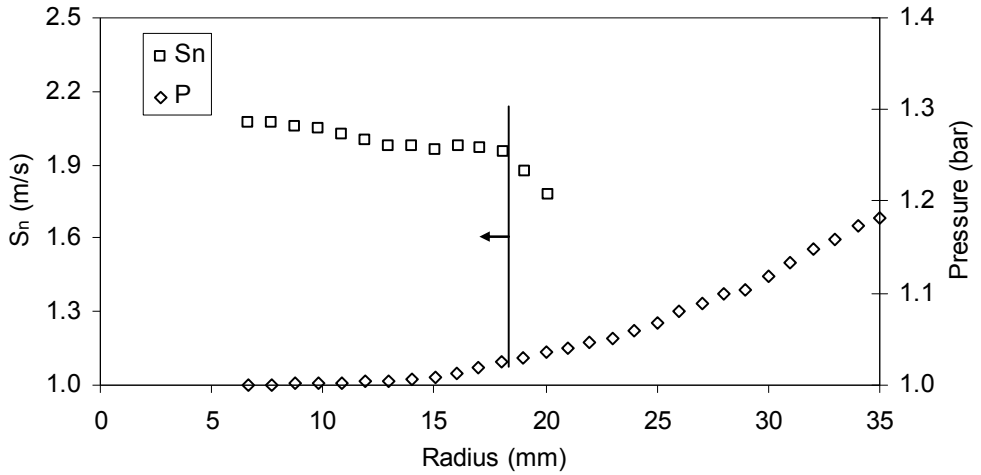

Figure 4.4- Flame speed and pressure versus radius for stoichiometric downdraft syngas-air mixture at 1.0 bar.

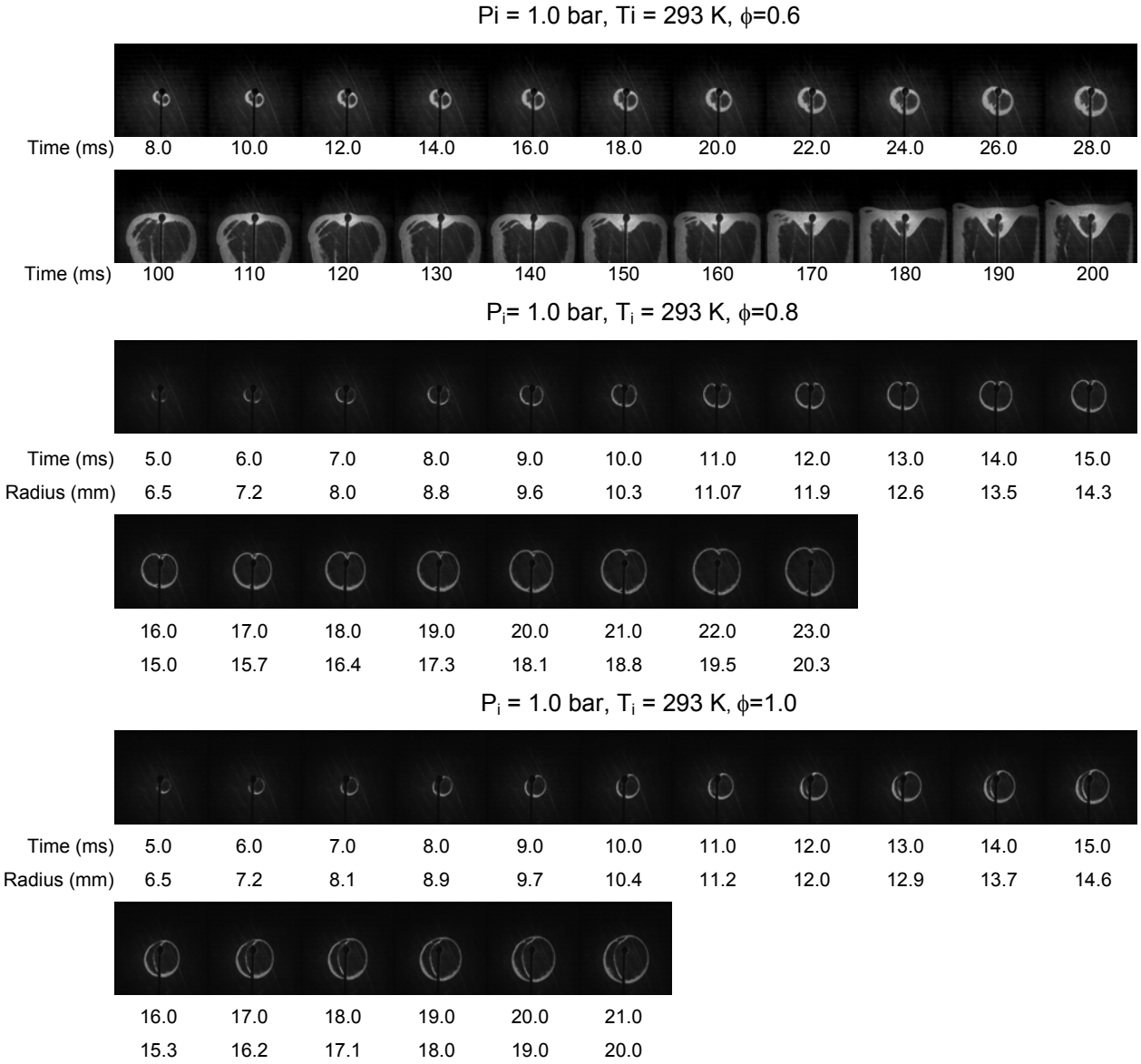

Figure 4.5 - Schlieren images of fluidized bed syngas-air mixture flames at 1.0 bar.

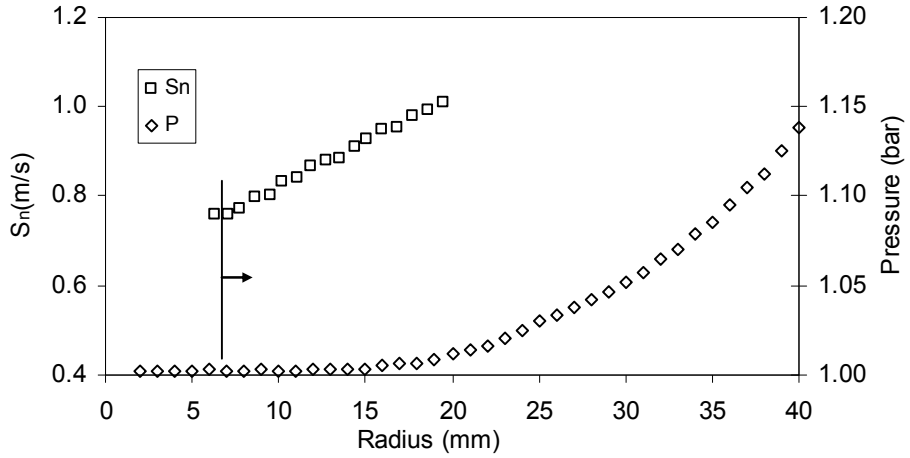

Figure 4.6 - Flame speed and pressure versus radius for stoichiometric fluidized bed syngas-air mixture at 1.0 bar.

Figure 4.5 shows schlieren flame images of fluidized bed syngas-air mixture. Rich mixture (ϕ=1.2) is not shown due to unsuccessful ignition. For the lean mixture with ϕ=0.6, the flame speed is remarkably slow being gravity effect felt making the flame to propagate to the bottom of the combustion chamber. Also in this case, stoichiometric mixture is the faster one. The low flame speed of this syngas composition is highlighted in the figure 4.6, in which the pressure rise is also lower than its homologous, 0.01 bar. In opposite, the radius to work out could be extended to 20 mm due to no significant pressure rise keeping the flame a spherical pattern. However, due to coherency the radius range to burning velocity determination was kept between 6-18 mm.

Figures 4.7-4.9 show schlieren flame images of syngas-air mixtures at 2.0 bar and 293 K. Spherical expansion of the flame was found only in the cases of stoichiometric mixtures and rich mixtures of updraft and downdraft syngas. In all cases a cellular flame structure was observed. Indeed, it can be seen from the figures the transformation of the smooth spherical flame front to the polyhedral flame structures which increase the surface area of the flame front. The increase in the surface area leads to a sudden increase in the flame speed and any inclusion of these data points would lead to higher burning velocity predictions (Saeed and Stone, 2004).

P_i = 2.0 bar, T_i = 293 K, ϕ=0.6

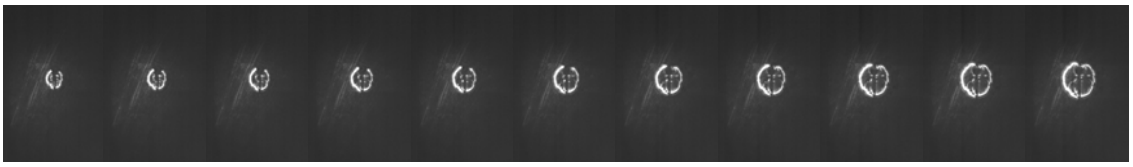

Time (ms)	5	6	7	8	9	10	11	12	13	14	15

P_i = 2.0 bar, T_i = 293 K, ϕ=0.8

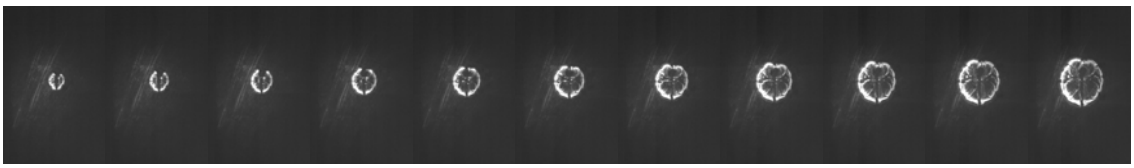

Time (ms)	3	4	5	6	7	8	9	10	11	12	13
Radius (mm)	5.8	7.1	8.8	10.1	11.1	12.3	13.5	14.5	15.6	16.6	17.8

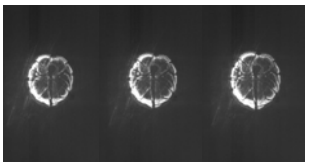

	14	15	16
	18.7	19.6	20.7

P_i =2.0 bar, T_i = 293 K, ϕ=1.0

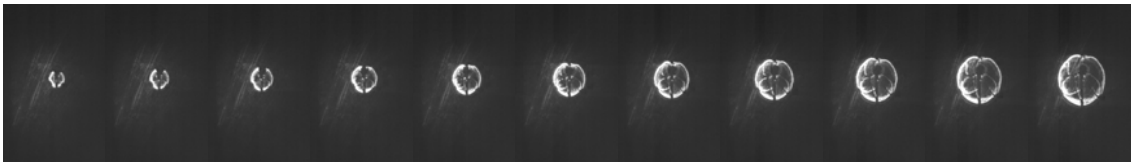

Time (ms)	3	4	5	6	7	8	9	10	11	12	13
Radius (mm)	6.0	7.8	9.2	10.6	11.9	13.3	14.6	15.9	17.2	18.4	19.6

P_i = 2.0 bar, T_i = 293 K, ϕ=1.2

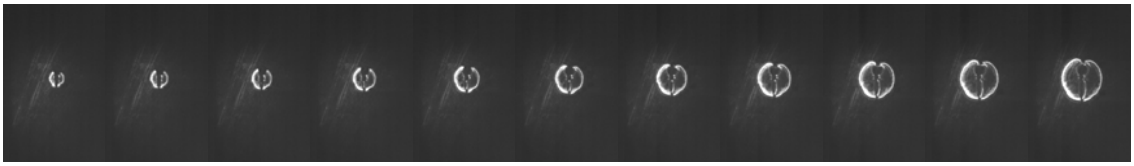

Time (ms)	4	5	6	7	8	9	10	11	12	13	14
Radius (mm)	6.0	7.2	8.3	9.3	10.5	11.5	12.8	13.9	15.0	15.9	17.0

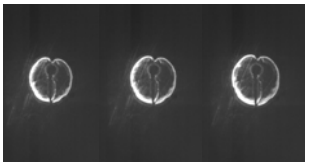

	15	16	17
	18.0	19.0	20.1

Figure 4.7- Schlieren flame images of the updraft syngas-air mixtures at 2.0 bar.

P_i = 2.0 bar, T_i = 293 K, ϕ=0.6

Time (ms)	5.0	6.0	7.0	8.0	9.0	10.0	11.0	12.0	13.0	14.0	15.0
Radius (mm)	6.3	7.3	8.3	9.3	10.2	11.1	11.9	12.7	13.6	14.3	15.2

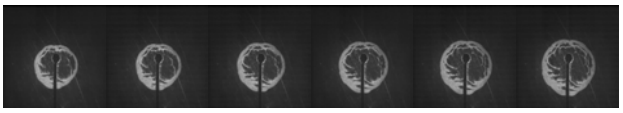

	16.0	17.0	18.0	19.0	20.0	21.0
	15.9	16.7	17.4	18.2	19.0	19.8

P_i = 2.0 bar, T_i = 293 K, ϕ=0.8

Time (ms)	4.0	5.0	6.0	7.0	8.0	9.0	10.0	11.0	12.0	13.0	14.0
Radius (mm)	6.5	7.9	9.5	10.9	12.5	13.9	15.2	16.5	17.8	19.0	20.4

P_i = 2.0 bar, T_i = 293 K, ϕ=1.0

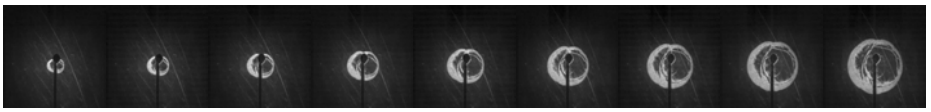

Time (ms)	3.0	4.0	5.0	6.0	7.0	8.0	9.0	10.0	11.0
Radius (mm)	6.5	8.2	10.0	11.9	13.7	15.3	17.0	18.7	20.4

P_i = 2.0 bar, T_i = 293 K, ϕ=1.2

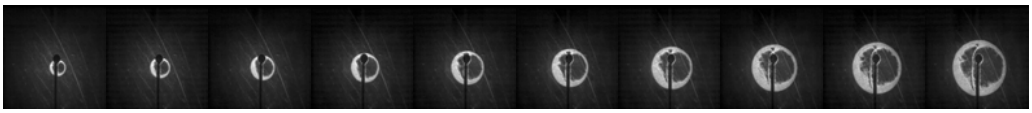

Time (ms)	4.0	5.0	6.0	7.0	8.0	9.0	10.0	11.0	12.0	13.0
Radius (mm)	6.4	8.0	9.6	11.3	12.7	14.3	15.9	17.4	18.9	20.4

Figure 4.8 - Schlieren flame images of the downdraft syngas-air mixtures at 2.0 bar.

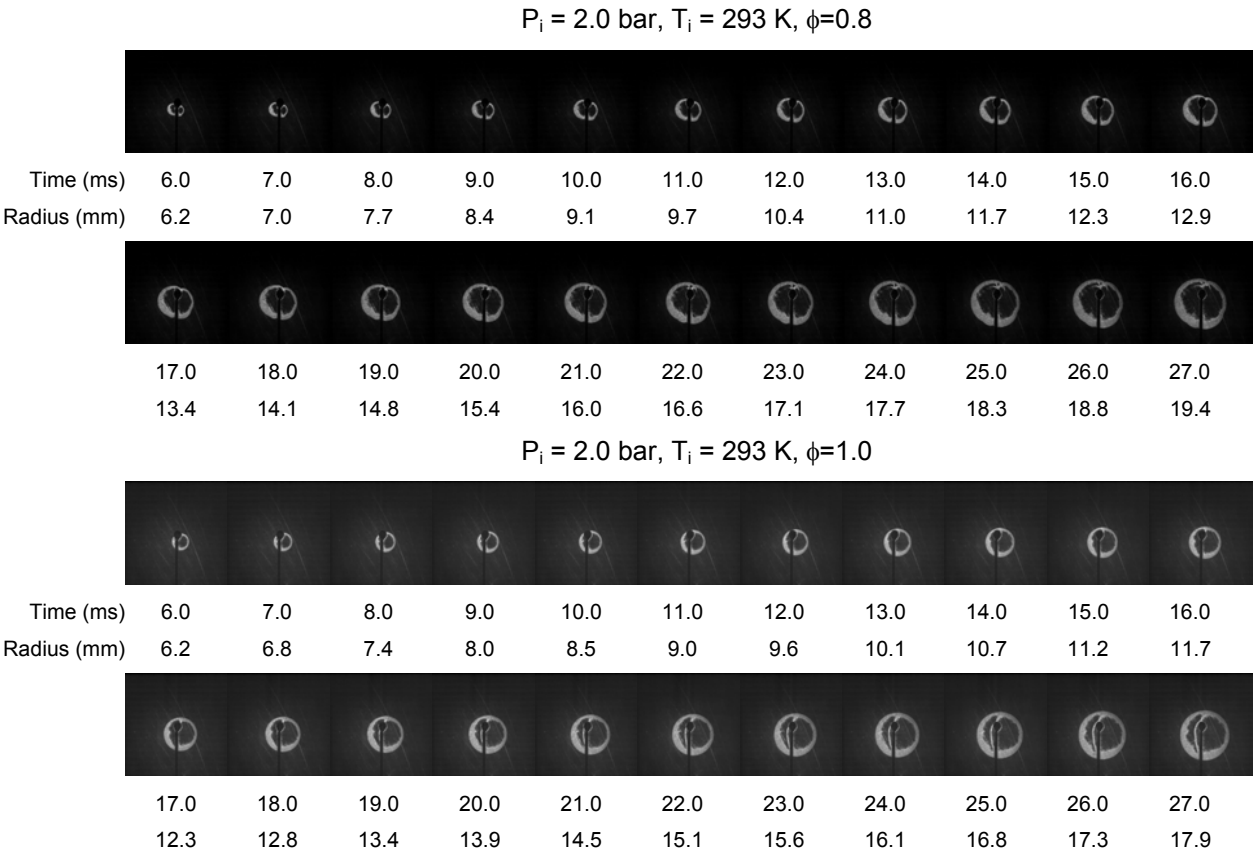

Figure 4.9 – Schlieren flame images of the fluidized bed syngas-air mixtures at 2.0 bar.

In order to verify the influence of the cell flame in the flame speed it is shown in figures 4.10 – 4.12 the flame speed and pressure versus flame radius for stoichiometric syngas-air mixtures at 2.0 bar.

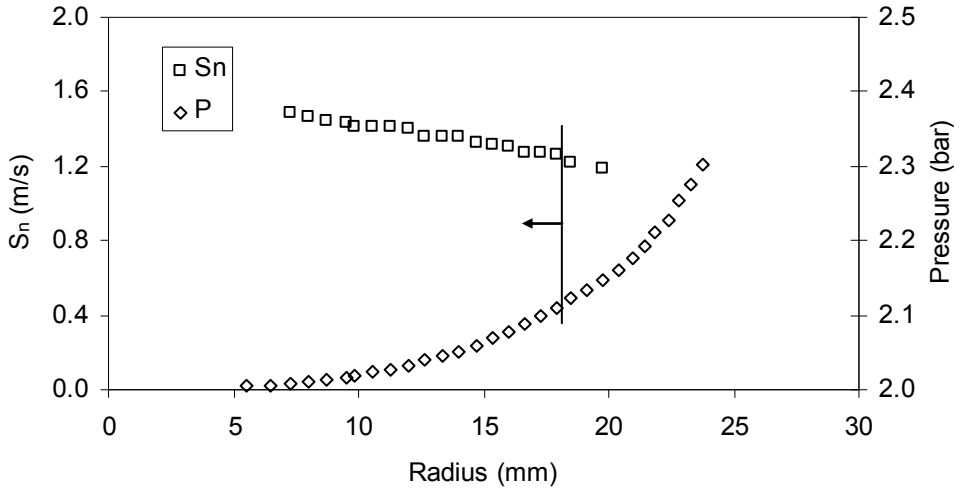

Figure 4.10 - Flame speed and pressure versus radius for stoichiometric updraft syngas-air mixture at 2.0 bar.

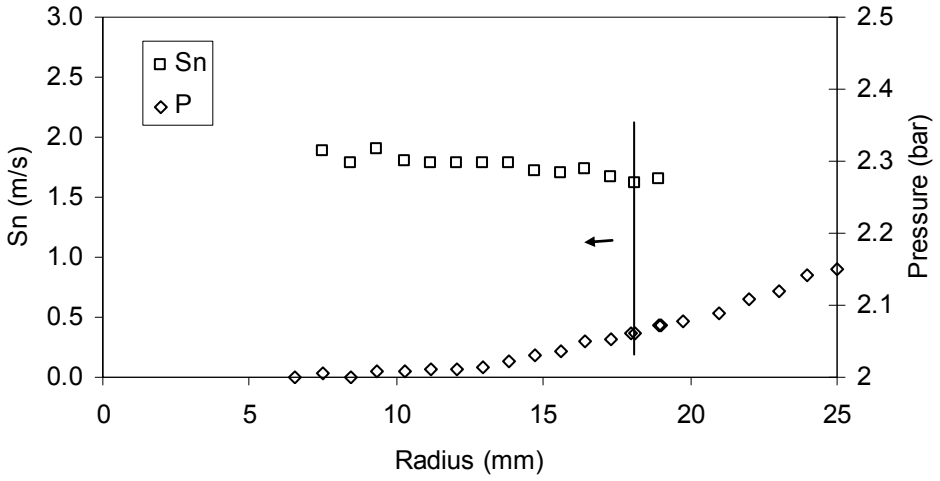

Figure 4.11 - Flame speed and pressure versus radius for stoichiometric downdraft syngas-air mixture at 2.0 bar.

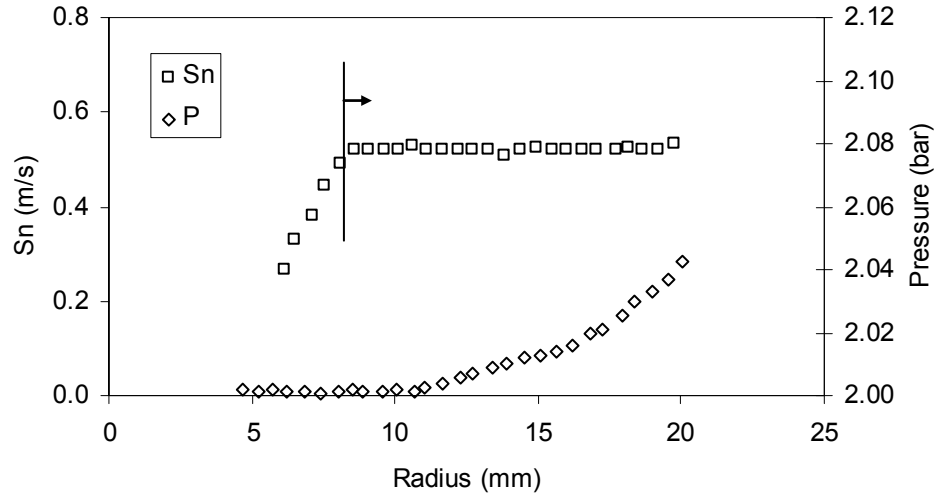

Figure 4.12 - Flame speed and pressure versus radius for stoichiometric fluidized bed syngas-air mixture at 2.0 bar

From figures 4.10 – 4.12 is not possible to observe the influence of cellular flame on the mean flame speed. According to Bradley and Harper, (1994) the onset of instability in a spherically propagating flame is associated with the surface propagation of discontinuities in the flame structure that have the appearance of cracks. Moreover, cells cannot form if their growth rate is smaller than that of flame expansion (Kwon et al., 2002). Since the expanding flame suffers the strongest stretch during the initial phase of its propagation when its radius is small, the tendency for cell development is expected to increase as the flame propagates outwardly. These situations are more clearly observed in the figures 4.13-4.15. In order to make the cellular flame effect on flame speed observable a larger combustion chamber is needed.

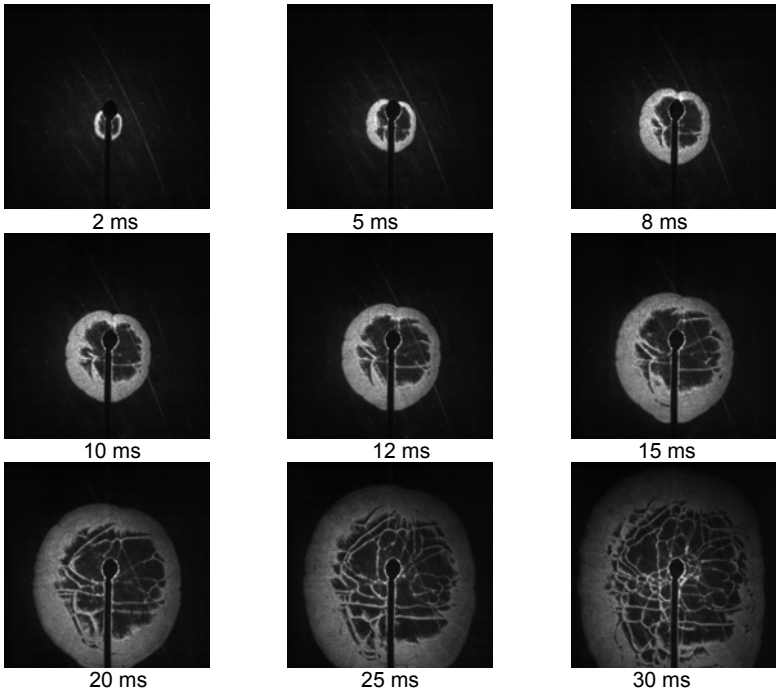

Figure 4.13 – Schlieren flame images of updraft syngas-air mixture at 3.0 bar.

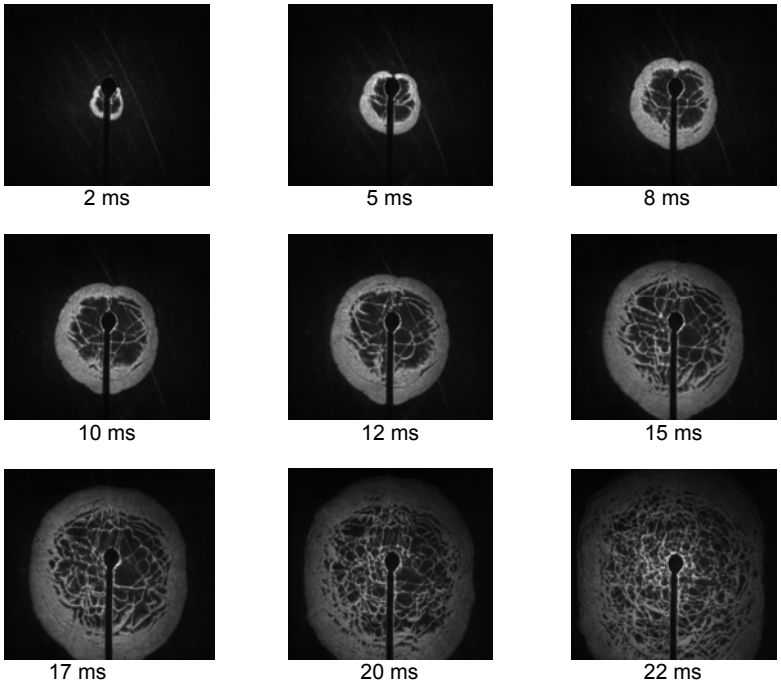

Figure 4.14 - Schlieren flame images of downdraft syngas-air mixture at 3.0 bar.

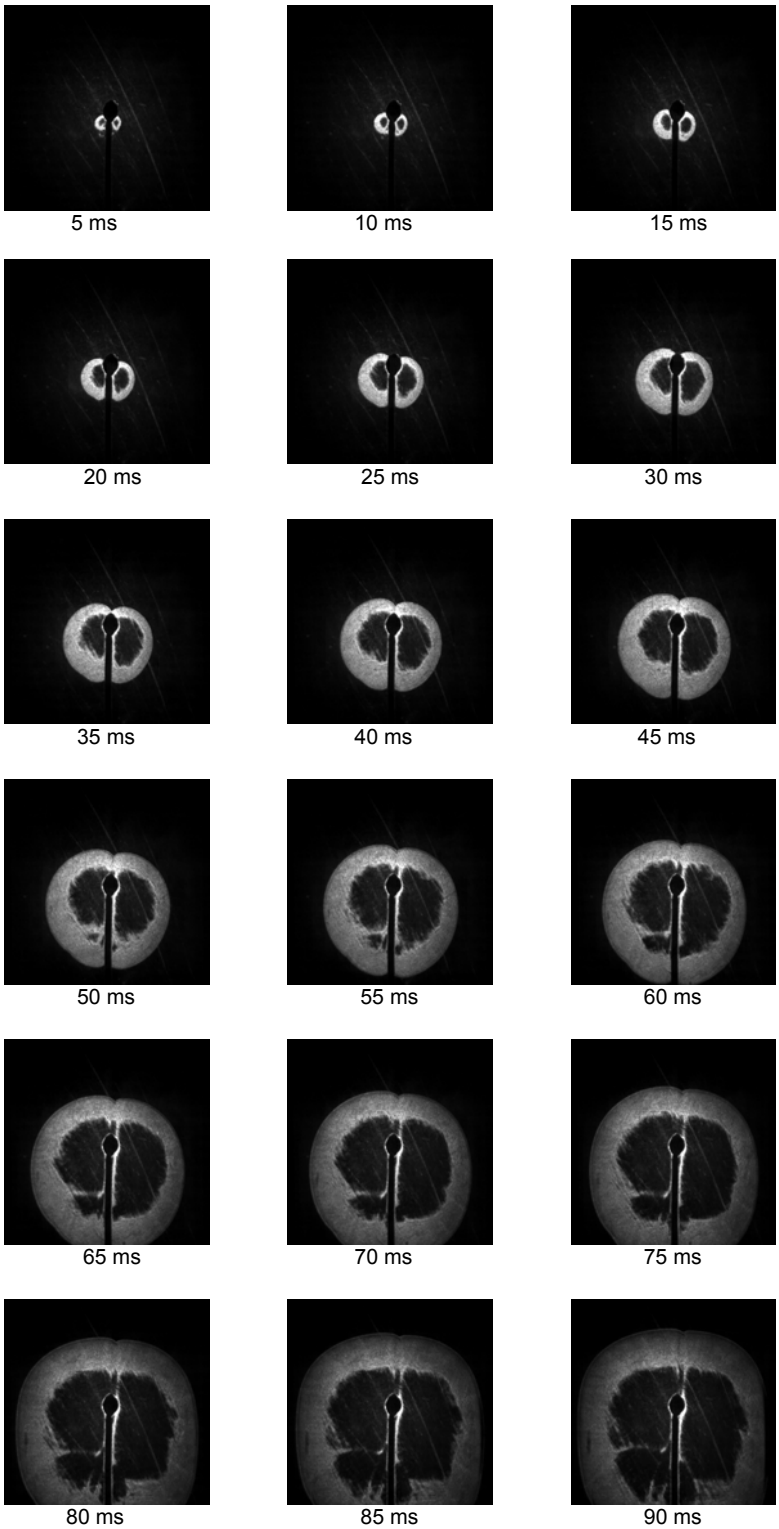

Figure 4.15 – schlieren flame images of fluidized bed syngas-air mixture at 3.0 bar.

The hydrodynamic theory of Darrieus (1938) and Landau (1944) shows that, in the limit of an infinitely thin flame propagating with a constant velocity, the flame is unstable to disturbances of all wavelengths. The growth rate is proportional to the density jump

across the flame, increasing with increasing density ratio, σ. Thus σ is probably the most sensitive parameter controlling the onset of hydrodynamic instability. Next to σ, the flame thickness, δ, is also expected to have a strong influence on the hydrodynamic instability, for two reasons. First, it measures the influence of curvature which, being positive for the outwardly propagating spherical flame, has a stabilizing effect on the cellular development. The thinner the flame, the weaker is the influence of curvature and consequently the stronger is the destabilizing propensity. The second influence is that it controls the intensity of the baroclinic torque developed over a slightly wrinkled flame surface, which depends on the density gradient across the flame and the pressure gradient along the flame (Sun et al., 1999).

For the development of the diffusional-thermal instability, an appropriate parameter representing the effect of non-equidiffusion is the flame Lewis number, L_e [Markstein, (1951); Matalon and Matkowsky, (1982); Law and Sung, (2000)]. It is well established and understood theoretically that unstretched flames are diffusionally unstable (stable) for L_e that are smaller (greater) than a value slightly less than unity. However, the calculation of effective Lewis number for a multi-component fuel mixture is not as straightforward as for pure fuel-air mixtures and is a subject that is out of the scope of the present work.

4.1.1.2 Flame Radius

Fig. 4.16 gives the variations of flame radius versus the time for syngas-air mixtures. The study shows that flame expands spherically after the ignition, and the flame radius will increase rapidly in the subsequent process. There are a quasi-linear correlation between flame radius and time for all syngas cases. The higher gradient of radius-time curves is obtained for stoichiometric syngas-air mixtures. The lean (ϕ=0.8) and rich (ϕ=1.2) syngas-air mixtures have similar gradients in the updraft case. This difference increases for the downdraft syngas case. Fluidized syngas has the lowest radius-time curve gradients. Information for rich mixture of fluidized syngas is missing due to ignition difficulties.

According to the Markstein view the gradient of the radius-time curve reflects the stretching effectiveness of flame. For an unstable flame, the gradient of the radius-time curve will decrease with the flame expansion, while for a stable flame; the gradient of the radius-time curve will increase with the flame expansion. The quasi-linear

behaviour of the curves radius-time shows that that the stretch rate has low effect in the syngas-air mixtures.

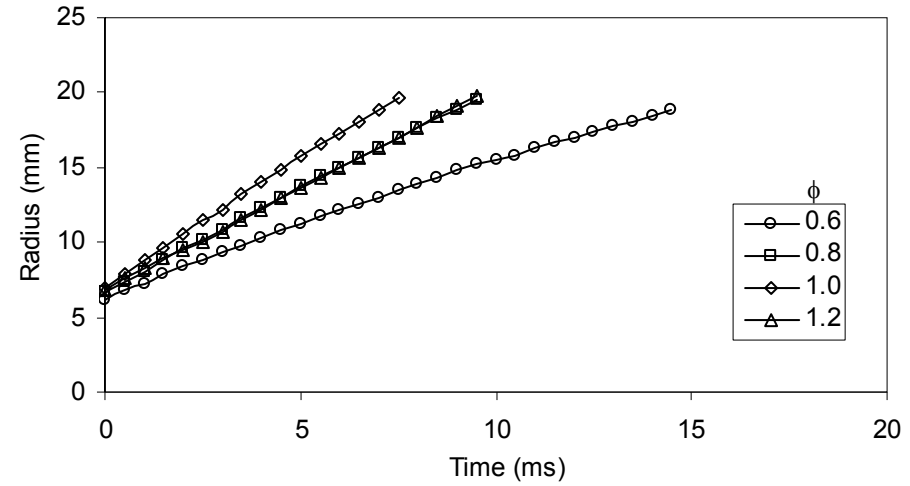

(a)

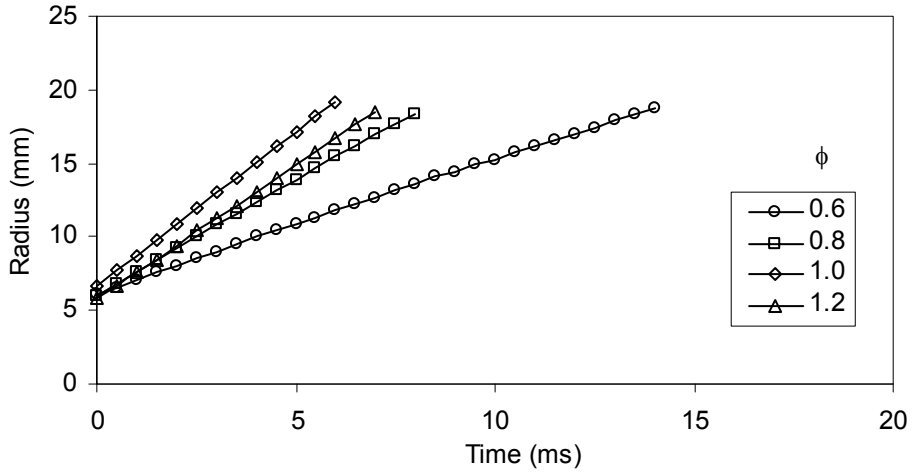

(b)

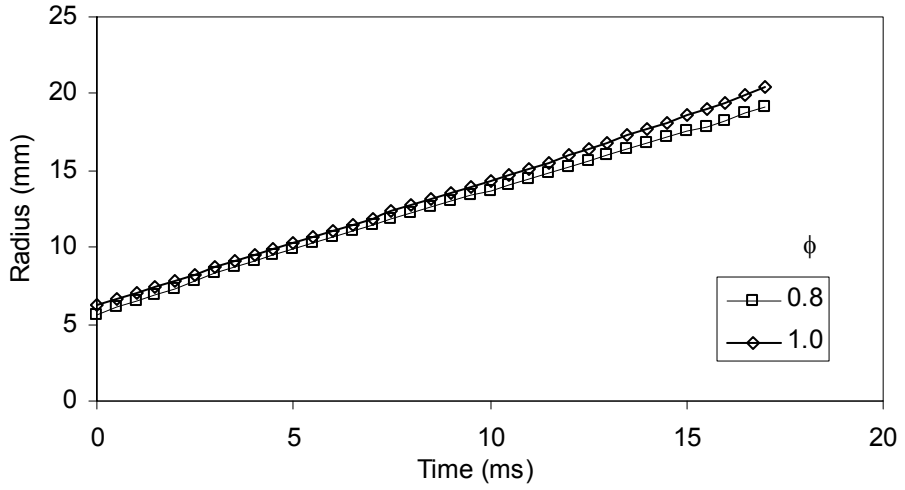

(c)

Figure 4.16 – Flame radius versus time for syngas-air mixtures at various equivalence ratios and 1.0 bar. (a) Updtraft. (b) Downdraft (c) Fluidized bed.

4.1.1.3 Flame speed

Fig. 4.17 gives the stretched flame speed versus the flame stretch rate for three typical syngas compositions. Removing the parts influenced by ignition energy and high pressure at late stages of flame propagation. A linear correlation between the stretched flame speed and the flame stretch rate is found. The unstretched flame speed is obtained by extrapolating the line to $\kappa = 0$, while the gradient of the S_n–κ curve gives the value of the Markstein length.

The maximum value of syngas-air flame speeds is presented at the stoichiometric equivalence ratio, while lean or rich mixtures decrease the flame speeds. Downdraft syngas composition shows the highest flames speeds for all the equivalence ratios considered. The stretched flame speed increases with the increase of flame stretch rate for lean (ϕ=0.8) syngas-air mixtures. This behavior remains for stoichiometric and rich (ϕ=1.2) mixtures in the case of updraft and downdraft compositions.

A remarkable decrease of the stretched flame speed versus the stretch rate is demonstrated for stoichiometric fluidized composition. This might result from the occurrence of incomplete combustion.

Positive gradients of S_n–κ curves are derived for three equivalence ratios in the updraft and downdraft syngas cases. A positive gradient of S_n–κ curve is also shown by the lean fluidized syngas. These correspond to negative values of Markstein number, indicating the instability of flames.

On the other hand, positive values of Markstein number indicate stability of flames of mixture combustion. These correspond to stoichiometric fluidized syngas.

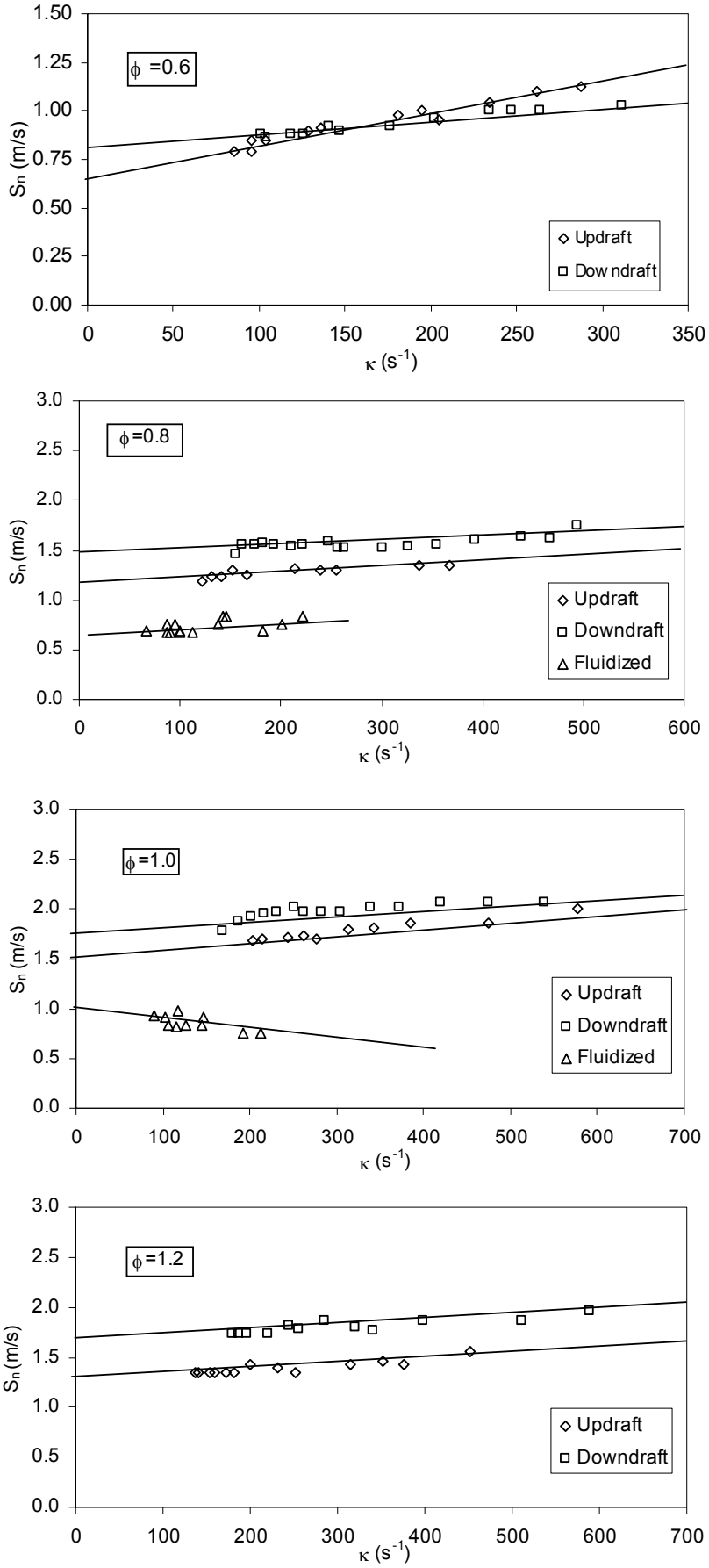

Figure 4.17 - Stretched flame speed versus stretch rate for syngas-air mixtures at various equivalence ratios and 1.0 bar.

4.1.1.4 Laminar burning velocity

Fig. 4.18 gives the stretched laminar burning velocity versus the flame stretch rate for typical syngas compositions.

The maximum value laminar burning velocity is presented at the stoichiometric equivalence ratio, while lean or rich mixtures decrease the burning velocities. Downdraft syngas composition shows the highest burning velocities for all the equivalence ratios considered. The stretched burning velocity increases with the increase of flame stretch rate for lean (ϕ=0.8) syngas-air mixtures. This behavior remains for stoichiometric and rich (ϕ=1.2) mixtures in the case of updraft and downdraft compositions. In opposite, burning velocity decreases with the increase of stretch rate for stoichiometric fluidized syngas-air case.

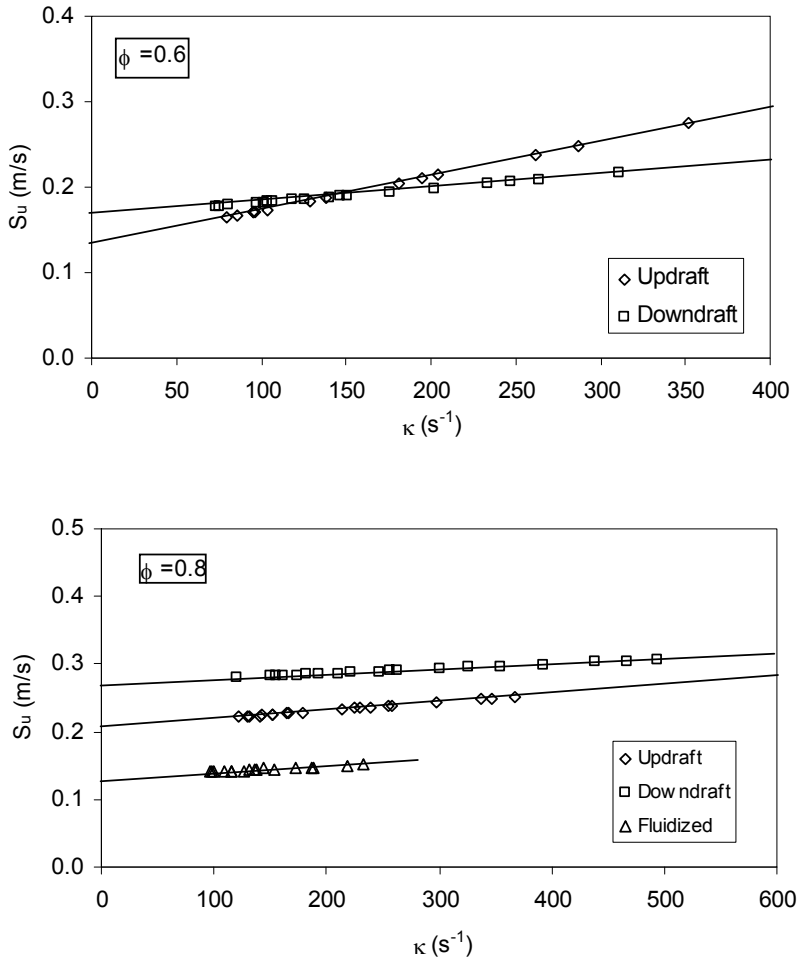

Figure 4.18a – Stretched burning velocity versus stretch rate for syngas-air mixtures at various equivalence ratios.

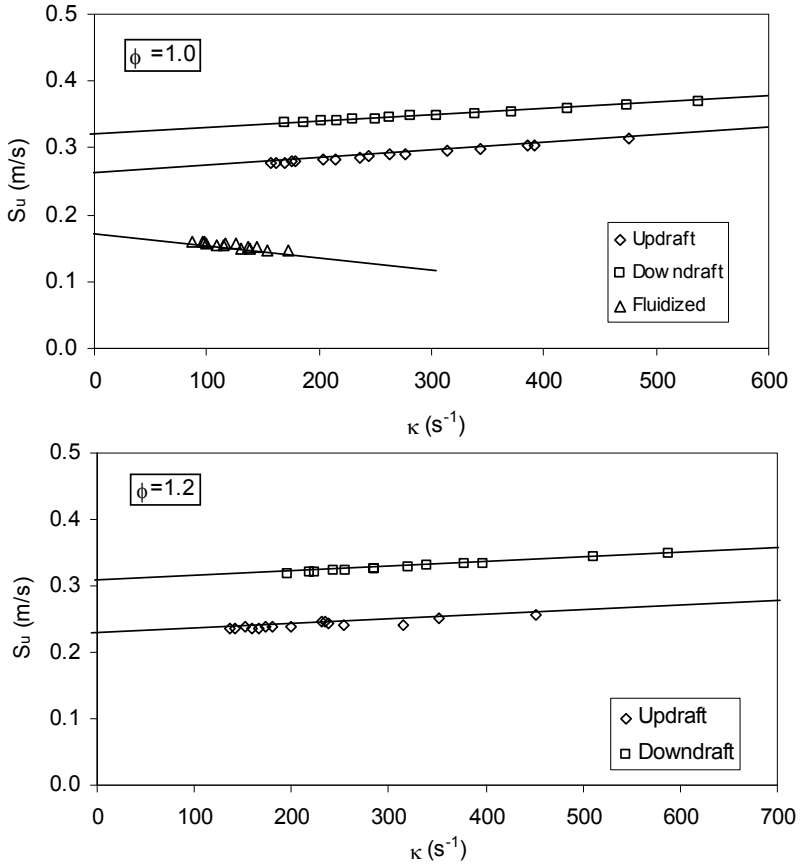

Figure 4.18b – Stretched burning velocity versus stretch rate for syngas-air mixtures at various equivalence ratios.

The unstretched laminar burning velocity, S_u^0, shown in Fig. 4.19 is derived from the value of the unstretched flame speed and the expansion factor which is evaluated using the adiabatic flame calculation via the Gaseq code package, which can be found in the Appendix B.

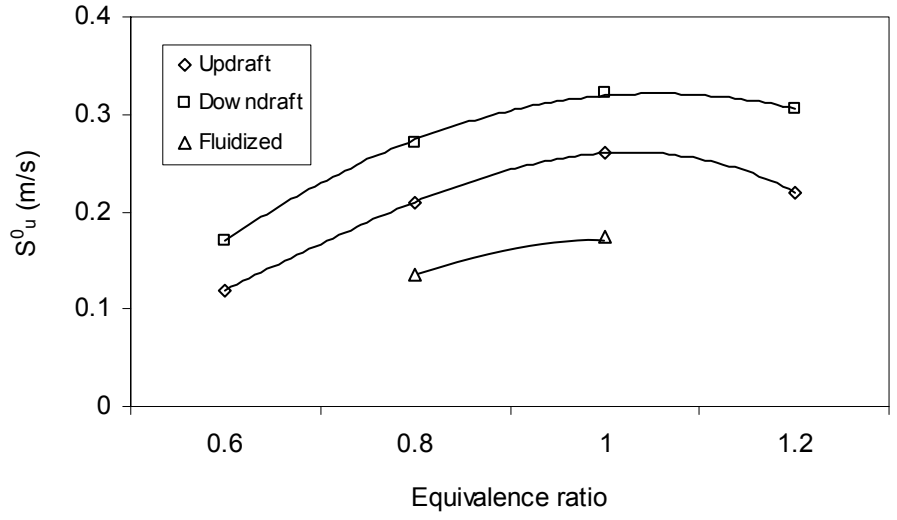

Figure 4.19- Unstretched flame speed versus equivalence ratio of syngas-air mixtures.

Similar curves are obtained for all syngas compositions under study being shifted by a value around 0.06 m/s in average between downdraft and updraft compositions and about 0.1 m/s between fluidized and updraft syngas. These results could be endorsed to:

- the heat value of the syngas compositions. This value varies from 5.4 (fluidized bed syngas) to 5.7 MJ/m^3 (downdraft syngas), which is in agreement, however not proportional to the burning velocities.
- the amount of H_2, due to its high reactivity, is a very important parameter to be considered. As shown in the Table 3.1 the amount of H_2 of fluidized bed syngas (9% by volume) is very close to the updraft syngas (11% by volume) and about half of the downdraft syngas (17% by volume). This explains the lowest burning velocity of the fluidized bed syngas and the highest shift when compared to downdraft syngas. However, the close amount of H_2 between fluidized bed and updraft syngas is not reflected in the burning velocity values shown in the Fig. 4.19.
- and the amount of dilution by N_2 and CO_2 in the fuel gases H_2-CO-CH_4 that compose the typical syngas mixtures. Again, fluidized bed syngas is he highest diluted syngas (70% by volume), being updraft and downdraft less diluted with 61% and 62% by volume, respectively. Therefore, the highest shift in burning velocity of fluidized bed syngas could be explained by its highest dilution.

Based on the experimental data the correlations of unstretched laminar burning velocities as function of equivalence ratio can be fitted as follows:

$$S_u^0 = -0.8125\phi^2 + 1.6375\phi - 0.5725 \quad \text{(Updraft)} \tag{4.10}$$

$$S_u^0 = -0.7313\phi^2 + 1.5428\phi - 0.4924 \quad \text{(Downdraft)} \tag{4.11}$$

$$S_u^0 = -0.7500\phi^2 + 1.5450\phi - 0.6210 \quad \text{(Fluidized)} \tag{4.12}$$

for updraft, downdraft and fluidized bed syngas–air mixture combustion, respectively. Information for fluidized syngas is limited due to ignition difficulties of this mixture. Formula (4.12) was fitted for equivalence ratios between 0.8 and 1.0.

4.1.1.5 Karlovitz and Markstein numbers

Figures 4.20-4.22 illustrates the evolution of the normalized laminar burning velocity, S_u/S^0_u, as a function of the normalized stretch rate, the Karlovitz number for typical syngas compositions at various equivalence ratios. From Fig. 4.20 one can see that the

variation of the normalized burning velocity of updraft syngas with the Karlovitz number is linear. From Fig. 4.21 one can see that the variation of the normalized burning velocity of downdraft syngas with the Karlovitz number is generally linear and quasi-linear for ϕ=0.8. From Fig. 4.22 one can see that the variation of the normalized burning velocity of fluidized bed syngas with the Karlovitz number is linear for ϕ=0.8 and quasi-linear for ϕ =1.0.

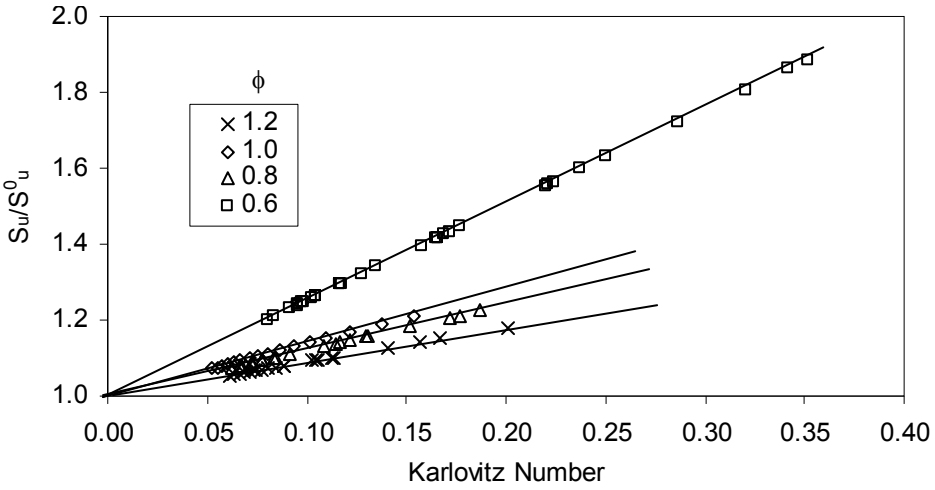

Figure 4.20 – Evolution of the laminar burning velocity versus Karlovitz number for updraft syngas-air mixture at different equivalence ratios and 1.0 bar.

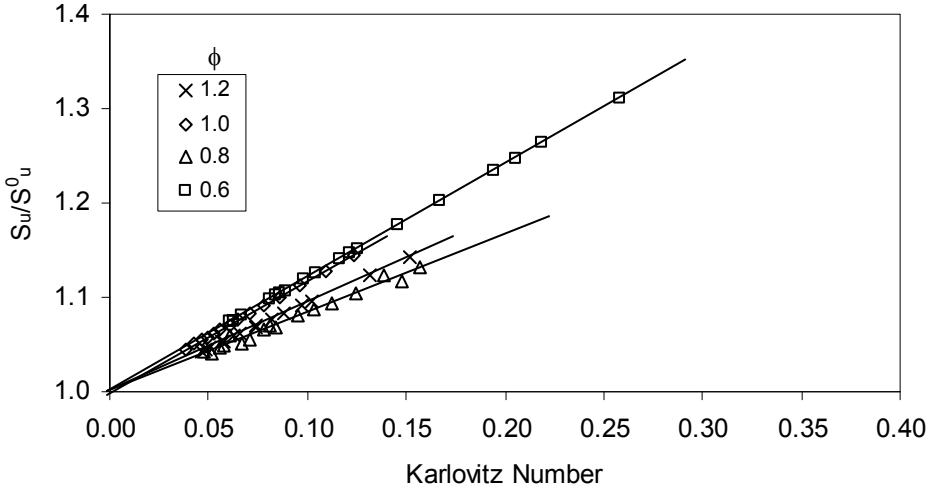

Figure 4.21 – Evolution of the laminar burning velocity versus Karlovitz number for downdraft syngas-air mixture at different equivalence ratios and 1.0 bar.

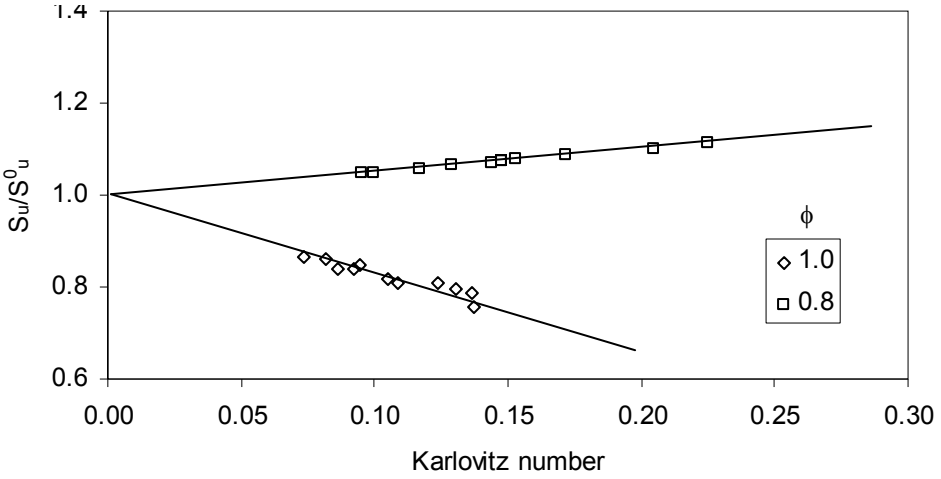

Figure 4.22 – Evolution of the laminar burning velocity versus Karlovitz number for fluidized bed syngas-air mixture at different equivalence ratios and 1.0 bar.

The linear behavior of the normalized burning velocity with Karlovitz number supports that the Markstein number is independent of the Karlovitz number as it was verified by Aung et al. (1997). Also the generally low Karlovitz numbers obtained for all the typical syngas compositions and equivalence ratios indicates small influence of stretch rate on the syngas-air flames.

As it was pointed out by Aung at al., (1997) and Bradley et al., (1996) the Markstein length is a fundamental property of premixed laminar flames and it is necessary to measure it precisely. Table 4.2 shows Markstein lengths and Markstein numbers for syngas-air mixture at various equivalence ratios. If *Ma*<0, the flame is in the preferential diffusion instability regime, and if *Ma*>0, It is in the stable regime (Law, 2006). If *Ma*=0, the flame is neutrally stable, and $S_u = S_u^0$ at all values of stretch rate.

Table 4.2– Markstein lengths and Markstein numbers versus equivalence ratio of syngas-air mixtures at 1.0 bar and 293 K.

Eq. Ratio	Updraft			Downdraft			Fluidized bed		
	L_b	L_u	Ma	L_b	L_u	Ma	L_b	L_u	Ma
ϕ=0.6	-2×10^{-3}	-4.1×10^{-4}	-1.55	-9×10^{-4}	-1.9×10^{-4}	-1.4	n.d.	n.d.	n.d.
ϕ=0.8	-7×10^{-4}	-1.3×10^{-4}	-1.21	-4×10^{-4}	-7.4×10^{-5}	-0.84	-4×10^{-4}	-7.5×10^{-5}	-0.5
ϕ=1.0	-7×10^{-4}	-1.2×10^{-4}	-1.39	-5×10^{-4}	-8.7×10^{-5}	-1.17	8×10^{-4}	1.4×10^{-4}	1.18
ϕ=1.2	-5×10^{-4}	-8.9×10^{-5}	-0.90	-4×10^{-4}	-7.4×10^{-5}	-0.94	n.d.	n.d.	n.d.

Updraft and downdraft syngas shows to be in the preferential diffusion instability regime as the Markstein number is negative for all cases. The flame can be seen to be neutrally stable for fluidized bed syngas somewhat between ϕ=0.8 and ϕ =1.0 as the Markstein number changes from a negative to a positive value.

4.1.1.6 Comparison with other fuels

The experimental values of the syngas are compared in Fig. 4.23 with those for other fuels obtained by other workers. The laminar burning velocity of typical syngas compositions besides its lower heat of reaction is not dissimilar to that of methane especially the downdraft syngas case, although somewhat slower than propane.

For lean mixtures (ϕ=0.6) the burning velocity of methane is the same as the updraft syngas while the burning of propane is equal to the downdraft syngas. For stoichiometric mixtures S_u^0 of downdraft and updraft typical syngas–air mixtures is respectively 15% and 42% slower than those of methane–air mixtures, being lower for other equivalence ratio.

In the case of propane, it is observed an increasing difference of the laminar burning velocity of the typical syngas mixtures from lean to rich mixtures. For ϕ=1.2. S_u^0 is 25% and 75% slower for downdraft and updraft cases, respectively. For these results contributes the fact that the syngas stoichiometric air–fuel ratio ranges between 1.0 (downdraft) to 1.2 (fluidized bed) compared with the value of 9.52 for the methane and 23.8 for the propane. Thus, the energy content per unit quantity of mixture (air + fuel) inducted to the chamber is only marginally lower when using syngas, compared with the corresponding common gas fuels.

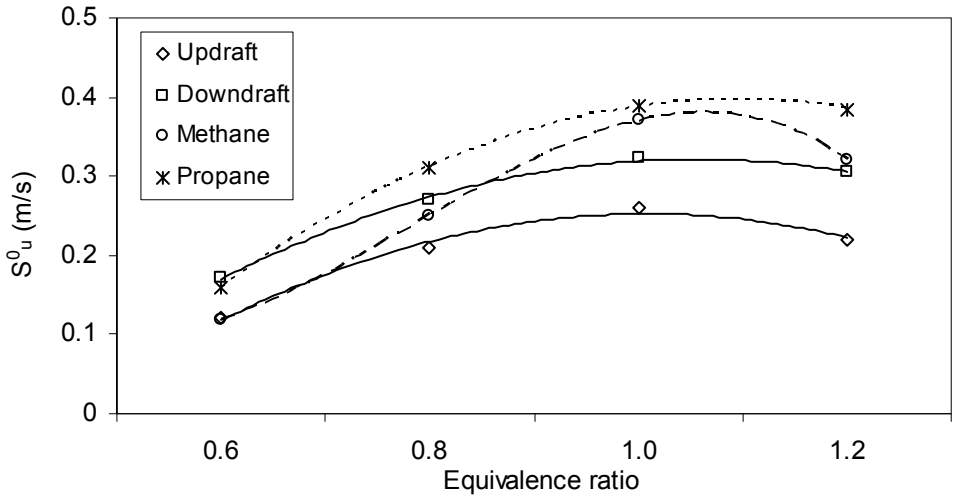

Figure 4.23 – Comparison of laminar burning velocity for different fuels: syngas (this work). Methane (Gu et al., 2000) and Propane (Bosschaart and Goey, 2004)

A number of other workers (Huang et al., 2004; Hassan et al., 1997; Prathap et al., 2008; Natarajan et al., 2007) have published laminar burning velocity data over a range of equivalence ratios at 1.0 bar and room temperature for various other H_2/CO fuels (with and without excess nitrogen or carbon dioxide), which could bring more insightful understanding of the syngas burning velocity behaviour. The results obtained in these various studies are compared in Fig.4.24.

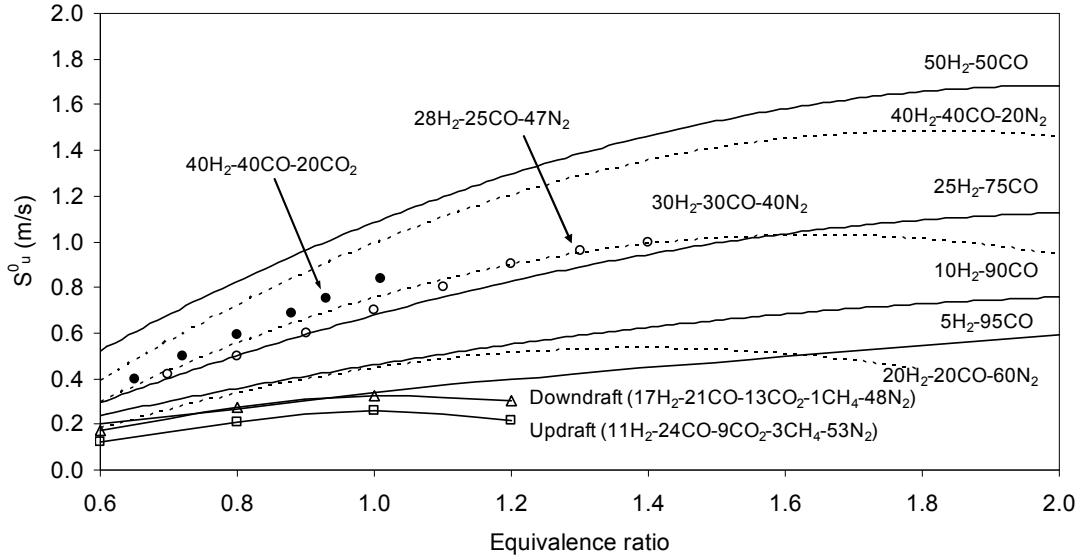

Figure 4.24 - Comparison of laminar burning velocity for different fuels: syngas (this work). H_2-CO mixtures (Hassan et al., 1997), H_2-CO-N_2 mixtures (Prathap et al., 2008), 40H_2-40CO-20CO_2 (Natarajan et al., 2007) and 28H_2-25CO-47CO_2 (Huang et al., 2004).

The continuous lines in Fig. 4.24 show the laminar burning velocity values for a range of H_2/CO mixtures obtained by Hassan et al., (1997); these data clearly show that S_u^0 increases proportionally with H_2/CO ratio at any given equivalence ratio.

The dashed lines in Fig. 4.24 show the laminar burning velocity values for a range of H_2/CO/N_2 mixtures obtained by Prathap et al., (2008); these data clearly show that S_u^0 decreases as dilution by N_2 increases but not proportionally. The reason for this behaviour is the contribution of nitrogen dilution in reducing the thermal diffusivity and flame temperature of the mixture. Also a shift to higher equivalence ratios in the burning velocity peak is observed. By crossing both collections of curves one can say that the effect of dilution is to reduce the burning velocity and the shift to latter equivalence ratios of the burning velocity peak is primarily due to the amount of CO in the mixture.

The values of laminar burning velocity reported by Natarajan et al. (2007) for syngas ($40H_2$-$40CO$-$20CO_2$) (dot symbols in Fig. 4.24) show that CO_2 has higher influence on the reduction of the burning velocity than N_2, when compared with the ($40H_2$-$40CO$-$20N_2$) mixture. The reason for the substantial reduction on burning velocity when dilution is made with CO_2 (37.28 J/mol K) instead of N_2 (29.07 J/mol K) is the increase in heat capacity of the mixture. Consequently, the flame temperature also decreases. Adiabatic flame temperature obtained by Gaseq gives 2535 K for the mixture comprising CO_2 and 2624 K for the mixture comprising N_2.

The values of laminar burning velocity reported by Huang et al. (2004) for syngas ($28H_2$-$25CO$-$47N_2$) (circular symbols in Fig. 4.24) can be seen to be higher than those obtained for the syngas in the current study; this is associated with the lower H_2 content, greater N_2 content and the presence of CO_2 in the typical syngas compositions considered in this work. Similar behaviour of the laminar burning velocity is found between ($30H_2$-$30CO$-$40N_2$) and ($28H_2$-$25CO$-$47N_2$) mixtures given its analogous composition.

Downdraft syngas has a similar composition as $20H_2$-$20CO$-$60N_2$ mixture. Therefore, the comparison shows that for very lean mixtures (ϕ=0.6) the burning velocity values are similar. However, an increasing difference in burning velocity is observed for latter equivalence ratios. Thus, emphasis the influence of the H_2 amount in the mixture, which in this case is only 3% by volume lower and the increased heat capacity of the mixture due to the dilution by CO_2 (13%) instead of N_2.

It can be observed that the magnitude of laminar burning velocity for the typical syngas compositions is similar to that of a mixture comprising $5\%H_2/95\%CO$, although the value of S_u^0 of the former peaks at a lower equivalence ratio than that of the latter. The heat value of this mixture is more than three times higher than the typical syngas composition. In opposite, the air-fuel ratio is about the double. Thus, the energy content per unit quantity of mixture (air + fuel) introduced in the chamber is only marginally lower when using typical syngas compositions.

4.1.2 Constant volume method

For a spherical flame, laminar burning velocity is a function of radius because of its dependency on flame curvature (Markstein, 1964). The stretched laminar burning velocity, S_u, at a given radius can be calculated by the pressure history of combustion according to Lewis and von Elbe, (1987), as follows:

$$\frac{r_b}{r_v} = \left[1 - \left(\frac{P_i}{P}\right)^{\frac{1}{\gamma}} \frac{P_v - P}{P_v - P_i}\right]^{\frac{1}{3}} \tag{4.13}$$

Where P_i and P_v are the initial and maximum pressure, respectively. The maximum pressure was obtained by the chemical equilibrium calculation in the constant volume condition. γ is the specific heat ratio of the mixture. P_v and γ were calculated by Gaseq package, which values are shown in the appendix B. r_v is the radius of the chamber.

The stretched burning velocity, S_u, of the propagating flame is calculated by the following expression (Lewis and von Elbe, 1987):

$$S_u = \frac{r_v}{3(P_v - P_i)} \left(\frac{P_i}{P}\right)^{\frac{1}{\gamma}} \left(1 - \left(\frac{P_i}{P}\right)^{\frac{1}{\gamma}} \frac{P_v - P}{P_v - P_i}\right)^{-\frac{2}{3}} \frac{dP}{dt} \tag{4.14}$$

A typical pressure curve is shown in the figure 4.25:

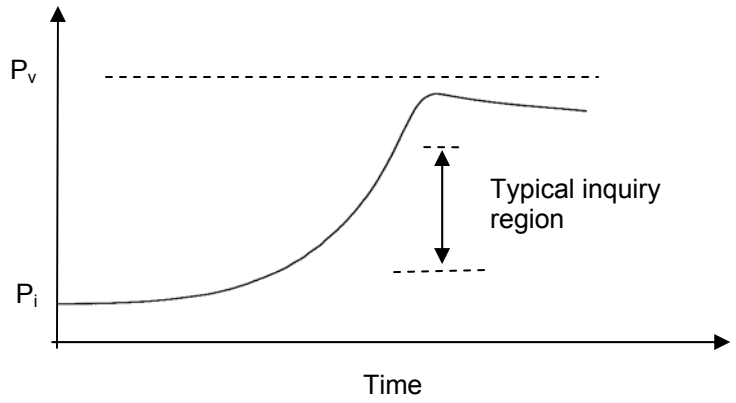

Figure 4.25 – Typical pressure curve and inquiry region for burning velocity calculation.

Burning velocity is calculated from this type of pressure records in all points of the pressure curve within the inquiry region indicated in figure 4.25. Low pressures are excluded due to imprecision of the pressure derivative. High pressures are excluded due to the inflection of the pressure curve caused by increasing thermal losses when the flame approaches the chamber walls.

4.1.2.1 Pressure evolution

Figure 4.26 to 4.28 shows pressure evolution for typical syngas-air mixtures under various equivalence ratios.

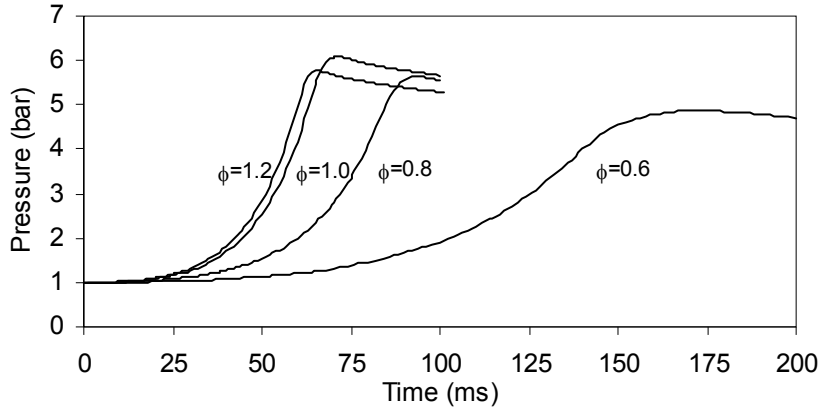

Figure 4.26 - Pressure versus time for updraft syngas-air mixture.

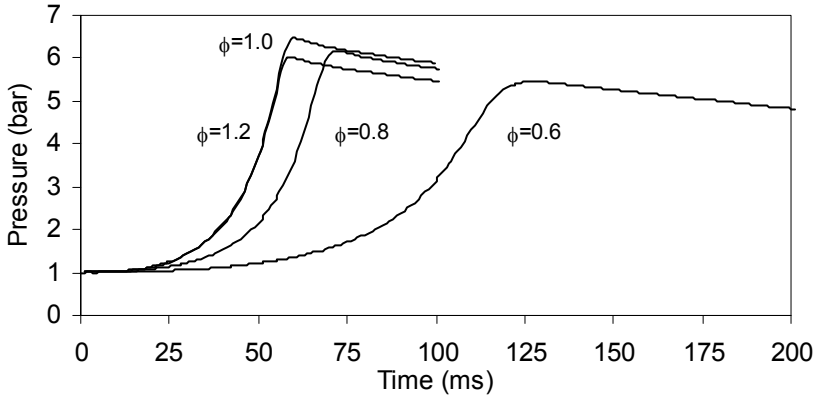

Figure 4.27- Pressure versus time for downdraft syngas-air mixture.

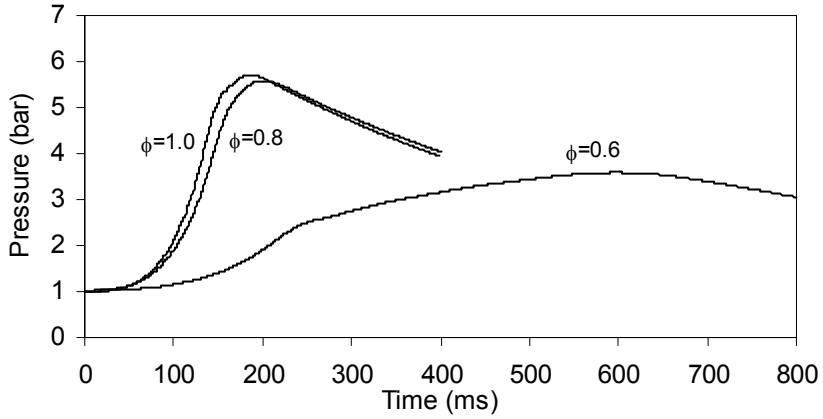

Figure 4.28 – Pressure versus time for fluidized bed syngas-air mixture.

In all cases of typical syngas-air mixtures presented herein, stoichiometric mixture is shows the best performance in terms of pressure peak. Rich mixtures (ϕ=1.2), not shown for fluidized bed case due to unsuccessful ignition, shows to be the faster ones for updraft and downdraft cases. Very lean mixtures (ϕ=0.6) shows, in all cases, to depart remarkably from the stoichiometric mixture. In the case of fluidized bed syngas

this is endorsed to no spherical propagation as shown above by schilieren flame images.

Tests runs with initial pressures of 0.5, 2.0, 5.0, and in some cases 6.0 bar were also performed in order to increase the burning velocity range of pressures. At initial pressure of 7.0 bar and room temperature (293 K) all typical syngas-air mixtures fail to ignite.

4.1.2.2 Burning velocity

Figures 4.29 - 4.31 shows stretched burning velocity for typical syngas-air mixtures for various equivalence ratios using Eq. (4.14). At this stage all the range of points are shown to emphasize the inaccuracy of the burning velocity calculation due to the pressure derivative fluctuation in the early stage of flame propagation, where the pressure does not change to much. After this stage a fast increase in pressure makes the burning velocity to increase rapidly up to a stable value. Afterwards, a nearly linear increase in burning velocity is observed. In some cases there is a sudden increase in burning velocity, which according to Saeed and Stone, (2004) is attributed to the development of cellular flame. In the final stage burning velocity start to decrease due to inflection in the pressure curve which gives place to lower pressure derivatives. The highest pressure derivative defines the upper limit of the inquiry region.

Workers such as Gülder (1984), Metghalchi and Keck, (1982), and Ryan and Lestz (1980) who used the constant-volume method for the determination of the burning velocities have assumed that the flame front is smooth, with no cellular or wrinkling flames. However, cellular flames can be formed under certain conditions, and in the present study cellularity was found for syngas flames. When cellularity triggers, the increase in the surface area leads to a sudden increase in the burning velocity and any inclusion of these data points would lead to higher burning velocity predictions. This is due to the transformation of the smooth spherical flame front to the polyhedral flame structures which increase the surface area of the flame front, thereby invalidating the smooth flame assumption of Eq. (4.14). Therefore, in this work the sudden increase of burning velocity was removed from the inquiry region.

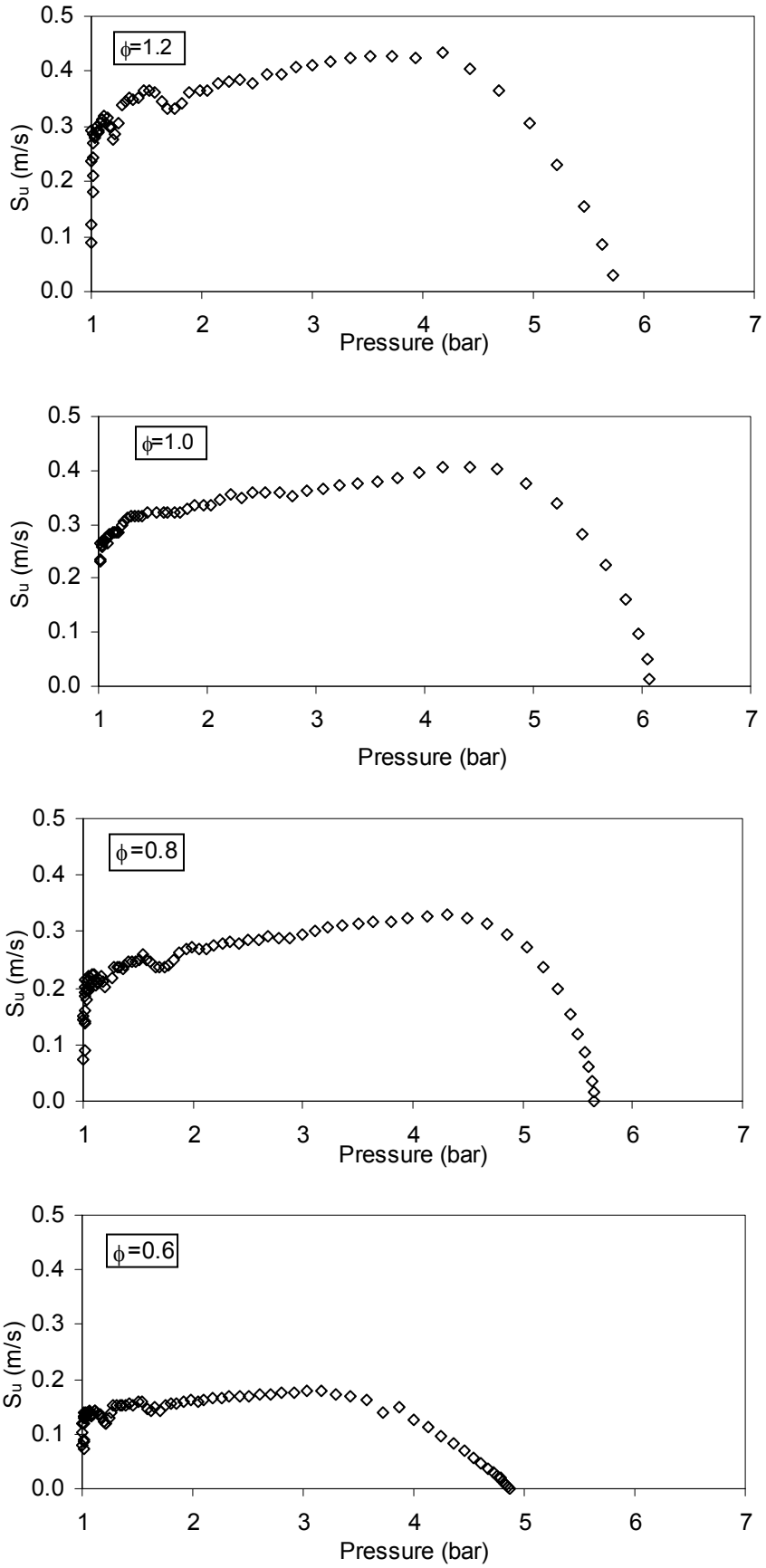

Figure 4.29 - Burning velocity versus pressure for updraft syngas-air mixture at various equivalence ratios

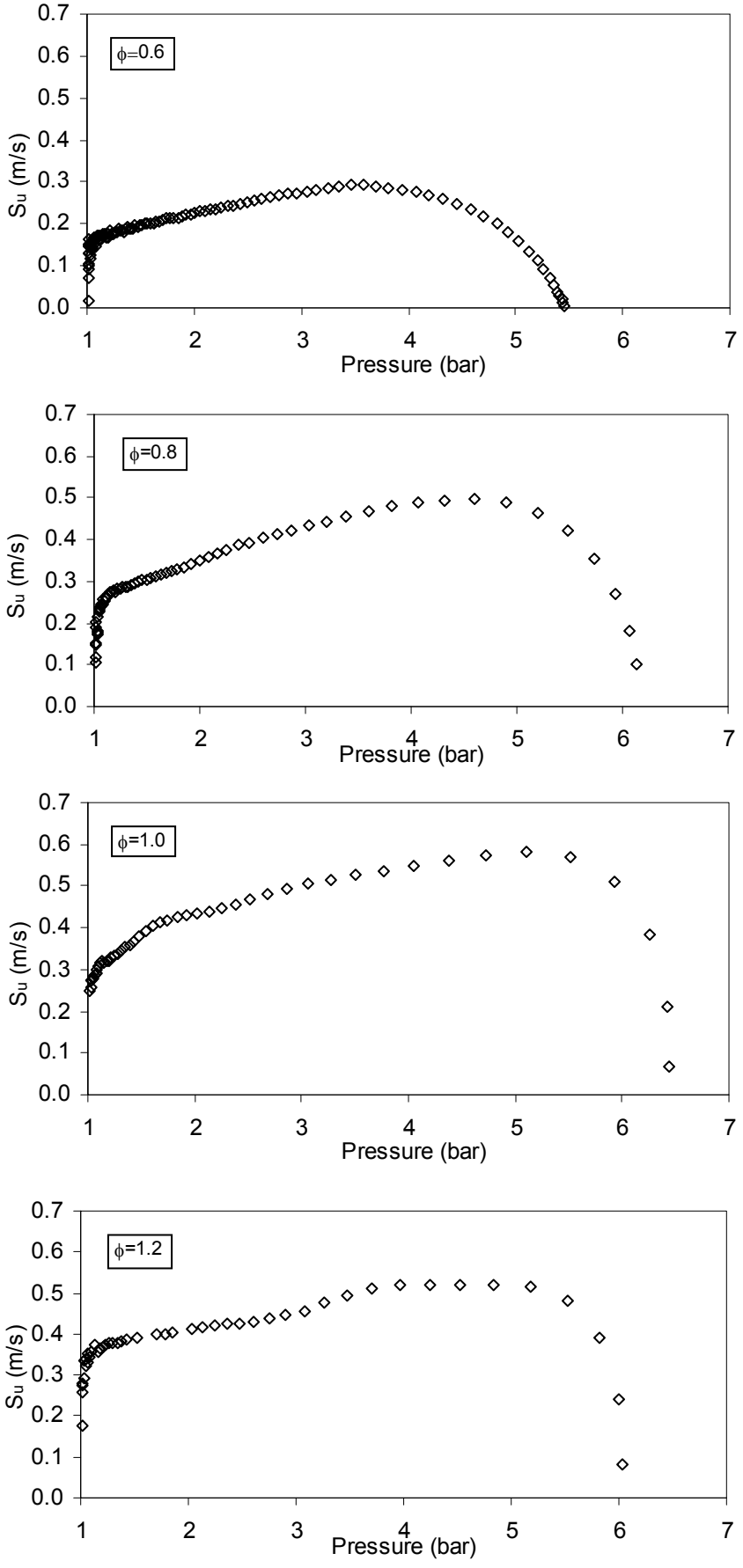

Figure 4.30 – Burning velocity versus pressure for downdraft syngas-air mixture at various equivalence ratios.

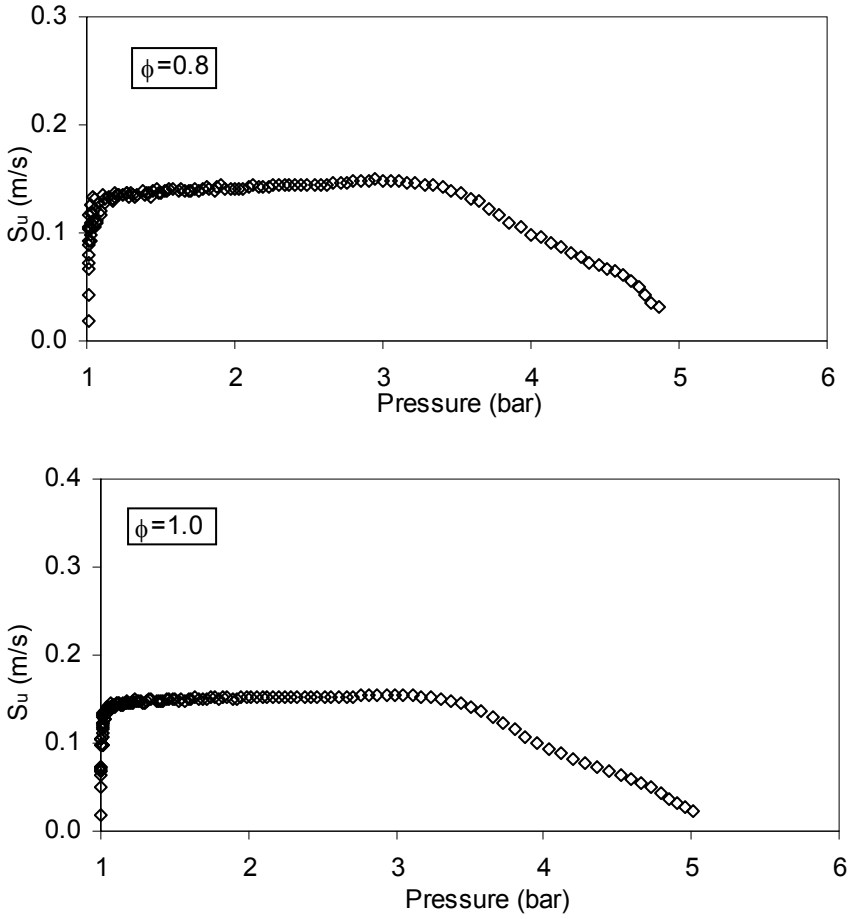

Figure 4.31 - Burning velocity versus pressure for fluidized bed syngas-air mixture at various equivalence ratios.

The lower limit for the inquiry region have been defined by Fiock and Marvin, (1937) and Rakotoniana, (1998), respectively, for the regime after the first 25% and 50% of flame propagation, when the pressure could be measured with sufficient accuracy. In this work the criterion was the stretch rate, due to its influence on burning velocity.

The flame speeds, S_n, are obtained by plotting values of r_b obtained from Eq. (4.13) as a function of time and determining the slopes of dr_b/dt. With the relationship between the values of r_b and S_n, the value of flame stretch, κ, can be specified from Eq. (4.2) for expanding spherical flames. Figures 4.32-4.34 shows stretch rate versus pressure for typical syngas-air mixtures under study at various equivalence ratios.

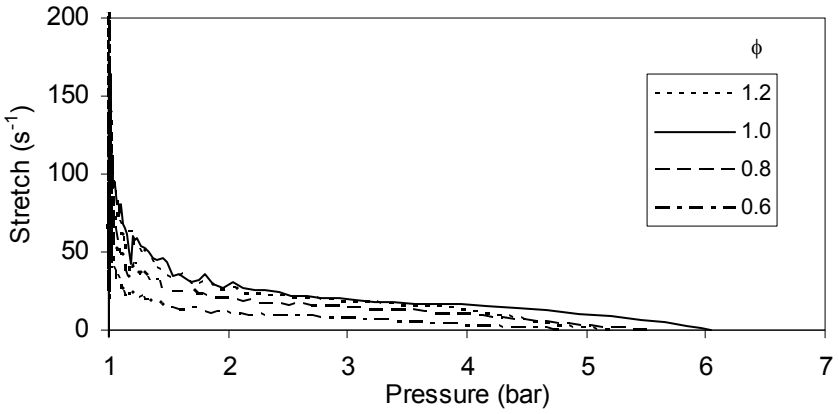

Figure 4.32 – Stretch rate versus pressure for updraft syngas-air mixture at 1.0 bar.

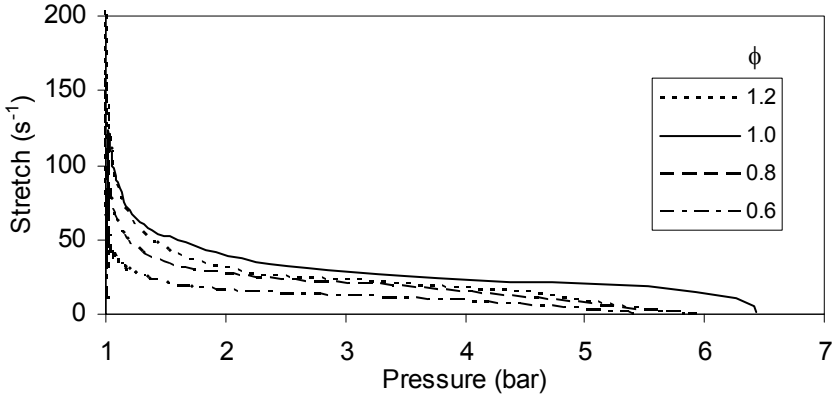

Figure 4.33 – Stretch rate versus pressure for downdraft syngas-air mixture at 1.0 bar.

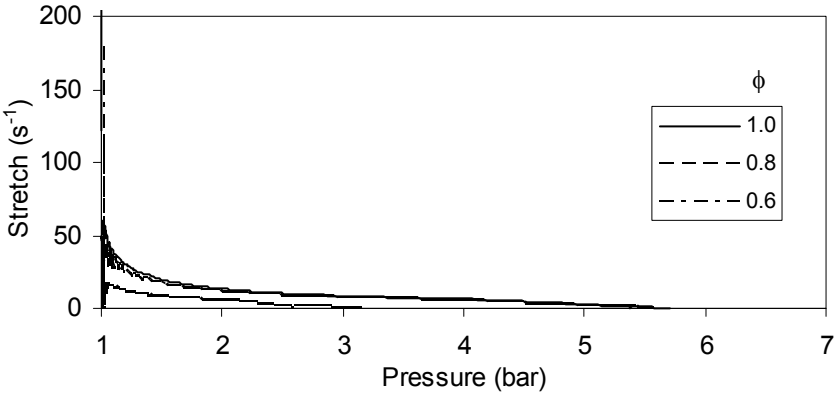

Figure 4.34 – Stretch rate versus pressure for fluidized bed syngas-air mixture at 1.0 bar.

These figures show a very similar behavior of the stretch rate versus pressure for all the syngas–air mixtures and equivalence ratios. Stoichiometric mixtures are highly stretched and stretch decreases with the equivalence ratio. The criterion of establishing

a minimum pressure to explore the burning velocity is doubtful because it corresponds to different stretch rate values, as easily could be seen from figures 4.32-4.34. Therefore, in this work, the criterion is a fixed stretch rate of 50 s^{-1}. For this level of stretch, the stretched burning velocity is close to the unstretched burning velocity.

4.1.2.3 Laminar burning velocity correlations

The simultaneous change in the pressure and temperature of the unburned mixture during a closed vessel explosion makes it necessary to rely on correlations which take these effects into account like the one proposed by Metghalchi and Keck, (1980):

$$S_u = S_{u_0} \left(\frac{T}{T_0} \right)^{\alpha} \left(\frac{P}{P_0} \right)^{\beta} \tag{4.15}$$

Where, T_0 and P_0, are the reference temperature and pressure, respectively. The influence of the equivalence ratio is incorporated through the temperature and pressure exponents, α and β, and through the reference burning velocity S_{u0} as square or linear functions.

Following the procedure described in the appendix A, this three unknowns are obtained for the three typical syngas compositions and are shown in the table 4.3.

In all syngas cases the temperature coefficient is positive and the pressure coefficient negative. This means that the burning velocity increases with temperature increase and decreases with the increase of pressure. The stretch rate in these correlations is lower than 50 s^{-1}. This means that these values of the stretched burning velocity are close to the unstretched ones. Notice the different range of validity of the expressions with the equivalence ratio and syngas composition. This is due to the unsuccessful ignition.

Table 4.3– Parameters α, β and S_{u0} (m/s) in function of the of the mixture syngas-air.

Parameter	P_0 = 1.0 bar; T_0 = 293 K			
	ϕ= 0.6	ϕ= 0.8	ϕ= 1.0	ϕ= 1.2
Updraft syngas				
α	2.466	2.047	1.507	1.869
β	-0.428	-0.289	-0.259	-0.355
S_{u0} (m/s)	0.135	0.212	0.303	0.314
Validity range	0.75<P(bar)<9.5 293 <T(K) <425	0.75<P(bar)<20 293 <T(K) <443	0.75<P(bar)<20 293 <T(K) <450	0.75<P(bar)<14.5 293 <T(K) <445
Downdraft syngas				
α	1.698	1.581	1.559	1.600
β	-0.181	-0.120	-0.159	-0.289
S_{u0} (m/s)	0.174	0.282	0.345	0.381
Validity range	0.75<P(bar)<15.5 293 <T(K) <413	0.75<P(bar)<20 293 <T(K) <443	0.75<P(bar)<20 293 <T(K) <450	0.75<P(bar)<20 293 <T(K) <450
Fluidized bed syngas				
α	-	1.827	2.124	-
β	-	-0.238	-0.518	-
S_{u0} (m/s)	-	0.095	0.137	-
Validity range	-	1.0<P(bar)<9.5 293 <T(K) <408	1.0<P(bar)<10 293 <T(K) <430	-

Figure 4.35 shows laminar burning velocity on the reference conditions of pressure and temperature as a function of the equivalence ratio of the mixture syngas-air.

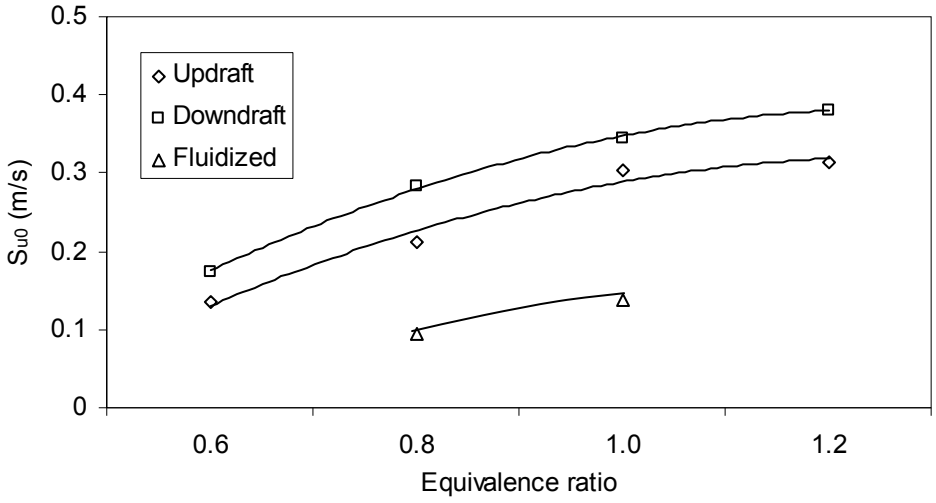

Figure 4.35 – Evolution of the reference laminar flame speed as a function of the equivalence ratio.

Notice the similar behavior of the S_{u0} curves with the unstretched burning velocity, S_u^0, of the figure 4.19. However, the effect of stretch (κ <50 s^{-1}) on S_{uo} as well as cellular flame development gives higher burning velocity values in comparison with the unstretched burning velocity (κ=0).

The influence of the equivalence ratio is included through the temperature and pressure exponents, α and β, and through the reference burning velocity S_{u0} as square functions for updraft (Eq. 4.16) and downdraft (Eq. 4.17) syngas compositions and as a linear function for fluidized bed syngas (Eq. 4.18) due to the limit data available:

$$\begin{aligned} S_{u0} &= -0.413\phi^2 + 1.056\phi - 0.355 \\ \alpha &= 4.881\phi^2 - 9.952\phi + 6.731 \\ \beta &= -1.469\phi^2 + 2.786\phi - 1.561 \end{aligned} \quad (4.16)$$

$$\begin{aligned} S_{u0} &= -0.45\phi^2 + 1.152\phi - 0.354 \\ \alpha &= 0.988\phi^2 - 1.936\phi + 2.502 \\ \beta &= -1.194\phi^2 + 1.967\phi - 0.931 \end{aligned} \quad (4.17)$$

$$\begin{aligned} S_{u0} &= 0.21\phi - 0.073 \\ \alpha &= 1.485\phi + 0.639 \\ \beta &= -1.4\phi + 0.882 \end{aligned} \quad (4.18)$$

Figure 4.36 shows a comparison between these correlations and the experimental burning velocity in order to address about its accuracy.

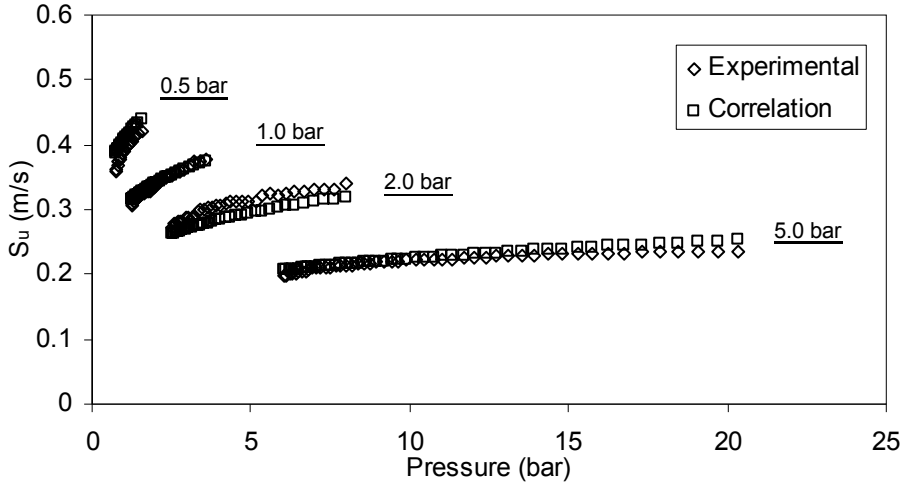

(a)

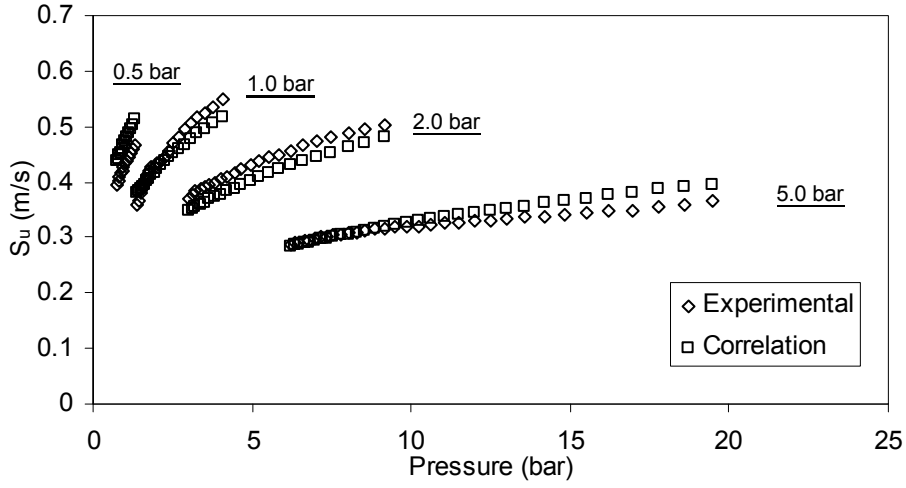

(b)

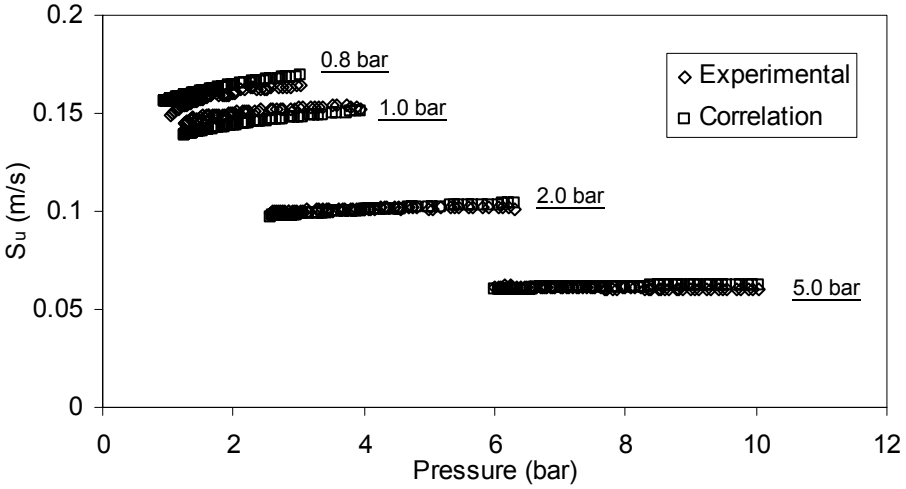

(c)

Figure 4.36 – Comparison between experimental and correlated burning velocities of syngas-air stoichiometric mixtures at different initial pressures within the chamber. (a) updraft; (b) downdraft; (c) fluidized bed.

A very good agreement between the correlation and the experimental burning velocity is found for every initial pressure test runs performed. Notice that for fluidized bed syngas the lower initial pressure with successful ignition was 0.8 bar. The maximum error of the burning velocity correlation is 8% for updraft syngas, 9% for downdraft syngas and 5% for fluidized bed syngas. These errors are perfectly reasonable and the discrepancy between syngas compositions errors has to do with experimental burning velocity scattering.

4.2. Multi-zone spherical combustion

In an engine cycle, the heat losses could be endorsed 25% to wall-flame interaction and 75% to the wall-burned gases interaction (Boust, 2006). Therefore, robust heat transfer models of wall-flame interaction should be employed. A multi-zone numerical heat transfer simulation code developed at the Laboratoire de Combustion et Détonique for methane-air mixtures by Boust, (2006) is adapted herein to syngas-air mixtures. The code allows simulating the combustion of homogeneous premixed gas mixtures within constant volume spherical chamber centrally ignited. In spherical combustion conditions, the model could also be used for predicting the quenching distance.

4.2.1 Mathematical model

4.2.1.1 Flame propagation

The flame is considered a perfect sphere without thickness. The propagation of the flame is imposed by its burning velocity that determines the thickness of the zone to burn during a predefined time Δt. The combustion is supposed isobaric, being the burning velocity S_u given by the empirical correlation of Metghalchi and Keck, (1980) expressed by the Eqs. 4.16 - 4.18.

The criterion that defines the end of combustion is the flame quenching distance. The quenching distance defines how close the flame approaches the wall and plays a definitive role on the wall-flame interaction as shown by Boust, (2006). The quenching implementation in the computational code consists of stopping the propagation of the flame when it approaches the wall in an equal distance to the frontal quenching distance δ_q. In order to estimate the quenching distance, the correlation of Westbrook et al., (1981) is used:

$$Pe_b = \frac{\delta_q}{\lambda_b / \rho_u S_u^0 C_{pb}} = 3.5 P^{-0.06} \tag{4.19}$$

Where Pe_b is the Peclet number and P the pressure in MPa. This correlation was obtained for stoichiometric methane-air and methanol-air mixtures for pressures 1-40 atm. Recently Boust, (2006) shows that this correlation is also valid for lean (ϕ=0.7) methane-air mixtures and stoichiometric hydrogen-air mixtures. For these reasons, we shall use correlation (4.19) for syngas-air mixtures.

4.2.1.2 Chemical equilibrium

Gases can have two possible states, burned and unburned. The composition of the burned gases is calculated by the Brinkley method, suggested by Heuzé et al., (1985). This method is based on the determination of the free energy of Gibbs from the Gordon & McBride, (1971) polynomials. The chemical equilibrium is calculated by canceling the chemical affinity in the chemical reactions. It appeals to the thermodynamic properties of the species instead of the equilibrium constants.

The combustion products considered are H_2O, CO_2, CO, O_2, N_2, NO, OH and H_2. As pressure and temperature conditions change during the compression and cooling phases, is possible to previously recalculate the composition of burned gases.

4.2.1.3 Heat transfer

A common approach exploiting a combined convective and radiative heat transfer coefficient has been implemented as representative of heat transfer through the chamber walls, Q_w. The formulation couples a convective-equivalent heat transfer coefficient to a radiative term, for taking into account the effects due to high temperature burned gases:

$$Q_w = Q_c + Q_r \tag{4.20}$$

Where Q_c and Q_r represents the convective and radiative heat transfer, respectively. The unburned gases in contact with the wall are heated by compression under the effect of expansion flame. Due to the higher temperature of the unburned gases in comparison with the chamber wall, which is at room temperature, they yield heat by conduction. This conductive heat transfer is simulated using a convective model (Boust, 2006).

$$Q_c = h\left(T_g - T_w\right) \tag{4.21}$$

with T_g and T_w, respectively, the temperature of the gases and wall and, *h,* the convective heat transfer coefficient. T_w is considered constant as it varies less than 10 K during combustion as reported by Boust, (2006). T_g is the local temperature of the gases. The determination of the convective heat transfer coefficient is case sensitive and several models are available in the literature [Annand (1963), Woschni (1967), or Hohenberg (1979)]. In this code the Woschni, (1967) model, which is based on the hypotheses of forced convection is applied and compared with the recent heat transfer model of Rivère, (2005) based on the gases kinetic theory (see appendix C). The Woschni (1967) heat transfer correlation is given as:

$$h_g(t) = 130B^{-0.2}P(t)^{0.8}T(t)^{-0.55}v(t)^{0.8} \tag{4.22}$$

where *B* is the bore (m), *P* and *T* are the instantaneous cylinder pressure (bar) and gas temperature (K), respectively. The instantaneous characteristic velocity, *v* is defined as:

$$v = \left(2.28\bar{S}_p + 0.00324\frac{V_s T_r}{\mathrm{P_r} V_r}(P - P_{mot}) \right) \tag{4.23}$$

Where $P_{mot}=P_r(V_r/V)^{\gamma}$ is the motored pressure. S_p is mean piston speed (m/s), V_s is swept volume (m^3), V_r, T_r and P_r are volume, temperature and pressure (m^3, K, bar) evaluated at any reference condition, such as inlet valve closure, *V* is instantaneous cylinder volume (m^3) and γ is the specific heat ratio. The second term in the velocity expression allows for movement of the gases as they are compressed by the advancing flame.

In the model of Rivère, (2005) the heat transfer coefficient is obtained as follows:

$$h = \rho_g . \sqrt{T_g} \sqrt{\frac{2}{\pi}} \left(\frac{R}{M} \right)^{\frac{3}{2}} \left(\eta + \frac{\chi}{\sqrt{T_w}} - \frac{\lambda}{T_w} \right) \tag{4.24}$$

where ρ_g, T_g and *M* are, respectively, the density, the temperature and molar mass of the gases. The last parenthesis in the right side of the Eq. (4.26) represents the heat transfer coefficient that depends on the gases temperature that determines the length of the boundary layer. χ and λ are the material constants and η a function of the aerodynamic conditions equal to zero in the advection absence.

Heat radiation of the burned gases to the chamber walls are modeled neglecting the radiation of the particles. This assumption is reasonable due to the high purity of the tested mixtures. During combustion, heat radiation can have origin on unburned gases, which contains: H_2, CO, CH_4, CO_2, N_2 and O_2, and also on the burned gases, which mainly contains: CO_2, H_2O and N_2, being irrelevant the remaining combustion products. Only molecules that have a non null dipolar moment are susceptible to emit thermal radiation (Boust, 2006). Therefore only CO_2, H_2O and CH_4 are considered. In practical terms, the radiation of the unburned gases heated by compression is insignificant comparatively with the burned gases, which temperature is 6-7 times higher. Thus, it is assumed that only CO_2 and H_2O radiates significantly.

The radiation heat transfer is modeled by the Stefan's law considering the burned gases as a grey body with uniform temperature T_g and ε the apparent grey-body emissivity calculated from the contributions of H_2O and CO_2. As the spectral emissivities of these species are similar, the emissivity variation term $\Delta\varepsilon$ is included.

$$\varepsilon = \varepsilon_{CO_2} + \varepsilon_{H_2O} - \Delta\varepsilon \tag{4.25}$$

At the end of combustion, only burned gases are inside the chamber. Then, the net superficial radiative flow $Q_{,r}$ received by the wall, with absorption factor α, from the burned gases is given by the Stefan's constant.

$$Q_r = \alpha\,\varepsilon\,\sigma\left(T_g^4 - T_w^4\right) \tag{4.26}$$

When the sphere of burned gases (radius r) does not occupy the entire chamber (radius R), the sphere surface ratio gives the radiative flow.

$$Q_r(r) = \frac{4\pi r^2}{4\pi R^2} Q_r \tag{4.27}$$

The emissivity of H_2O and CO_2 as well as the variation term are calculated using the correlation of Leckner, (1972). This correlation reproduces the gases temperature influence, the partial pressure of each species and the length of the average radius.

4.2.2 Calculation procedure

In the multi-zone model, flame propagation is seen as the consecutive consumption of unburned mixture within the zones with an equal mass distribution between the zones

in the spherical vessel (Fig. 4.37). Before ignition, the mass in the spherical vessel is divided into n zones. At the time when combustion has just begun in the bomb, the flame front will consume zone 1 first. As a result, the temperature and hence pressure of zone 1 will increase, thereby compressing the rest of the unburned gas (considered as single entity) and increasing the pressure inside the vessel to a higher value. After the consumption of the first zone, combustion of the second and subsequent zones will take place at a higher pressure than the initial pressure. At any instant of time when the flame front is passing through the n_{th} zone, the combustion of this zone takes place at a temperature of $T_{u,n-1}$ ($> T_i$) and a constant pressure $P_{u,n-1}$ ($> P_i$). The combustion within a given zone takes place progressively. After the flame has consumed the n_{th} zone, it is then assumed to be adiabatic. Subsequent combustion further compresses the burned gas and the unburned gas. As a result, temperature and density gradients are established in the burned gas region. At the end of combustion, the burned gas cooling is computed.

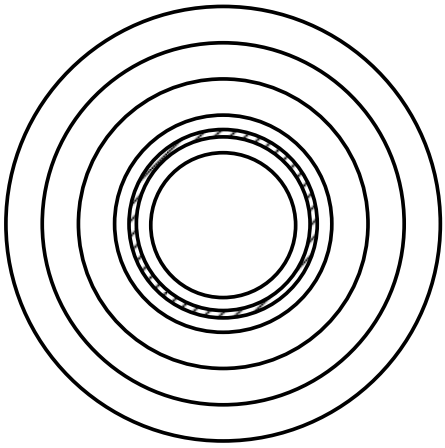

Figure 4.37 – Radial distribution of the multiple zones inside a spherical vessel. Hatched portion indicates the position of the flame front at an instant of time.

Figure 4.38 shows the flowchart of the adapted Fortran code. The output data of the code are: the burned gas temperature, flame radius and flame speed, pressure, as well as the wall thermal flux. At the end of combustion, an energy balance is made.

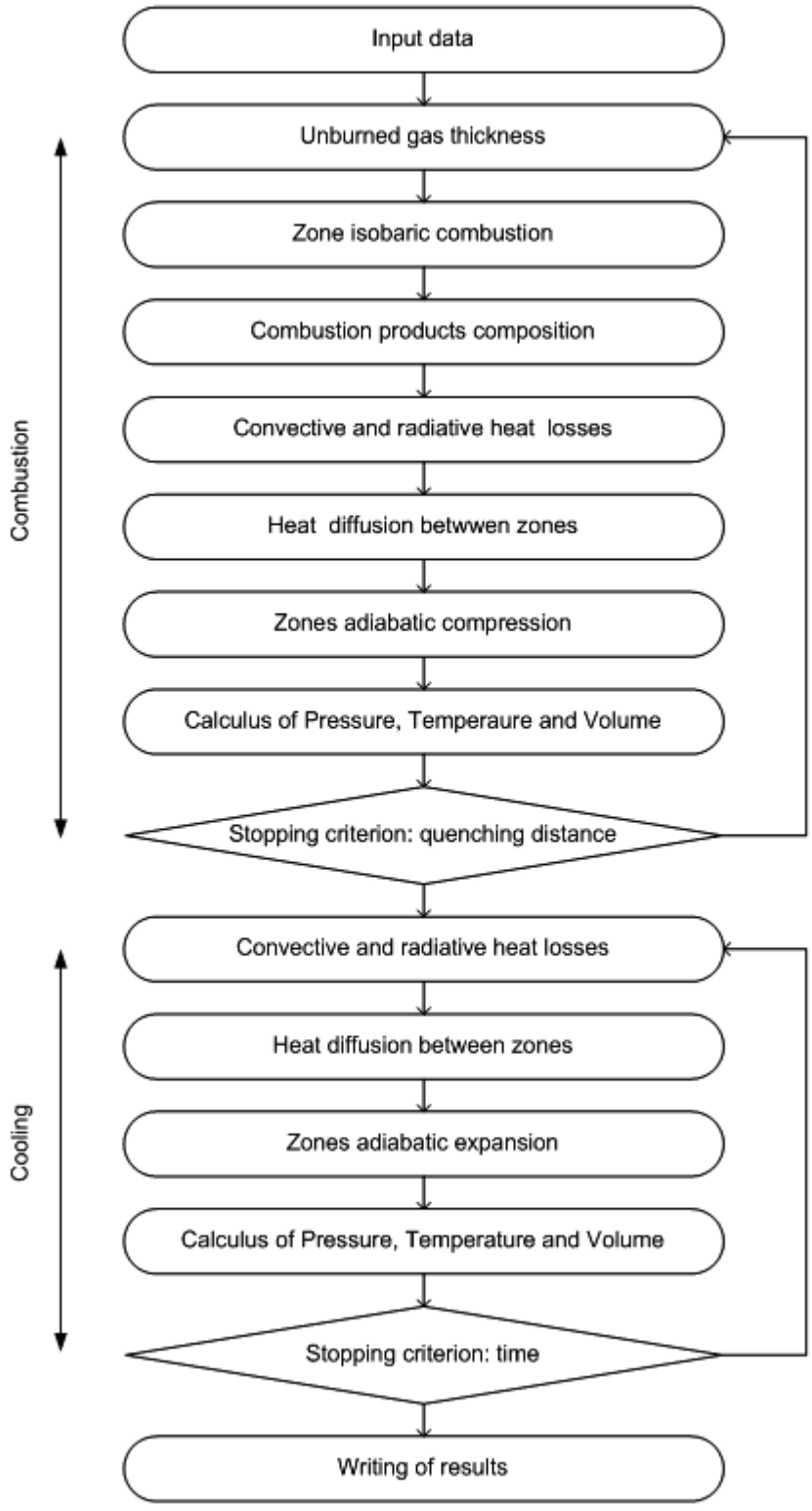

Figure 4.38 – Combust flowchart.

4.2.3 Results discussion and code validation

The numerical results are validated for syngas-air mixtures by comparison with experimental results of pressure evolution. Different equivalence ratios and pressures

are tested and discussed. The numerical code described above is then used to estimate the heat flux and quenching distance of syngas-air mixtures.

4.2.3.1 Influence of the heat transfer model

In order to define the heat transfer model to use, one first compare two formulations already mentioned above: the classical Woschni (1967) correlation and the recent Rivère (2005) formulation. The comparison of both formulations is made in the figure 4.39.

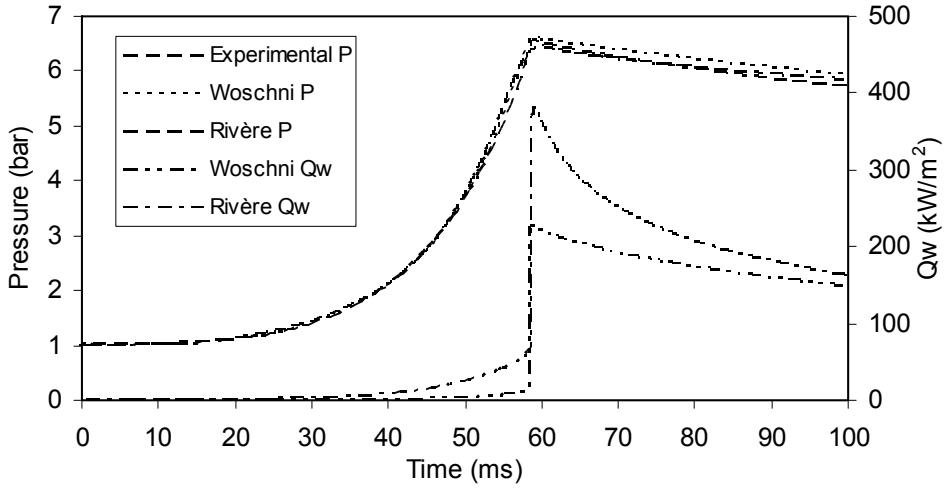

Figure 4.39 – Influence of the heat transfer model – stoichiometric downdraft syngas-air, P=1.0 bar.

From figure 4.39 is possible to conclude that the heat transfer model has only marginal influence on pressure curve. However, the Rivère model shows to better follow the pressure curve on the cooling side. The reason is the higher value of the heat flux through the wall using this model. This result is in agreement with Boust, (2006), who compared these models with experimental heat flux values for methane-air mixtures and concluded that Rivère model is most suitable to simulate the wall-flame heat transfer and that Woschni model is inadequate in the absence of a strong flow. Thus, Rivère model is applied throughout the following results.

4.2.3.2 Influence of equivalence ratio

The influence of the equivalence ratio in the burning velocity and pressure was experimentally determined for the syngas compositions under study. It was seen that the pressure and burning velocity decreases when departing from stoichiometric

conditions. Figures 4.40 – 4.42 shows experimental and numerical pressure and the heat flux for updraft syngas-air mixture at ϕ=0.8, ϕ=1.0 and ϕ=1.2, respectively.

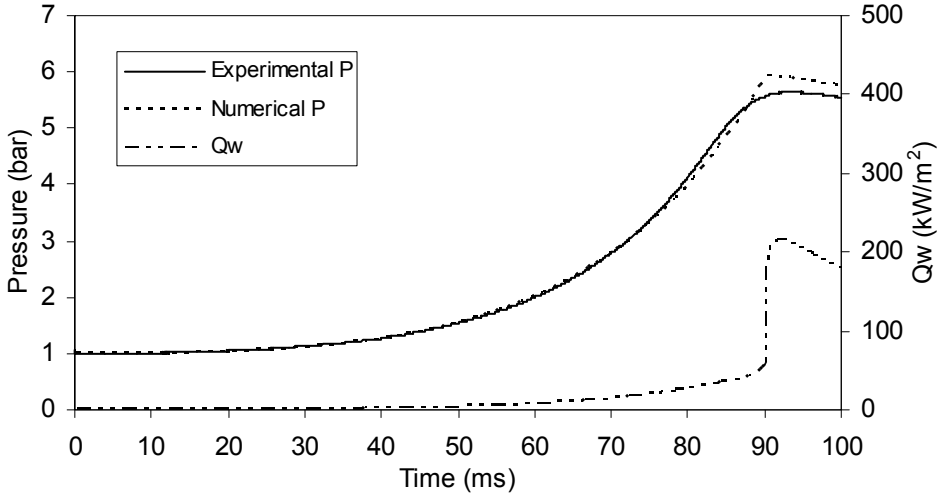

Figure 4.40 – Pressure and heat flux for updraft syngas-air at ϕ=0.8, P=1.0 bar, T= 293 K.

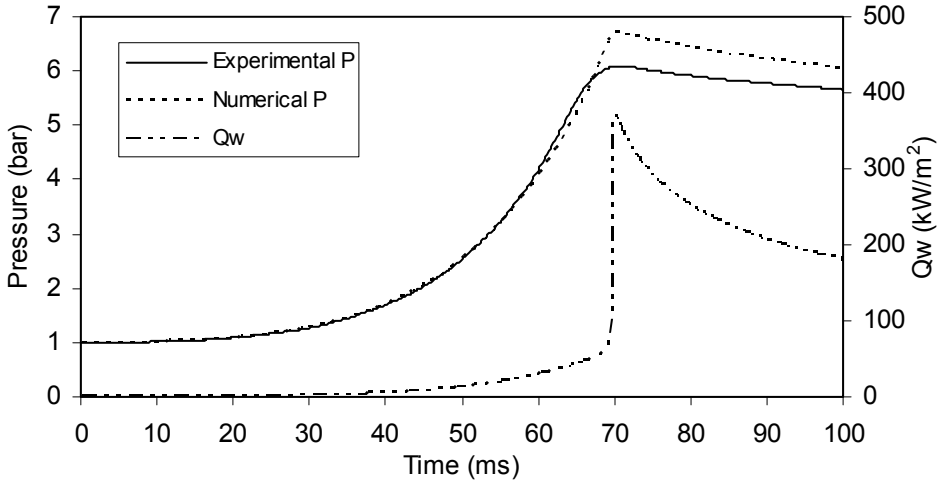

Figure 4.41– Pressure and heat flux for updraft syngas-air at ϕ=1.0, P=1.0 bar, T= 293 K.

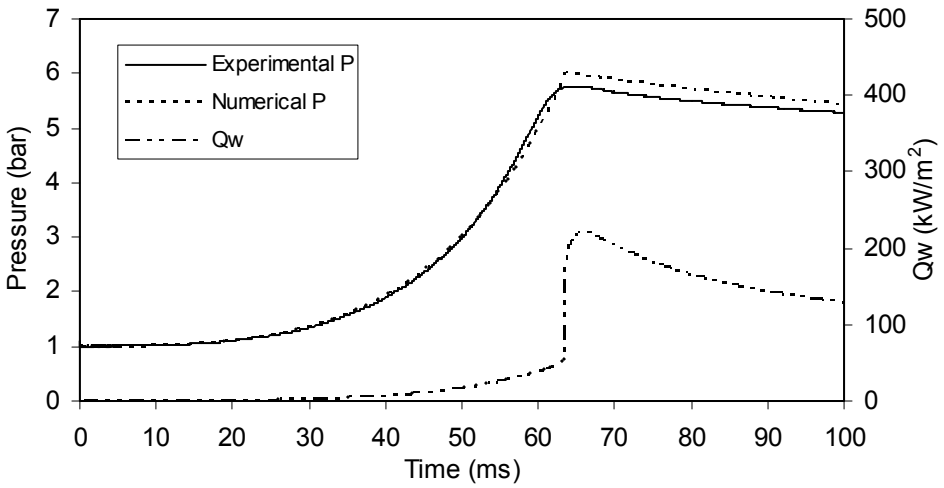

Figure 4.42 – Pressure and heat flux for updraft syngas-air at ϕ=1.2, P=1.0 bar, T= 293 K.

From figures 4.40-4.42 one can conclude that pressure evolution of updraft syngas-air mixtures is accurately reproduced by the code for each equivalence ratio. However, pressure peak is always higher than the experimental measurement as well as in the cooling phase. It was found important chamber leakages at this stage, and so the chamber was repaired. The following results were obtained after the reparation.

Figures 4.43 - 4.45 shows experimental and numerical pressure and the heat flux for downdraft syngas-air mixture at ϕ=0.8, ϕ=1.0 and ϕ=1.2, respectively.

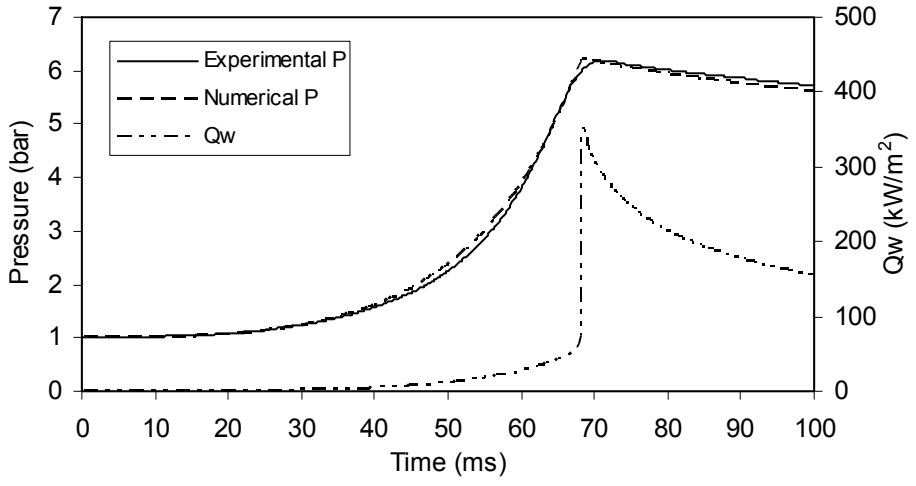

Figure 4.43 – Pressure and heat flux for downdraft syngas-air at ϕ=0.8, P=1.0 bar, T= 293 K.

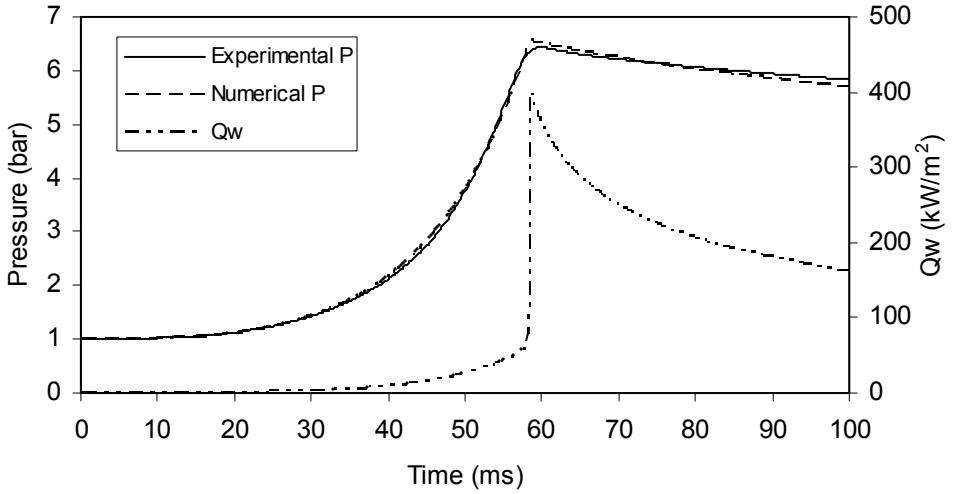

Figure 4.44 – Pressure and heat flux for downdraft syngas-air at ϕ=1.0, P=1.0 bar, T= 293K.

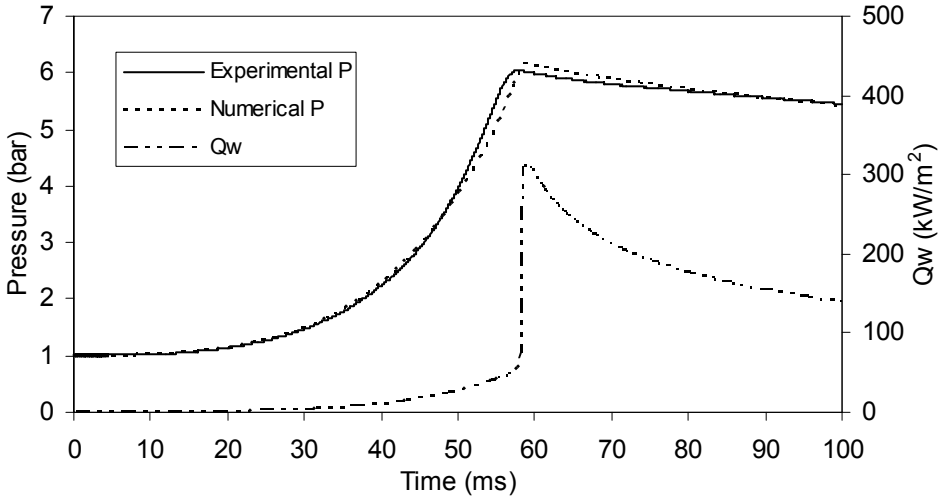

Figure 4.45 – Pressure and heat flux for downdraft syngas-air at ϕ=1.2, P=1.0 bar, T= 293 K.

Figures 4.46 - 4.47 shows experimental and numerical pressure and the heat flux for fluidized bed syngas-air mixture at ϕ=0.8 and ϕ=1.0, respectively.

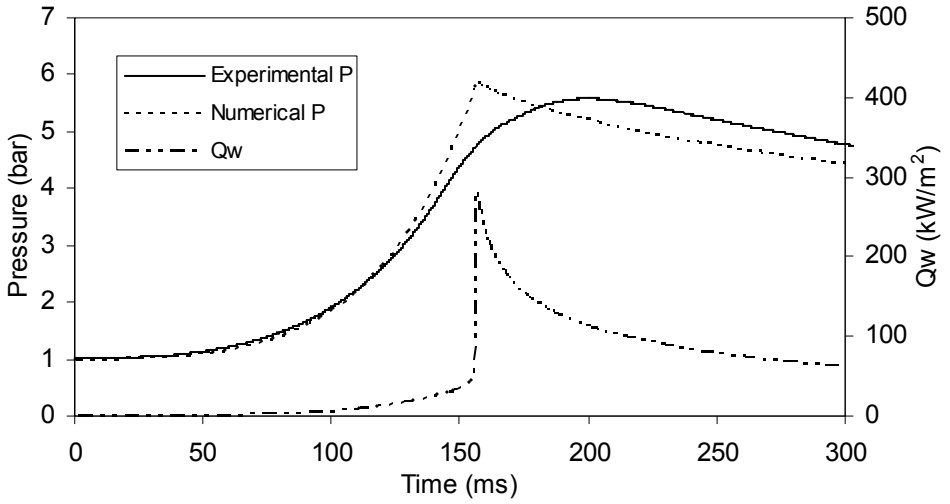

Figure 4.46 – Pressure and heat flux for fluidized bed syngas-air at ϕ=0.8, P=1.0 bar, T= 293 K.

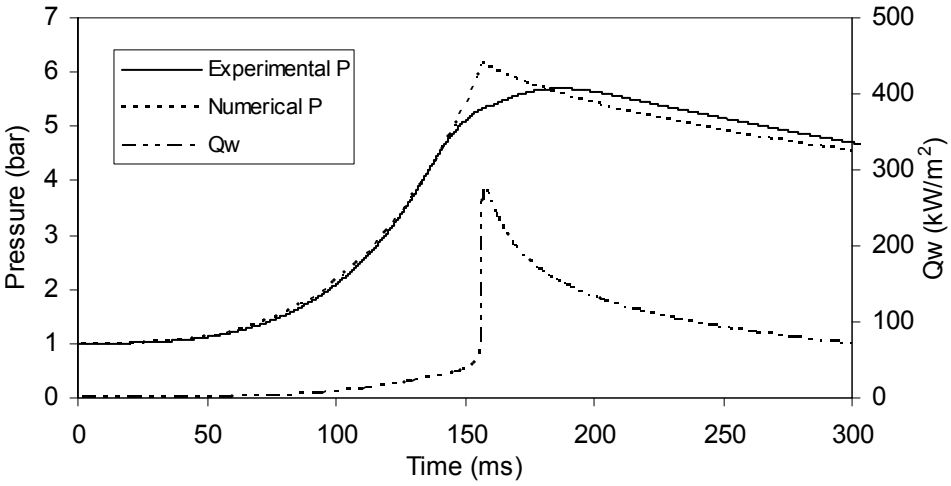

Figure 4.47 – Pressure and heat flux for fluidized bed syngas-air at ϕ=1.0, P=1.0 bar, T= 293 K.

From these figures, it is possible to conclude that the code over-estimates the pressure for fluidized bed syngas. The extremely low burning velocity of this syngas composition makes gravity forces being felt within the chamber, which makes the burned gases to move to the top of the chamber and the flame to propagate to the bottom as shown in the figure 4.5. Therefore, the assumption of spherical combustion is no longer valid.

4.2.3.3 Influence of the pressure

Let us now verify if pressure effect is accurately reproduced by the code. Figures 4.48 - 4.49 shows pressure and heat flux for stoichiometric syngas-air mixtures at 5.0 bar.

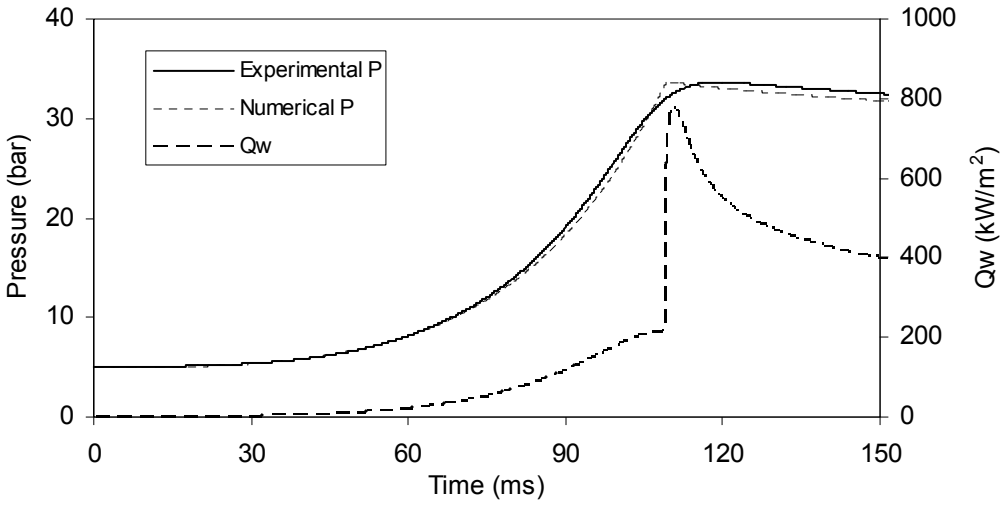

Figure 4.48 – Pressure and heat flux for updraft syngas-air at 5.0 bar and 293 K.

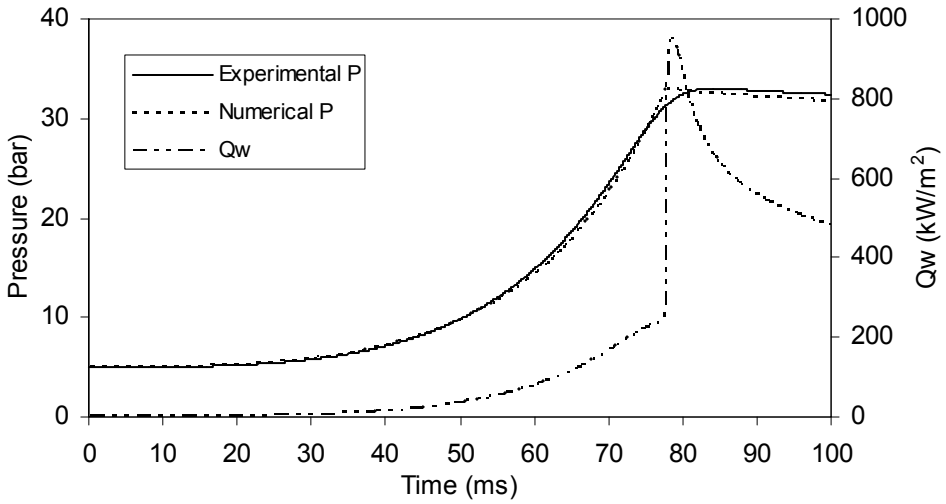

Figure 4.49 – Pressure and heat flux for downdraft syngas-air at 5.0 bar and 293 K.

As reported in 4.1.1.1 cellular flame are present in syngas-air flames for initial pressures higher than 2.0 bar. Therefore, pressure curves of 5.0 bar are not perfectly spherical, which makes the flame to reach the wall non-uniformly. Thus, the heat flux peak is not synchronized in the entire chamber surface, which explains that the pressure peak is reached after some relaxation. This behavior was also observed by Boust, (2006) when dealing with lean (ϕ=0.7) methane-air mixtures.

Notice that the code reproduces well the pressure evolution beyond the validity of the burning velocity correlation established in 4.1.2.3 for updraft and downdraft syngas compositions. For these syngas compositions, the experimental correlation is valid up to 20 bar, however we show numerically that value could be used beyond 33 bar.

4.2.3.4 Quenching distance and heat flux estimations

After validating the numerical code for updraft and downdraft syngas compositions, under various conditions of pressure and equivalence ratios, one can then use it to predict the quenching distance and heat flux of syngas-air mixtures.

As flame propagates from the centre of the chamber, pressure increases, and consequently the temperature also increases. This is the compression phase (1) in the figure 4.50. The heat transfer from the unburned gases to the wall, manly by conduction, but also marginally by radiation. The heat flux through the wall increases up to the flame quenching.

During wall-flame interaction, the flame transfer in average one third of its thermal power to the wall (Boust, 2006), which makes a heat flux peak to appear. The flame is quenched at a finite distance to the wall, the quenching distance. It remains, therefore, a thin layer of unburned gases between the burned gases and the wall. The instant of the heat flux peak is less reproducible than its amplitude. In fact, such instant is somewhere between the inflexion point of the pressure curve and the instant of maximum pressure. During this phase (2), the wall-flame interaction is gradually dispersed throughout the chamber, which explains the inflexion point in the pressure curve. The existence of the phase (2) indicates that combustion is not strictly spherical. After the peak of pressure, the combustion phase gives place to the cooling phase (3). The wall heat losses are now only due to the burned gases heat source. The heat transfer is made through the thin layer of unburned gases between the burned gases and wall.

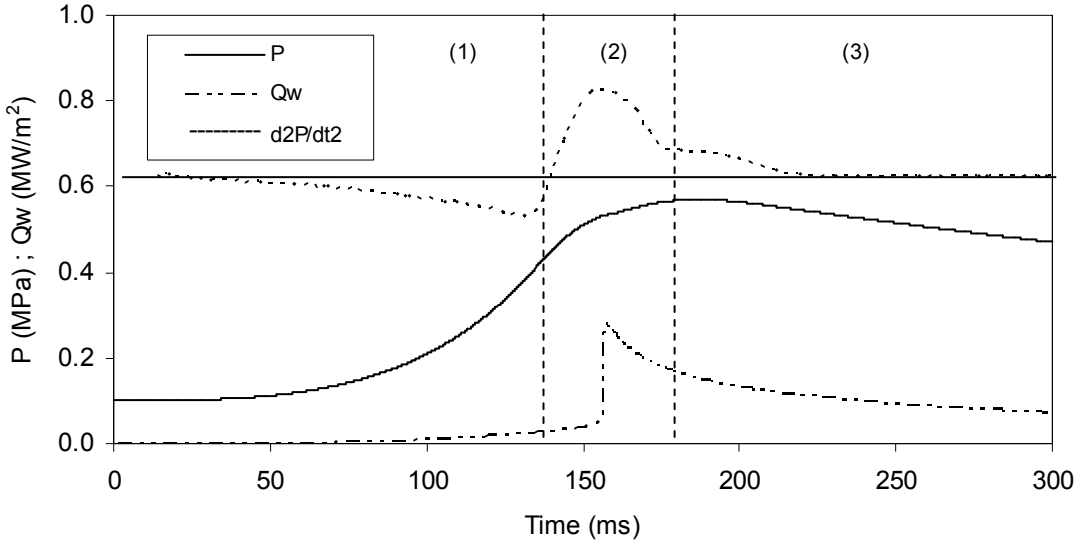

Figure 4.50 – Combustion development in spherical chamber fluidized bed syngas.

In order to quantify the thermal losses of different mixtures special care must be taken in the heat flux integration. The integration time should capture the entire phenomenon. The cooling time is possible to control by establishing a certain cooling period. However, the combustion time changes with the fuel, initial pressure and equivalence ratio, which calculation is not straightforward. Therefore, the comparison of heat flux estimative already shown in figures 4.41-4.49 is made based on the heat flux peaks (Table 4.4).

Table 4.4 – Heat Flux peaks for stoichiometric syngas-air and methane-air mixtures.

Qw (kW/m^2)	Updraft	Downdraft	Methane (Boust, 2006)
1.0 bar, ϕ=0.8	216 kW/m^2	350 kW/m^2	-
1.0 bar, ϕ=1.0	368 kW/m^2	402 kW/m^2	649 kW/m^2
1.0 bar, ϕ=1.2	220 kW/m^2	313 kW/m^2	-
5.0 bar, ϕ=1.0	777 kW/m^2	949 kW/m^2	(*) 1622 kW/m^2

(*) linear interpolation.

From Table 4.4 some conclusions can be drawn:

- The heat flux increases with initial pressure increase for all cases. The amount (volume and energy) of the explosive mixture inside the vessel increases with initial pressure increase.
- The heat flux increases with the heat value of the fuel-air mixture. In this case, one should also take into account the air-fuel ratio.
- The equivalence ratio has the influence of decreasing the heat flux compared to stoichiometric mixtures and follows the behavior of pressure peak.

The thickness of wall quench layers is a primary source of unburned fuels (Saeed and Stone, 2004). Thus, this combustion characteristic is very important and was predicted for stoichiometric updraft and downdraft syngas compositions by the Westbrook criterion defined by a zero flame stretch (figure 4.51). This is practically the case when the flame reaches the wall given the large curvature radius. The Westbrook criterion is valid in pressure range 1-40 bar and burning velocity correlation used in the code shows to be valid up to 33 bar, thus one impose this limit to quenching distance estimation.

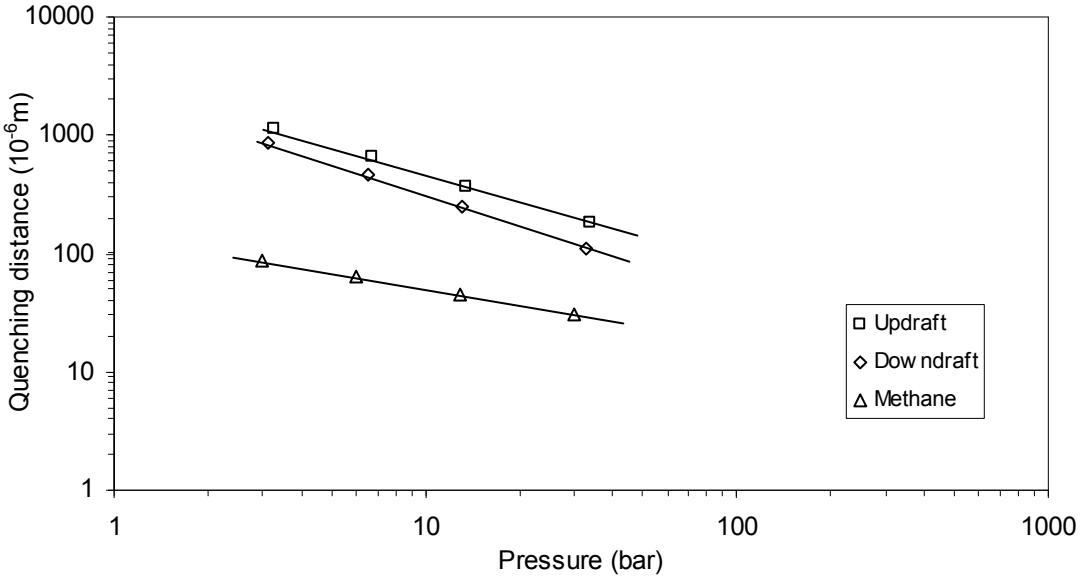

Figure 4.51 – Quenching distance estimation for stoichiometric syngas-air mixtures and comparison with stoichiometric methane-air mixture (Boust, 2006).

Figure 4.51 also includes quenching distance of stoichiometric methane-air mixture for comparison reasons. The following correlation determined by Boust, (2006) was adopted δ_q =50 $P^{-0.45}$ (P>3.0 bar) with P in Mpa and δ_q in μm. One can conclude that quenching distance decreases with the increase of pressure and is higher for lower heating value mixtures.

The following correlations are developed for stoichiometric updraft and downdraft syngas-air mixtures, similar to the one presented by Westbrook et al., (1981) and Boust, (2006) for methane-air mixtures:

$$\delta_q = 450\ P^{-0.79}\ ,\ P>0.3\ \text{MPa} \qquad \text{(Updraft)} \qquad (4.28)$$

$$\delta_q = 300\ P^{-0.89}\ ,\ P>0.3\ \text{MPa} \qquad \text{(Downdraft)} \qquad (4.29)$$

With δ_q in μm and *P* in MPa.

4.3 Conclusion

Laminar flame characteristics of three typical syngas compositions were studied in a constant volume chamber for various equivalence ratios. The influence of stretch rate on flame was determined by the correspondent Markstein and Karlovitz numbers. Combustion demonstrates a linear relationship between flame radius and time for syngas–air flames. The maximum value of syngas-air flame speeds is presented at the stoichiometric equivalence ratio, while lean or rich mixtures decrease the flame speeds.

Tendency observed on the unstretched burning velocity is in agreement with the heat of reaction of the syngas composition. The higher heat value is associated with the higher amount of H_2 and lower dilution by N_2 and CO_2 in the syngas composition. The incomplete combustion and ignition difficulty of the typical fluidized bed syngas composition makes it a less candidate to stationary power applications without addition of another fuel. Markstein numbers shows that syngas-air flames are generally unstable. Karlovitz numbers indicates that syngas-air flames are little influenced by stretch rate. Based on the experimental data a formula for calculating the laminar burning velocities of syngas–air flames is proposed.

The laminar burning velocity of typical syngas compositions is not dissimilar to that of methane especially the downdraft syngas case, although somewhat slower than propane. This could be due to the syngas stoichiometric air–fuel ratio that is ten times lower than the methane air-fuel ratio and more than twenty times in the case of propane. Thus, the energy content per unit quantity of mixture (air + fuel) inducted to the chamber is only marginally lower when using syngas, compared with the corresponding common gas fuels. The values of laminar burning velocity reported for syngas ($28H_2$-$25CO$-$47N_2$) can be seen to be higher than those obtained for the syngas in the current study; this is associated with the lower H_2 content, greater N_2 content and the presence of CO_2 in the typical syngas compositions. The simulated syngas mixture that better matches the magnitude of laminar burning velocity for the typical syngas compositions is the mixture comprising $5\%H_2/95\%CO$.

Base on the experimental data some empirical formulations of the burning velocities have been establish for pressure range 0.75-20 bar and temperature range 293K-450K.

The numerical simulation code of the laminar spherical combustion allows the pressure and wall heat flux reproduction under a various conditions of pressure, equivalence ratio and fuel. Quenching distance correlations for typical syngas-air flames were developed tanks to this code. One can conclude that quenching distance decreases with the increase of pressure and is higher for lower heating value mixtures.

CHAPTER 5

EXPERIMENTAL STUDY OF ENGINE-LIKE TURBULENT COMBUSTION

The main advantage that comes from the use of syngas (as well as other gases) in SI engines over the conventional liquid, petroleum-based fuels is the potential for increased thermal efficiency (Rakopoulus and Michos, 2008). This is attributed to the relatively high compression ratios permitted, usually by converting Diesel engines for gaseous fuel operation in the SI mode (Stone and Ladommatos, 1991), since CO and CH_4 are characterized by high anti-knock behavior (Li and Karim, 2006). On the contrary, the relatively increased end-gas temperature, which the fast flame propagation rate of H_2 can produce during combustion and can be responsible for knock onset, is compensated for by the presence of diluents in the fuel (N_2 and CO_2). Their effect on combustion is to lower flame speed and consequently decrease the in-cylinder pressures and temperatures. The lean-burn combustion mode usually adopted in gas engines also contributes to this aim. They are charged with fresh mixtures having air–fuel ratios sufficiently greater than stoichiometric (Rousseau et al., 1999). The moderation of peak gas temperatures during combustion, attributed to the last two features, has also a reduction effect on NO_x emissions (Heywood, 1988).

Besides, the drawback of reduced power output using fuels with relatively low heating values can be partially balanced by turbo-charging the engine. Towards the direction of minimizing this power derating when, for example, syngas with low heating value equal to 4–6 MJ/Nm^3 is used instead of natural gas with low heating value of approximately 30 MJ/Nm^3, contributes the fact that the syngas stoichiometric air–fuel ratio is about 1.2 compared with the value of 17 for the natural gas case (Rakopoulos and Michos, 2008). Thus, the energy content per unit quantity of mixture (air + fuel) inducted to the cylinder is only marginally lower when using syngas, compared with the corresponding natural gas case (Sridhar et al., 2001).

In this chapter an experimental approach to syngas engine performance on a rapid compression machine (RCM) is made.

5.1 RCM single compression

A rapid compression machine (RCM) is an instrument to simulate a single cycle of an internal combustion engine, thus also allowing the study of various parameters under

more favorable conditions than those existing in real engines (Strozzi et al., 2008), specially the spontaneous ignition (Brett et al., 2001). RCM can operate under two different modes: single compression and compression – expansion.

The study of the compression process in a RCM operating without combustion is useful to identify different parameters related with its operation, namely the heat transfer to the walls. Once determined, these parameters can also be used during the usual firing cycle. In fact, a common practice in engine testing for combustion diagnostic is, prior to the usual firing tests, to test the engine in motored conditions, with air as the only working gas (Lapuerta et al., 2003).

5.1.1 Sensibility analysis

In this section a sensibility analysis is made with the objective of evaluating the influence of errors in measurement techniques and in the estimation of various parameters on the main experimental results. In this analysis the chamber wall temperature is considered as constant.

5.1.1.1 TDC position

In order to determine the precision of the RCM top dead center (TDC) position, a position sensor was placed at TDC and various tests performed without combustion in order to eliminate the effect of the spark time scattering. The analysis of the TDC signal for the whole single compression experiments without combustion performed with syngas-air and methane-air mixtures enables to define a typical scattering of the TDC position on less than 1.67 ms. Considering that the compression stroke duration is 44 ms, this gives an overall uncertainty of 3.8% on the TDC position. In order to determine the influence of this scattering on pressure signal for the updraft-syngas case both signals are plotted in figure 5.1.

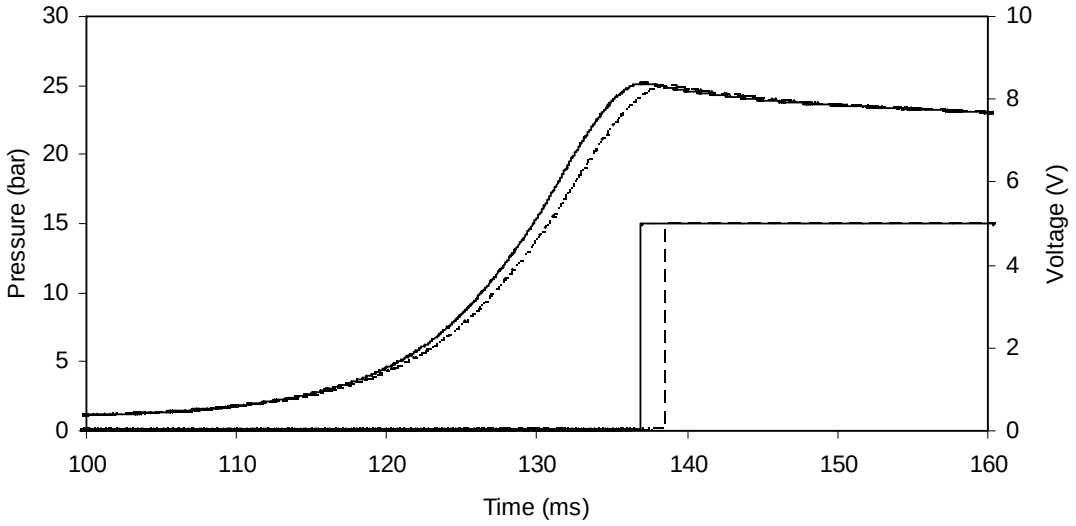

Figure 5.1 – TDC position: compression of updraft syngas-air mixture.

In this case, the jitter on the TDC position is 1.67 ms, which makes the pressure signal being shifted to the right. Therefore, synchronization with reference to TDC is needed. Figure 5.2 shows the result after TDC synchronization, where both signals are overlapped.

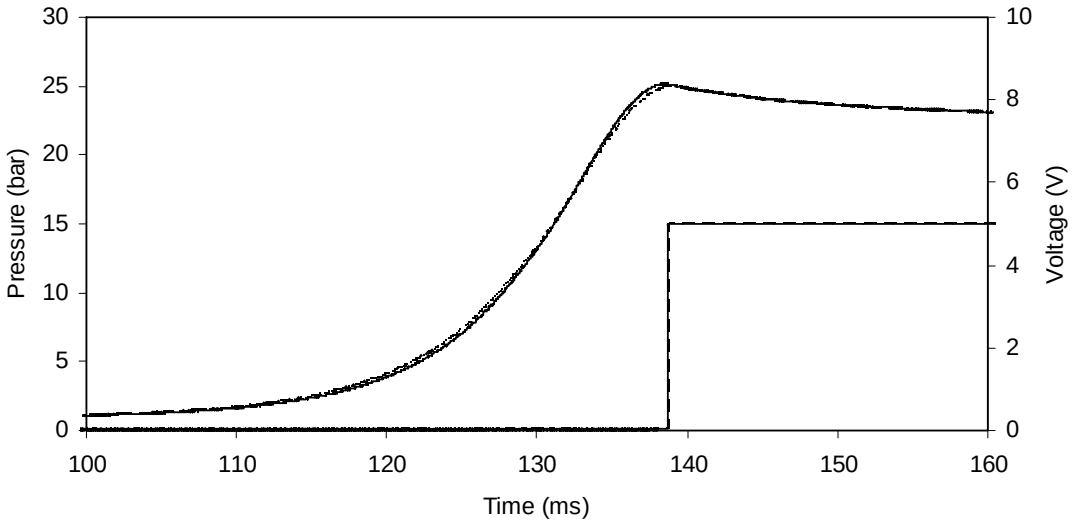

Figure 5.2 – Pressure signal after TDC synchronization for compression of updraft syngas-air mixture

This procedure was followed for every RCM experimental data.

5.1.1.2 Initial piston position

The initial piston position is only dependent of piston mechanical adjustment at the bottom dead center (BDC). The analysis of the initial position of the piston for the whole

single compression experiments performed enables to define a typical scattering on less than 4.0 mm (from -13 mm to -17 mm).

The TDC position has also some scattering but only of 1 mm (from 419 mm to 420 mm) which could be endorsed to some mechanical deformation imposed by elevated in-cylinder pressures. Considering a piston stroke of 419 mm, the overall uncertainty of the piston initial position is lower than 1.0%. This jitter on the initial position can be converted to time scale by considering the average piston speed of 9.5 m/s. This conversion gives a maximum value of 0.42 ms.

Considering that the volume inside the chamber is obtained from the piston position, the influence of this jitter on the piston position from one experiment to another is then analyzed in figure 5.3 for the case of updraft syngas without combustion in order to avoid the effect of the spark time scattering. The choice of the same fuel also avoids differences in the polytropic coefficient of the mixture being compressed.

In the case shown in the figure 5.3, the difference in the initial piston position is 1.75 mm. It is observed that there is no significant difference on the piston position along time.

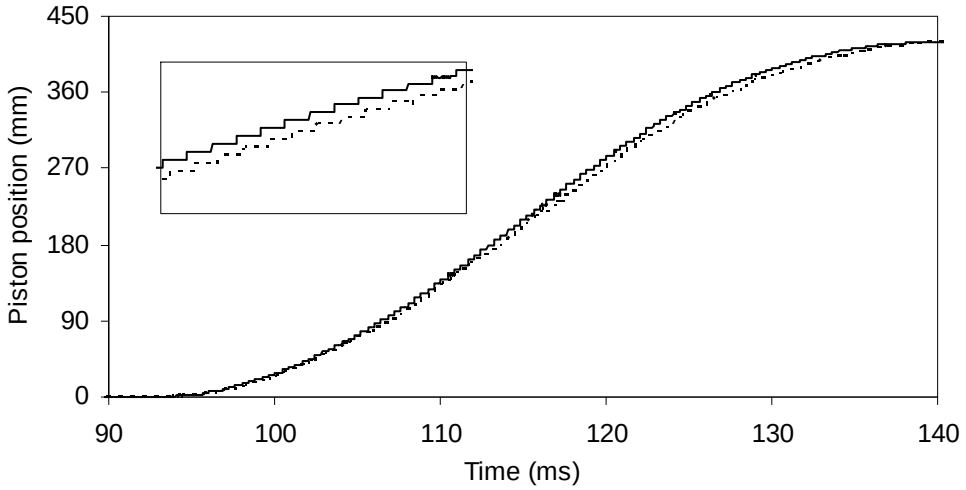

Figure 5.3- Piston displacement during single compression of updraft syngas-air.

From figure 5.3 it is also observed the evolution in a “stair” mode of the laser piston position signal. As the in-cylinder volume variation is obtained from this signal, therefore a peak detection filter was applied to this signal (figure 5.4).

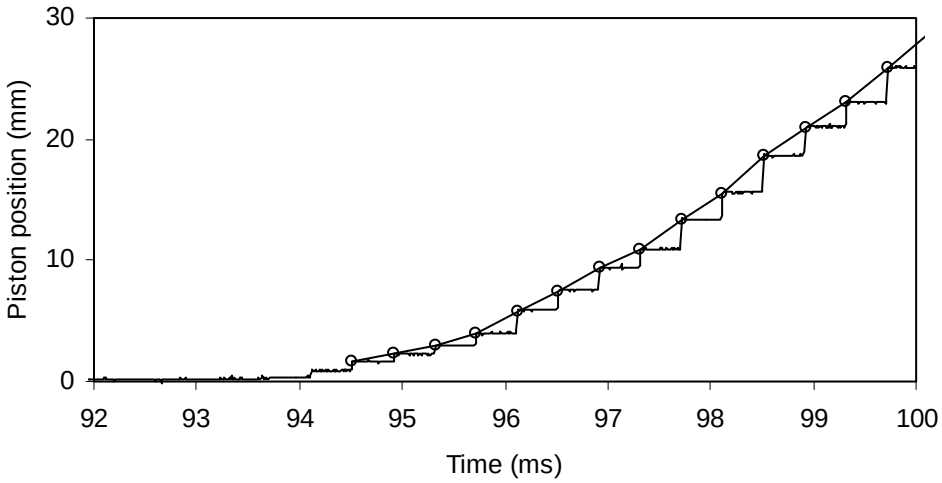

Figure 5.4 – Peak detection filter.

5.1.1.3 Spark time

Spark time is defined by the diagnostic system of the RCM in a time scale. Thus, this signal is independent of the piston displacement. In order to analyze the jitter of the spark time, figure 5.5 shows the three signals for the case of ignition at TDC and in addition the TDC position in a time scale.

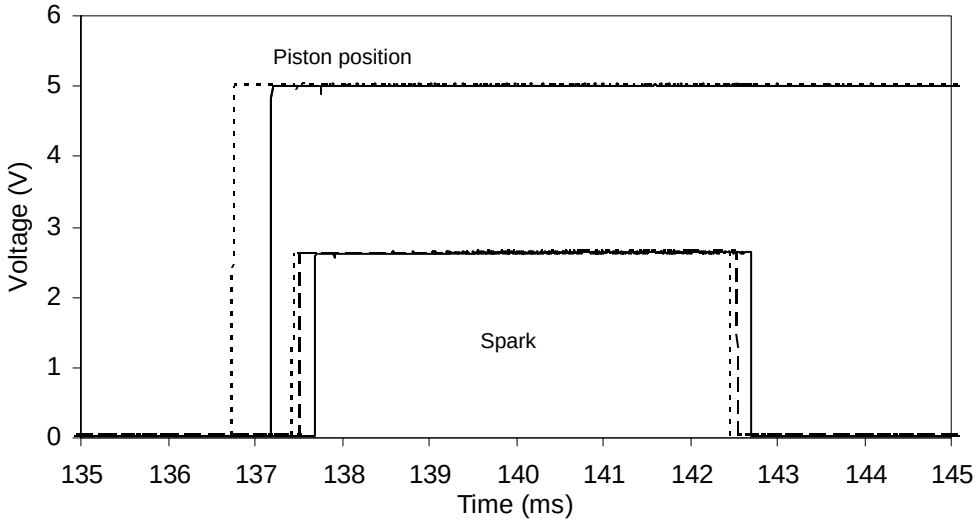

Figure 5.5 – Spark time at TDC and TDC position signals.

Analysing the figure 5.5 it is observed that the spark signal varies slightly (<0.5 ms) from experiment to experiment while keeping the duration of 5.0 ms. Comparing with the TDC position given by the laser position sensor at TDC it is observed that they are not synchronized. The maximum unsynchronized signals are out of phase 0.7 ms.

Let us now verify the influence of spark time jitter on the pressure signal. For this analysis two cases with similar scatter of spark time (0.84 ms and 0.87 ms, respectively) are presented for different ignition timings, 5.0 ms BTDC and 12.5 ms BTDC.

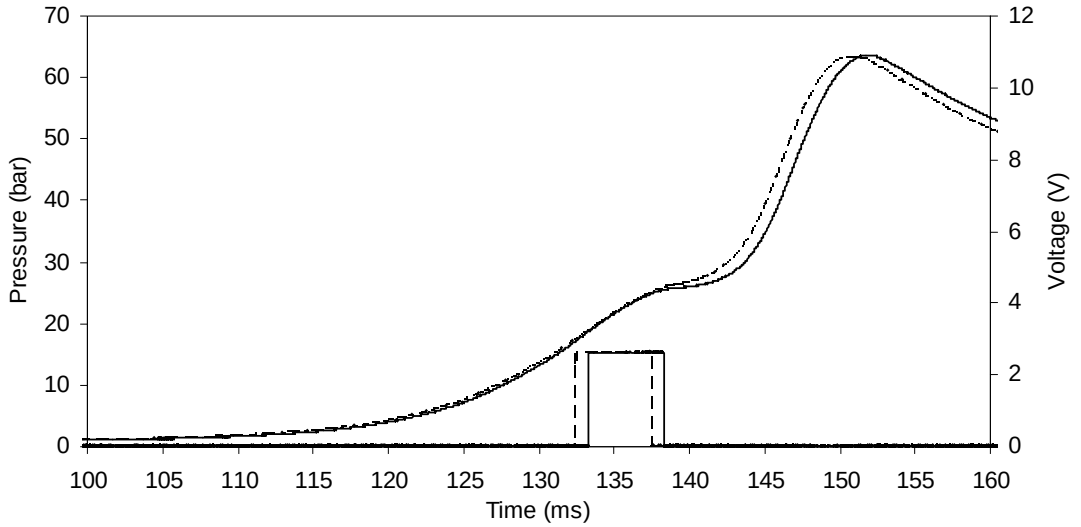

Figure 5.6 – Pressure and spark signals for updraft syngas: ignition at 5.0 ms BTDC.

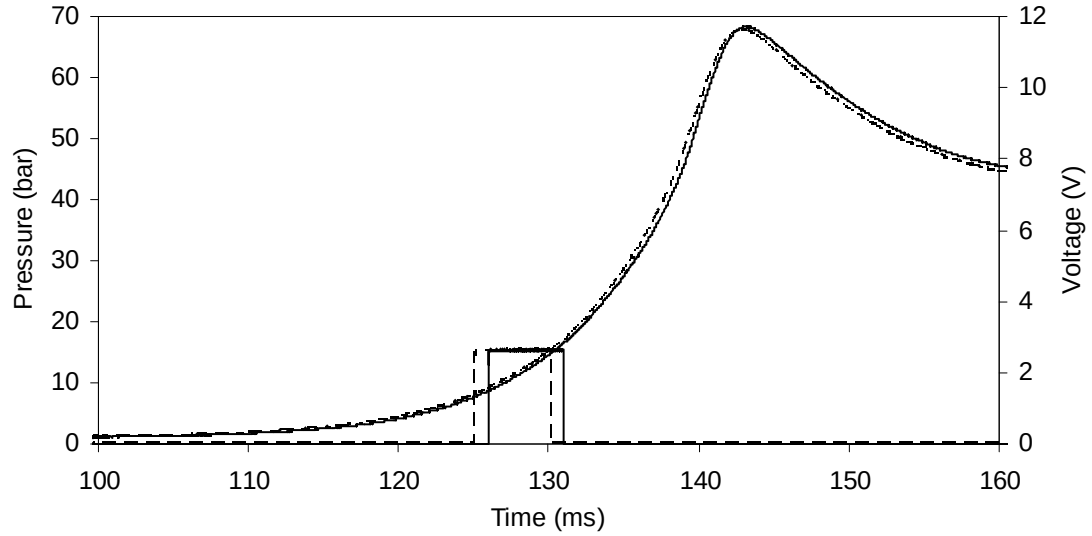

Figure 5.7 – Pressure and spark signals for downdraft syngas: ignition at 12.5 ms BTDC.

Analyzing figures 5.6 and 5.7 is observed that the effect of the spark time scatter has higher influence on in-cylinder pressure when the ignition is made close to TDC. This could also justify the fact of lower reproducibility of pressure signal for ignition timings close to TDC as shown in the next section.

5.1.1.4 In-cylinder pressure reproducibility

A set of three experiments was carried out for each syngas composition with various ignition timings in order to verify its repetition. The pressure traces are shown in figure 5.8 for downdraft syngas composition after TDC synchronization.

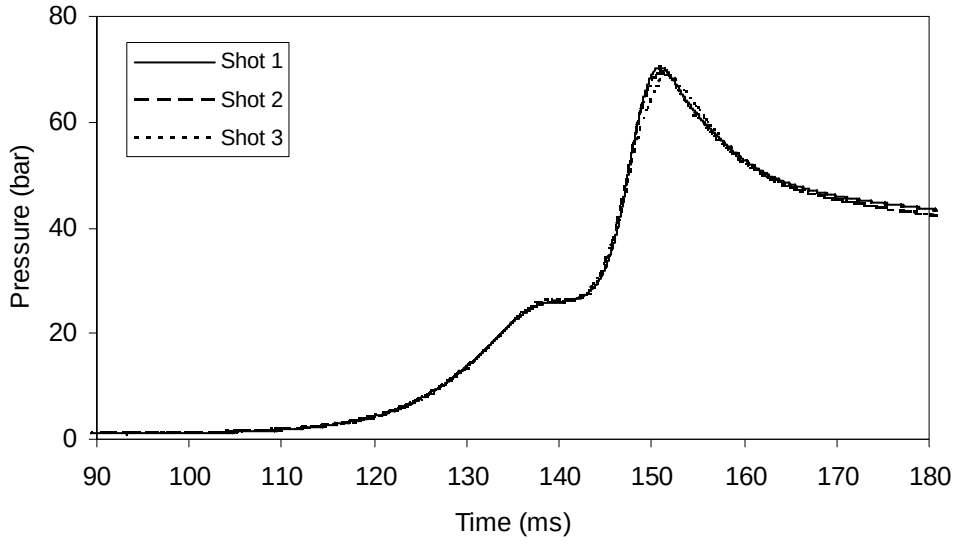

(a)

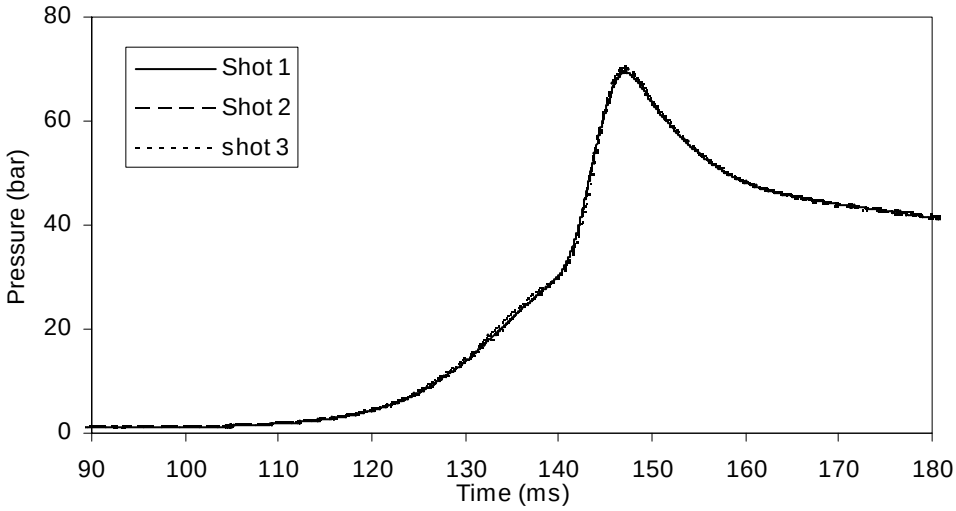

(b)

Figure 5.8a – Pressure signals for various ignition timings. (a) TDC. (b) 5 ms BTDC. (c) 7.5 ms BTDC.

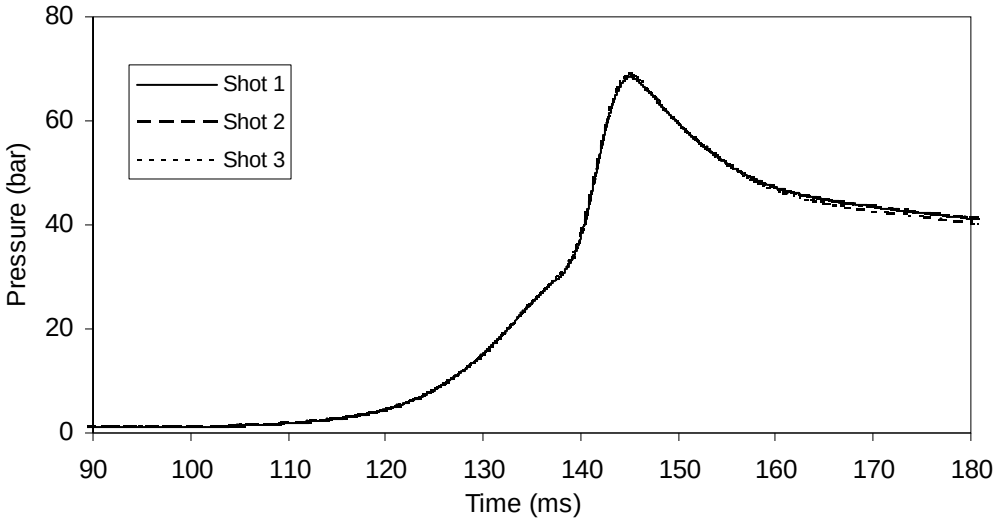

(c)

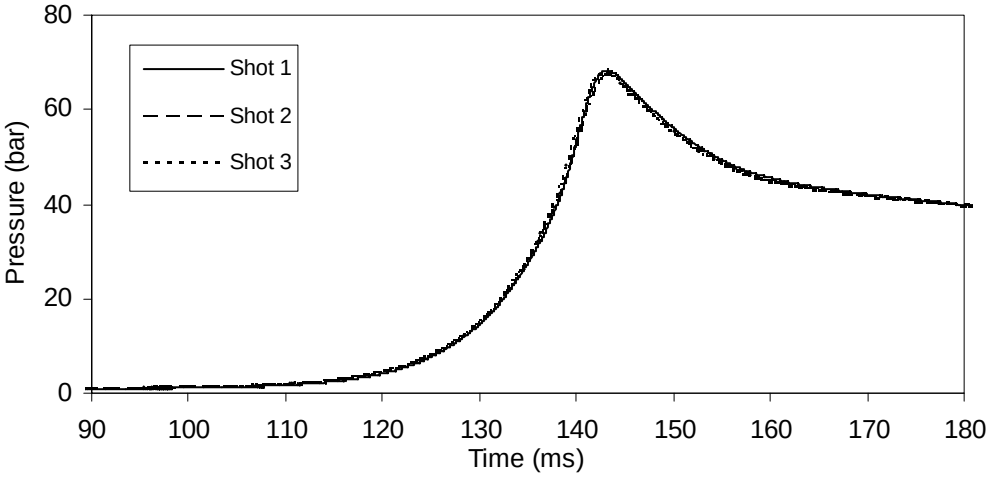

(d)

Figure 5.8 b – Pressure signals for various ignition timings. (c) 7.5 ms BTDC. (d) 12.5 ms BTDC.

Figure 5.8 shows the good reproducibility of the pressure signal for various ignition timings. The maximum difference between peak pressures is: 1.8 bar for ignition at TDC (70 bar on average, which represents an error of 2.5%); 0.8 bar for ignition timing at 5 ms BTDC (69.2 bar on average representing an error of 1.1%); 0.5 bar for ignition timing at 7.5 ms BTDC (68.8 bar on average, which represents an error of 0.7%);0.5 bar for ignition timing at 12.5 ms BTDC (68.4 bar on average representing an error of 0.7%).

5.1.1.5 Conclusion

The quality of the RCM experimental measurements was evaluated on this section throughout a sensibility analysis of errors in measurement techniques and in the

estimation of various parameters on the main experimental results: in-cylinder pressure and volume. This analysis shows the high precision of the Institute Pprime RCM for every measured parameter, which ensures about the quality of the results that will be shown in the following sections.

5.1.2 In-cylinder pressure

Figures 5.9-5.10 show RCM experimental pressure histories of stoichiometric syngas-air mixtures for various spark times and compression ratio ε=11. Four ignition timings were tested: TDC, 5.0, 7.5 and 12.5 ms before TDC, respectively.

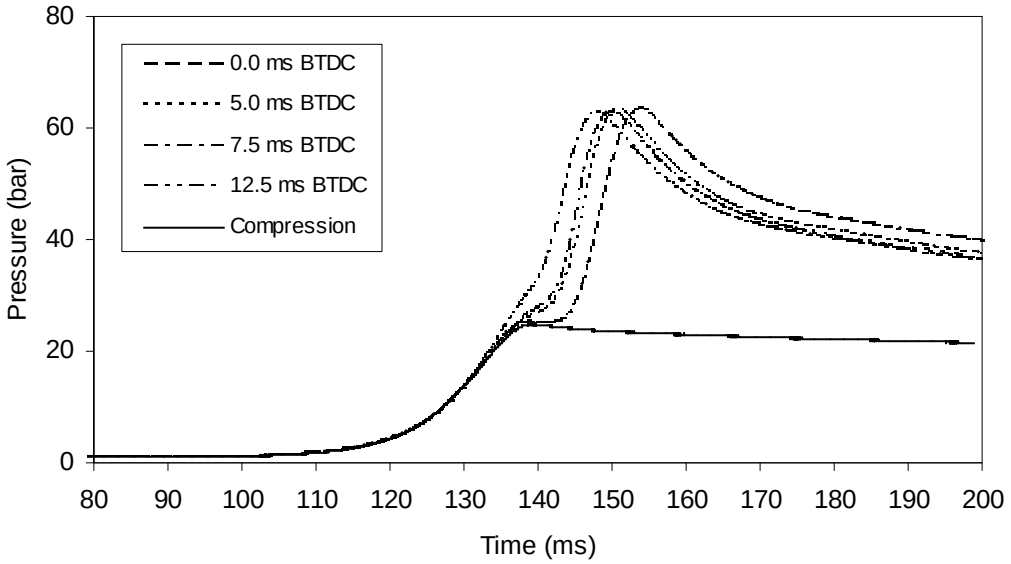

Figure 5.9 – Pressure versus time for stoichiometric updraft syngas-air mixture at various spark times.

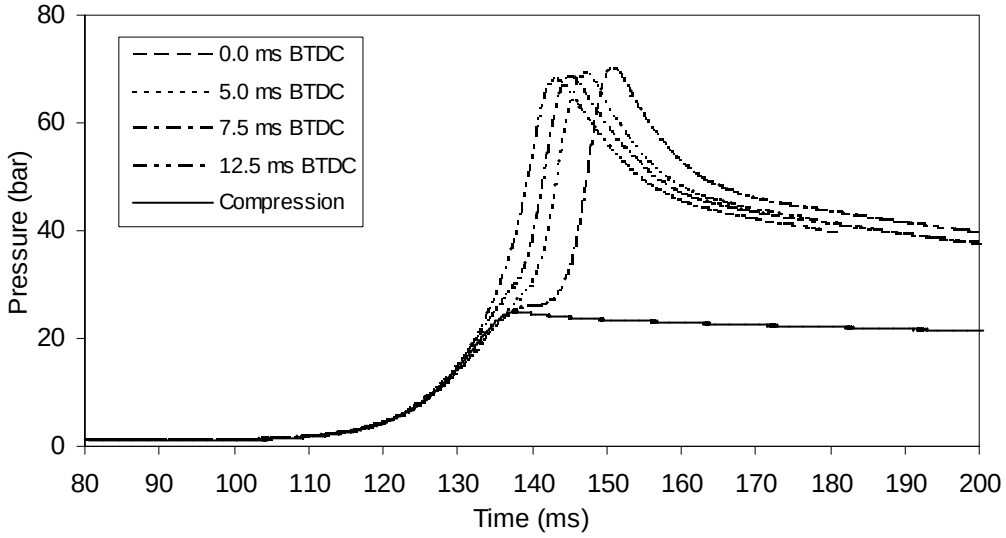

Figure 5.10– Pressure versus time for stoichiometric downdraft syngas-air mixture at various spark times.

In both syngas cases, peak pressure decreases as the ignition time increases. When ignition is made at TDC, combustion occurs at constant volume, in the clearance volume. In this case, one has higher initial pressure and temperature and no influence of the flow of the fresh mixture being compressed by the piston movement. This reduces turbulence and, in turns, the heat transfer. As far as ignition timing is concerned, the deviation from TDC allows lower initial pressure and temperature for combustion in the compression stroke. It is also observed a reduction in the pressure gradient after TDC, which means that the heat released by combustion of syngas-air mixtures is not high enough to keep the same pressure gradient.

As mentioned above stoichiometric methane-air mixture was also used for comparison reasons and the results are shown in figure 5.11.

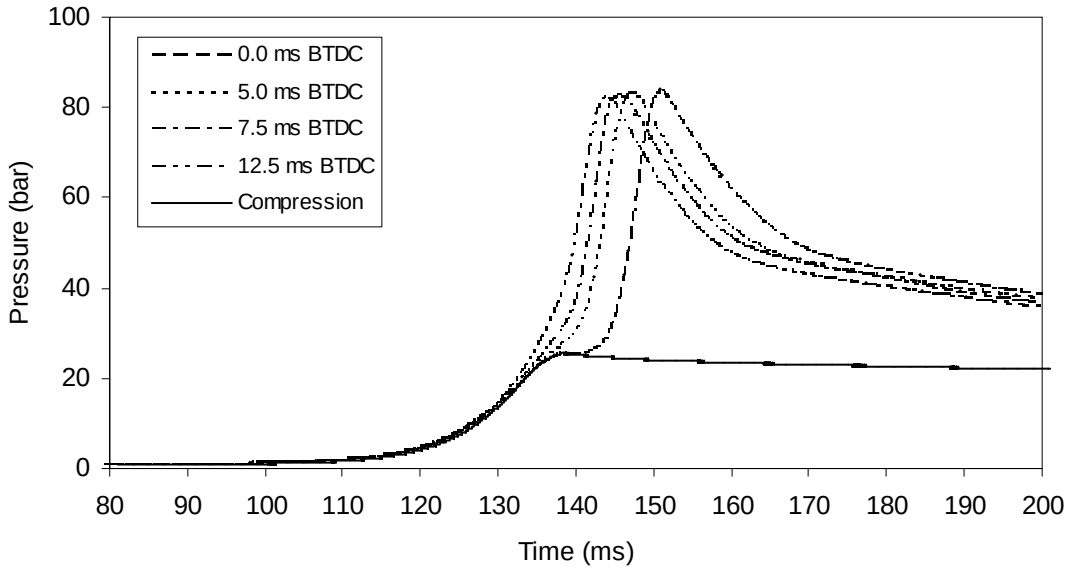

Figure 5.11– Pressure versus time for stoichiometric methane-air mixture at various spark times.

This mixture follows the same behaviour of the typical syngas compositions, nevertheless with higher pressures. For these results contributes the higher heat value of methane, meanwhile counter-balanced by the higher air to fuel ratio.

5.1.3 In-cylinder flame propagation

Direct visualizations of the flame propagation in a RCM are shown in the figure 5.12 for updraft syngas and for two distinctive ignition times, TDC and 12.5 ms BTDC, to clearly set the difference.

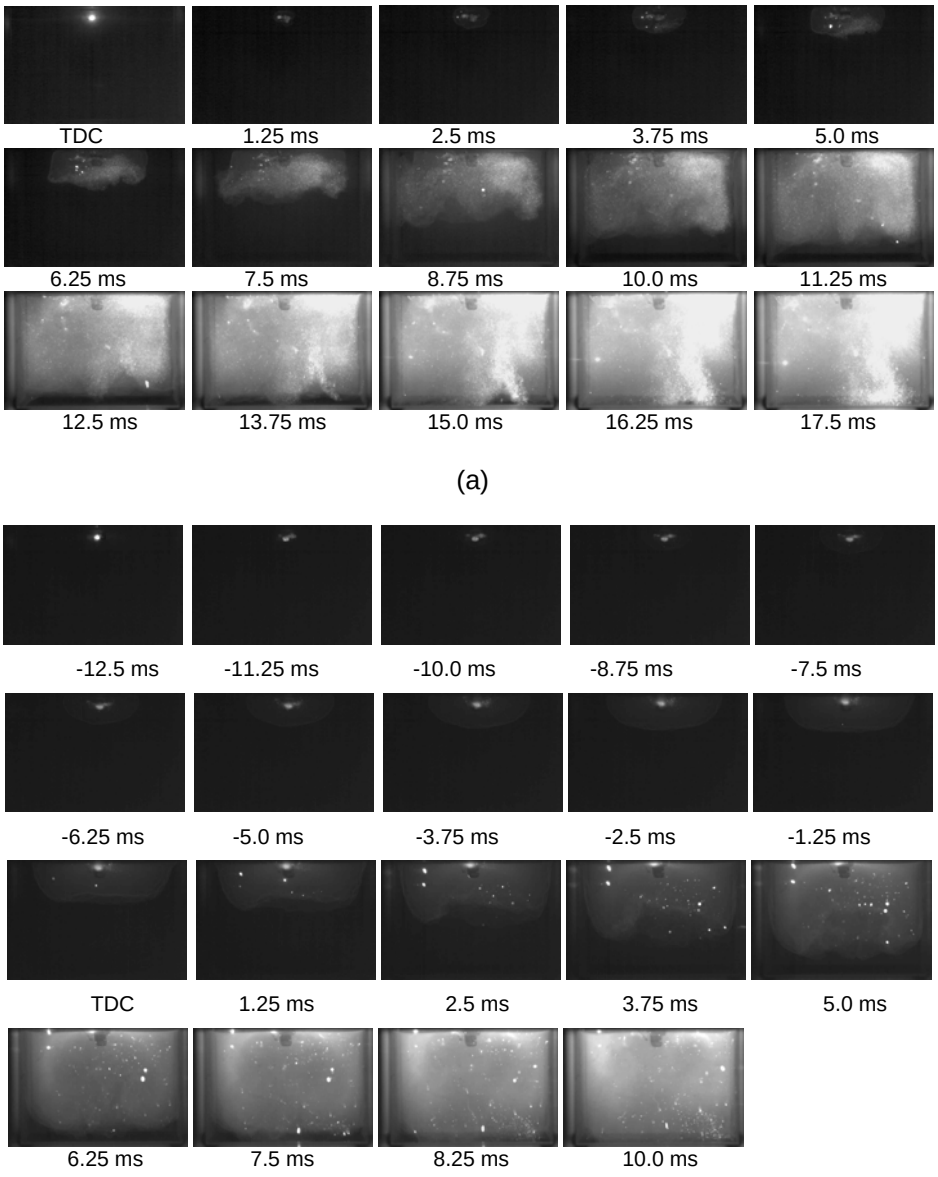

Figure 5.12 –Direct visualization of stoichiometric updraft syngas-air mixtures combustion in a RCM. (a) Ignition at TDC; (b) ignition at 12.5 ms BTDC.

When the ignition is made at TDC the combustion occurs at constant volume, in the clearance volume. Direct visualizations show an explosion with fast and turbulent flame propagation with combustion duration of about 17.5 ms. In opposite, the initial phase of combustion shows a quasi-spherical relatively smooth flame kernel specially for ignition timing of 12.5 ms BTDC. The flame kernel propagation is laminar and at some point experience flattening due to piston movement reaching the TDC. After that, a change to constant volume combustion occurs. The whole combustion duration is around 22.5 ms, a remarkable increase compared with the full constant volume combustion. This is due to the deviation from TDC ignition that allows lower initial pressure and temperature for combustion in the compression stroke, lower turbulence intensity as seen in 3.2.5 and higher heat transfer areas.

5.2 RCM Compression-expansion

Engine-like conditions can be reproduced in a RCM when working on two strokes mode simulating a single cycle of an internal combustion engine. Together with in-cylinder pressure measurements, direct visualizations are also carried out to follow the early stage of the ignition process.

Stationary power applications usually use natural gas as fuel, thus a methane-air mixture, the main constituent of the natural gas, is also included in this work as a reference fuel for comparison with the typical syngas compositions under study.

5.2.1 Sensibility analysis

In this section a sensibility analysis is made with the objective of evaluating the influence of the fuel in the estimation of various parameters such as equivalent rotation speed and ignition timing.

5.2.1.1 Piston position

The compression stroke is imposed by the RCM hydraulic system. Thus, it is not expected to be influenced by the ignition timing and fuel type. The same is not true for the expansion stroke that is expected to be a function of the heat release of the mixture being burned.

In order to evaluate the influence of the ignition timing and fuel type on piston displacement, the average the piston position signal is plotted against time in figure 5.13 for stoichiometric updraft syngas-air mixture and for various ignition timings. The same is shown in figure 5.14 for the three fuels under study at the same ignition timing of 12.5 ms BTDC.

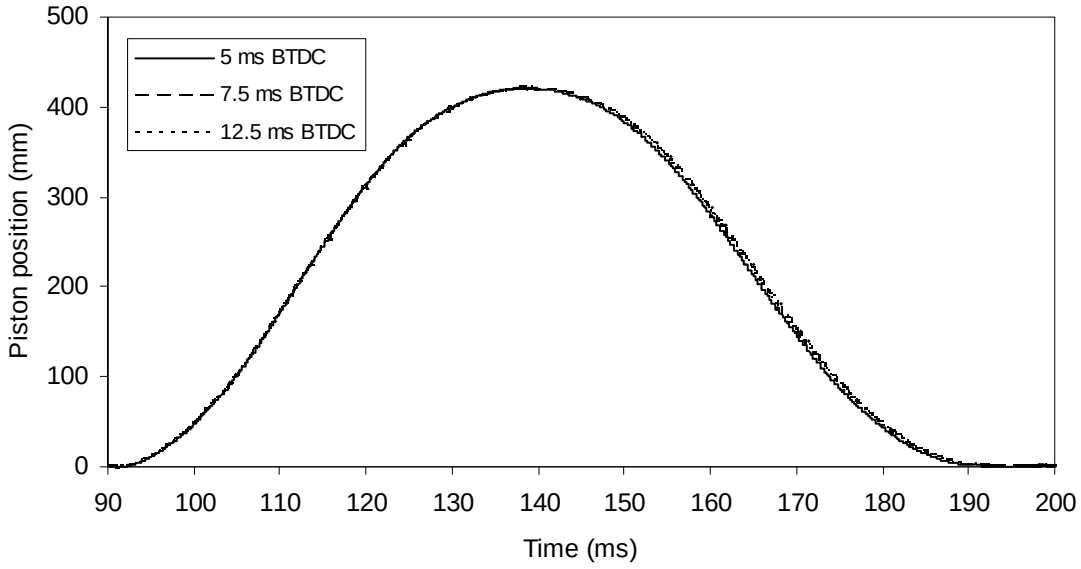

(a)

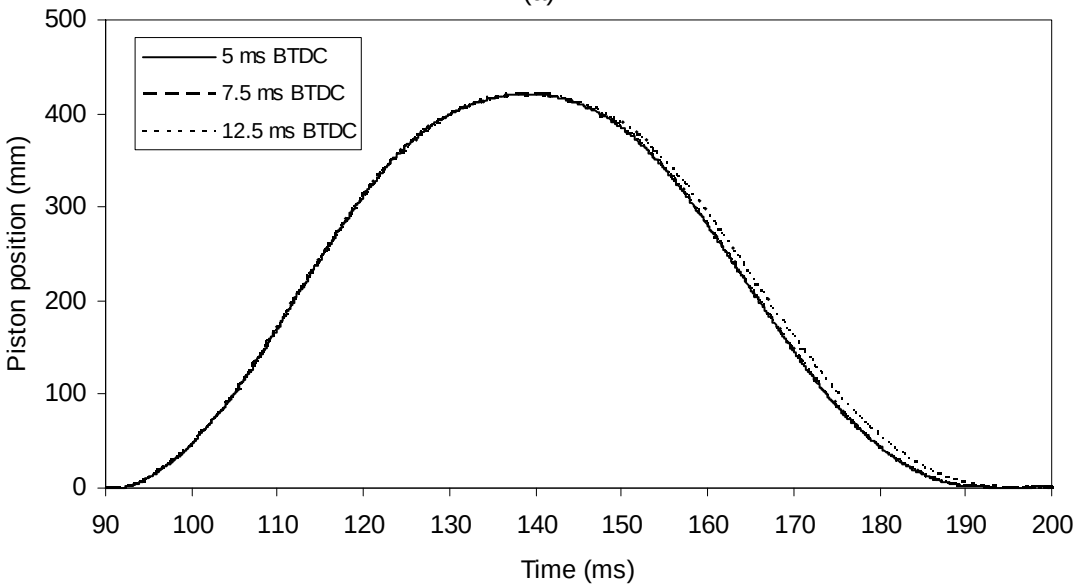

(b)

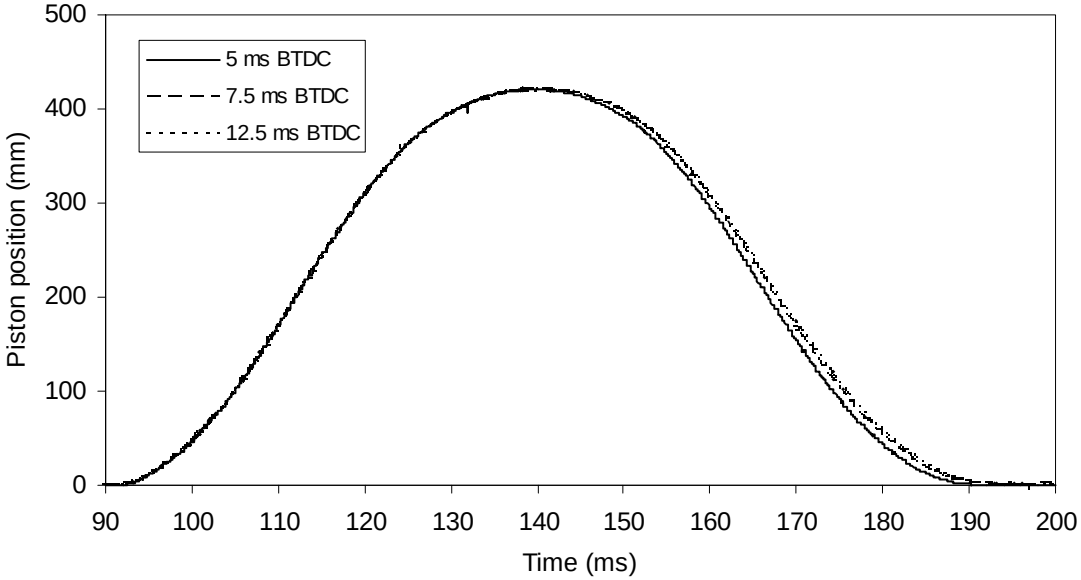

Figure 5.13- Piston position for various fuels and ignition timings. (a) updraft, (b) downdraft, (c) methane.

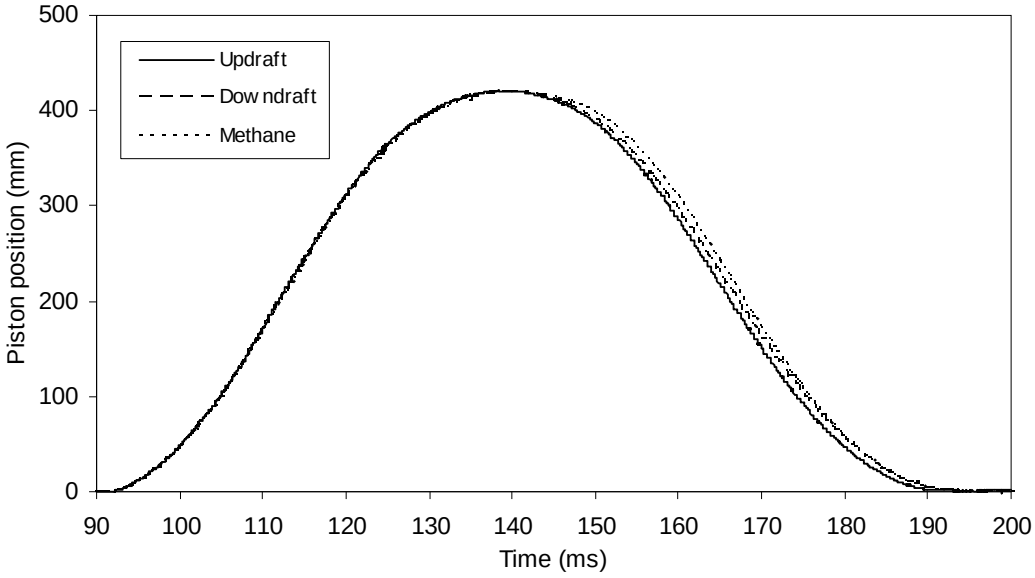

(a)

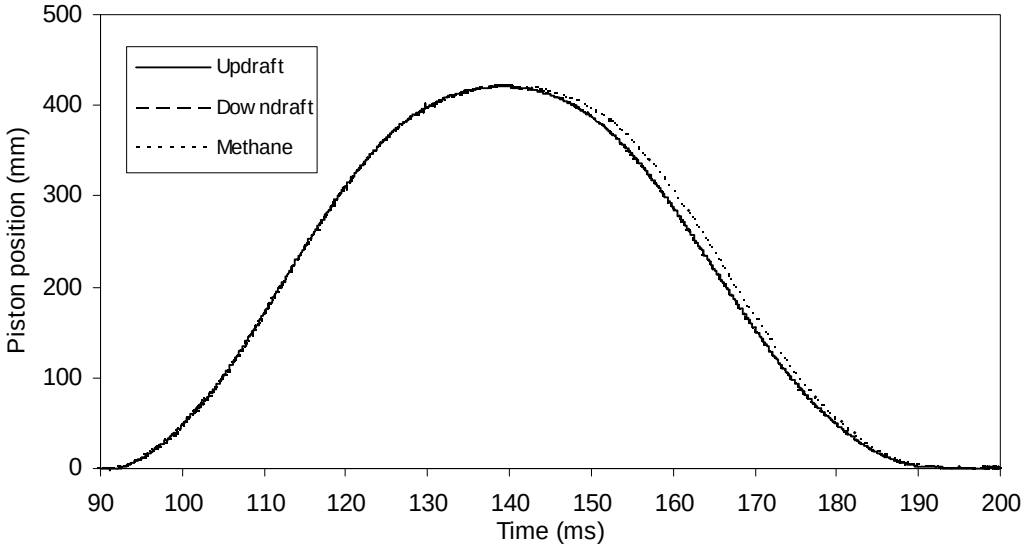

(b)

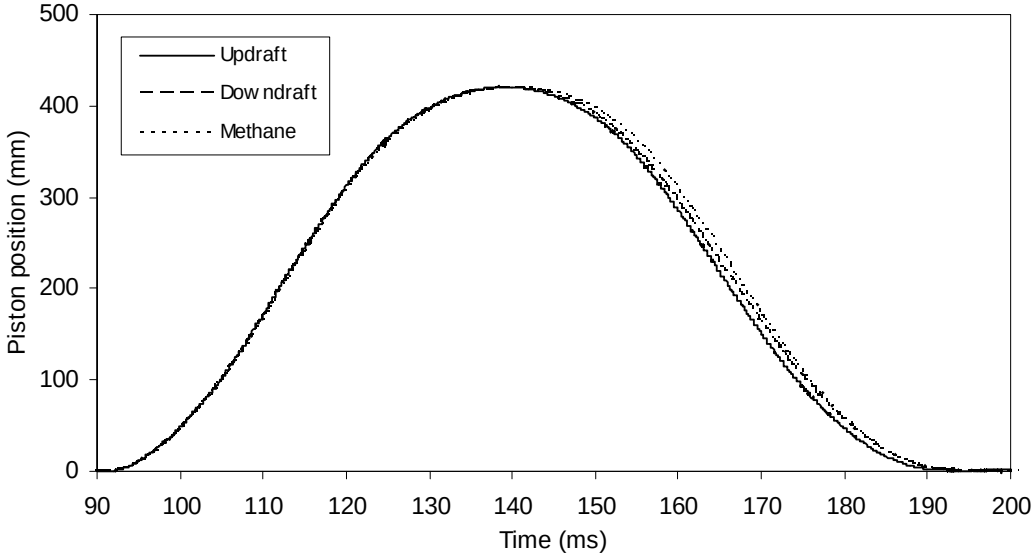

(c)

Figure 5.14-Piston position for various fuels and ignition timings. (a) 5 ms BTDC; (b) 7.5 ms BTDC; (c) 12.5 ms BTDC.

From figure 5.13 it is observed that the compression stroke is independent of the ignition timing. The TDC position is reached at 137 ms and is kept during around 4 ms to 141 ms. The measured compression stroke duration is about 44 ms. Expansion stroke is indeed slightly influenced by the ignition timing, which become slower when the ignition is made far from TDC. However, as seen in the figure 5.13 the ignition timings of 5 ms BTDC and 7.5 ms BTDC could be considered to have the same piston displacement along time. The 12.5 ms BTDC ignition timing is the one with lower displacement for every fuel under study. Therefore, considering a criterion of 1.0 mm for the final piston position the duration of the expansion stroke is around 49 ms for ignition timing of 5 ms and 7.5 ms BTDC and 51 ms for 12.5 ms BTDC ignition timing. This could be explained by the fact that when the combustion starts to earlier in relation to TDC (12.5 ms BTDC) a large part of heat is released when the piston is still moving up. Therefore, when the ignition is made close to TDC the heat released is available on the expansion stroke to push the piston down. Thus, it is expected that some influence of the fuel type on the expansion stroke exists (figure 5.14).

From figure 5.14 it is observed that both syngas compositions show similar time evolution of the piston position. However, methane shows a different time evolution of the piston position in the expansion stroke to the whole igniting timings. This is explained by the combustion time of the mixtures that are lower for methane, followed by the downdraft and finally by updraft. Thus, the heat released is not so much available on the expansion stroke for methane as it is for updraft syngas. This also indicates that the turbulent burning velocity of methane should be higher than the syngas compositions ones.

5.2.1.2 Equivalent rotation speed

The compression stroke is imposed by the RCM hydraulic system; the expansion stroke is a function of the heat release of the mixture being burned. Thus, the equivalent rotation speed is not constant and its variation should be evaluated taking into account the fuel and the ignition timing.

Figure 5.15 shows the average of the piston velocity during various experiments without combustion and different spark times and after TDC synchronization.

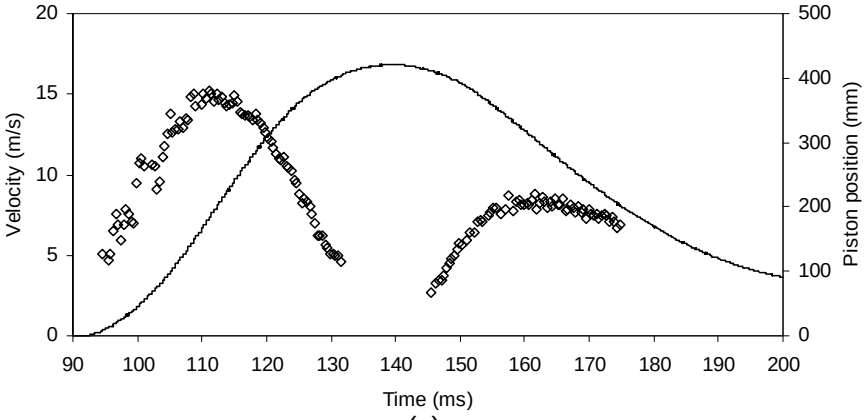

(a)

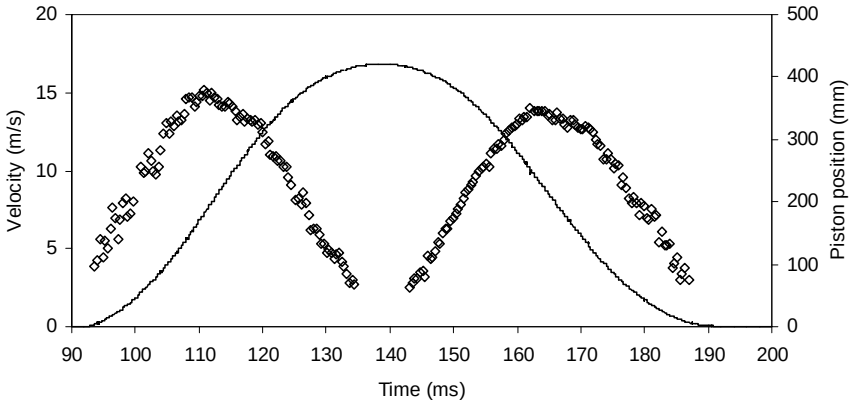

(b)

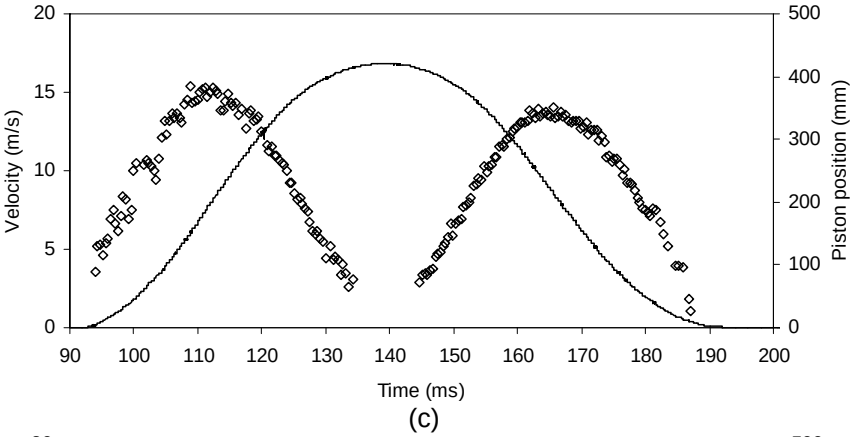

(c)

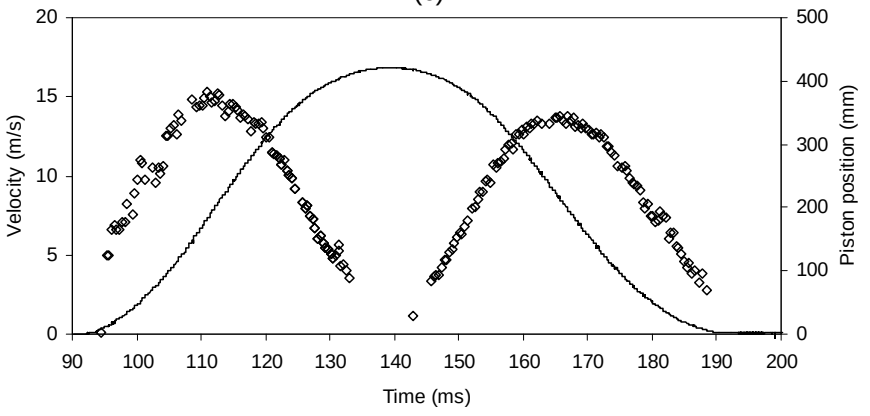

(d)

Figure 5.15 - Piston velocity: (a) Without combustion. (b) 5 ms BTDC. (c) 7.5 ms BTDC. (d) 12.5 ms BTDC

From figure 5.15 is possible to conclude that the piston velocity is higher on the compression stroke than on the expansion stroke for every case. The maximum velocity on the compression stroke is around 15 m/s decreasing to around 14 m/s on the expansion stroke. The piston speed of the movement is constantly changing in the cylinder. Relatively great in the middle of the stroke, some nearby the dead centre speed is relatively small and it is zero in the dead centre. On the compression stroke the maximum velocity occurs around 110 ms and is not influenced by combustion because ignition is made after that instant for the whole cases. On the expansion stroke the maximum speed occurs at around 162 ms for ignition timing of 5.0 ms BTDC, around 165 ms for 7.5 ms BTDC and 166 ms for 12.5 ms BTDC. An equivalent rotation speed could be defined by the following expression:

$$\Delta\theta = 6N\Delta t \tag{5.1}$$

Where θ is the crank angle in degrees, N the rotation speed and t the time. Taking into account that each stroke represents 180 crank angle degrees, the mean equivalent rotation speed for the compression stroke is 682 rpm. Considering the differences verified on the piston displacement on the expansion stroke for the different fuels and ignition timings, the mean equivalent rotation speed is also slightly changed. Considering a criterion of 1.0 mm for the final piston position, we have an equivalent rotation speed for the expansion stroke of 612 rpm for ignition timing of 5 ms BTDC and 588 rpm for other ignitions timings for updraft syngas.

5.2.1.3 In-cylinder pressure repeatability

A set of three experiments was made for each syngas composition with various ignition timings in order to verify its repetition. The pressure traces are shown in figure 5.16 for updraft syngas after TDC synchronization.

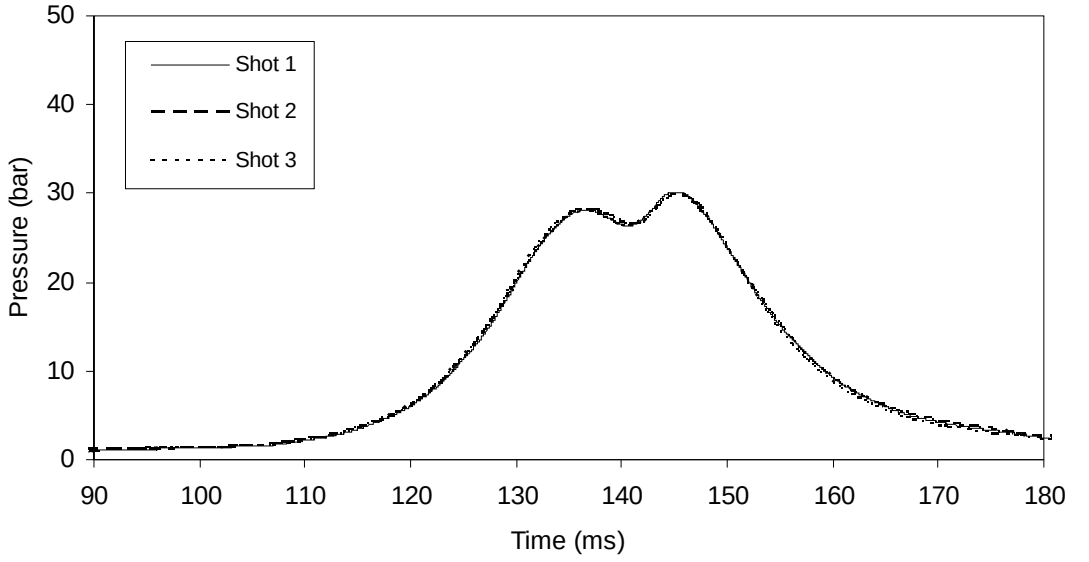

(a)

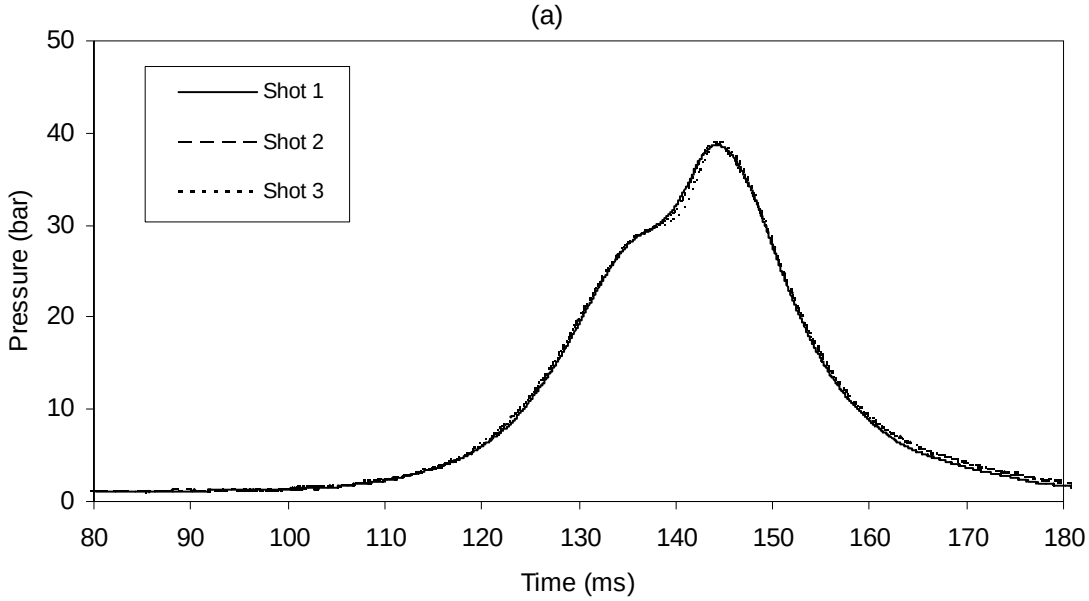

(b)

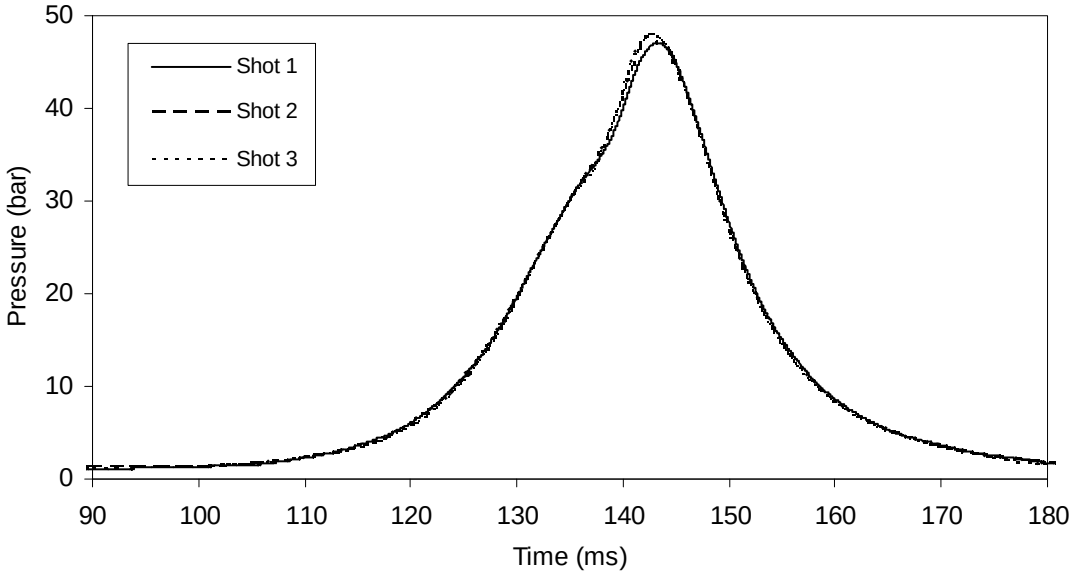

(c)

Figure 5.16 – In-cylinder pressure reproducibility: updraft-syngas. (a) 5 ms BTDC; (b) 7.5 ms BTDC; (c) 12.5 ms BTDC

From figure 5.16 is observed a good reproducibility of the pressure signal for the various ignition timings. The maximum difference between peak pressures is: 0.2 bar for ignition timing at 5 ms BTDC (30 bar on average representing an error of 0.7%); 0.1 bar for ignition timing at 7.5 ms BTDC (38 bar on average, which represents an error of 0.03%); 0.8 bar for ignition timing at 12.5 ms BTDC (47.5 bar on average representing an error of 1.7%).

5.2.1.4 Conclusion

The quality of the RCM experimental measurements was evaluated on this section throughout a sensibility analysis of errors in measurements techniques or in the estimation of various parameters on the main experimental results: in-cylinder pressure and piston displacement. This analysis shows high precision of the Institute Pprime RCM for every measured parameter also on the two strokes mode, which ensures about the quality of the results that will be shown in the following sections.

5.2.2 In-cylinder pressure

Ignition timing of typical stoichiometric syngas-air mixtures are determined in the RCM described in 3.1.4. Together with pressure measurements, direct visualizations from chemiluminescence emission are also carried out to follow the early stage of the ignition process.

Figures 5.17-5.19 show RCM experimental pressure histories of stoichiometric syngas-air mixtures and methane-air for various spark times and compression ratio ε=11. The ignition timings tested were 5.0 ms, 7.5 ms and 12.5 ms BTDC.

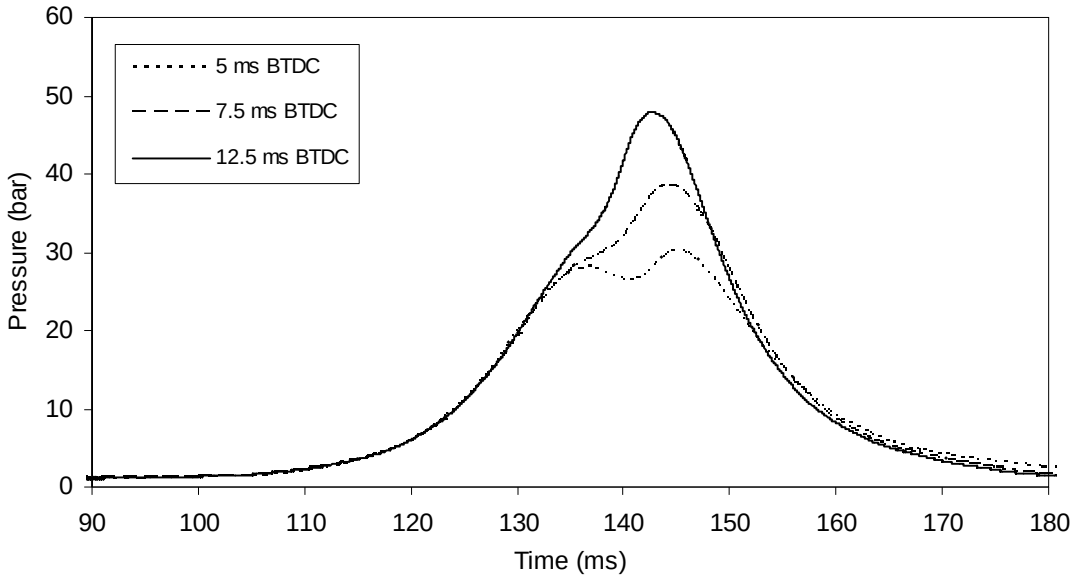

Figure 5.17 – Pressure versus time for stoichiometric updraft syngas-air mixture at various spark times.

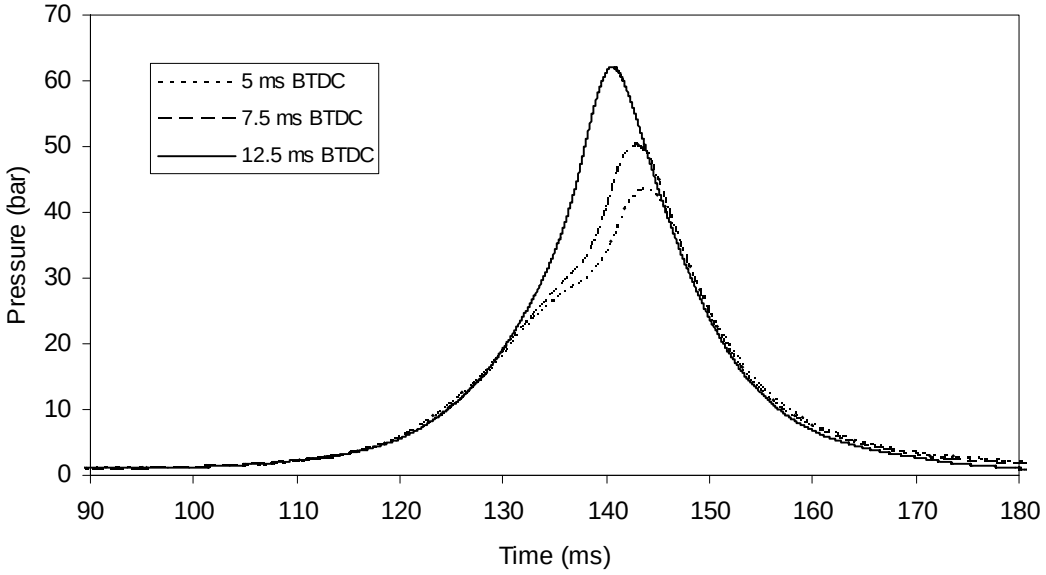

Figure 5.18– Pressure versus time for stoichiometric downdraft syngas-air mixture at various spark times.

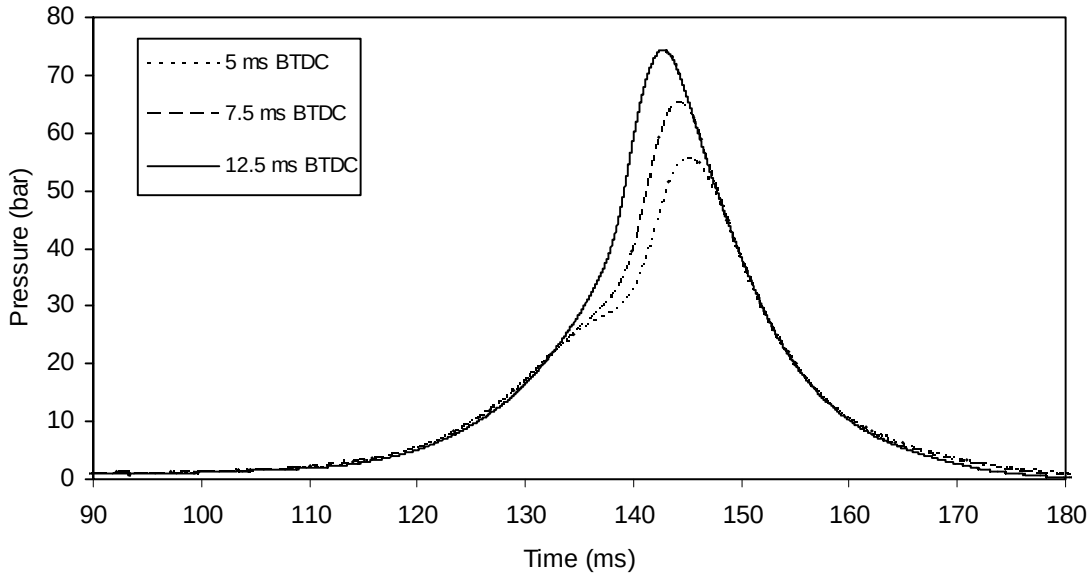

Figure 5.19– Pressure versus time for stoichiometric methane-air mixture at various spark times.

From figures 5.17-5.19 it is observed that the in-cylinder pressure increases as the spark time deviates from TDC. If combustion starts too early in the cycle, the work transfer from the piston to the gases in the cylinder at the end of the compression stroke is too large. If the combustion starts too late, the peak cylinder pressure is reduced, and the stroke work transfer from the gas to the piston decreases.

Another observation that is brought out from these figures is that higher pressures are obtained with methane-air mixture followed by downdraft syngas-air mixture and lastly by updraft syngas-air mixture. These results could be endorsed to the energy introduced into the RCM chamber, which can be determined by the heating value of the fuels and the air to fuel ratio. Taking into account that the RCM chamber has 1.0 Litre, the energy introduced in to the chamber is 2.60 KJ in the updraft case, 2.85 KJ in the downdraft case and 3.38 KJ in the methane case for stoichiometric conditions. These values are in agreement with the obtained cylinder pressures, however not proportional in terms of peak pressures due to the influence of heat losses. These are mainly dependent of the quenching distance as well as thermal conductivity of the mixture. The higher burning velocity of methane compared to syngas compositions also cause a more intensified convection.

Making a parallel with the laminar combustion case where the performances of updraft and downdraft syngas are similar, one can observe that the same behaviour is not found in turbulent conditions. On turbulent conditions peak pressures higher in about

25% higher are obtained with the downdraft syngas. As the turbulent burning velocity could be considered proportional to the laminar one (Verhelst and Sierens, 2007), this result could be endorsed to:

- the effect of pressure on the laminar burning velocity. The correlations of laminar burning velocity of the typical syngas compositions developed on 4.1.2.3 show that the effect of pressure is very significant (coefficient β for updraft is 40% higher when compared to downdraft syngas β coefficient). For example, at the same temperature an increase in pressure from 1.0 to 20.0 bar results in an increasing difference on burning velocity from 12% to 35%.
- The higher pressure used on RCM also implies temperature to increase due to compression but the effect of temperature on burning velocity of syngas typical compositions is irrelevant since the coefficient α is of the same order (see 4.1.2.3).

5.2.3 Ignition timing

Timing advance is required because it takes time to burn the air-fuel mixture. Igniting the mixture before the piston reaches TDC will allow the mixture to fully burn soon after the piston reaches TDC. If the air-fuel mixture is ignited at the correct instant, maximum pressure in the cylinder will occur sometime after the piston reaches TDC allowing the ignited mixture to push the piston down the cylinder. Ideally, the time at which the mixture should be fully burned is about 20º ATDC (Hartman, 2004). This will utilize the engine power producing potential. If the ignition spark occurs at a position that is too advanced relatively to piston position, the rapidly expanding air-fuel mixture can actually push against the piston still moving up, causing detonation and lost power. If the spark occurs too retarded relatively to the piston position, maximum cylinder pressure will occur after the piston has already traveled too far down the cylinder. This results in lost power, high emissions, and unburned fuel. For further analysis of these experimental results, figure 5.20 synthesizes the peak pressure P_{max}, and the position of peak pressure θ_{max} expressed in milliseconds ATDC for the variable ignition timing in milliseconds BTDC.

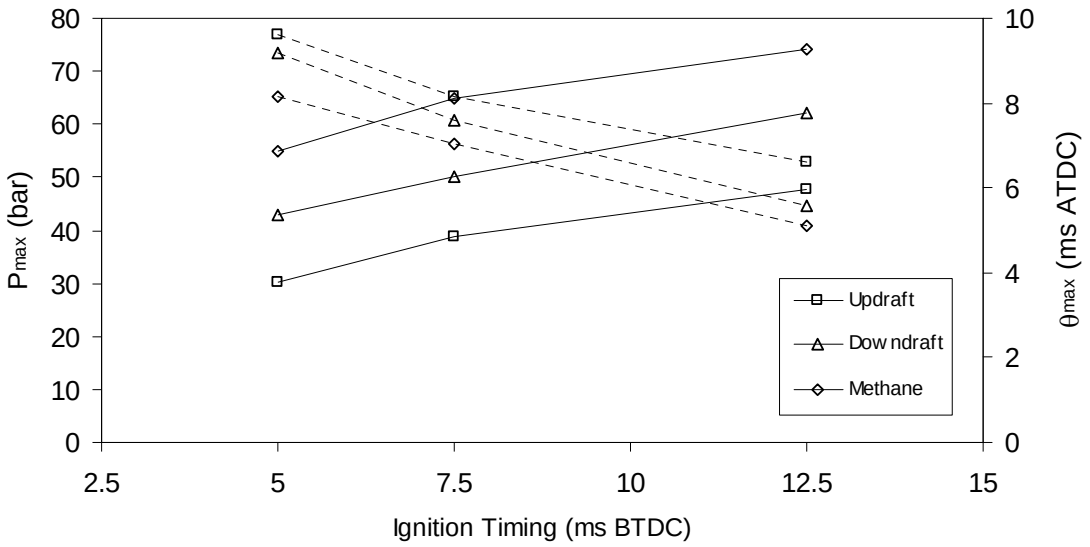

Figure 5.20 – Peak pressure (continuous lines) and peak pressure position (dashed lines) versus ignition timing for stoichiometric syngas-air and methane-air mixtures.

From figure 5.20 it is clear that the in-cylinder pressure increases as the ignition timing is retarded. The peak pressure occurs later as the ignition timing decreases. In opposite to the static chamber combustion, the peak pressure does not represent the end of combustion. However, it is possible to conclude that the peak pressure occurs always after TDC.

5.2.4 In-cylinder flame propagation

Burning of a mixture in a cylinder of a SI engine may be divided into the following phases: (1) spark ignition, (2) laminar flame kernel growth and transition to turbulent combustion, (3) turbulent flame development and propagation, (4) near-wall combustion and after burning. Figures 5.21-5.23 show flame propagation images of stoichiometric syngas-air mixtures combustion and stoichiometric methane-air mixtures in a RCM, where it is possible to observe these first three phases of combustion.

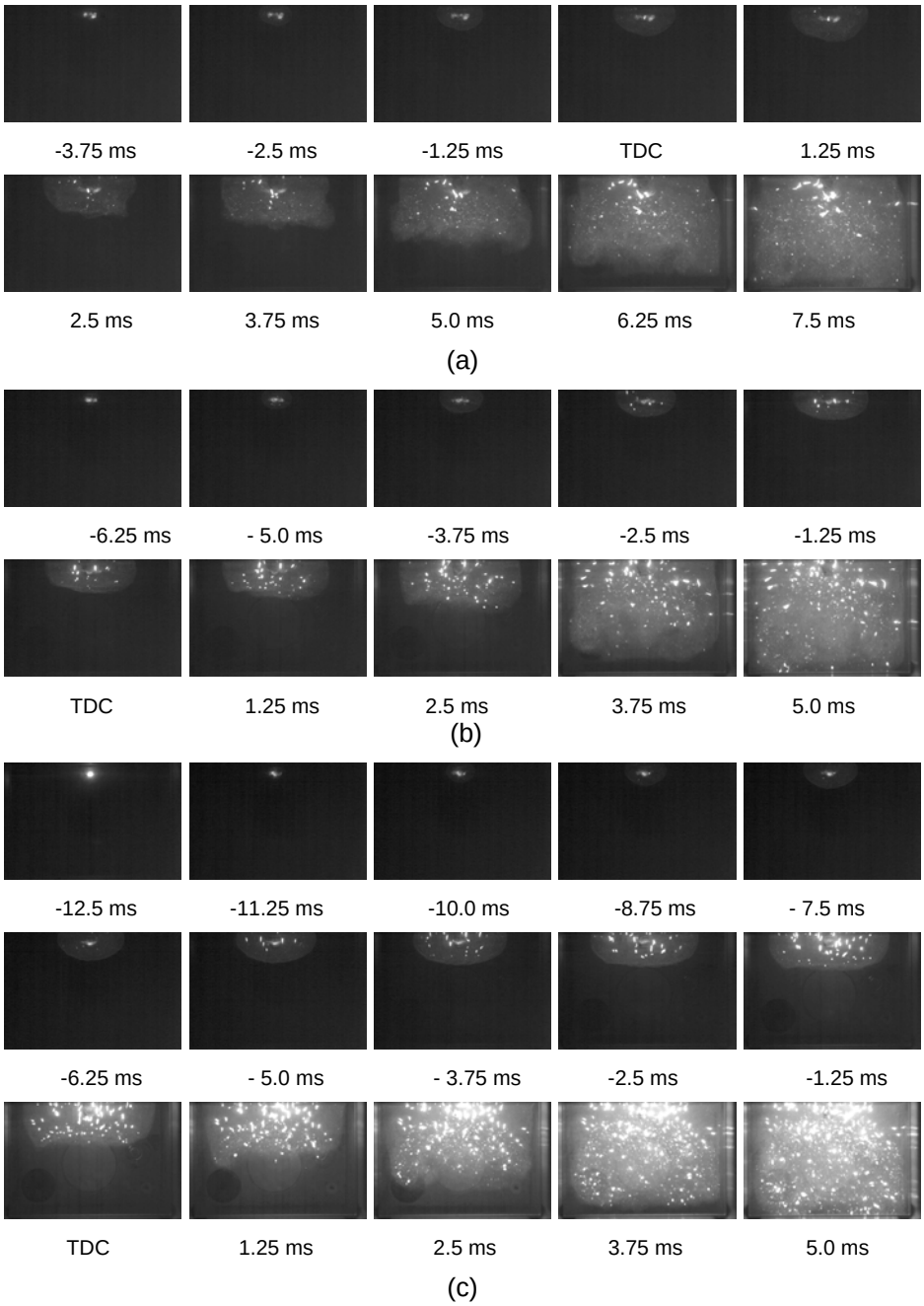

Figure 5.21 – Direct visualization of stoichiometric updraft syngas-air flame in a RCM for various Ignition timings. (a) 5 ms BTDC; (b) 7.5 ms BTDC; (c) 12.5 ms BTDC.

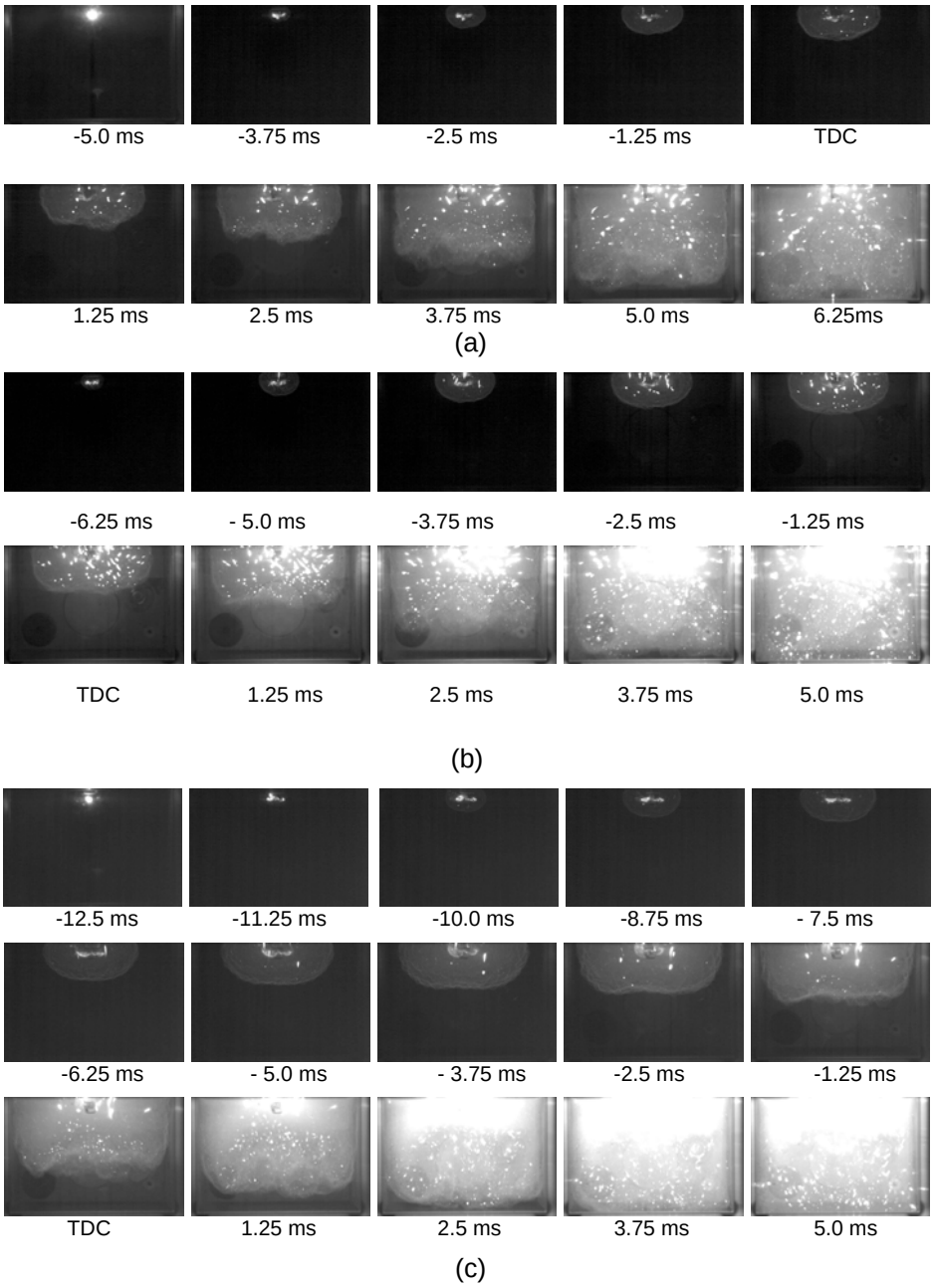

Figure 5. 22 – Direct visualization of stoichiometric downdraft syngas-air flame in a RCM for various Ignition timings. (a) 5 ms BTDC; (b) 7.5 ms BTDC; (c) 12.5 ms BTDC.

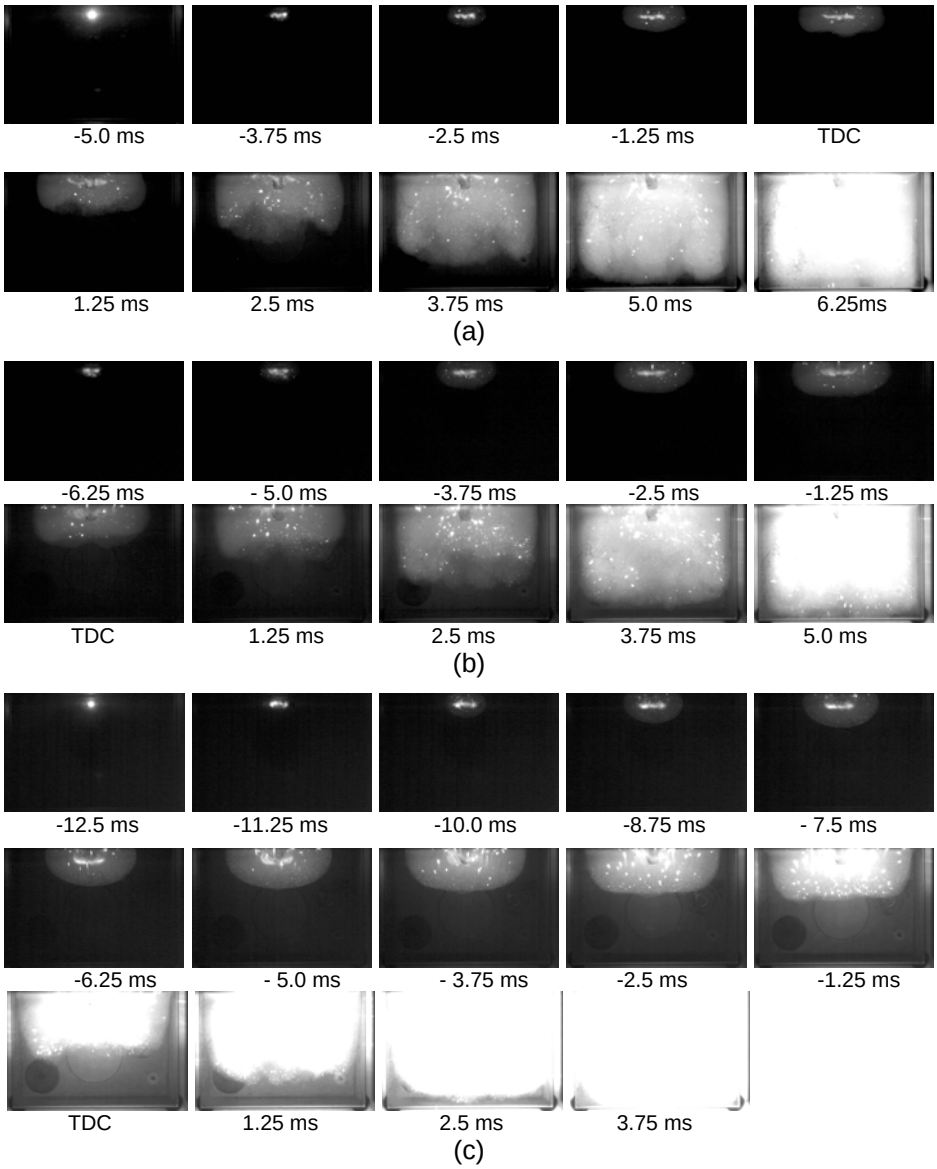

Figure 5.23- Direct visualization of stoichiometric methane-air flame in a RCM for various Ignition timings. (a) 5 ms BTDC; (b) 7.5 ms BTDC; (c) 12.5 ms BTDC.

Pictures of the initial phase of combustion show an initially quasi-spherical, relatively smooth flame kernel for syngas compositions and methane cases for the various ignition timings. The laminar behavior of the flame remains longer time as the ignition is made far from TDC. In the case of ignition timing at 12.5 ms BTDC, the flame kernel grows and experience flattening when piston is close to TDC position before the transition to turbulent combustion.

Because the combustion continues in the expansion stroke, it is not possible to determine from direct flame visualizations of the combustion chamber the combustion duration. However, estimation about the rapidity of the combustion can be made from figures 5.21-5.23. It is observed that the time at which the flame occupies the entire chamber increases as the igniting timing increases for the whole fuels. This

observation emphasis the fact of the lower peak pressures for ignition timings close to TDC. As seen on 3.2.5 turbulence intensity is higher close to TDC on the RCM, thus the increased turbulence in the unburned mixture at the time of combustion will increase the burning rate (Alla, 2002).

Comparing the three fuels, it is observed that combustion is faster for methane, followed by downdraft syngas and finally by updraft syngas. This behavior is in agreement with the heat of reaction of the mixtures as well as with the laminar burning velocity determined on 4.1.2.3 for typical syngas compositions.

5.3 Conclusion

An experimental approach to syngas engine-like conditions on a rapid compression machine is made.

There is an opposite behavior of the in-cylinder pressure between single compression and compression-expansion strokes. The first is that one gets higher in-cylinder pressures on single compression event than for compression-expansion events, which emphasis the fact of the constant volume combustion to be the way of getting higher pressures. The second is that for single compression peak pressure decreases as the ignition delay increases. In opposite, for compression-expansion the peak pressure increases with the ignition delay increase. This opposite behaviour in relation to the ignition timing has to do with the deviation of the spark from TDC position that influences the extent of the combustion in the compression stroke and this extent has different consequences on peak pressure regarding to the number of strokes events. For single compression it reduces the constant volume combustion duration. For compression-expansion strokes it increases the combustion duration on the compression stroke where the heat released has the effect of generate pressure before expansion.

In both experimental events, higher pressures are obtained with methane-air mixture followed by downdraft-syngas and lastly by updraft-syngas. These results could be endorsed to the heat of reaction of the fuels and air to fuel ratio under stoichiometric conditions, but also to burning velocity. Crossing the heat value with the air to fuel ratio conclusion could be drawn that the energy content inside the combustion chamber is in agreement, however not proportional with the obtained pressures.

Updraft and downdraft syngas compositions have similar burning velocities in laminar conditions but the same is not found in turbulent conditions, where the difference on peak pressure is higher by about 25%. As the turbulent burning velocity is proportional to the laminar burning velocity, analysing the correlations for laminar burning velocity of the typical syngas compositions developed on this work show that the effect of pressure is very significant (coefficient β for updraft is 40% higher in relation to downdraft syngas). The higher pressure used on RCM also makes temperature to increase due to compression but the effect of temperature on burning velocity for typical syngas compositions is irrelevant since the coefficient α is of the same order.

Another major finding is that syngas typical compositions are characterized by high ignition timings due to their low burning velocities. One should be aware of the low equivalent rotation speed used on the RCM. This could compromise the use of typical syngas compositions on high rotation speed engines.

CHAPTER 6

NUMERICAL SIMULATION OF A SYNGAS- FUELLED ENGINE

Over the past years, several simulation codes of varying degree of sophistication of the SI engine combustion process have been developed and applied to predict engine performance (Rakopoulus, 1993). However, sparse theoretical studies have been reported so far in the literature as regards modeling syngas combustion in SI engines (Sridhar et al. 2006; Rakopoulus et al., 2008). Therefore, computational models of syngas combustion in SI engines are strongly desirable; in order to supplement the relevant experimental studies that usually concern operation of pure syngas.

Several model frameworks are used for the simulation of the 'closed' part of the spark-ignition engine cycle; these can be classified as 'zero-', 'multi-zone' and 'multi-dimensional' models. The first two types are classified as thermodynamic models, where the equations constituting the basic structure of the model are based on conservation of mass and energy and are only dependent on time (resulting in ordinary differential equations). Multidimensional models are also termed fluid mechanic or fluid dynamic models, where the governing equations are the Navier–Stokes equations in addition to conservation of mass and energy. Multi-zone models are distinguished from zero-dimensional models by the inclusion of certain geometrical parameters in the basic thermodynamic approach.

The choice of multi-zone or multi-dimensional model is largely determined by the application. If the objective is to evaluate a large range of conditions, perform parametric studies and/or predict optimum engine settings, a reasonable accuracy and fast computation on a PC system is desirable. These conditions are satisfied by multi-zone models. Recent examples are the investigations of causes for cycle-to-cycle variations in engines (Aghdam et al., 2007) and causes for the increased combustion variability leading to lean limits (Ayala and Heywood, 2007). Multi-dimensional models are inappropriate for such studies as they are computationally too demanding. Their best use is for more detailed studies for limited conditions or particular features (e.g. flow through valves, fuel injection, bulk in-cylinder flow and turbulence development), or to support theory and model development.

The following reports in detail the development and validation of a multi-zone thermodynamic combustion model. The purpose is the prediction of the engine in-cylinder pressure. The validation of the code is made by comparison with experimental

literature data and in addition with the rapid compression machine results obtained in this work. For this propose some adaptations to the engine-like code are needed and are shown in advance.

6.1 Thermodynamic model

The basis for multi-zone models is formed by consideration of conservation of mass and energy. In the following, the equations for the cylinder pressure and temperature(s) are derived. This will show where additional information, in the form of sub-models, is necessary in order to close these equations.

Before conservation of energy is written down for the cylinder volume, from inlet valve closing (IVC) time to exhaust valve opening (EVO) time (i.e. the power cycle), some assumptions are generally adopted to simplify the equations. During compression and expansion, pressure is invariably assumed uniform throughout the cylinder; with fixed unburned and burned gas regions in chemical equilibrium. During flame propagation, burned and unburned zones are assumed to be separated by an infinitely thin flame front, with no heat exchange between the two zones. All gases are considered ideal gases; possible invalidity of the ideal gas law at high pressures is countered by the associated high temperatures under engine combustion conditions. As the model is zero-dimensional in nature, it does not account for any geometrical considerations of the flame front position during combustion. As an example, figure 6.1 shows a schematic, only of qualitative nature, of the combustion chamber.

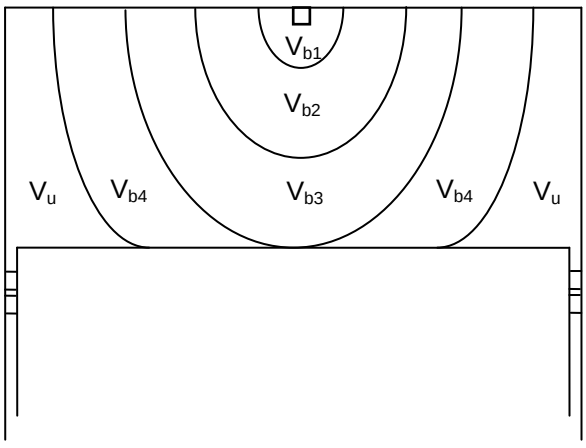

Figure 6.1– Schematic of the combustion chamber with four burned zones.

This is the most frequently used approach for engine combustion models, where the flame area is a spherical flame front truncated by the cylinder walls and the piston,

centered at the spark plug (Verhelst and Sheppard, 2009). The multi-zone approach is retained throughout the expansion phase, i.e. from the end of combustion until the EVO.

6.1.1 Conservation and state equations

The governing equations are presented for the combustion process. During compression and expansion the same equations are retained, with adaptations regarding the number of zones included.

Assuming that '*n*' is the number of the current burned zones, with the latest-generated burned zone indicated by subscript '*n*', the energy conservation equation is applied for the unburned zone, the *n-1* already burned zones and the total cylinder charge, yielding, respectively.

$$\frac{dQ_u}{d\theta} = \frac{dU_u}{d\theta} + p\frac{dV_u}{d\theta} + \frac{dm_b}{d\theta}h_u \tag{6.1}$$

$$\frac{dQ_{b,i}}{d\theta} = \frac{dU_{b,i}}{d\theta} + p\frac{dV_{b,i}}{d\theta} \qquad (i = 1,...,n-1) \tag{6.2}$$

$$\frac{dQ}{d\theta} = \frac{dU}{d\theta} + p\frac{dV}{d\theta} \tag{6.3}$$

Zero blow-by rate is assumed during the whole closed cycle period. The instantaneous cylinder volume is equal to the sum of the volumes of the unburned and burned zones, resulting in the following relation after differentiating with respect to crank angle:

$$\frac{dV}{d\theta} = \sum_{i=1}^{n}\frac{dV_{b,i}}{d\theta} + \frac{dV_u}{d\theta} \tag{6.4}$$

where V is the instantaneous cylinder volume, calculated from the engine geometric characteristics as a function of crank angle:

$$V = V_{TDC}\left\{1 + \frac{r_c - 1}{2}\left[1 - \cos\theta + \frac{1}{\varphi}\left(1 - \sqrt{1 - \varphi^2\sin\theta}\right)\right]\right\} \tag{6.5}$$

with φ being the crank radius to piston rod length ratio. The rate of change of the instantaneous cylinder volume against crank angle is

$$\frac{dV}{d\theta} = V_{TDC}\left(\frac{r_c - 1}{2}\right)\sin\theta\left(1 + \frac{\varphi\cos\theta}{\sqrt{1-\varphi^2\sin^2\theta}}\right) \tag{6.6}$$

The mass fraction of each burned zone is defined as

$$x_{b,i} = \frac{m_{b,i}}{m} \quad (i = 1,...,n) \tag{6.7}$$

with the result for the total burned zone

$$x_b = \frac{m_b}{m} = \sum_{i=1}^{n} x_{b,i} \tag{6.8}$$

The mass conservation equation is also applied to the cylinder charge, assuming zero blow-by, providing

$$\frac{dm}{d\theta} = \frac{dm_u}{d\theta} + \frac{dm_b}{d\theta} = \frac{dm_u}{d\theta} + \frac{dm_{b,n}}{d\theta} = 0 \tag{6.9}$$

The previous relation has been derived assuming that the mass of each of the already burned zones remains constant after its combustion: $dm_{b,i}/d\theta = 0$ ($i=1,\ldots, n-1$), resulting for the rate of change of mass of the total burned zone:

$$dm_b/d\theta = \sum_{i=1}^{n} dm_{b,i}/d\theta = dm_{b,n}/d\theta \tag{6.10}$$

Also, the perfect gas state equation is applied to each zone.

$$pV_j = m_j R_j T_j \quad (j = u, b_1 - b_n) \tag{6.11}$$

6.1.2 Chemical composition and thermodynamic properties

The unburned zone is considered to be a mixture of air and fuel, while also allowance is made for the presence of residual gas trapped in the engine cylinder. The composition and thermodynamic properties of the unburned mixture during compression and combustion are determined from the values of pressure, temperature, fuel–air equivalence ratio and residual gas mass fraction (Ferguson, 1986).

After the start of combustion and until the end of expansion at EVO, the combustion products of each burned zone consist of a set of eleven chemical species: (1) CO_2, (2)

H_2O, (3) N_2, (4) O_2, (5) CO, (6) H_2, (7) H, (8) O, (9) OH, (10) NO, and (11) N, which are considered to be in chemical equilibrium. The calculation of their concentrations and, subsequently, each zone's thermodynamic properties is based on the values of pressure, temperature and fuel–air equivalence ratio. For this reason, the atom balance equations of the C–H–O–N system are considered along with the following eight equilibrium reactions (Ferguson, 1986):

$$\begin{aligned}
&H_2 + \tfrac{1}{2}O_2 \Leftrightarrow H_2O \\
&CO + \tfrac{1}{2}O_2 \Leftrightarrow CO_2 \\
&CH_4 + 2O_2 \Leftrightarrow CO_2 + 2H_2O \\
&\tfrac{1}{2}H_2 + \tfrac{1}{2}O_2 \Leftrightarrow OH \\
&\tfrac{1}{2}O_2 + \tfrac{1}{2}N_2 \Leftrightarrow NO \\
&\tfrac{1}{2}H_2 \Leftrightarrow H \\
&\tfrac{1}{2}O_2 \Leftrightarrow O \\
&\tfrac{1}{2}N_2 \Leftrightarrow N
\end{aligned} \tag{6.12}$$

The various thermodynamic properties (specific enthalpy, specific internal energy, specific volume, specific heat capacity at constant pressure) and thermodynamic derivatives (derivative of logarithmic specific volume with respect to logarithmic temperature and pressure) of the unburned and burned mixtures, needed for the calculations, are computed according to the mole fraction of each species and the gas mixture rule. For this purpose, the well established coefficients (Heywood, 1988) of the polynomial curves that have been fitted to the various species thermodynamic data from JANAF tables are used. For the evaluation of specific internal energy of species *i*, the following relation can be applied according to JANAF Table thermodynamic data (Gordon and McBride, 1971; Heywood, 1988):

$$u_i(T) = R_{si}\left[\left(\sum_{n=1}^{5}\frac{a_{in}}{n}T^n\right) + a_{i6} - T\right] \tag{6.13}$$

where constants a_{in} for the above polynomial relation can be found, for example, in (Ferguson, 1986; Heywood, 1988). Two sets of data are available for constants a_{in}, one for temperatures up to 1000 K and another for temperatures from 1000 to 5000 K. The reference temperature is 298 K. Also,

$$h_i(T) = u_i(T) + R_{si}T \tag{6.14}$$

The rate of internal energy change for a mixture is given by:

$$\frac{dh}{d\theta} = \sum_i u_i \frac{dm_i}{d\theta} + \sum_i m_i c_{vi} \frac{dT}{d\theta} \tag{6.15}$$

where m_i is the mass of species i (O_2, N_2, CO_2,H_2O, N, NO, OH, H, O, etc.) and c_v is the specific heat under constant volume (a function of temperature only $c_v=du/dT$), with

$$c_{vi}(T) = R_{si}\left[\left(\sum_n a_{i,n} T^{n-1}\right) - 1\right] \tag{6.16}$$

with the values of m_i, dm_i, T, dT found from the corresponding first-law analysis of the cylinder contents. The rate of entropy change is:

$$\frac{dS}{d\theta} = \sum_i \frac{dm_i}{d\theta} S_i\left(T, x_i p\right) + \sum_i \frac{m_i}{T} c_{pi} \frac{dT}{d\theta} - \frac{V}{T}\frac{dp}{d\theta} \tag{6.17}$$

With

$$S_i\left(T, x_i p\right) = S_i^{'}\left(T, p_i\right) - R_{si} \ln\left(\frac{x_i p}{p_i}\right) \tag{6.18}$$

and $S_i^{'}\left(T, p_i\right)$ the standard state entropy of species i, which is a function of temperature only, with x_i the molar fraction of species i in the mixture (Ferguson, 1986; Heywood, 1988), given by the following property relation:

$$s_i^{'}(T, p_i) = R_{si}\left[a_{i1} \ln T\left(\sum_{n=2}^{5} a_{i,n} \frac{T^{n-1}}{n-1}\right) + a_{i7}\right] \tag{6.19}$$

For the Gibbs free enthalpy or energy:

$$\frac{dG}{d\theta} = \sum_i \frac{dm_i}{d\theta} \mu_i \tag{6.20}$$

where $\mu_i=g_i\,(T,p_i)$ is the chemical potential of species i in the mixture, with

$$\begin{aligned} g_i(T, p_i) &= g_i(T, x_i p) = h_i(T) - T s_i(T, x_i p) \\ &= h_i(T) - T\left[s_i(T, p_i) - R_{si} \ln\left(\frac{x_i p}{p_i}\right)\right] \end{aligned} \tag{6.21}$$

For all the above expressions, it is assumed that the unburned mixture is frozen in composition and the burned mixture is always in equilibrium. Finally, the well-known ideal gas relation is given by:

$$pV = mR_sT \tag{6.22}$$

6.1.3 Heat Transfer

The heat transfer from gas to the walls is formulated as:

$$\dot{Q} = h_g\, A\, \left(T_g - T_w\right) \tag{6.23}$$

where h_g is the heat transfer coefficient, A is the area in contact with the gas, T_g is the gas temperature and T_w is the wall temperature. In the single zone analysis, the heat transfer coefficient is the same for all surfaces in the cylinder. In general, a classic global heat transfer model is applied to calculate the heat transfer coefficient and an area-averaged heat transfer rate.

Several correlations for calculating the heat transfer coefficient in SI and CI engines have been published in the literature. These studies have generally relied on dimensional analysis for turbulent flow that correlates the Nusselt, Reynolds, and Prandtl numbers. Using experiments in spherical vessels or engines and applying the assumption of quasi-steady conditions has led to empirical correlations for both SI and CI engine heat transfer. These correlations provide a heat transfer coefficient representing a spatially-averaged value for the cylinder. Hence, they are commonly referred to as global heat transfer models, e.g. Woschni (1967), Annand (1963), or Hohenberg (1979). In this code one applies the classical Woschni's correlation.

The Woschni heat transfer correlation is given as:

$$h_g(t) = a_s\, B^{-0.2} P(t)^{0.8} T(t)^{-0.55} v(t)^{0.8} \tag{6.24}$$

where a_s is a scaling factor used for tuning of the coefficient to match a specific engine geometry calculated and used by Hohenberg, (1979) as 130, B is the bore (m), P and T are the instantaneous cylinder pressure (bar) and gas temperature (K), respectively. The instantaneous characteristic velocity, v is defined as:

$$v = \left(2.28\bar{S}_p + 0.00324 \frac{V_s T_r}{P_r V_r} (P - P_{mot}) \right) \tag{6.25}$$

Where $P_{mot}=P_r(V_r/V)^{\gamma}$ is the motored pressure. S_p is mean piston speed (m/s), V_s is swept volume (m^3), V_r, T_r and P_r are volume, temperature and pressure (m^3, K, bar) evaluated at any reference condition, such as inlet valve closure, V is instantaneous cylinder volume (m^3) and γ is the specific heat ratio. The second term in the velocity expression allows for movement of the gases as they are compressed by the advancing flame.

6.1.4 Mass burning rate

In the combustion modeling studies, the main purpose is to specify the mass fraction of burned gases at any time during the combustion process. This is achieved by using several approaches. In general, two approaches have been widely used for determining the mass fraction burned. In the first approach, the mass fraction burned at any crank angle is specified by using empirical burning laws, such as the cosine burn rate formula and Wiebe function (Heywood et al., 1979). This approach does not necessitate detailed combustion modeling, hence modeling of combustion in this manner is more practical, but it gives less reliable or less sensitive results about SI engine combustion [Heywood et al., (1979); Bayraktar and Durgun, (2003)]. Empirical burning equations include some constants that must be determined suitably at the beginning of computation. In the case of using the Wiebe function, these are the efficiency parameter, the form factor, the crank angle at the start of combustion and the combustion duration. For the cosine burn rate formula, these are spark advance and combustion duration. In such models, these parameters are generally determined either by matching the experimental mass fraction burned curves obtained from the cylinder pressure measurements with the calculated ones or by making an engineering judgment [Zeleknik (1976); Heywood et al. (1979)]. If sufficient agreement is achieved between the calculated and measured pressures, then the chosen parameters are used for parametric studies. In the second approach, the combustion is modeled by considering the turbulent flame propagation process (Heywood, 1988). This modeling technique is generally called quasi-dimensional modeling because it accounts for the details of engine geometry and the flame propagation process and therefore will be followed in this work.

The role of in-cylinder air motion begins from the very start of the engine cycle. During the intake stroke, the incoming air generates flow structures with large-scale turbulent

motions within the cylinder, which in turn determines the extent of mixing between the fresh charge and the residuals, as well as internal and external heat transfer rates. The key to the premixed combustion modeling is the prediction of $S_{te,}$ the turbulent flame speed normal to the surface of the flame. In turbulent flames, the flame speed depends on both chemical kinetics and the local turbulence characteristics.

Many methods for describing and calculating the turbulent flame speed have been developed (see for instance the excellent review of Lipatnikov and Chomiak, (2002)). The goal of this work is to develop a fast simulation program for the combustion of syngas in spark ignition engines. The main interest is the pressure development in the engine cylinders, which is directly related to the power output and the efficiency. Therefore, in this work the so-called DamkÖhler method is used and according to this model turbulent flame speed is as follows (Blizard and Keck, 1974):

$$S_{te} = C_2 u' + S_u \tag{6.26}$$

Where, *u'* is the root mean square (rms) turbulent velocity, C_2 a calibration constant dependent of the engine geometry and S_u the laminar burning velocity.

Obviously, proper in-cylinder turbulence modeling needs to be estimated. For this propose, a simple turbulence model, firstly proposed by Hall and Bracco, (1987) and used by several authors [Verhelst and Sierens, (2007); Farhad et al., (2009); Federico et al., (2010)] has been considered:

$$u'_{TDC} = 0.75\,\bar{u}_p = 0.75(2sn),\ u' = u'_{TDC}\left(1 - 0.5\frac{\theta - 360}{45}\right) \tag{6.27}$$

where u'_{TDC} is the rms turbulent velocity at TDC, taken to be 0.75 times the mean piston speed; θ is the crank angle and, *s,* is the stoke. A linear decay of the rms turbulent velocity *u'* from top dead center is imposed.

6.2. Numerical solution procedure

The basic concept of the model is the division of the burned gas region into several distinct zones for taking into account the temperature stratification of the burned gas.

The multi-zone simulation model is applied throughout the closed part of the engine cycle, between IVC and EVO, i.e. compression, combustion and expansion. Admission phase is also included in the code in order to take into account the heating of the

mixture due to wall interaction. The entire flowchart of the developed code is shown in figure 6.2.

It requires as input data the engine geometric characteristics, engine speed, fuel–air equivalence ratio, combustion chamber walls temperature, compression ratio, ignition delay, and temperature and pressure of charge at IVC event. It is assumed that during compression the cylinder content, consisting of air–fuel mixture and any residual gases, comprises one zone. From the start of combustion, multiple burned zones (whose number is user-defined) are sequentially generated, with the latest-generated burned zone being separated from the unburned zone by an infinitesimally thin flame front. The multi-zone approach is retained throughout the expansion phase, i.e. from the end of combustion until the EVO.

All zones considered are assigned spatially uniform pressure, temperature and composition at any instant of time. During all phases, the pressure is uniform throughout the cylinder at any instant of time. It is noted that the model, being zero-dimensional in nature, does not predict geometrically the actual position of the flame front and the various zones inside the cylinder. Rather, simulation follows purely the thermodynamic approach.

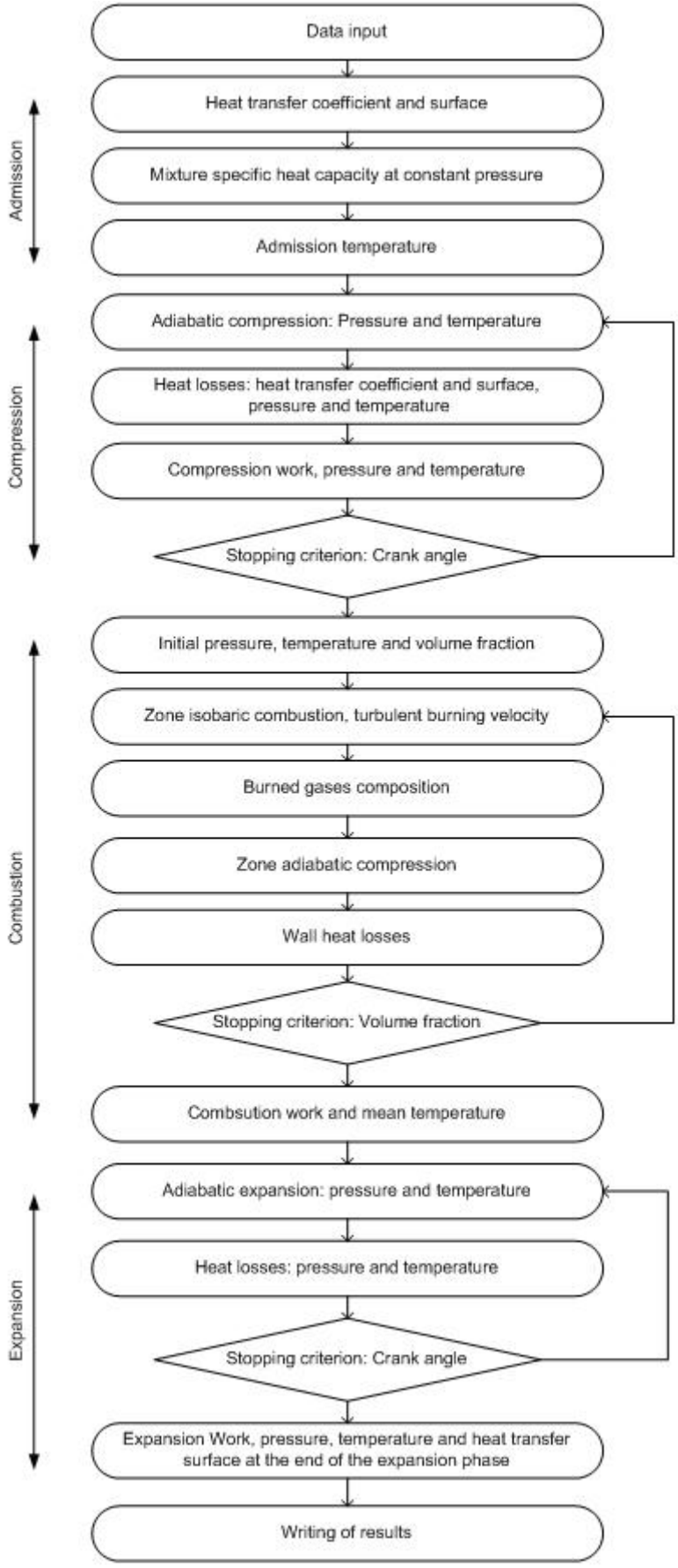

Figure 6.2 – Engine-like code flowchart.

6.3 Code validation

Due to the lack of experimental apparatus, model testing has been carried on over detailed experimental data available in literature and, in particular, the standard CFR, single cylinder, engine has been chosen for the simulations. Two fuels were selected that are present on syngas: hydrogen and methane. As far as hydrogen fueling is concerned, the extensive measurements of Verhelst, (2005) have been chosen as a reference, while the in-cylinder pressures traces by Bade and Karim, (2001) have been considered when dealing with methane. An attempt to validate the code by comparison with experimental results obtained in this work in the RCM is made.

6.3.1 CFR engine

A Cooperative Fuel Research engine, known as the CFR engine, is an engine originally used for the determination of fuel octane numbers, now also equipped for gaseous fuels. It is characterized by its engine speed kept constant by coupled electric motor, and its variable compression ratio. The main engine specifications are given in Table 6.1.

Table 6.1 - Basic CFR engine data

Items	Specification
Engine type	Cooperative Fuel Research (CFR)
Number of cylinders	1
Bore × Stroke	82.55 × 114.2 (mm)
Connecting rod length	254 mm
Displacement	611.7 cm^3
Compression ratio	Variable
Engine speed	Variable

6.3.1.1 Sub-models

Most of the predictive capability of a quasi-dimensional model relies on the accuracy of the implemented sub-models. Sub-models are needed for closing the equations for pressure, temperatures and masses of the two zones: in particular, a combustion sub-model for computing the mass burning rate, and a model of heat transfer through the walls; a detailed description of them is given in the following for hydrogen-air and methane-air mixtures.

Heat transfer

Wei et al., (2001) and Shudo and Suzuki, (2002) have measured instantaneous heat transfer coefficients in hydrogen fuelled engines. Wei et al. (2001) found transient heat transfer coefficients during hydrogen combustion to be twice as high as during gasoline combustion. They evaluate heat transfer correlations and found Woschni's equation to underpredict the heat transfer coefficient by a factor of two.

Shudo and Suzuki (2002) compared the heat transfer coefficients during stoichiometric hydrogen and methane combustion, finding them to be larger in the case of hydrogen. The shorter quenching distance of a hydrogen flame is put forward as the cause of this increased heat transfer, leading to a thinner thermal boundary layer. Furthermore, for near-stoichiometric combustion, flame speeds are high and cause intensified convection. Hydrogen has also a higher thermal conductivity compared to hydrocarbons. Shudo and Suzuki, (2002) construct an alternative heat transfer correlation with an improved correspondence with their measurements. However, the correlation contains two calibration parameters, dependent on ignition timing and equivalence ratio. These dependencies are started to be the subject of further studies, so the correlation is not useful for the present work.

The correlation by Woschni and Annand have cited to be inadequate [Borman and Nishiwaki, (1987)], even for gasoline and diesel engines, although the correlations have been based on measurements on such engines and use hydrocarbon mixture properties. However, the development of heat transfer correlation for SI engines is not within the scope of this work, it was decided to use the standard model of Woschni with separate values during compression, combustion and expansion as reported by Verhelst and Sierens, (2007). This calibration was made by matching a simulated cylinder pressure trace to a measured pressure trace. The compression heat transfer coefficient can be calibrated to a motored pressure trace. The other coefficients need to be set more or less simultaneously.

Turbulent burning velocity

The turbulent burning velocity models need laminar burning velocity data of the air/fuel/residuals mixture at the instantaneous pressure and temperature. As most models use the laminar burning velocity as the local burning velocity, such as the Damköhler model, the stretched burning velocity should be used.

Concerning hydrogen-air flames, the extensive experimental work done by Verhelst, (2005) has been chosen for including the dependence on the air-fuel ratio, temperature, pressure and residual burned gas content:

$$S_u = S_{u_0}\left(\frac{T}{T_0}\right)^{\alpha}\left(\frac{P}{P_0}\right)^{\beta}(1-\gamma f) \tag{6.28}$$

Here, the reference conditions T_0 and P_0 are 365K and 5 bar, respectively. The influence of the equivalence ratio at these conditions is embodied in S_{u0} and is estimated at:

$$S_{u_0} = -4.77\phi^3 + 8.65\phi^2 - 0.394\phi - 0.296 \tag{6.29}$$

The values for α, β and γ are the following:

$$\begin{aligned} &\alpha = 1.232 \\ &\beta = 2.9\phi^3 - 6.69\phi^2 + 5.06\phi - 1.16\,,\ \phi < 0.6 \\ &\beta = 0.0246\phi + 0.0781\,,\ \phi \geq 0.6 \\ &\gamma = 2.715 - 0.5\phi \end{aligned} \tag{6.30}$$

Where γ expresses the effect of residual gases. Verhelst and Sierens, (2007) selected a residual mass fraction of 27% given the best correspondence for the pressure trace during compression and maximum combustion pressure.

Concerning methane–air flames, the correlation expressing the laminar burning velocity of Muller et al., (1997) has been adopted, since it is reliable for a wide range of pressures and preheats temperatures:

$$\begin{aligned} S_u &= A\left(T^0\right) y_{F,u}^m \frac{T_u}{T^0}\left(\frac{T_b - T^0}{T_b - T_u}\right)^n \\ A\left(T^0\right) &= F\exp\left(-\frac{G}{T^0}\right) \end{aligned} \tag{6.31}$$

Where, $y_{F,u}$ = (1+AFR$_s$/ϕ) represents the mass fuel fraction in the unburned mixture, AFR$_s$ is the stoichiometric air–fuel ratio;T^0=*-E/ln(p/B)* is a representative temperature of the inner layer, defined by Peters and Williams, (1987) as the thin layer within which the first oxidation of methane into CO, hydrogen and water occurs; *p* is pressure, and the fuel-dependent constants are equal to: *B=3.1557×10^8 (bar), E=23873 (K), F=2.21760×10^1(cm/s) ,G=-6444.27 (K)*, *m* =0.565175 and *n=2.5158.*

The calibration coefficient C_2 in the Damköhler model was set equal 1.7 as reported by Verhelst and Sierens, (2007).

6.3.1.2 Results and discussion

The simulations results, compared to the respective references, have been presented in figures 6.3 and 6.4.

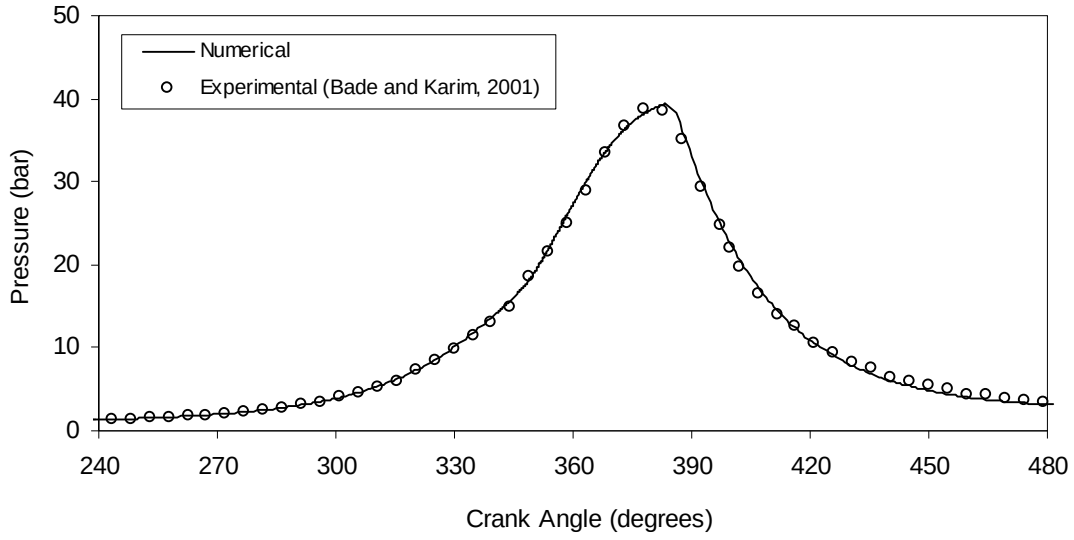

Figure 6.3 – In cylinder pressure validation for CFR engine fueled by methane: ε=8.5, 900 rpm, IT=20º BTDC, ϕ=0.99.

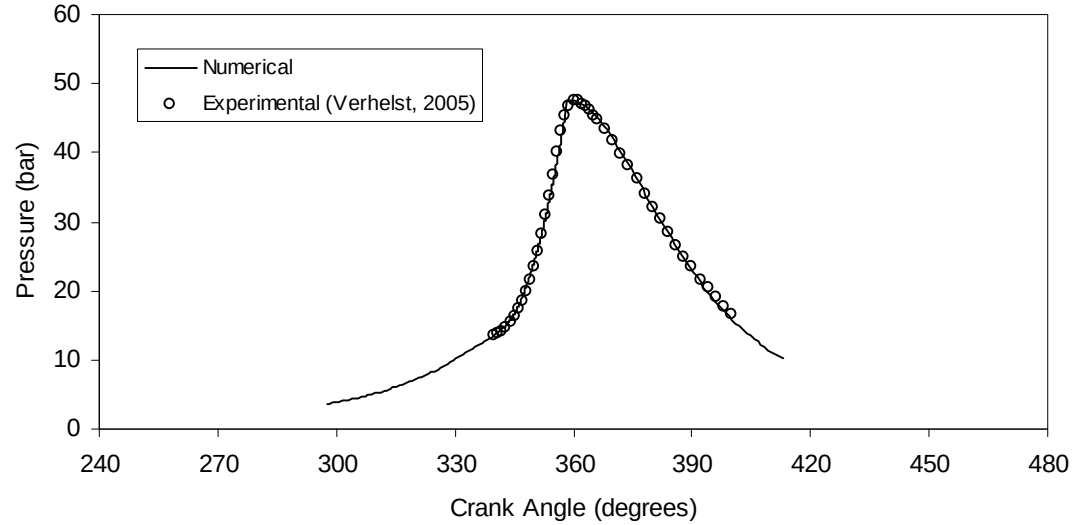

Figure 6.4 – In cylinder pressure validation for CFR engine fueled by hydrogen: ε=9.0, 600 rpm, IT=20º BTDC, ϕ=0.59.

As clearly visible from these figures, a very good agreement is found. This allows validate the developed model and applied it to typical syngas compositions.

6.3.2 RCM

As shown in chapter 5, RCM simulates a single engine cycle and some adaptations to the model presented above are needed in order to take into account the dynamic and geometrical specificness of the RCM. Three main aspects should be considered, the instantaneous volume, heat transfer and burning rate. Two distinctive cases are considered in the code: single compression, and compression and expansion strokes.

6.3.2.1 Flame propagation

The flame development in the combustion chamber of a RCM was shown above for the compression and expansion strokes. In order two verify the assumption frequently used for engine combustion models, where the flame area is a spherical flame front truncated by the cylinder walls and the piston, centered at the spark plug adopted in this work, the flame images are used in an image treatment Matlab code developed by Strozzi, (2008), which allows visualizing the flame contours.

Figures 6.5 show the flame contours in a RCM combustion chamber for downdraft syngas-air stoichiometric mixture. The window has 613×337 pixels with resolution of 2.835 pixels/mm. The frequency of the each contour is kept to 1.4 KHz.

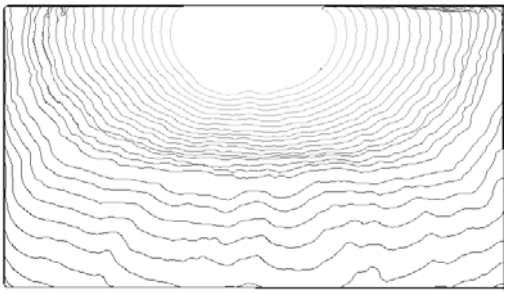

Figure 6.5 - RCM flame contours of stoichiometric downdraft syngas-air mixture with ignition at 12.5 ms BTDC.

The earlier stage of flame kernel with influence of the spark plug was removed from the contours due to lack of definition. After around 5.0 ms (the duration of the spark), the flame contours are well defined and shows that the propagation is spherical. At this moment the piston is reaching TDC and the flame shows a remarkable slow down due to piston deadening, which is felt on the pressure signal by a decreasing gradient. After TDC, the flame contour shows to near double the displacement due to expansion.

6.3.2.2 In-cylinder volume

The instantaneous cylinder volume is calculated based on the piston position as a function of crank angle and fitted by polynomial functions in order to be implemented in the code. Thus, first one evaluates the error in the polynomial approach.

Figure 6.6 shows the comparison between the experimental volume inside the cylinder and the corresponding six degree polynomial expression applied up to top dead center to better fitting. The remaining part is constant and equal to the clearance volume. The maximum error is about 0.5% (5 cm^3).

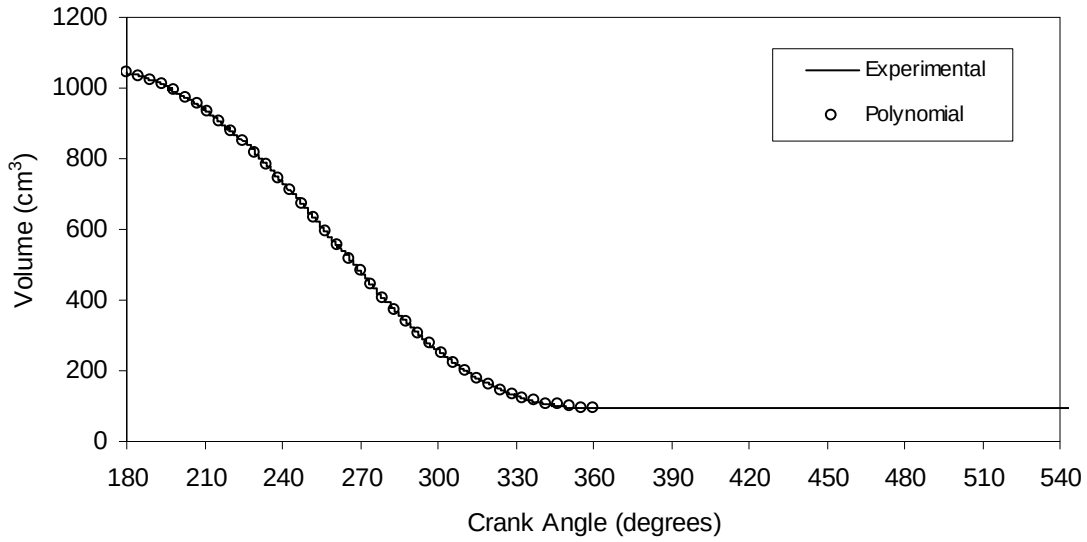

Figure 6.6 – In-cylinder volume polynomial fitting: single compression downdraft syngas case, ignition timing at 12.5 ms BTDC.

Figure 6.7 shows in-cylinder volume variation during compression and expansion and the corresponding six degree polynomial. The maximum error is 1.5% (15 cm^3) obtained at TDC.

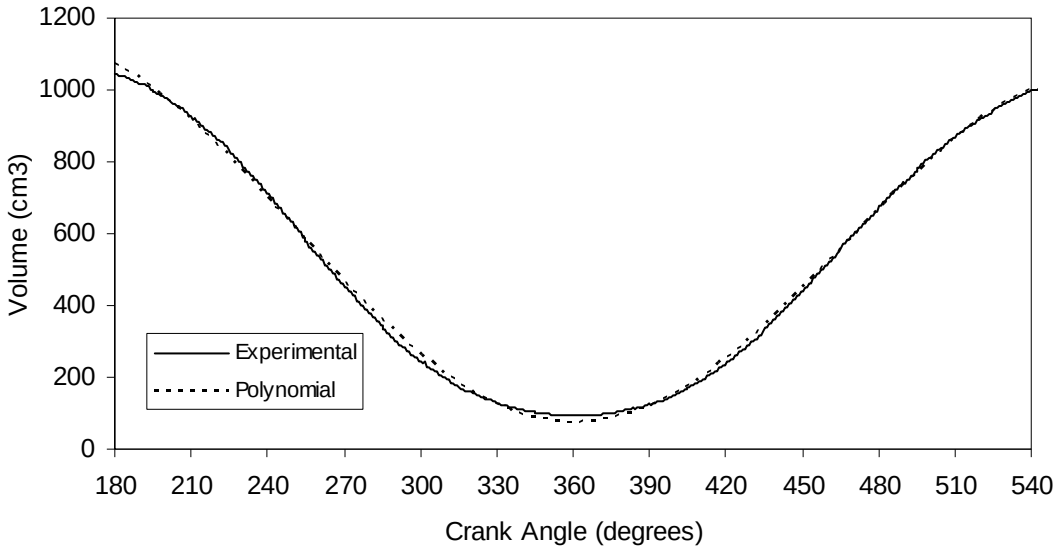

Figure 6.7 – In-cylinder volume polynomial fitting: compression and expansion of downdraft syngas with ignition 12.5 ms BTDC.

For this reason, the volume fitting function was divided into two parts one for compression and another for expansion reducing the fitting error to 0.5%.

6.2.2.3 Heat transfer

A common practice in engine testing for combustion diagnostic is, prior to the usual firing tests, to test the engine in motored conditions, with air as the only working gas, and the in-cylinder pressure being recorded by a piezoelectric transducer (Lapuerta et al., 2003). The study of the compression process in a RCM operating without combustion is useful to identify different parameters related with its operation, namely the heat transfer to the walls. Once determined, these parameters can also be used during the usual firing cycle. In fact, a determinant parameter in the code is the heat transfer coefficient, which should be calibrated. The pressure signals of single compression are used to determine the heat transfer on the RCM. Figure 6.8 shows the comparison between experimental and numerical in-cylinder pressure without combustion.

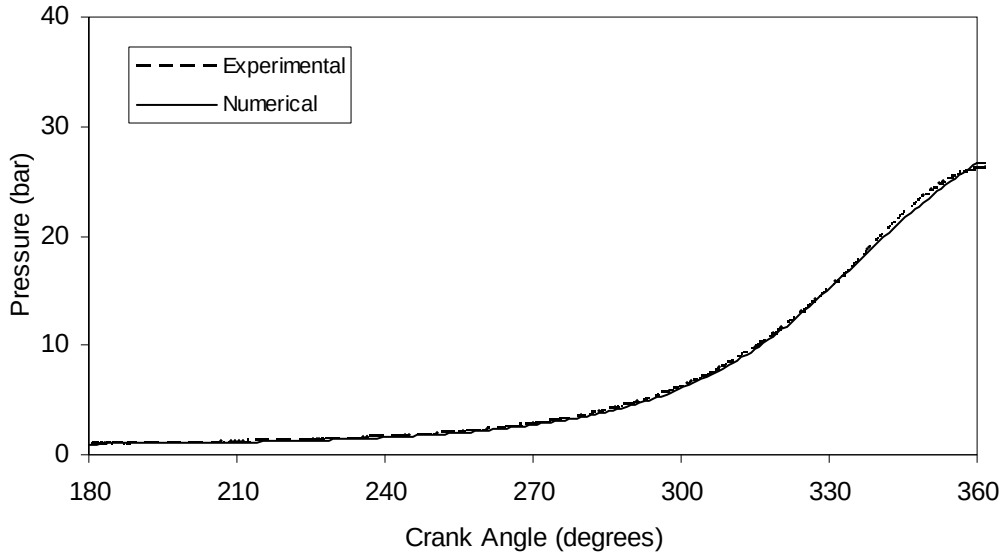

Figure 6.8 - Comparison between experimental and numerical in-cylinder pressure during compression of downdraft syngas without combustion.

From figure 6.8 is seen that the Woschni model works well in its original formulation and represent the heat transfer of the RCM compression stroke.

6.3.2.4 Turbulent burning velocity

As reported in section 3.2.5 the turbulence intensity was experimentally determined for the RCM, and was implemented in the code in the expression (6.26) for validation proposes. The laminar burning velocity formulation obtained in the section 4.1.2.3 was also used to close expression (6.26).

6.3.2.5 Results and discussion

Figures 6.9-6.10 show experimental and numerical cylinder pressure for typical downdraft syngas-air mixture and methane-air mixture for various ignition timings, respectively.

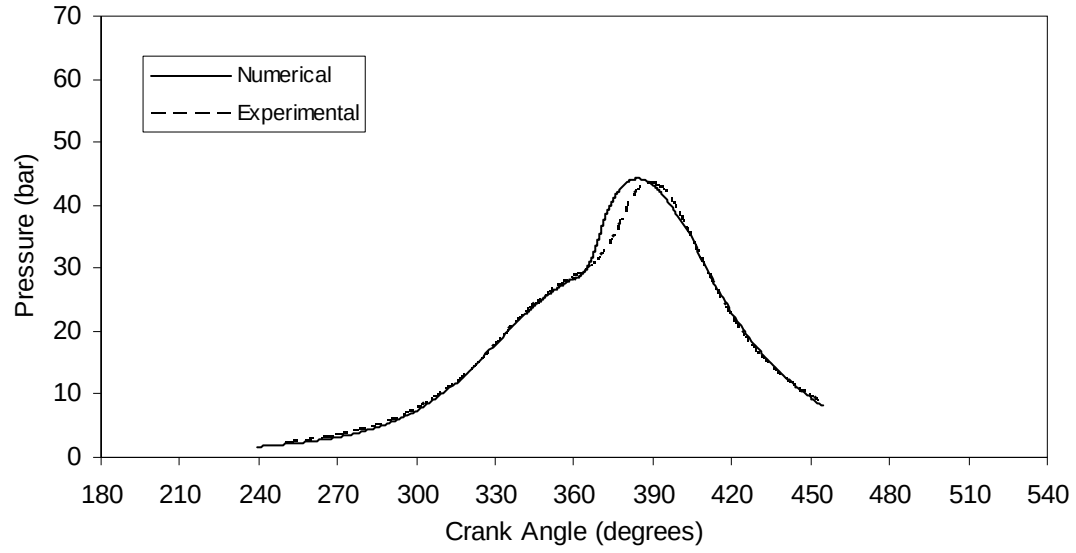

(a)

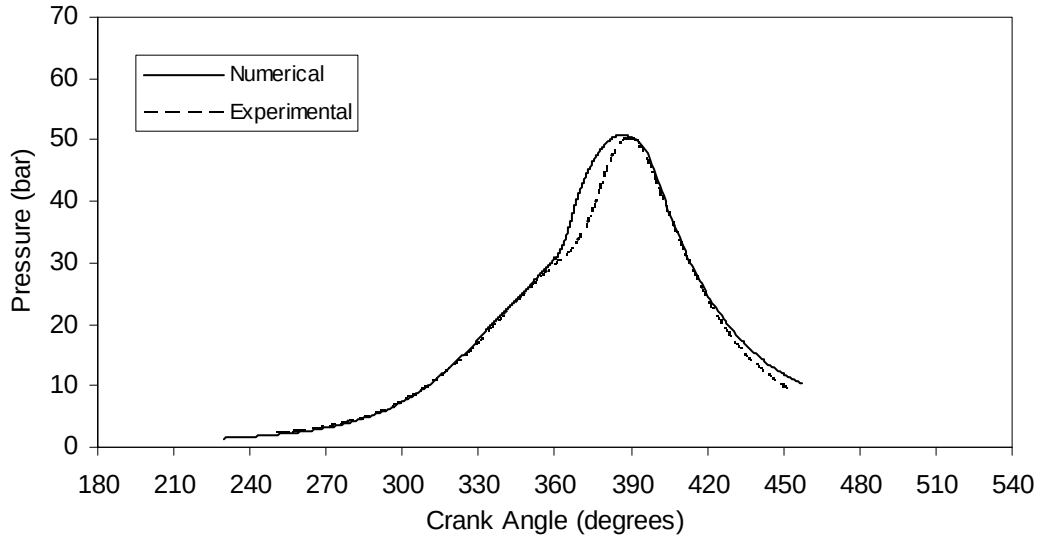

(b)

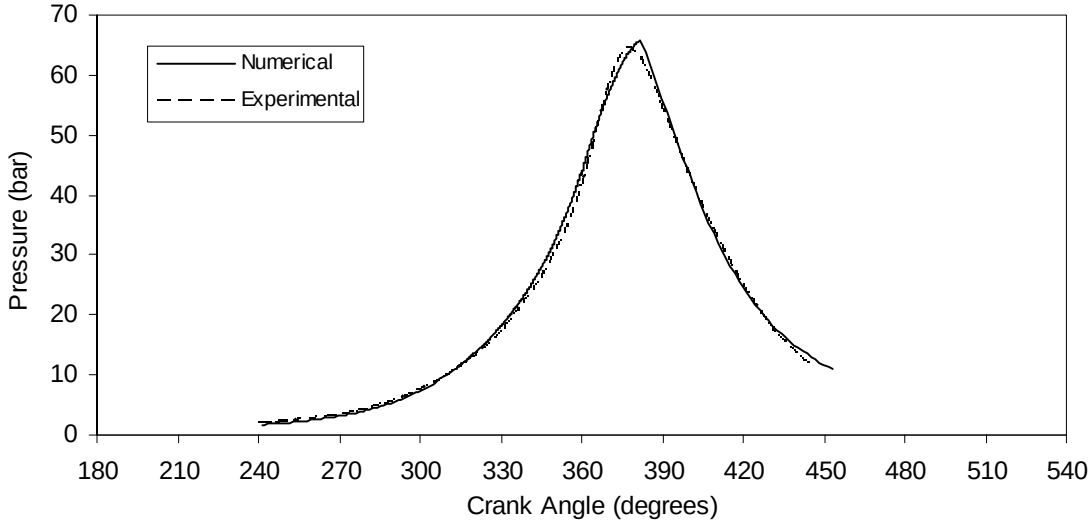

(c)

Figure 6.9 – Experimental and predicted cylinder pressure diagrams as a function of crank angle for downdraft syngas. (a) ignition timing 20º BTDC, (b) 30º BTDC, (c) 50º BTDC.

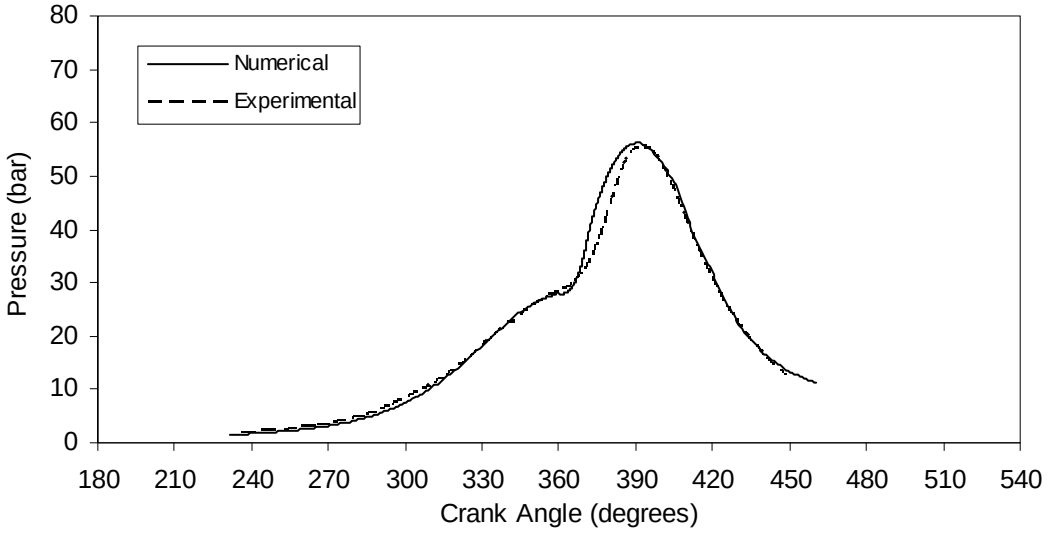

(a)

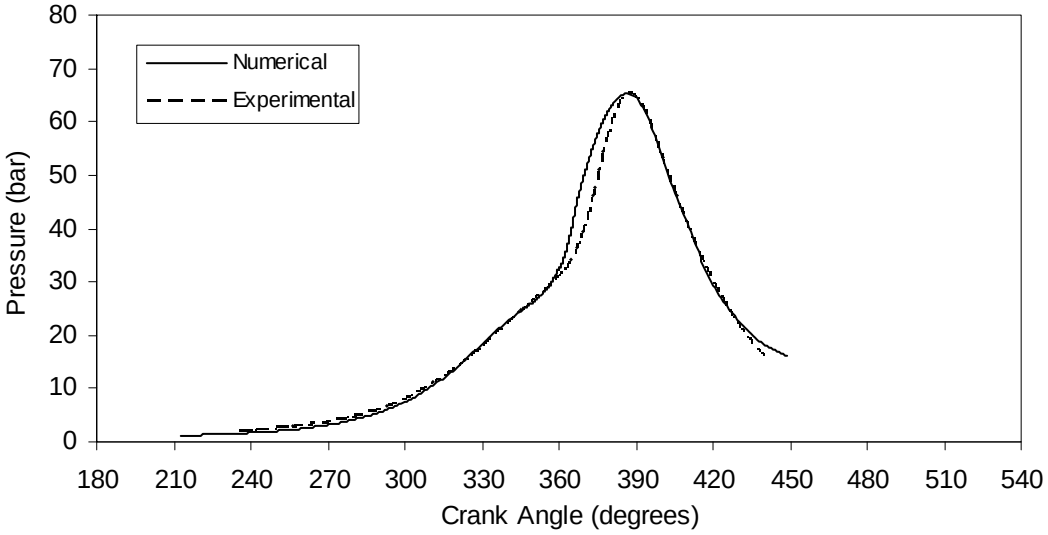

(b)

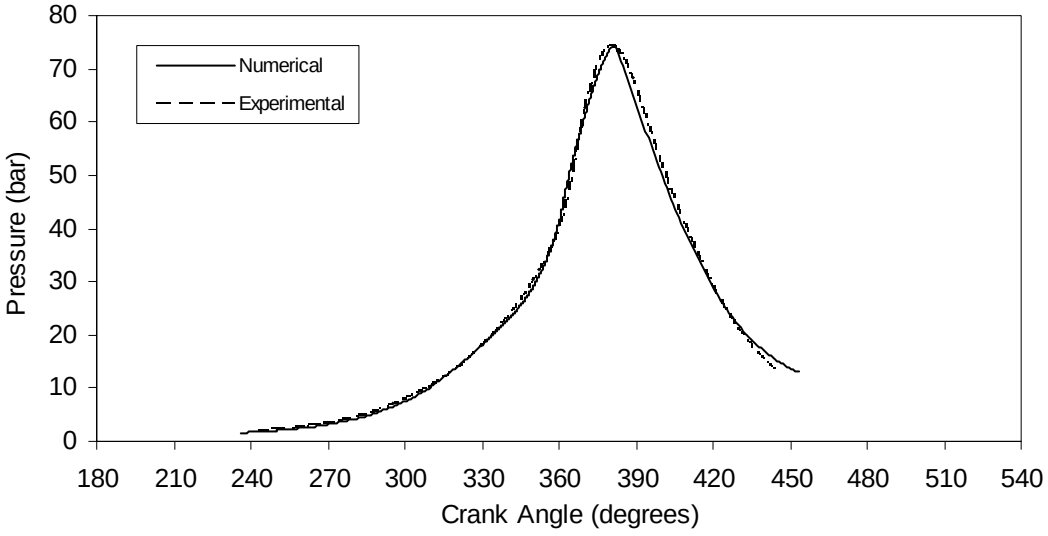

(c)

Figure 6.10 – Experimental and predicted cylinder pressure diagrams as a function of crank angle for methane. (a) ignition timing 20º BTDC, (b) 30º BTDC, (c) 50º BTDC.

Figures 6.9-6.10 show that the adapted code is able to reproduce fairly good the RCM in-cylinder pressure. Main discrepancies are found in the combustion phase especially for short ignition timings. On the expansion phase, pressure curve come back to match with experimental result fairly well. These discrepancies can be explained from both the experimental and numerical results. From the experimental point of view, RCM leakages, which correspond to mass losses especially at elevated pressures, can be a reasonable cause for the lower pressures. From the numerical point of view, there are various factors that can be source of errors due to the code adaptation to the RCM characteristics, namely:

- The heat transfer coefficient that was tested on the compression stroke with very good performance, however it lacks of verification for the expansion stroke.
- The turbulence intensity used on the burning rate model was tacked from experimental results of the single compression, thus it lacks of verification for the expansion stroke;
- Other minor errors like the in-cylinder volume polynomial fitting and the equivalent rotation speed. The latter directly affects the heat transfer coefficient.

6.4. Syngas fuelled-engine

For small scale cogeneration units (<1.0 MW), the engine rotation speed is generally about 1500 rpm. Another division is made for cogeneration units below 50 kW, which are known as micro-CHP units (Monteiro et al., 2009). In this power range rotation speed of 3000 rpm is often found. Thus, in this study three rotation speeds are tested of 750, 1500 and 3000 rpm and stoichiometric syngas-air mixtures.

Once the model was calibrated for the CFR engine it is wise to use it for testing the syngas performance for different rotation speeds. Compression ratio is equal to 11 in order to be somewhat comparable with RCM results.

6.4.1 Results and discussion

Spark timing is the major operating variable that affects spark ignition engine performance, efficiency and emissions (Alla, 2002). Therefore, ignition timing ranging for syngas-air mixtures was selected in order to keep the combustion end between 10º to 20º crank angle degrees after top dead center. Figures 6.11-6.12 depicts the simulated in-cylinder pressure traces during the closed part of the cycle for various ignition timings and rotation speeds. These figures show that the possible ignition timings are very similar for typical syngas compositions. However, they are lower for

downdraft syngas than for updraft syngas, which agrees with the heat of reaction of the fuels and with the burning velocities. Another conclusion is that varying the ignition timing is possible to keep closely the same peak pressure for different rotation speeds.

As far as pressure is concerned, one obtains higher pressures for downdraft syngas, which follows the results obtained experimentally in the RCM. The increase of maximum cylinder pressure with ignition timing is evident. Pressure varied between 49-62 bar for updraft syngas, 48-61 bar for downdraft syngas. These levels of peak pressure are in agreement with the ones obtained in RCM in the section 5.2.2.

Conclusion can be drawn that typical syngas compositions besides its lower heat value and burning velocities can be used on SI engines even at elevated rotation speeds.

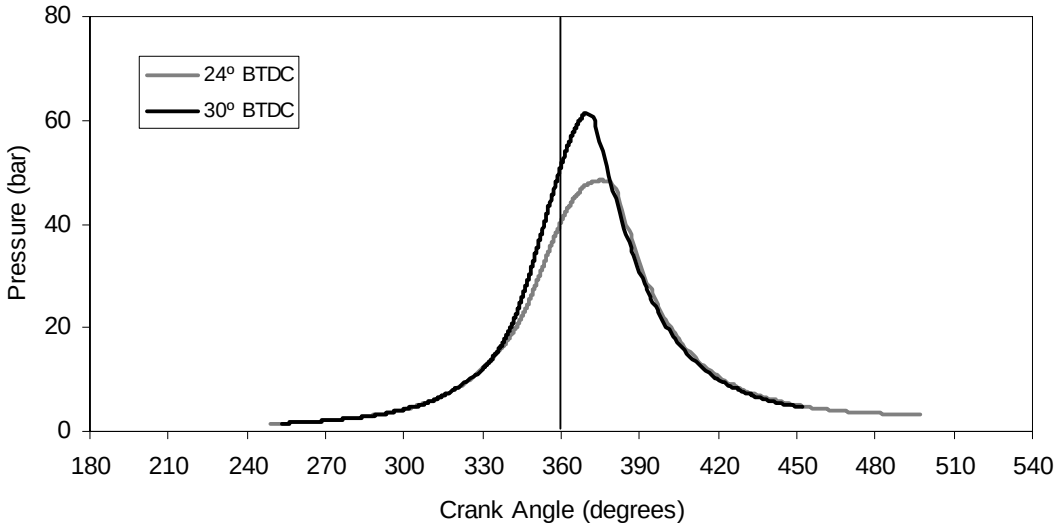

(a)

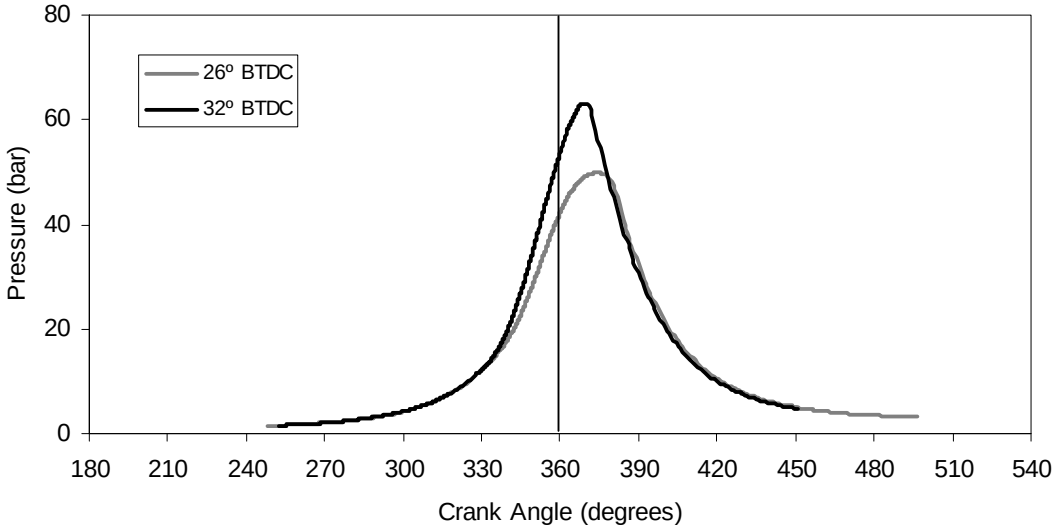

(b)

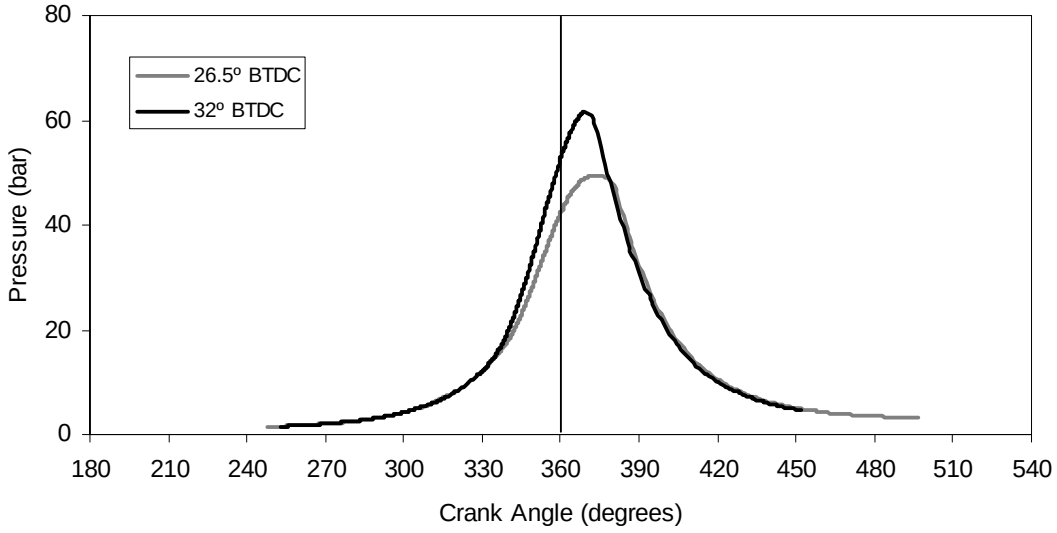

(c)

Figure 6.11 – Cylinder pressure versus crank angle for updraft syngas at various ignition timings. (a) 750 rpm, (b) 1500 rpm, (c) 3000rpm.

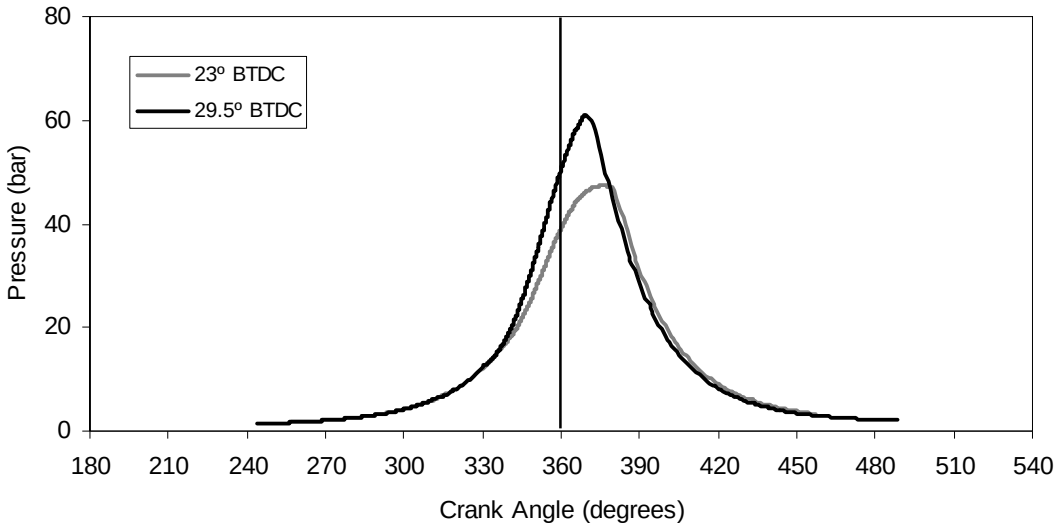

(a)

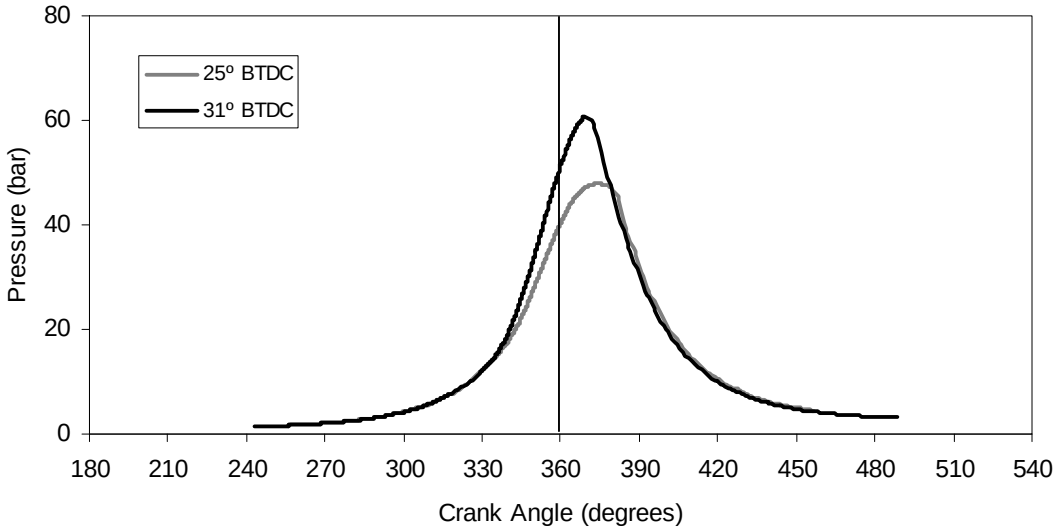

(b)

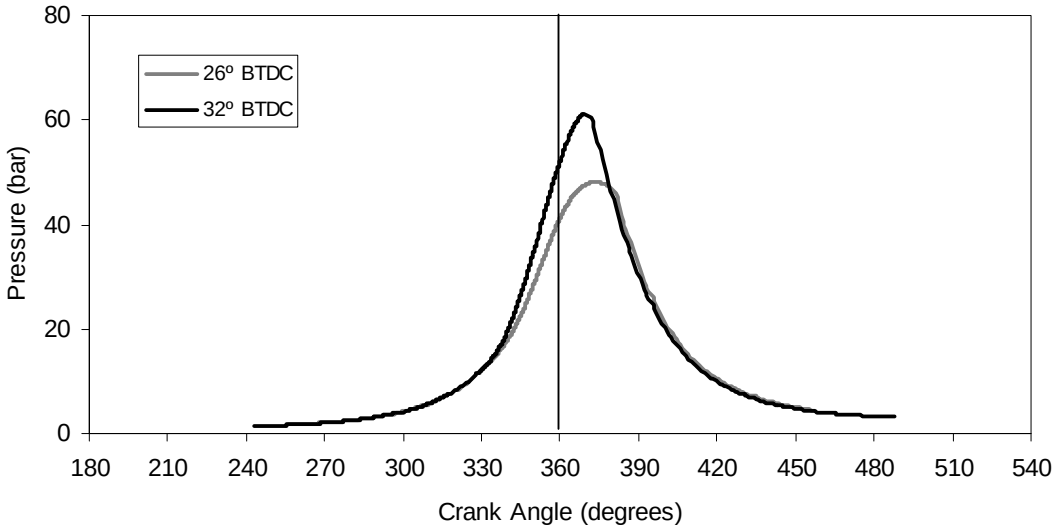

(c)

Figure 6.12- Cylinder pressure versus crank angle for downdraft syngas at various ignition timings. (a) 750 rpm, (b) 1500 rpm, (c) 3000 rpm

In order to compare pressure evolution of the different fuels at the same ignition timing, figure 6.13 shows this cylinder pressure comparison.

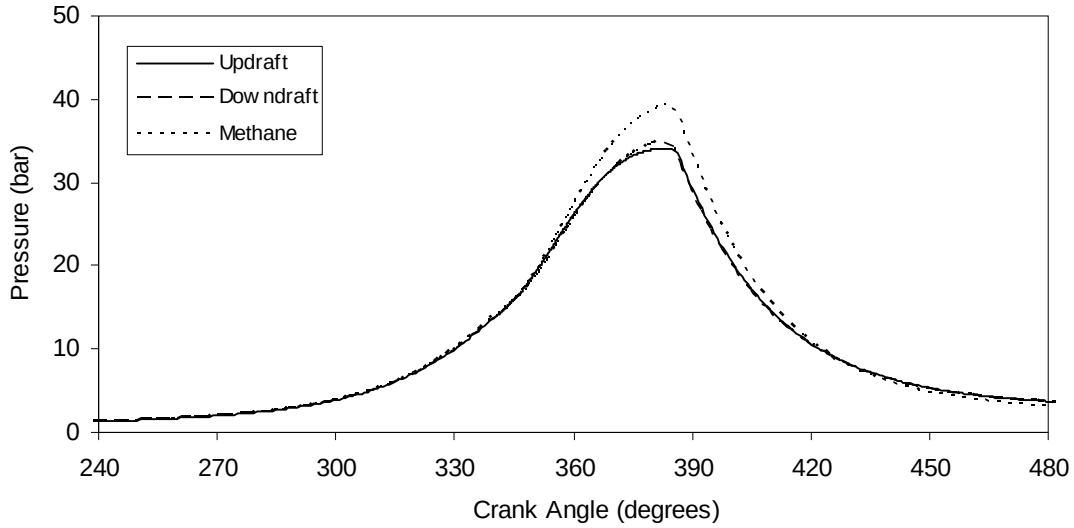

Figure 6.13- Cylinder pressure versus crank angle for various fuels. ε= 8.5, IT= 20º BTDC, 900 rpm.

Figure 6.13 shows that higher peak pressure is obtained for methane-air (39 bar) mixture in comparison to both syngas compositions. Syngas compositions have similar behavior. Peak pressures are 35 bar for downdraft syngas and 34 bar for updraft syngas. These results are qualitatively in agreement with the RCM experimental results. However, quantitatively the difference in the maximum pressure is not as high as in RCM. This could be endorsed to the different characteristics of the experimental set ups, emphasized in sections 6.3.1 and 6.3.2.

6.5 Conclusion

A simulation code for the power cycle of syngas-fuelled engines has been described, using a quasi-dimensional model with 'standard' modeling assumptions. A combustion model consisting of two differential equations was used, one for the mass conservation and one for energy conservation.

Model testing has been carried on over detailed experimental data available in literature for hydrogen and methane, two of the main constituents of syngas. The very good agreement found allows validating the developed model and applied it to typical syngas compositions.

An attempt to adapt the model to the RCM is made by changing several aspects of the model namely the in-cylinder volume function and burning rate model. The comparison

with experimental results obtained in this work in the RCM shows that the adapted code is able to reproduce fairly well the in-cylinder pressure.

The validated model is then applied to a syngas-fuelled engine in order determine its performance. Conclusions can be drawn that typical syngas compositions besides its lower heat value and burning velocities can be used on SI engines even at elevated rotation speeds. Another conclusion is that varying the ignition timing is possible to keep closely the same peak pressure for different rotation speeds.

CHAPTER 7

CONCLUSIONS

7.1 Summary of present work and principal findings

In the currently reported work, three typical syngas mixtures of H_2, CO, CH_4, CO_2 and N_2 have been considered as representative of the producer gas coming from forest biomass gasification, and its combustion characterization is made in order to improve current knowledge and provide reference data for modeling and simulation with the objective of its application in stationary energy production systems based on internal combustion engines.

A detailed bibliographic study was performed concerning two fundamental topics evolving this work - gasification and combustion. First, in its widest sense the term *gasification* covers the conversion of any carbonaceous fuel to a gaseous product with an useable heating value. The result of the gasification is a fuel gas - the so-called syngas - consisting mainly of CO, H_2, CO_2, H_2O, CH_4, N_2, some hydrocarbons in very low quantity and contaminants, such as carbon particles, tar and ash. Key parameters for successful gasification are the feedstock properties (moisture, ash, alkalis and volatiles) and feedstock pre-treatment (drying, particle size, fractionation and leaching). The main advantage of gasification over direct combustion of biomass is the improved balance of carbon dioxide, nitrogen oxides and sulphur in the atmosphere. The main attraction of this technology is the production of a fuel gas, which can be used into an engine or turbine for power production. This is remarkable important if one considerer that biomass power plants today operate on a steam-Rankine cycle with low efficiencies due to modest steam conditions. Gasification is being used to improve the efficiency and to reduce investment costs of biomass electricity generation through the use of gas turbines and combined cycles where efficiencies of 50% are obtained.

Gasifiers are of two main types, fixed bed and fluidized bed, with variations within each type and specific characteristics which determine the need for and extent of feedstock preparation/pre-treatment. For use in gas engines gas produced from a fixed bed, downdraft gasifier provides a low tar gas, with a high particulates loading: as tar is a major contaminant for engine operation and particulates can be relatively easily removed, this system is considered best for fuelling gas engines. There is a significant discrepancy in the final composition of the syngas, even considering the same type of biomass and type of gasifier. This highlights the strong dependence of the syngas

composition on the condition of biomass used, the type of gasifier and conditions of pressure and temperature.

Another issue evolved in this work is the combustion, which detailed bibliographic revision allows to verify that in premixed flames, the laminar burning velocity and flame structure data can be extremely useful in the analysis of fundamental processes such as ignition, NO, and soot formation, and flame quenching. Also, turbulent flame models often prescribe the turbulent burning velocity as a function of laminar burning velocity. Thus, detailed information describing the dependence of the laminar burning velocity, flame thickness, ignition temperature, heat release rate and flame quenching on various system parameters can be a valuable diagnostic and design aid. Burning velocity is a physicochemical constant for a given mixture. It is the velocity, relative of unburned gas, which a plane, one-dimensional flame front travels along the normal to its surface. Clearly, it is the volume of combustible mixture, at its own temperature and pressure, consumed in unit time by unit area of flame front. It is independent of flame geometry, burner size and flow rate. The experimental methods for burning velocity determination are described with emphasis for the constant volume and constant pressure methods. In the constant pressure method the laminar burning velocity and Markstein length are deduced from schlieren photographs. Moreover, any experimental or computed value of laminar burning velocity should be associated with a value of the flame stretch rate. Ideally, the stretch-free value of the burning velocity should be quoted and the influence of stretch rate upon this value should be indicated by the value of the appropriated Markstein length. This is the main reason of the increasing use of the constant pressure method in which the stretch rate is clearly defined. The main advantage of the constant volume method for determining the burning velocity is the possibility of exploring a wide range of pressures and temperatures with one explosion. This is the main reason of its utilization for burning velocity determination in engine conditions.

Following the biographic revision, the combustion characterization of typical syngas-air mixtures was initiated by the determination of the flammability limits in spherical chamber. These results show that the pressure has a definite effect on flammability limits of the syngas-air mixtures reducing the flammable region in the lean side. The syngas combustion characterization continues with the laminar flame characteristics to four equivalence ratios (0.6, 0.8, 1.0 and 1.2) within the flammability limits. The influence of stretch rate on flame was determined by the correspondent Markstein and Karlovitz numbers. Combustion demonstrates a linear relationship between flame

radius and time for syngas–air flames. The maximum value of syngas-air flame speeds is presented at the stoichiometric equivalence ratio, while lean or rich mixtures decrease the flame speeds. Tendency observed on the unstretched burning velocity is in agreement with the heat of reaction of the syngas composition. The higher heat value is associated with the higher amount of H_2 and lower dilution by N_2 and CO_2 in the syngas composition. Markstein numbers shows that syngas-air flames are generally unstable. Karlovitz numbers indicates that syngas-air flames are little influenced by stretch rate. Based on the experimental data a formula for calculating the laminar burning velocities of syngas–air flames is proposed,

$$S_u^0 = -0.8125\phi^2 + 1.6375\phi - 0.5725 \quad \text{(Updraft)}$$

$$S_u^0 = -0.7313\phi^2 + 1.5428\phi - 0.4924 \quad \text{(Downdraft)}$$

$$S_u^0 = -0.7500\phi^2 + 1.5450\phi - 0.6210 \quad \text{(Fluidized bed)}$$

for updraft, downdraft and fluidized bed syngas–air mixture combustion, respectively.

When compared with common gas fuels like methane and propane, the laminar burning velocity of typical syngas compositions shows to be similar to that of methane, especially the downdraft syngas case, although somewhat slower than propane. This could be due to the syngas stoichiometric air–fuel ratio that is ten times lower than the methane air-fuel ratio and more than twenty times in the case of propane. Thus, the energy content per unit quantity of mixture (air + fuel) inducted to the chamber is only marginally lower when using syngas, compared with the corresponding common gas fuels. The values of laminar burning velocity reported for simulated syngas can be seen to be higher than those obtained for typical syngas compositions. The simulated syngas mixture that better matches the magnitude of laminar burning velocity for the typical syngas compositions is the mixture comprising 5%H2/95%CO.

In order to determine laminar burning velocity at elevated pressures relevant to engine applications, the constant volume method was used. Based on the experimental data obtained, empirical formulations of the form $S_u = S_{u0}(T/T_0)^{\alpha}(P/P_0)^{\beta}$ have been establish for pressure range 0.75-20 bar and temperature range 293-450 K tanking into account the stretch effect. The influence of the equivalence ratio is included through the temperature and pressure exponents, α and β, and through the reference burning velocity S_{u0} as square functions for updraft and downdraft syngas compositions and as a linear function for fluidized bed syngas due to the limited possible data:

$$\text{(Updtraft)} \quad \begin{cases} S_{u0} = -0.413\phi^2 + 1.056\phi - 0.355 \\ \alpha = 4.881\phi^2 - 9.952\phi + 6.731 \\ \beta = -1.469\phi^2 + 2.786\phi - 1.561 \end{cases}$$

$$\text{(Downdraft)} \quad \begin{cases} S_{u0} = -0.45\phi^2 + 1.152\phi - 0.354 \\ \alpha = 0.988\phi^2 - 1.936\phi + 2.502 \\ \beta = -1.194\phi^2 + 1.967\phi - 0.931 \end{cases}$$

$$\text{(Fluidized bed)} \quad \begin{cases} S_{u0} = 0.21\phi - 0.073 \\ \alpha = 1.485\phi + 0.639 \\ \beta = -1.4\phi + 0.882 \end{cases}$$

Conclusion can be drawn that the burning velocity decreases with the increase of pressure. In opposite, an increase in temperature induces an increase of burning velocity. The higher burning velocity value is obtained for downdraft syngas. This result is endorsed to the higher heat value, lower dilution and higher volume percentage of hydrogen in the downdraft syngas.

This information about laminar burning velocity of syngas-air flames is then applied on a multi-zone numerical heat transfer simulation code of the wall-flame interaction developed at the Laboratoire de Combustion et Détonique. The adapted code allows simulating the combustion of homogeneous premixed gas mixtures within constant volume spherical chamber in order to predict the quenching distance of typical syngas-air flames. Thus, it was possible to establish analytical expressions of quenching distance for typical stoichiometric syngas-air flames.

$\delta_q = 450\ P^{-0.79}$ (μm), P>0.3 MPa (Updraft)

$\delta_q = 300\ P^{-0.89}$ (μm), P>0.3 MPa (Downdraft)

Another major finding is that the code reproduces well the pressure evolution beyond the validity of the burning velocity correlation established in this work for updraft and downdraft syngas compositions. Fluidized bed syngas composition due to cellular flame development, which violates the assumption of spherical flame was removed from this study.

Engine-like conditions were experimentally reproduced in a rapid compression machine (RCM) when working on two strokes mode simulating a single cycle of an internal combustion engine. Stationary power applications usually use natural gas as fuel, thus a methane-air mixture is also included in this work as a reference fuel for comparison with the typical syngas compositions under study. A common practice in engine testing for combustion diagnostic is, prior to the usual firing tests, to test the engine in motored

conditions, therefore single compression tests were also performed in the RCM operating with and without combustion in order to identify different parameters related with its operation, namely the heat transfer to the walls.

Higher pressures are obtained with methane-air mixture followed by downdraft-syngas and lastly by updraft-syngas. These results could be endorsed to the heat of reaction of the fuels and air to fuel ratio under stoichiometric conditions, but also to burning velocities. Updraft and downdraft syngas compositions have similar burning velocities in laminar conditions but the same is not found in turbulent conditions, where the difference in peak pressure is higher by about 25%. As the turbulent burning velocity is proportional to the laminar burning velocity, analysing the correlations for laminar burning velocity of the typical syngas compositions developed on this work show that the effect of pressure is very significant (coefficient β for updraft is 40% higher in relation to downdraft syngas coefficient). The higher pressure used on RCM also makes temperature to increase due to compression but the effect of temperature on burning velocity for typical syngas compositions is irrelevant since the coefficient α is of the order. Another major finding is that syngas typical compositions are characterized by high ignition timings due to their low burning velocities.

A simulation code for the power cycle of syngas-fuelled engines has been developed, using a quasi-dimensional model with ‘standard’ modeling assumptions. Model testing has been carried on over detailed experimental data available in literature for hydrogen and methane, two of the main constituents of syngas. The very good agreement found allows validating the developed model and applied it to typical syngas compositions. An attempt to adapt the model to the RCM is made by changing several aspects of the model namely the in-cylinder volume function and burning rate model. The comparison with experimental results obtained in this work in the RCM shows that the adapted code is able to reproduce fairly well the in-cylinder pressure and that the Woschni model works well in its original formulation and represent the heat transfer of the RCM compression stroke.

The validated model is then applied to a syngas-fuelled engine in order determine its performance. Conclusions can be drawn that typical syngas compositions besides its lower heat value and burning velocities can be used on SI engines even at elevated rotation speeds.

7.2 Recommendations for future work

Research works are open narratives and hence some recommendations are made for possible developments.

In order to make precise studies on the use of syngas will be necessary to consider that its composition will be rather constant. The development of mathematical models fully validated experimentally may be a very useful tool to determine the final composition of syngas by changes in initial conditions without laborious and expensive experimental tests. Besides the best performance of the downdraft syngas composition, fluidized bed gasification is the technology that has been topic of the most recent developments. This is due to the fact that downdraft gasification is the ultimate technology and is limited to low scale systems. In opposite, fluidized bed gasification can be significant improved by optimizing all the variables evolved to a determined biomass kind or multi-biomass systems.

Various methods for burning velocity determination are available in the literature, and thus, some comparison between them could be done in order to determine the error. The linear methodology adopted in the constant pressure method is currently the most used, however a novel linear methodology of Tahtouh, (2009) as well as the non-linear theory of Buckmaster, (1977) could be follow. Thus a research line is open in this case in terms of comparison between linear and non-linear theories.

In the constant volume method there are also various approaches to the mass burning rate that could be compared. The linear approximation, introduced by Lewis and Von Elbe (1961), is still the most widespread analytical relation to interpret burning velocity data. Differences in laminar burning velocities between the varieties of fractional pressure rise were quantified by Luijten et al., (2009) for the example case of stoichiometric methane–air combustion, demonstrating that deviations between burning velocities from bomb data and other methods can at least partly be ascribed to the limited accuracy of the linear approximation. For the example case, differences up to 8% were found.

Several simulation codes of varying degree of sophistication of the SI engine combustion process have been developed and applied to predict engine performance over the past years. Multi-zone models are useful when the objective is to evaluate a large range of conditions, perform parametric studies and/or predict optimum engine settings. The main drawback of this kind of modeling is presence of calibration

coefficients, dependent of engine characteristics, on the turbulent burning velocity and heat transfer models. A number of turbulent burning velocity models are available, such as Blizard and Keck, (1974); Tabaczynski et al. (1980); Gülder (1990); Matthews and Chin, (1991); Bradley et al., (1992); Zimont, (2000); Peters, (2000). These models could be applied in the code in order to verify each one best reproduce the turbulence of syngas-air flames. Several correlations for calculating the heat transfer coefficient in SI engines have been published in the literature. These correlations provide a heat transfer coefficient representing a spatially-averaged value for the cylinder. Hence, they are commonly referred to as global heat transfer models, e.g. Annand (1963), Woschni (1967), Hohenberg (1979) and Chiodi and Bargende, (2001). The developed multi-zone model has shown to predict the in-cylinder pressure with very good accuracy. Additional simulations can then be run to evaluate the potential of supercharging the engine, which allow increasing the power and maybe the use of even poor syngas compositions like the fluidized bed composition. Improvements could be made adding a pollutants formation model including out of equilibrium reactions. An additional model to specific fuel consumption could be developed as this parameter is one of the most important to determine the viability of stationary power production systems IC engine based.

References

1. Aghdam A. E., Burluka A.A., Hattrell T., Liu K., Sheppard CGW, Neumeister J. Study of cyclic variation in an engine using quasi-dimensional combustion model. SAE technical paper 2007-01-0939 (2007).
2. Alla A.G.H. Computer simulation of a four stroke spark ignition engine. Energy Conversion and Management 43, 1043-1061 (2002).
3. Annand W.J.D. Heat transfer in the cylinders of reciprocating internal combustion engines. Proc. Instru Mech Eng.177 (36), 973-990 (1963).
4. Aung K.T., Hassan M.I., Faeth G.M. Flame stretch interactions of laminar premixed hydrogen/air flames at normal temperature and pressure. Combustion and Flame 109, 1-24 (1997).
5. Aung K.T., Hassan M.I., Faeth G.M. Effects of pressure and nitrogen dilution on flame/stretch interactions of laminar premixed $H_2/O_2/N_2$ flames. Combustion and Flame 112, 1-15 (1998).
6. Ayala F.A., Heywood J.B. Lean SI engines: the role of combustion variability in defining lean limits. SAE technical paper 2007-24-0030 (2007).
7. Bade S.O., Karim G.A. Predicting the effects of the presence of diluents with methane on spark ignition engine performance. Applied Thermal Engineering 21, 331-342 (2001).
8. Bayraktar H., Durgun O. Mathematical modeling of spark-ignition engine cycles. Energy Sources 25 (5), 439–455 (2003).
9. Bhattacharya S.C. Commercialization options for biomass energy technologies in ESCAP countries. Economic and Social Commission for Asia and the Pacific, Asian Institute of Technology, 2001.
10. Blizard N.C., Keck J.C. Experimental and theoretical investigation of turbulent burning model for internal combustion engines. SAE Paper no. 740191 (1974).
11. Borman G. and Nishiwaki K. Internal-combustion engine heat transfer. Progress in Energy and Combustion Science 13, 1-46 (1987).
12. Bosschaart K.J., L.P.H. de Goey. Detailed analysis of the heat flux method for measuring burning velocities. Combustion and Flame 136, 261–269 (2004).
13. Boust B., (2006). Etude expérimentale et modélisation des pertes thermiques pariétales lors of l'interaction flame-paroi instationnaire. PhD Thesis, University of Poitiers, France.

14. Bradley D., Lau A.K.C., Lawes M. Flame stretch rate as a determinant of turbulent burning velocity. Philosophical Transactions of the Real Society of London A338, 359-387 (1992).
15. Bradley D., Harper C.M. The development of instabilities in laminar explosion flames. Combustion and Flame 99, 562-572 (1994).
16. Bradley D., Gaskell P.H., Gu X.J. Burning Velocities, Markstein Lengths, and Flame Quenching for Spherical Methane- Air Flames: A computational Study. Combustion and Flame 104 (1 –2), 176 –198 (1996).
17. Bradley D., Hicks R.A., Lawes M., Sheppard C.G.W., Wooley R. The Measurement of Laminar Burning Velocities and Markstein Numbers for Iso-octane-Air and iso-octane-n-heptane-Air mixtures at elevated temperatures and pressures in an Explosion bomb. Combustion and Flame 115 (1–2), 126–144 (1998).
18. Bradley D., Lawes M., Kexin L., Verhelst S., Woolley R. Laminar burning velocities of lean hydrogen–air mixtures at pressures up to 1.0 MPa. Combustion and Flame 149, 162-172 (2007).
19. Brander J.A., Chase D.L. Repowering application considerations. Trans. ASME A.J. Eng. Gas Turb. Power 114, 643-652 (1992).
20. Brett L., Macnamara J., Musch P., Simmie J.M. Simulation of methane autoignition in a rapid compression machine with creviced pistons. Combustion and Flame 124, 326-329 (2001).
21. Bridgwater A.V., Evans G.D. An Assessment of Thermochemical Conversion Systems for Processing Biomass and Refuse. Energy Technology Support Unit (ETSU) on behalf of the Department of Trade, ETSU B/T1/00207/REP, 1993.
22. Bridgwater A.V. The technical and economic feasibility of biomass gasification for power generation. Fuel 74 (5), 631-653 (1995).
23. Bridgwater AV. Towards the ‘bio-refinery’ fast pyrolysis of biomass. Renewable Energy World, James & James, London Vol. 4, (1), 66-83 (2001).
24. Bridgwater A.V., Toft A.J., Brammer J.G. A Techno-economic comparison of power production by biomass fast pyrolysis with gasification and combustion. Journal of Renewable & Sustainable Energy Reviews, 181-248 (2002).
25. Bridgwater A.V. Renewable fuels and chemicals by thermal processing of biomass. Chemical Engineering Journal 91, 87–102 (2003).
26. Brown M.J., McLean I.C., Smith D.B., Taylor S.C. Markstein lengths of CO/H_2/Air flames, using expanding spherical flames. Proceedings of the Combustion Institute 26, 875-881 (1996).

27. Buckmaster J. Slowly varying laminar flames. Combustion and Flame 28, 225-239 (1977).
28. Burke M.P., Qin X., Ju Y., Dryer F.L. Measurements of hydrogen syngas flame speeds at elevated pressures. 5th US Combustion Meeting, March 25–28, 2007.
29. Candel S.M., Poinsot T.J. Flame Stretch and the Balance Equation for the Flame Area. Combustion Science Technology 70, 1-15 (1990).
30. Carpentieri M., Corti A., Lombardi L. Life cycle assessment (LCA) of an integrated biomass gasification combined cycle (IBGCC) with CO_2 removal. Journal of Energy Conversion and Management 46, 1790–1808 (2005).
31. Ciferno J.P., Marano J.J. Benchmarking Biomass Gasification Technologies for Fuels, Chemicals and Hydrogen Production. U.S. Department of Energy, National Energy Technology Laboratory, 2002.
32. Chiodi M., Bargende M. Improvement of Engine Heat-Transfer Calculation in the Three-Dimensional Simulation Using a Phenomenological Heat-Transfer Model. SAE Technical Paper 2001-01-3601 (2001).
33. Chomiak J. Combustion: A study in Theory, Fact and Application (Energy and Engineering Science Series). Gordon and Breach Science Publishers, 1990.
34. Chung S.H., Law C.K. An Integral Analysis of the Structure and Propagation of Stretched Premixed Flames. Combustion and Flame 72, 325-336 (1988).
35. Clarkson J., Griffiths J.F., Macnamara J.P., Whitaker B.J. Temperature fields during the development of combustion in a rapid compression machine. Combustion and Flame 125, 1162-1175 (2001).
36. Clavin P., Williams F.A. Effects of molecular diffusion and of thermal expansion on the structure and dynamics of premixed flames in turbulent flows of large scale and low intensity. J. Fluid Mechanics 116, 251-282 (1982).
37. Clavin. P. Dynamic behavior of premixed flame fronts in laminar and turbulent flows. Progress in Energy Combustion Sciences 11, 1-59 (1985).
38. Clavin P., Joulin G. Flamelet library for turbulent wrinkled flames. Lecture Notes in Engineering:Turbulent Reactive Flows 40, 213–239 (1989).
39. Coppens F.H.V., Ruyck J., Konnov A. The effects of composition on burning velocity and nitric oxide formation in laminar premixed flames of $CH_4+H_2+O_2+N_2$. Combustion and Flame 149, 409-417 (2007).
40. Coward H.F., Hartwell F.J. Studies in the mechanism of flame movement. Part II. The fundamental speed of flame in mixtures of methane and air. J. Chem. Soc. 2672-2874 (1932).
41. Coward H. F., Payman W. Problems in flame propagation. Chemical Reviews 21 (3), 359-366 (1937).

42. Cuellar B.S. Aplicaciones de las fracciones obtenidas en la pirolisis del sarmiento de la vid Proyecto Fin de carrera. EE.II. Universidad de Extremadura, 2003.
43. Dahoe A. E., Zevenbergen J. F., Lemkowitz S. M., Scarlett B. Dust explosions in spherical vessels: the role of flame thickness in the validity of the 'cube-root-law'. Journal of Loss Prevention in the Process Industries 9, 33–44 (1996).
44. Dahoe A.E., Goey L.P.H. On the determination of the laminar burning velocity from closed vessel gas explosions. Journal of Loss Prevention in the Process Industries 16, 457–478 (2003).
45. Darrieus G. unpublished work presented at La Technique Moderne, and at Le Congrès de Mécanique Appliqué (1945) and (1938).
46. Demirbaş A. Recent advances in biomass conversion technologies. Energy Educ. Sci. Technology 6, 19-41 (2000).
47. Demirbaş A. Hydrogen Production from Biomass by the Gasification Process. Energy Sources 24, 59-68 (2002).
48. Directive 2001/77/EC, Journal of European Community, 2001.
49. Dixon-Lewis G. Structure of laminar flames. Symposium (International) on Combustion. The Combustion Institute 23 (1), 305-324 (1991).
50. Elvingson P., Luften och MiljÖn. Department of Applied Environmental Science, Goteborg University, 2001.
51. Engstrom F. Overview of Power Generation from Biomass. Foster Wheeler development Corporation, Presented at the Gasification Technology conference, San Francisco CA, October 1999.
52. Etlicher A. Différentes approches de la détermination de la vitesse de combustion laminaire d'un mélange gazeux explosif par la méthode de la bombe sphérique à volume constant. Rapport de stage ingénieur, ENSMA, 1995.
53. Evans A.A. Deflagrations in spherical vessels: a comparison among four approximate burning velocity formulae. Combustion and Flame 97, 429-434 (1994).
54. Farhad S., Shamecki A. H., Ali M. P. Effects of spark advance, A/F ratio and valve timing on emissions and performance characteristics of hydrogen internal combustion engine. SAE paper 2009-01-1424, (2009).
55. Federico P., Fabrizio P., Enrico M. A quasi-dimensional combustion model for performance and emissions of SI engines running on hydrogen-methane blends. Int. J. Hydrogen Energy 35, 4687-4701 (2010).
56. Fercher E., Hofbauer H., Fleck T., Rauch T., Veronik G. Two years experience with the FICFB-gasification process. In: Proceedings of the 10th European conference and technology exhibition, Wurzburg, 1998.

57. Ferguson C.R. Internal combustion engines. New York: Wiley, 1986.
58. Ferreira S., Moreira N.A., Monteiro E. Bioenergy overview for Portugal. Biomass and Bionergy 33, 1567-1576 (2009).
59. Fiock E.F., Marvin C.F. The measurement of flame speeds. Chemical Reviews 21 (3), 367-387 (1937).
60. Fisson F., Henry J.D., Kageyma T. Influence of la turbulence sur la phase initiale du développement of flammes of mélanges préalables. Final Rapport du Contract ELF, 1994.
61. Floch A., (1990). Etude de la Turbulence Instationnaire dans une Chambre de Combustion à Volume Constant-Interaction avec la Propagation d'une Flamme Allumée par Etincelle. PhD Thesis, University of Rouen, France.
62. Gañan J., A. Al-Kassir Abdulla, A.B. Mirandab, J. Turegano, S. Correia, E.M. Cuerda. Energy production by means of gasification process of residuals sourced in Extremadura (Spain). Renewable Energy 30, 1759–1769 (2005).
63. Ganesan V. Internal Combustion Engines. McGraw-Hill companies, 1995.
64. Gerstein M., Levine O., Wong E. L. Flame Propagation. II. The Determination of Fundamental Burning Velocities of Hydrocarbons by a Revised Tube Method. Journal of the American Chemical Society 73 (1), 418-422 (1951).
65. González J.F., Encinar J.M., Canito J.L., Sabio E., Chacón M. Pyrolysis of cherry stones: energy uses of the different fractions and kinetic study. J. Analytical and Applied Pyrolysis 67 (1), 165–190 (2003).
66. Gordon S., McBride J. Computer program for calculation of complex chemical equilibrium compositions, rocket performance, incident and reflected shocks, and Chapman-Jouguet detonations. Scientific and Technical Information Office NASA, 1971.
67. Graham R.G., Bain R. Biomass gasification - hot gas cleanup. Report submitted to the International Energy Agency Biomass Gasification Working Group, IEA 1993.
68. Griffiths J.F, Liao Q., Schreiber A., Meyer J., Knoche K.F, Kardylewski W. Experimental and numerical studies of ditertiary butyl peroxide combustion at high pressures in a rapid compression machine. Combustion and Flame 93, 303-315 (1993).
69. Groot G. R. A., Oijen J. A., Goey L. P. H., Seshadri K., Peters N. The Effects of Strain and Curvature on the Mass Burning Rate of Premixed Laminar Flames, Combustion Theory and Modeling 6, 675-695 (2002).

70. Gu X. J., M. Z. Haq, M. Lawes, and R. Woolley. Laminar Burning Velocity and Markstein Lengths of Methane–Air Mixtures. Combustion and Flame 121, 41–58 (2000).
71. Guénoche H., Manson N., Mannot G. La propagation uniforme d'une déflagration dans une tube cylindrique lisse. Comptes Rendus 226, 163-164, (1948).
72. Guézet J., (1996). Étude de l'interaction entre l´aérodynamique et la combustion dans une machine à compression rapide. PhD. Thesis, University of Poitiers, France.
73. Gülder O.L. Turbulent premixed flame propagation models for different combustion regimes. Proc. Combustion Institute, 743-750 (1990)
74. Hall M.J. and Bracco F.V. A study of velocities and turbulence intensities measured in firing and motored engines. SAE paper 870453, (1987).
75. Halter C. Chauveau, Djebaili-Chaumeix N., Gokalp I. Characterization of the effects of pressure and hydrogen concentration on laminar burning velocities of methane-hydrogen-air mixtures. Proc. Combustion Institute 30, 201-208 (2005).
76. Hartman J. How to Tune and Modify Engine Management Systems. Motorbooks, 2004.
77. Hasler P., Nussbaumer T., Buhler R. Vergasung von Biomasse fur die Methanol-Synthese [Biomass gasification for methanol synthesis]. Swiss Federal Office of Energy, Berne, 1994.
78. Hasler P., Nussbaumer T. Gas cleaning for IC engine applications from fixed bed biomass gasification. Biomass and Bioenergy 16, 385-395 (1999).
79. Hassan M.I., Aung K.T., Faeth G.M. Properties of laminar premixed CO/H_2/air flames at various pressures. J. Propulsion Power 13 (2), 239–245 (1997).
80. Hassan M.I., Aung K.T. Faeth G.M. Measured and Predicted Properties of Laminar premixed Methane/Air Flames at Various Pressures. Combustion and Flame 115, 539-550 (1998).
81. Henry J. D., (1996). Contribution à l'Etude de l'Influence des Conditions Hydrodynamiques sur la Combustion d'un Mélange Préalable dans un Milieu Confiné. PhD Thesis, University of Poitiers, France.
82. Herguido J., Corella J., Gonzalez-Saiz J. Steam gasification of lignocellulosic residues in a fluidized bed at a small pilot scale. Industrial Engineering Chemical Research 31, 1274-1282 (1992).
83. Heuzé O., Presles H-N, Bauer P. Computation of Chemical Equilibria. Journal of Chemistry and Physics 83, 4734-4737 (1985).

84. Heywood J.B., Higgins J.M., Watts P.A., Tabaczynski, R.J. Development and use of a cycle simulation to predict SI engine efficiency and NOx emissions. SAE Paper 790291, (1979).
85. Heywood J.B. Internal combustion engine fundamentals. New York: McGraw-Hill, 1988.
86. Higman C., M. van der Burgt. Gasification. Elsevier Science, 2003.
87. Hill P.G., Zhang D. The Effects of Swirl and Tumble on Combustion in Spark-Ignition Engines. Prog. Energy Combustion Sciences 20, 373-429 (1994).
88. Hinrichs, R. A. and Merlin Kleninbach. Energy: its use and the environment. Thompson Learning, Inc. 2004.
89. Hohenberg G.F Advanced Approaches for Heat Transfer Calculations. SAE Paper 790825, (1979).
90. Huang Y., Sung CJ. Eng J.A. Laminar flame speeds of primary reference fuels and reformer gas mixtures. Combustion and Flame 139, 239–251 (2004).
91. Iijima T., Takeno T. Effects of temperature and pressure on burning velocity. Combustion and Flame 65, 35–43 (1986).
92. Javier G., Aznar M.P., Caballero Eva Frances M.A., Corella J., Biomass Gasification in Fluidized Bed at Pilot Scale with Steam- Oxigen Mixtures. Product Distribution for Very Different Operating Conditions. Energy & Fuels 11(6), 1109–1118 (1997).
93. Javier G., Corella J., Aznar M., Caballero M. Biomass gasification in atmospheric and bubbling fluidized bed: Effect of the type of gasifying agent on the product distribution. Biomass and Bioenergy 17, 389-403 (1999).
94. Karlovitz B., Deninston D. W., Knappschaefer D. H., Wells F. Studies on turbulent flames. Fourth Symposium on Combustion. Williams and Wilkins. Baltimore 613-620, (1953).
95. Kim Y.J., Lee S.H., Kim S.D. Coal gasification characteristics in a downer reactor. Fuel 80, 1915–1922 (2001).
96. Kitagwawa T. Effects of pressure on burning velocity and instabilities of propane-air premixed flames. JSME Int. Journal, Serie B, 48 (1), 2-8 (2005).
97. Klein A., (2002). Gasification: An Alternative Process for Energy Recovery and Disposal of Municipal Solid Wastes. MSc Thesis in Earth Resources Engineering, Columbia University, USA.
98. Klimov A. M. Laminar flame in a turbulent flow. Zhournal Prikladnaya Mekhanika i Tekhnicheskaya Fizika 3, 49-58 (1963).
99. Knoef H. Gasification of Biomass & Waste – Practical Experience. III International Slovach Biomass Forum, 2003.

100. Kuo K. K. Principles of Combustion. 2nd edition John Wiley & Sons, 2005.
101. Kurkela E., Stshlberg P. Air Gasification of peat, wood and brown coal in a pressurized fluidized bed reactor. I. Carbon conversion, gas yields and tar formation. Fuel Processing Technology 31(1), 1-21 (1992).
102. Kwon O.C., Rozenchan G., Law C.K. Cellular instabilities and self-acceleration of outwardly propagating spherical flames. Proceedings of the combustion Institute 29, 1775-1763 (2002).
103. Lamoureux N., Djebaili – Chaumeix.N., Paillard. C.–E. Laminar flame velocity determination for H_2–air–He–CO_2 mixtures using the spherical bomb method. Experimental Thermal and Fluid Science 27, 385–393 (2003).
104. Landau L. D. On the theory of slow combustion. Acta Physicochim (URSS) 19, 77-85 (1944).
105. Lapuerta M., Armas O., Molina S. Study of the compression cycle of a reciprocating engine through the polytropic coefficient. Applied Thermal Engineering 23, 313-323 (2003).
106. Launder B.E., Spalding D.B. The numerical computation of turbulent flows. Comput. Methods Appl. Mech. Eng. 3, 269-289 (1974).
107. Law C. K. Dynamics of stretched flames. Symposium (International) on Combustion 22 (1), 1381-1402 (1989).
108. Law C.K., Sung C. J. Structure, Aerodynamics, and Geometry of Premixed Flamelets. Prog. Energy Combustion Sciences 26, 459-505 (2000).
109. Law C.K. Combustion Physics. Cambridge University Press, Cambridge, UK, 2006.
110. Leckner B. Spectral and total emissivity of water vapor and carbon dioxide. Combustion and Flame 19, 33-48, (1972).
111. Lewis B., von Elbe G. Combustion, Flames and Explosions of Gases, 3rd Edition, Academic Press, 1987.
112. Li H., Karim G.A. Experimental investigation of the knock and combustion characteristics of CH4, H2, CO, and some of their mixtures. Proc Inst Mech Eng, J Power Energy 220, 459–71 (2006).
113. Liao S.Y., Jiang D.M., Cheng Q. Determination of laminar burning velocities for natural gas. Fuel 83, 1247-1250 (2004).
114. Lide D. R. Handbook of Chemistry and Physics. 84th edition, CRC Press, 2003.
115. Liekhus K.J., Zlochower I.A., Cashdollar K. L., Djordjevic S.M., Loehr C.A. Flammability of gas mixtures containing volatile organic compounds and hydrogen. Journal of Loss Prevention in the Process Industries 13, 377-384 (2000).

116. Lipatnikov A.N., Chomiak J. Turbulent flame speed and thickness: phenomenology, evaluation, and application in multi-dimensional simulations. Progress in Energy and Combustion Science 28, 1-74 (2002).
117. Liou T.M., Santavicca D.A. Cycle resolved LDV measurements in a motored IC engine. Transactions of the ASME 107, (1985).
118. Luijten C.C.M., Doosje E., Goey L.P.H. Accurate analytical models for fractional pressure rise in constant volume combustion. International Journal of Thermal Sciences 48, 1213–1222 (2009).
119. Mallard E. and LeChatelier H. Recherches Experimentales et Theoriques sur la Combustion des Melanges Gaseux Explosifs. Ann. Mines 8 (4), 274-568 (1883).
120. Malheiro S., (2002). Etude Expérimentale de la Combustion d'un Mélange Méthane-Air Hétérogène Globalement Pauvre. PhD Thesis, University of Poitiers, France.
121. Markstein G. H. Experimental and theoretical studies of flame instability. J. Aeronautical Sciences 18, 199-209 (1951).
122. Markstein G. H. Nonsteady Flame Propagation. Pergamon Press, Oxford, 1964.
123. Maroteaux, D. Détermination de la vitesse fondamentale de flamme et de la limite d'inflammabilité de mélanges pauvres d'hydrocarbures saturés et d'air en présence ou non d'éthylène. Rapport de DEA, ENSMA, 1987.
124. Maschio G., Lucchesi A., Stoppato G. Production of syngas from biomass. Bioresource Technology 48, 119-126 (1994).
125. Matalon M., Matkowsky B. J. Flames as Gasdynamic discontinuities. J. Fluid Mechanics 124, 239-259 (1982).
126. Matthews R.D, Chin Y-W. A fractal-based SI engine model: comparisons of predictions with experimental data. SAE Paper 910079, (1991).
127. McKendry P. Energy production from biomass (part 2): conversion technologies. Journal of Bioresource Technology 83, 47-54 (2002a).
128. McKendry P. Energy production from biomass (part 3): gasification technologies. Journal of Bioresource Technology 83, 55-63 (2002b).
129. McLean I.C., Smith D.B, Taylor S.C. The use of carbon monoxide/hydrogen burning velocities to examine the rate of the CO+OH reaction. Proc. Combustion Institute 25, 749-757 (1994).
130. Mehrling P., Vierrath H., Mannot G. gasification of lignite and wood in the Lurgi circulating fluidized bed gasifier. Electric Power Research Institute EPRI, Final Report GS-6436, Portland. 1989.
131. Metghalchi M., Keck J. C. Laminar Burning velocity of propane-air mixtures at high temperatures and pressure. Combustion and Flame 38, 143-154 (1980).

132. Metghalchi M., Keck J. C. Burning velocities of air with methanol, isooctane, and indolene at high pressure and temperature. Combustion and Flame 48, 191-210 (1982).
133. Miccio F. Gasification of two Biomass Fuels in Bubbling Fluidized Bed. Proceedings of the 15th International Conference on Fluidized Bed Combustion, Savannah GA, May 16 – 19, 1999.
134. Minetti R., Carlier M., Ribaucour M., E. Therssen, L.R. Sochet. Comparison of oxidation and autoignition of the two primary reference fuels by rapid compression. Proc. Combustion Institute 26, 747-753 (1996).
135. Mittall G. (2006). A rapid compression machine – design, characterization, and autoignition investigations. Phd Thesis, Case Western Reserve University. USA. Available from: < http://etd.ohiolink.edu/send-pdf.cgi?case1130184196 >
136. Monteiro E., Moreira N.A., Ferreira S. Planning of Micro-CHP Units in the Portuguese Scenario. Applied Energy 86, 290–298 (2009).
137. Muller U.C., Bollig M., Peters N. Approximations for burning velocities and Markstein numbers for lean hydrocarbon and methanol flames. Combustion and Flame 108, 349–56 (1997).
138. Nagy J. C.,Conn J., Verakis H. Explosion development in a spherical vessel. Tech. Rep. RI 7279, US Dept. of Interior, Bureau of Mines, 1969.
139. Natarajan J., Lieuwen T., Seitzman J. Laminar flame speeds of H2/CO mixtures: Effect of CO_2 dilution, preheat temperature, and pressure. Combustion and Flame 151, 104–119 (2007).
140. Narváez I., Grio A., Aznar M.P., Corella J. Biomass gasification with air in an atmospheric bubbling fluidized bed. Effect of six operational variables on the quality of the produced raw gas. Ind. Eng. Chem. Res. 35 (7), 2110-2120 (1996).
141. Nieminen J. Biomass CFB Gasifier Connected to a 350 MWth Steam Boiler Fired with Coal and Natural Gas -Thermie Demonstration Project in Lahti, Finland. Foster Wheeler Development Corporation, 2004.
142. Nolting E., Leuchs M. The use of gas from biomass in engines. Muich: M.A.N. – Neue Technologies, 1995.
143. O'Donovan K., Rallis C. A modified analysis for the determination of the burning velocity of a gas mixture in a spherical constant volume combustion vessel. Combustion and Flame 3, 201-204, (1959).
144. Paisley M.A., Anson D. Biomass Gasification for Gas Turbine Based Power Generation. Presented at the International Gas Turbine & Aeroengine Congress & Exhibition, 1997.

145. Peters N., Williams F.A. The asymptotic structure of stoichiometric methane-air flames. Combustion and Flame 68, 185-207 (1987).
146. Peters N. Turbulent combustion. Cambridge: Cambridge University Press, 2000.
147. Prathap C., Ray A., Ravi M.R. Investigation of nitrogen dilution effects on the laminar burning velocity and flame stability of syngas fuel at atmospheric condition. Combustion and Flame 155, 145-160 (2008).
148. Rakopoulos C.D. Evaluation of a spark ignition engine cycle using first and second law analysis techniques. Energy Conversion Management 34, 1299–1314 (1993)
149. Rakopoulos C.D, Antonopoulos K.A, Rakopoulos D.C, Hountalas D.T. Multi-zone modeling of combustion and emissions formation in a DI Diesel engine operating on ethanol–diesel fuel blends. Energy Conversion Management 49, 625–643 (2008).
150. Rakopoulus C.D, Michos C.N. Development and validation of a multi-zone combustion model for performance and nitric oxide formation in syngas fueled spark ignition engine. Energy Conversion and Management 49 (10), 2924-2938 (2008).
151. Rakotoniaina, Jean-Elysée., (1998). Études de la célérité fondamentale de la flamme laminaire de mélanges préalables par la méthode de la chambre de combustion sphérique. PhD Thesis, University of Poitiers, France.
152. Rampling T., Gill P. Fundamental Research on the thermal treatment of wastes and biomass: thermal treatment characteristics of biomass. ETSU B/T1/00208/Rep/2., 1993.
153. Reed T., Das A. Biomass Handbook of Downdraft Gasifier Engine Systems. Solar Energy Research Institute, U.S. Department of Energy, 1988.
154. Reed T., Siddhartha G. A Survey of Biomass Gasification, 2nd edition, 2001.
155. Rivère J.P., Mechkor M. Modélisation des échanges thermiques sur la paroi de la chambre de combustion, Rapport RENAULT, 2005.
156. Rolando Z., Krister S., Emilia B. Rapid pyrolysis of agricultural residues at high temperature. Biomass and Bioenergy 23, 357 – 366 (2002).
157. Rousseau S., Lemoult B., Tazerout M. Combustion characterization of natural gas in a lean burn spark-ignition engine. Proc. Inst. Mech Eng. J. Autom Engng 213, 481-489 (1999).
158. Neto R.A., Filomena P., Carlos F., M. Dias, I. Gulyurtlu, M. Matos, I. Cabrita. Fluidised bed co-gasification of coal and olive oil industry wastes. Fuel 84, 1635–1644 (2005).

159. Ryan T.W., Lestz S.J. The laminar burning velocity of isooctane, N-Heptane, Methanol, Methane and Propane at Elevated Temperature and Pressures in the presence of a diluent. SAE Paper 800103, (1980).
160. Saeed K., Stone C.R. Measurements of the laminar burning velocity for mixtures of methanol and air from constant-volume vessel using a multizone model. Combustion and Flame 139, 152 –166 (2004).
161. Schuster G., Loffler G., Weigl K., Hofbauer H. Biomass steam gasification - an extensive parametric modeling study. Bioresource Technology 77, 71-79 (2001).
162. Schroder V., Molnarne M. Flammability of gas mixtures Part 1: Fire potential. Journal of Hazardous Materials A121, 37-44 (2005).
163. Settles, G.S. Schlieren and shadowgraph techniques: visualizing phenomena in transparent media. Springer - Verlag, Berlin, 2001.
164. Sharma S.P., Agrawal D.D., Gupta C.P. The pressure and temperature dependence of burning velocity in a spherical combustion bomb. In Proceedings of the eighteenth symposium on combustion. The Combustion Institute, 493–501 (1981).
165. Shudo T., Suzuki H. New heat transfer equation applicable to hydrogen-fuelled engines. ASME Fall Technical Conference, paper ICEF2005-515, New Orleans, Louisiana, 2002.
166. Souza-Santos M. L. Solid Fuels Combustion and Gasification: modelling, simulation, and equipment operation. Marcel Dekker Inc. 2004
167. Sridhar G., Paul P.J., Mukunda H.S. Biomass derived producer gas as a reciprocating engine fuel-an experimental analysis. Biomass Bioenergy 21, 61–72 (2001).
168. Sridhar G., Paul P.J., Mukunda H.S. Zero-dimensional modeling of a producer gas-based reciprocating engine. Proc Inst Mech. Eng, J. Power Energy 220, 923–931 (2006).
169. Staiss C., Pereira H. Instituto Superior de Agronomia, Centro de Estudos Florestais, 2001.
170. Stone C.R., Ladommatos N. Design and evaluation of a fast-burn spark-ignition combustion system for gaseous fuels at high compression ratios. J. Inst. Energy 64, 202–211 (1991).
171. Stone R. Introduction to internal combustion engines. London: MacMillan; 1999.
172. Strozzi C., Sotton J., Mura A., Bellenoue M. Experimental and numerical study of the influence of temperature heterogeneities on self-ignition process of methane-air mixtures in a rapid compression machine. Combust. Sci. and Tech. 180, 1829-1857 (2008).

173. Strozzi C., (2008). Étude expérimentale de l'auto-inflammation de mélanges gazeux en milieux confines et sa modélisation avec une description cinétique chimique détaille. PhD Thesis, University of Poitiers, France.
174. Stultz S.C., Kitto J.B. Steam - its generation and use. The Babcock & Wilcox Company, Barberton, Ohio USA, 1992.
175. Sun C.J., Sung C.J., He L., Law C K. Dynamics of weakly stretched flames: quantitative description and extraction of global flame parameters. Combustion and Flame 118, 108-128 (1999).
176. Sun H., Yang S.I., Jomaas G., Law C.K. High-pressure laminar flame speeds and kinetic modelling of carbon monoxide/hydrogen combustion. Proc. Combust. Inst. 31, 439-446 (2007).
177. Taillefet T., (1999). Combustion en Milieu Confiné d'un mélange pauvre initiée pair un jet of gaz chauds. PhD Thesis, University of Poitiers, France.
178. Tahtouh T., Fabien H., Christine R. Measurements of laminar burning speeds and Markstein lengths using a novel methodology. Combustion and Flame 156 (9), 1735-1743 (2009).
179. Tschalamoff T. Wood gas operation of spark ignited gas engines in the power range 100-2000 kW. Proceedings of the International Energy Agency Seminar: IC Engines for LCV Gas from Biomass Gasifiers, Zurich, 1997.
180. Tutare, Chandrrkant, Biomass Gasification - Technology and Utilisation. ARTES Institute, Glucksburg, Germany. 1999.
181. Vagelopoulos C.M., Egolfopoulos F.N. Laminar flame speeds and extinction strain rates of mixtures of carbon monoxide with hydrogen, methane, and air Proc. Combust. Inst. 25 1317-1327 (1994).
182. Verhelst, S., (2005). A study of the combustion in hydrogen-fuelled internal combustion engines. Ph.D. Thesis, Ghent University, Belgium. Available at: http://hdl.handle.net/1854/3378.
183. Verhelst S., Sierens R. A quasi-dimensional model for power cycle of a hydrogen-fuelled ICE. Int. J. of Hydrogen Energy 32, 3545-3554 (2007)
184. Verhelst S., Sheppard C.G.W. Multi-zone thermodynamic modeling of spark-ignition engine combustion – An overview. Energy Conversion Management 50, 1326-1335 (2009).
185. Vielhaber K. The use of process gases as sources of heat and power using spark ignition gas engines. Proceedings of the Institution of Diesel and Gas Turbine Engineers. INPOWER 96, London, 1996.

186. Wang D. Czernik S., Montane D., Mann M., Chornet E. Biomass to hydrogen via fast pyrolysis and catalytic steam reforming of the pyrolysis oil or its fractions. Ind. Eng. Chem. Res. 36, 1507-1518 (1997).
187. Warnatz J., Peters N. Stretch effects in plane premixed hydrogen-air-flames. Progress in Astronautics and Aeronautics 95, 61-74 (1984).
188. Wei S. W., kim Y.Y., kim H.J., Lee J.T. A study on transient heat transfer coefficient of in-cylinder gas in the hydrogen fuelled engine. 6th Korea-Kapan Joint Symposium on Hydrogen Energy, 2001.
189. Westbrook C.K., Adamczyk A.A., Lavoie G.A. A numerical study of laminar flame wall quenching. Combustion and Flame 40, 81-89 (1981).
190. Williams F.A. Combustion Theory, 2nd ed., Adison Wesley. 1985.
191. Woschni G. A universal applicable equation for the instantaneous heat transfer coefficient in the internal combustion engine. SAE Technical Paper 670931, (1967).
192. Zeleknik F.J. Combustion modeling in internal combustion engines. Combustion Sci Technol 12, 159–164 (1976).
193. Zimont V.L. Gas premixed combustion at high turbulence. Turbulent flame closure combustion model. Experimental Thermal Fluid Science 21, 179-186 (2000).

Appendix A - OVERDETERMINED LINEAR EQUATIONS SYSTEMS

The system of linear algebraic equations of the form:

$$A\vec{X} = \vec{b}\,, \tag{A-1}$$

Where $A \in IR^{m\times n}$, $\vec{X} \in IR^{n}$, and $\vec{b} \in IR^{n}$ is said to be an overdetermined system if $m>n$ i.e., there are more equations than unknowns.

This type of systems appears as a consequence of experimental errors; in order to obtain a more accurate result one requires more measurements than the strictly necessary ones. For example, curve fitting which is the process of constructing a curve that has the best fit to a series of data points. Given m data points (x_i, y_j) for $i = 1,\ldots m$, we want to adjust these points to a curve of the form:

$$P(x) = a_0 u_0(x) + a_1 u_1(x) + \cdots + a_n u_n(x) = \sum_{j=1}^{n} a_j u_j(x) \tag{A-2}$$

Where u_j ($j=0,\ldots,n$) are linearly independent given functions and a_j ($j=0,\ldots,n$) parameters to be determine.

The linear systems (A-1) only as a solution when $\vec{b}$ belongs to the column space of A. However, it is also possible to determine $\vec{X}$ such that it minimizes some vector norm of the residual

$$\vec{r} = \vec{b} - A\vec{X} \tag{A-3}$$

i.e., determine $\vec{X}$ such that the residual vector $\vec{r}$ is as small as possible.

Due to the differentiability of the Euclidean norm, allowing determining the minimum by the usual process is in general the used norm to minimize the residual. This is called *least squares method.*

The goal of the least squares method is to determine the vector $\vec{X}$ which minimizes the sum of the squared residuals, i.e.,

$$\|r\|^2 = \left\|\vec{b} - A\vec{X}\right\|^2 \tag{A-4}$$

in other words, determine $\vec{X}$ such that $\vec{b} - A\vec{X}$ is close to zero.

Developing the expression (A-4), we obtain:

$$\begin{aligned}\|r\|^2 = \left\|\vec{b} - A\vec{X}\right\|^2 &= \left(\vec{b} - A\vec{X}\right)^T \left(\vec{b} - A\vec{X}\right) \\ &= \vec{X}^T A^T A\vec{X} - 2\vec{X}^T A^T \vec{b} + \vec{b}^T \vec{b}\end{aligned} \tag{A-5}$$

The expression (A-5) is minimized when its gradient with respect to each parameter is equal to zero. The elements of the gradient vector are the partial derivatives of $\|r\|^2$ with respect to each parameter

$$\frac{\partial \|\vec{r}\|^2}{\partial x_i} = 2\sum_{j=1}^{m} r_j \frac{\partial r_j}{\partial x_i}. \tag{A-6}$$

Substituting $r_j = b_j - \sum_{i=1}^{n} A_{ji} x_i$ and its derivative $\frac{\partial r_j}{\partial x_i} = -A_{ji}$ in equation (A-6) follows:

$$\frac{\partial \|r\|^2}{\partial x_i} = -2\sum_{j=1}^{m} A_{ji} \left(b_j - \sum_{k=1}^{n} A_{jk} x_k \right) \tag{A-7}$$

Taking $\frac{\partial \|r\|^2}{\partial x_i} = 0,$ for all *i=1,…n* and upon a rearrangement of (A-7) we obtain the following normal equations

$$\sum_{j=1}^{m} A_{ji} b_j + \sum_{j=1}^{m} \sum_{k=1}^{n} A_{ji} A_{jk} x_k = 0. \tag{A-8}$$

Using matrix notation, the normal equations are given by

$$A^T A\vec{X} - A^T \vec{b} = 0 \tag{A-9}$$

or equivalently by

$$A^T A\vec{X} = A^T \vec{b} \tag{A-10}$$

This is a system of *n* equations and *n* unknowns for which a solution is expected.

In order to prove the existence and unicity of solution of the normal equations (A-10) it is necessary to prove that: *The matrix $A^T A$ is invertible if and only if the columns of the matrix A are linearly independent.*

If the columns of *A* would be linearly independent, then it implies that $A\vec{X} \neq 0$. Therefore, we have:

$$\left\| A\vec{X} \right\|^2 = \left(A\vec{X} \right)^T \left(A\vec{X} \right) = \vec{X}^T \left(A^T A \right) \vec{X} > 0, \quad \forall \vec{X} \neq 0 \tag{A-11}$$

which means that $A^T A$ is a symmetric positive definite matrix, consequently invertible.

Let us now assume that $A^T A$ it is not invertible. In this case there exits a vector $\vec{X} \neq 0$ such that $A^T A\vec{X} = 0$, i.e.,

$$\vec{X}^T A^T A\vec{X} = 0 \Rightarrow \left(A\vec{X} \right)^T \left(A\vec{X} \right) = \left\| A\vec{X} \right\|^2 = 0 \Rightarrow A\vec{X} = 0 \tag{A-12}$$

Therefore, we concluded that the columns of *A* are not linearly independent.

The existence and unicity of a solution of the normal equations depend on the linear independence of the columns matrix associated. In the case of curve fitting, where the curve *P* takes the form

$$P(x) = \sum_{j=1}^{n} a_j u_j \left(x \right) \tag{A-13}$$

we have that the elements of the matrix *A* are given by

$$A_{ij} = u_j \left(x_i \right) \tag{A-14}$$

Therefore, the linear independence of the columns of *A* depends on the functions u_j and on the number and localization of the points x_i, In general, it is not easy to know *a priori* if that linear independence is verified.

At this point we guaranty the existence and unicity of solutions of normal equations (A-10). Our next goal is to prove that this solution gives us the minimum residue, i.e., the solution $\vec{X}$ of the equation (A-10) satisfies the relation

$$\left\|\vec{b} - A\vec{X}\right\| \le \left\|\vec{b} - A\vec{Y}\right\|, \quad \forall \vec{Y} \in R^n \tag{A-15}$$

Rewriting $\vec{b} - A\vec{Y}$ as

$$\vec{b} - A\vec{Y} = \left(\vec{b} - A\vec{X}\right) + A\left(\vec{X} - \vec{Y}\right) \tag{A-16}$$

and taking the norm, we obtain

$$\begin{aligned} \left\|\vec{b} - A\vec{Y}\right\|^2 &= \left\|\left(\vec{b} - A\vec{X}\right) + A\left(\vec{X} - \vec{Y}\right)\right\|^2 \\ &= \left(\left(\vec{b} - A\vec{X}\right) + A\left(\vec{X} - \vec{Y}\right)\right)^T \left(\left(\vec{b} - A\vec{X}\right) + A\left(\vec{X} - \vec{Y}\right)\right) \\ &= \left\|\left(\vec{b} - A\vec{X}\right)\right\|^2 + 2\left(A\left(\vec{X} - \vec{Y}\right)\right)^T \left(\vec{b} - A\vec{X}\right) + \left\|A\left(\vec{X} - \vec{Y}\right)\right\|^2 \end{aligned} \tag{A-17}$$

Moreover, by (A-9) we have

$$\left(A\left(\vec{X} - \vec{Y}\right)\right)^T \left(\vec{b} - A\vec{X}\right) = \left(\vec{X} - \vec{Y}\right)^T A^T \left(\vec{b} - A\vec{X}\right) = 0 \tag{A-18}$$

Therefore, we conclude:

$$\left\|\vec{b} - A\vec{Y}\right\|^2 = \left\|\left(\vec{b} - A\vec{X}\right)\right\|^2 + \left\|A\left(\vec{X} - \vec{Y}\right)\right\|^2 \ge \left\|\left(\vec{b} - A\vec{X}\right)\right\|^2 \tag{A-19}$$

The equality in (A-19) only occurs when $A\left(\vec{X} - \vec{Y}\right) = 0$. Furthermore, once the columns of the matrix A are linearly independent, then $A\left(\vec{X} - \vec{Y}\right) = 0$ which implies that $\left(\vec{X} - \vec{Y}\right) = 0$, i.e., $\vec{X} = \vec{Y}$.

Appendix B - SYNGAS-AIR MIXTURE PROPERTIES

P_i (bar)	ϕ	P_v (bar)	C_p/C_v	T_v (K)	ρ_u (kg/m^3)	ρ_b (kg/m^3)	μ (m^2/s)	α (m^2/s)
Updraft syngas-air mixture properties								
0.5	0.6	2.980	1.395	1859.5	0.581	0.09621	3.08E-05	4.24E-05
	0.8	3.312	1.394	2091.2	0.5773	0.10426	3.08E-05	4.32E-05
	1	3.494	1.393	2218.6	0.5743	0.09624	3.09E-05	4.39E-05
	1.2	3.373	1.392	2125.2	0.5718	0.10298	3.09E-05	4.44E-05
1.0	0.6	5.962	1.395	1860.2	1.162	0.23535	1.54E-05	2.12E-05
	0.8	6.637	1.394	2095.8	1.1546	0.20854	1.54E-05	2.16E-05
	1	7.026	1.393	2232.7	1.1486	0.19289	1.54E-05	2.19E-05
	1.2	6.752	1.392	2127.3	1.1437	0.20415	1.54E-05	2.22E-05
2.0	0.6	11.927	1.395	1860.8	2.324	0.38485	7.69E-06	1.06E-05
	0.8	13.293	1.394	2099.3	2.3093	0.41702	7.70E-06	1.08E-05
	1	14.119	1.393	2245.2	2.2973	0.38508	7.71E-06	1.10E-05
	1.2	13.511	1.392	2128.7	2.2874	0.41192	7.72E-06	1.11E-05
5.0	0.6	29.825	1.395	1861.3	5.8101	1.17669	3.08E-06	4.24E-06
	0.8	33.281	1.394	2102.7	5.7731	1.04223	3.08E-06	4.32E-06
	1	35.491	1.393	2259.5	5.7432	0.9608	3.09E-06	4.39E-06
	1.2	33.796	1.392	2129.9	5.7184	1.02068	3.09E-06	4.44E-06
Downdraft syngas-air mixture properties								
0.5	0.6	2.914	1.393	1838.2	0.5743	0.1187	3.10E-05	4.54E-05
	0.8	3.218	1.392	2057.5	0.5695	0.10573	3.11E-05	4.67E-05
	1	3.383	1.391	2179.4	0.5657	0.09825	3.12E-05	4.77E-05
	1.2	3.252	1.390	2080.8	0.5626	0.10387	3.13E-05	4.86E-05
1.0	0.6	5.829	1.393	1838.8	1.1486	0.23738	1.55E-05	2.27E-05
	0.8	6.447	1.392	2061.4	1.139	0.2114	1.56E-05	2.33E-05
	1	6.800	1.391	2192.1	1.1314	0.19613	1.56E-05	2.39E-05
	1.2	6.508	1.390	2082.4	1.1252	0.20774	1.56E-05	2.43E-05
2.0	0.6	11.662	1.393	1839.8	2.2971	0.47475	7.76E-06	1.13E-05
	0.8	12.910	1.392	2064.5	2.2781	0.42271	7.78E-06	1.17E-05
	1	13.660	1.391	2203.2	2.2628	0.39163	7.80E-06	1.19E-05
	1.2	13.021	1.390	2083.5	2.2504	0.41546	7.82E-06	1.21E-05
5.0	0.6	29.162	1.393	1839.9	5.7428	1.18683	3.10E-06	4.54E-06
	0.8	32.314	1.392	2067.4	5.6952	1.05657	3.11E-06	4.67E-06
	1	34.318	1.391	2215.8	5.6571	0.97742	3.12E-06	4.77E-06
	1.2	32.566	1.390	2084.4	5.6259	1.03903	3.13E-06	4.86E-06
Fluidized-bed syngas-air mixture properties								
0.5	0.6	2.851	1.388	1736.5	0.5944	0.12579	2.97E-05	4.03E-05
	0.8	3.186	1.386	1955.5	0.5933	0.11167	2.96E-05	4.07E-05
	1	3.395	1.384	2091.4	0.5923	0.10314	2.95E-05	4.11E-05
	1.2	3.203	1.382	1946.7	0.5916	0.11111	2.94E-05	4.13E-05
1.0	0.6	5.703	1.388	1736.8	1.1888	0.25158	1.49E-05	2.02E-05
	0.8	6.378	1.386	1957.4	1.1865	0.22329	1.48E-05	2.04E-05
	1	6.816	1.384	2100.4	1.1847	0.20604	1.47E-05	2.05E-05
	1.2	6.406	1.382	1947.1	1.1831	0.22221	1.47E-05	2.07E-05
2.0	0.6	11.406	1.388	1737	2.3776	0.50315	7.43E-06	1.01E-05
	0.8	12.764	1.386	1958.9	2.3731	0.44653	7.40E-06	1.02E-05
	1	13.675	1.384	2108.1	2.3694	0.41168	7.37E-06	1.03E-05
	1.2	12.814	1.382	1947.4	2.3663	0.44441	7.34E-06	1.03E-05
5.0	0.6	28.52	1.388	1737.3	5.9439	1.25785	2.97E-06	4.03E-06
	0.8	31.931	1.386	1960.3	5.9327	1.11623	2.96E-06	4.07E-06
	1	34.307	1.384	2116.7	5.9234	1.02815	2.95E-06	4.11E-06
	1.2	32.04	1.382	1947.7	5.9157	1.11102	2.94E-06	4.13E-06

Appendix C – RIVÈRE MODEL

The heat flux received by the wall is modelled using an original heat conduction approach in the fluid-wall boundary based on the kinetic theory of gases developed by Rivère, (2005), from Renault. The heat flux appears as a statistic result of the gas molecules over the wall. Random reflection is assumed in direction, not in module. Each gas molecule yields kinetic energy ΔE_c when collides with the wall, characterized by the kinetic energy fraction K:

$$\Delta E_c = E_c - E_c^{'} = \frac{1}{2} m_g \cos(\theta)\left(V^2 - V'^2\right) \qquad K = \frac{E_c - E_c^{'}}{E_c} = \frac{V^2 - V'^2}{V^2} \tag{C.1}$$

With m_g the molecular mass, θ the impact angle, V and V' the impact and reflection speeds (Figure C.1).

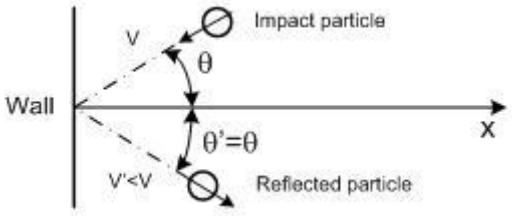

Figure C.1 – Fraction of energy received by the wall.

In order to know the kinetic energy fraction K yielded by one molecule of gas during rebound, the wall is modelled by a linear chain of atoms vibrating by translation along x only. The calculus shows that n=2 atoms are enough to take into account the phenomenon (Figure C.2). The cases of harmonic and non-harmonic systems are considered.

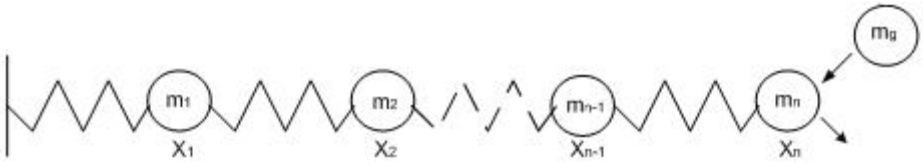

Figure C.2 – Molecules translation movement.

As a result of this calculation, the transfer coefficient K is obtained with error of about 2%. This coefficient is dependent of the gas temperature, which in turns determines the thickness of the thermal boundary layer.

$$K = \eta + \frac{\chi}{\sqrt{T_g}} - \frac{\lambda}{T_g} \tag{C.2}$$

With η,λ, and χ the integration constants to be determined using experimental results.

Heat flux

The gases, with a mean speed U_0 along X, are supposed to follow the speed distribution of Maxwell-Boltzmann. The particles volume density dn_g, which the thermal stirring speed is in the range [V; $V+dV$] is then:

$$dn_g = n_g \left(\frac{a_g}{\pi}\right)^{\frac{3}{2}} 4\pi V^2 e^{-a_g(\vec{V}-\vec{U}_0)^2} dV \tag{C.3}$$

With $a_g = M/2RT$, M is the gas molar mass and R the ideal gases constant. The number of particles dN_g with impact speed V on a surface dS during dt is:

$$dN_g = \frac{1}{2}\sin\theta\cos\theta.V.dt.dn_g.dS.d\theta \tag{C.4}$$

The elementary heat flux is then:

$$dQ = \Delta E_c\, dN_g = \rho_g \sin(\theta)\cos^3(\theta).\left(\frac{a_g}{\pi}\right)\pi.K.V^5 e^{-a_g(V-U_0)^2} dV.dt.dS.d\theta \tag{C.5}$$

Heat flux integration

Back to the heat flux actually received by the wall, the elementary flux dQ must be integrated on the thermal boundary layer thickness δ (Figure C.3) . This thickness is discretized with a step equal to the mean gas molecules path $\bar{\lambda}$.

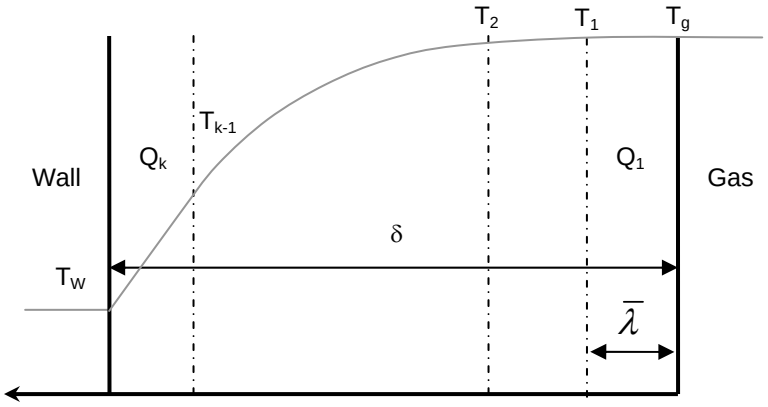

Figure C.3 – Thermal boundary layer.

The thickness can be estimated based on the mean free path $\bar{\lambda}$:

$$\delta = \frac{4}{3}\frac{\bar{\lambda}}{K}\sqrt{\frac{T_w}{T_g}} \tag{C.6}$$

The temperature profile of the thermal boundary layer is linearly fitted. The integration of the wall heat flux Q_w based on the elementary heat flux dQ shows a temperature difference between the gas and wall $\Delta T=T_g-T_w$:

$$Q_w = \rho_g.a\left(\frac{\eta}{\sqrt{\varpi}} + \frac{\chi}{\varpi\sqrt{T_g}} - \frac{\lambda}{\varpi^{3/2}T_g}\right).\left(\sqrt{\frac{a\varpi T_g}{4\pi}} + \frac{15}{32}U_0\left(1+\frac{\alpha\Delta T}{4\varpi T_g}\right)\right)\Delta T \tag{C.7}$$

With a, α and ω calcul parameters.

A heat transfer coefficient is then defined as $Q_w=h.\Delta T$. As the term U_0 is representative of the overall movement, is negligible compared with the term related to the thermal agitation in T_g, the expression simplifies as follows:

$$h = \rho_g.\sqrt{T_g}\sqrt{\frac{2}{\pi}}\left(\frac{R}{M}\right)^{\frac{3}{2}}\left(\eta + \frac{\chi}{\sqrt{T_w}} - \frac{\lambda}{T_w}\right) \tag{C.8}$$

Where ρ_g, T_g and M are, respectively, the density, the temperature and molar mass of the gases, T_w the wall temperature, χ and λ material constants and η a function of the aerodynamic conditions.

Integration constants evaluation

χ, λ and η are determined based on engine experimental results for several running conditions and combustion modes: spark ignition, compression ignition, controlled auto-ignition, etc.

χ and λ are constants wall related, hence identical for every engine experiments. On the other hand, η is flow dependent and follows a variation law under the conditions of operation. After the engine experiments, the evolution of η is linear in function of engine regime, e.g. mean piston speed:

$$\eta_{engine} = a + b < V_{piston} > \tag{C.9}$$

With a=7×10^{-4}, b=7×10^{-5}(m/s)$^{-1}$, $<V_{piston}>$ the mean piston speed around 2-10 m/s.

The work of Boust, (2006) also defines the evolution of η based on "fluid" speed seen by the wall instead of the mean piston speed, as follows:

$$\eta = \min\left(b'V^{0.5}, b''V^{0.2}\right) \tag{C.10}$$

With b'=5×10^{-4} (m/s)$^{-0.5}$ and b''= 8×10^{-4} (m/s)$^{-0.2}$, V is the local speed around 0-25 m/s.

Final formulation

The model of heat losses by conduction can be summarized as follows:

$$Q_w = h\left(T_g - T_w\right)$$

with

$$h = \rho_g \cdot \sqrt{T_g} \sqrt{\frac{2}{\pi}} \left(\frac{R}{M}\right)^{\frac{3}{2}} \left(\eta + \frac{\chi}{\sqrt{T_w}} - \frac{\lambda}{T_w}\right)$$

Where:

ρ_g, the gases density local

T_g the gases local temperature

R = 8.314 J/mol K, ideal gas constant.

M the gases molar mass

T_w the local wall temperature,

χ =0.0318 K$^{1/2}$ and λ= 0.37 K material constants

Engine (Rivère, 2005):

$$\eta_{engine} = a + b < V_{piston} >$$

With a=7×10^{-4}, b=7×10^{-5}(m/s)$^{-1}$, <V_{piston}> the mean piston speed around 2-10 m/s

Other conditions (Boust, 2006):

$$\eta = \min\left(b'V^{0.5}, b''V^{0.2}\right)$$

With b'=5×10^{-4} (m/s)$^{-0.5}$ and b''= 8×10^{-4}(m/s)$^{-0.2}$, V is the local speed around 0-25 m/s.

COMBUSTION STUDY OF MIXTURES RESULTING FROM A GASIFICATION PROCESS OF FOREST BIOMASS

Abstract

Syngas is being recognized as a viable energy source worldwide, particularly for stationary power generation. In the current work, three typical syngas compositions have been considered as representative of the syngas resultant from forest biomass gasification, and the possibility of using it in internal combustion engines is studied. First, laminar burning velocities have been determined from schlieren flame images at normal temperature and pressure, over a range of equivalence ratios within the flammability limits. The study of the effects of flame stretch rate is performed through the determination of Karlovitz and Markstein numbers. Second, because of the gaps in the fundamental understand of syngas combustion characteristics, especially at elevated pressures that are relevant to practical combustors, constant volume spherical expanding flames were employed to measure the laminar burning velocity for pressures ranges up to 20 bar. This information on laminar burning velocity of syngas-air flames is then applied in a multi-zone heat transfer simulation code of the wall-flame interaction in order to predict the quenching distance of typical syngas-air flames. Engine-like turbulent conditions were experimentally reproduced in a rapid compression machine (RCM) when working on two strokes mode simulating a single cycle of an internal combustion engine. Stationary power applications usually use natural gas as fuel, thus a methane-air mixture is also included in this work as a reference fuel for comparison with the typical syngas compositions under study. Single compression tests were also performed in the RCM operating with and without combustion in order to identify different parameters related with its operation, namely the heat transfer to the walls. A simulation code for the power cycle of syngas-fuelled engines has been developed. Model validation has been carried on over detailed experimental data available in literature for hydrogen and methane. An attempt to adapt the model to the RCM is made by changing several aspects of the model namely the in-cylinder volume function and burning rate model. Conclusion could e drawn that the adapted code is able to reproduce the in-cylinder pressure. The validated model is then applied to a syngas-fuelled engine in order determine its performance. Conclusion can be drawn that typical syngas compositions besides its lower heat values and burning velocities can be used on SI engines even at elevated rotation speeds.

Keywords: Gasification – Syngas - Combustion – Burning velocity – Rapid compression machine - Multi-zone modeling.